Università
degli Studi
di Padova

Sede Amministrativa: Università degli Studi di Padova

Dipartimento di Scienze Chimiche

Scuola di dottorato di ricerca in scienza ed ingegneria dei materiali
Ciclo: XXVI

Modelling of chirality propagation in self-assembling systems

Direttore della Scuola di Dottorato:
Ch.mo Prof. Gaetano Granozzi

Supervisore:
Prof.ssa Alberta Ferrarini

Dottoranda:
Elisa Frezza

2013-2014

"It is surprising that people do not believe that there is imagination in science. It is a very interesting kind of imagination, unlike that of the artist. The great difficulty is in trying to imagine something that you have never seen, that is consistent in every detail with what has already been seen, and that is different from what has been thought of; furthermore, it must be definite and not a vague proposition. That is indeed difficult."

— Richard P. Feynman, *The Meaning of It All: Thoughts of a Citizen-Scientist*

"Before the advent of multiscale modeling, the primary approach to addressing questions in chemistry was through experiment and the application of theory. The development of computational models created a new paradigm for solving problems in chemistry, a "third way" that stands between theory and experiment. The fundamental principles of physics and chemistry are used to create "in silico" representations of systems that can be interrogated at a level of detail that cannot be approached by experiment or captured by a single theory. Complex problems in chemical, biological, materials, and energy science are now routinely approached using a synergistic combination of theory, computational modeling, and experiment."

— John E. Straub, JCP Associate Editor, *comment on 2013 Chemistry Nobel Prize*

Contents

List of Figures

List of Tables

List of Acronyms and Symbols

ACRONYMS

A	Adenine
AA	All Atom
AMBER	Assisted Model Building with Energy Refinement
bp	Base pair
C	Cytosine
CD	Circular Dichroism
CG	Coarse-Grained
DFT	Density Functional Theory
DNA	Deoxyribonucleic acid
dsDNA	Double stranded DNA
l-DNA	Long DNA
FF	Force Field
G	Guanosine
GROMACS	GROningen MAchine for Chemical Simulations
I	Isotropic
LC	Liquid Crystal
L	Left-handed
MAG	[Leu^{21}]Magainin (GIGKFLHSAKKFGKAFVGEILNS)
MC	Monte Carlo
MD	Molecular Dynamics
N	Nematic phase
N*	Cholesteric phase

N_s^*	Screw-like nematic phase
NA	Nucleic Acid
dsNA	Double stranded Nucleic Acid
pdb	Protein Data Bank
R	Right-handed
Sm	Smectic phase
T	Thymine
TPP	5-(4′-carboxyphenyl)-10,15,20-triphenylporphyrin
TPP-MAG	TPP-[Leu^{21}]Magainin conujgate
U	Uracil
ua	united atom

SYMBOLS

$\mathbf{b}$	vector
b	scalar
$\hat{\mathbf{b}}$	versor
$\cdot$	scalar product
$\wedge$	vector product
A	Helmholtz free energy
a	Helmholtz free energy density
D	diameter
k_B	Boltzmann constant
k_2	chiral strength
K_{22}	twist elastic constant
L	Lenght
μ	chemical potential
m	mass
N	number of molecule
$\mathbf{\Omega}$	Euler angles $(= (\alpha, \beta, \gamma))$
$\langle P_2 \rangle$	nematic order parameter

p	pitch
p_{N^*}	cholesteric pitch
P	pressure
q	cholesteric wavenumber
r	radius
T	temperature
v_0	molecular volume
V	volume
ρ	number density ($= N/V$)
v	volume per molecule ($= 1/\rho$)
X_0	aspect ratio $(= L/D)$
ϕ	volume fraction or packing density ($= v/v_0$)

Abstract

Hierarchical self-assembly is a process in which molecular building blocks form intermediate structures that self organise at macroscopic level. Remarkable examples can be found in nature, like, for instance, DNAs or viruses. Self-assembly offers interesting strategies to build new complex materials: Therefore, it is very important to understand its mechanism to design and control molecular architectures and to build structures with desired properties and morphologies. A major question is how the shape of the building blocks influences self-assembly. In this context, chirality plays a crucial role: It is extremely sensitive to subtleties on the molecular scale and can guide self-assembly; furthermore, chirality can act as an amplifier of changes that occur at the molecular level.

From the theoretical point of view, the difficulty derives from the need of multiscale methods and models, able to connect the different length scales. To take into account the relationship among the building blocks, their supramolecular organization, and the properties of the aggregates, a detailed representation of intermolecular interactions is needed: This description has to be integrated into a suitable modeling of the system behaviour on a much longer length scale.

This thesis deals with the development and implementation of models for chirality propagation from the molecular to the meso- and macroscopic levels in self-assembling systems. In particular, the research has been carried out along three lines. The first deals with self-assembly of hard helices, leading to the formation of anisotropic phases of various symmetry. The second topic is the linear aggregation and formation of liquid crystal phases by double-stranded nucleic acid oligomers (dsNA): The relationship between the sequence of oligonucleotides, their self-assembly and the properties of their cholesteric phase is investigated. The last topic is the aggregation of porphyrin-polypeptide conjugates in water.

Depending on the problem and the length scale, we used different theoretical and computational methods, in particular: Statistical theories of liquids and molecular dynamics simulations (both atomistic and coarse-grained). The first and third topics have been carried out in collaboration with experimentalists, while for the second other groups of theoreticians have been involved.

This thesis is organized in three parts. In Chapter 1, the concepts of self-assembling, chirality propagation and multiscale modeling are introduced. Moreover this Chapter presents an outline of the main properties of liquid crystals.

The first Part, from Chapter 2 to Chapter 4, presents the study on the anisotropic phases formed by hard helices. Chapter 2 presents a study of the nematic phase, using an Onsager-like theory. The theoretical results are compared with Monte Carlo simulations. In Chapter 3, a theoretical model for the cholesteric phase is presented and used to investigate the relationship between the helical shape and the properties of the cholesteric phase. In Chapter 4, the complete phase diagram of hard helices is presented, together with the characterization of a novel chiral nematic phase.

The second Part deals with liquid crystal phases formed by dsNA. Chapter 5 focuses on the relation between the sequence of oligonucleotides and their organization in the cholesteric phase, using a molecular theory and coarse-grained modelling based on sequence dependent structural data. Chapter 6 describes the theoretical model for the cholesteric phase formed by self-assembling oligomers, which integrates the theory for cholesteric order presented in Chapter 3 with that for linear aggregation in the nematic phase.

The last Part, from Chapter 7 to Chapter 9, deals with the aggregation of porphyrin-peptide conjugates in water. In Chapter 7 the main concepts of circular dichroism are introduced and the state-of-the-art of self-assembly of porphyrins is reviewed. Chapter 8 describes atomistic molecular dynamics simulation of aggregates of porphyrin-peptide conjugates. Chapter 9 presents a study of the same systems by coarse-grained molecular dynamics simulations, using the MARTINI model. Finally, Chapter 10 presents a summary, which highlights the relevant results obtained in this Thesis, and three Appendices follow.

Sommario

L'autoassemblaggio gerarchico è un processo nel quale "building block" molecolari formano strutture intermedie che si auto-organizzano a livello macroscopico. Molti esempi possono essere trovati in natura, come il DNA o i virus. L'autoassemblaggio offre interessanti strategie per costruire nuovi materiali complessi: di conseguenza, risulta molto importante capirne i meccanismi per disegnare e controllare le architetture molecolari e per costruire strutture con proprietà e morfologie desiderate. Uno dei principali quesiti cui dare risposta è come la forma del building block influenzi l'autoassemblaggio. In questo contesto, la chiarità svolge un ruolo cruciale: è estremamente sensibile ai dettagli molecolari e può guidare l'autoassemblaggio; inoltre, essa può amplificare le differenze che avvengono su scala molecolare.

Dal punto di vista teorico, la difficoltà deriva dalla necessità di metodi e modelli multiscala, capaci di connettere le differenti scale di lunghezza. Per tenere in considerazione la relazione tra i building blocks, la loro organizzazione supramolecolare e le proprietà degli aggregati, si rende necessaria una rappresentazione dettagliata delle interazioni intermolecolari: questa descrizione deve poi essere integrata in una modellizazione opportuna del comportamento del sistema su scale di lunghezza più grandi.

Il tema di questa tesi è lo sviluppo e l'implementazione di modelli per la propagazione di chiralità dalla scala molecolare alla scala meso e macroscopica in sistemi autoassemblati. Tre diverse linee di ricerca sono state portate avanti. La prima si è concentrata sull'autoassemblaggio di eliche dure, ed in particolare sulla formazione di fasi anisotrope di diversa simmetria. Il secondo argomento riguarda l'aggregazione lineare e la formazione di fasi liquido-cristalline a partire da oligomeri di acidi nucleici a doppio filamento prendendo in considerazione le relazioni tra la sequenza di oligonucleotidi, l'autoassemblaggio e le proprietà della loro fase colesterica. L'ultimo argomento è dedicato all'autoassemblaggio di coniugati porfirina-peptide in acqua.

In base al problema e alla scala di lunghezza, sono stati utilizzati diversi metodi teorici e computazionali, in particolare: teorie statistiche dei liquidi e simulazioni di dinamica molecolare (sia atomistica che a grana grossa). La prima e la terza linea di ricerca sono stati condotte in collaborazione con sperimentali, mentre la seconda ha coinvolto altri gruppi teorici.

La tesi è organizzata in tre parti. Nel Capitolo 1, il processo di autoassemblaggio, la propagazione di chiralità e il concetto di modellizzazione multiscala vengono descritti. Inoltre in questo Capitolo si presentano le principali proprietà dei cristalli liquidi.

Nella prima Parte, dal Capitolo 2 al Capitolo 4, viene presentato il lavoro svolto sulle fasi anisotrope di eliche dure. Il Capitolo 2 presenta lo studio della fase nematica usando una teoria Onsager-like. I risultati teorici sono confrontati con simulazioni Monte Carlo. Nel Capitolo 3, viene presentato un modello teorico per la fase colesterica utilizzato poi per studiare l'effetto della forma elicoidale sulle proprietà della fase colesterica. Nel Capitolo 4 viene presentato l'intero diagramma di fase delle eliche dure, assieme alla caratterizzazione di una nuova fase nematica chirale.

La seconda Parte concerne le fasi liquido-cristalline formate da *dsNA*. Il Capitolo 5 si focalizza sulla relazione tra la sequenza di oligonucleotidi e la loro organizzazione nella fase colesterica utilizzando una teoria molecolare e la modellizzazione a grana grossa, basata su dati strutturali dipendenti dalla sequenza. Nel Capitolo 6, viene descritto il modello teorico per la fase colesterica formata da oligomeri autoassemblati, che mette assieme la teoria per l'ordine colesterico presentata nel Capitolo 3 con quella dell'aggregazione lineare in fase nematica.

L'ultima Parte, dal Capitolo 7 al Capitolo 9, si concentra sull'aggregazione di coniugati porfirina-peptide in acqua. Nel Capitolo 7, vengono introdotti i principali concetti relativi al dicroismo circolare e viene commentato lo stato dell'arte dell'autoassemblaggio di porfirine. Il Capitolo 8 descrive le simulazioni atomistiche di dinamica molecolare di aggregati porfirina-peptide . Capitolo 9 presente uno studio degli stessi sistemi condotto attraverso simulazioni di dinamica molecolare a grana grossa, che utilizzano il modello MARTINI. Infine, il Capitolo 10 presenta un sommario delle tre linee di ricerca, mettendo in evidenza i risultati notevoli ottenuti in questa tesi. Seguono poi tre Appendici.

Part I

Introduction

Chapter 1

Introduction

1.1 Self-assembly and propagation of chirality

The term *self-assembly* has been defined by Whitesides [1] as:

> "*the autonomous organization of components into patterns or structures without human intervention. They involve components from the molecular (crystals) to the planetary (weather systems) scale and many different kinds of interactions.*"

The size of the building blocks, e.g. small molecules, macromolecules or colloidal particles, can vary from few angstroms to microns, thus making self-assembly ubiquitous in nature and of interest in several fields, including materials science, soft matter and biophysics [1–3]. Understanding the relation between building blocks and their assemblies is essential for materials design because chemical and physical properties depend intimately on structure. Through self-assembly it is possible to design new materials whose physical properties are controlled by tuning the interactions of the building blocks [4–8].Recent investigations have revealed the unexpected complexity of the ordered structures obtained by changing the shape of hard particles [9, 10]. Figure 1.1 shows an example of how the shape of the particles can influence the self-assembled structures, leading to a variety of liquid crystals, plastic crystals, or crystals [9].

A relevant self-assembly process is the formation of filamentous aggregates induced by the anisotropy of interactions, by micellar systems [11–13], formation of fibers and fibrils [14–17], B-DNA composed of 10^2 to 10^6 base pairs [18–22], filamentous viruses [23–26], chromonic liquid crystals [27] as well as colloidal suspensions of inorganic nanoparticles [28] or rods [29]. If self-assembled linear aggregates possess sufficient rigidity, the system may exhibit liquid crystal (LC) phases.

In this context, chirality plays a crucial role: Chirality is extremely sensitive to subtleties on the molecular scale and can guide the self-assembly; moreover, chirality can propagate from the molecular level to *supramolecular level*, by formation of chiral aggregates. The common motif of chiral aggregates is a helical superstructure [30–32]. These architectures can have different complexity, length scale and can be obtained via hierarchical self-assembly processes.

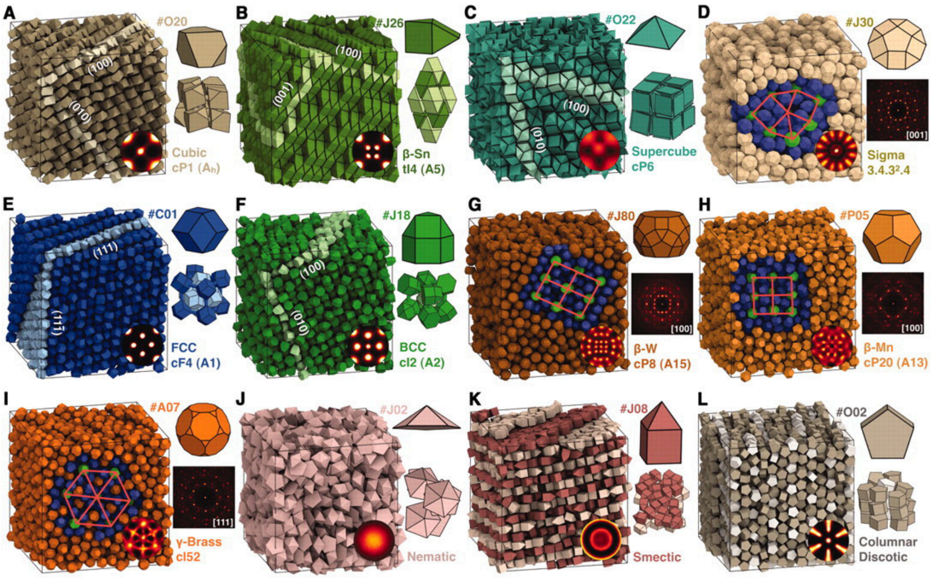

Figure 1.1: Example of systems of polyhedra assembled starting from the disordered fluid. The snapshots depict crystals (A to D), plastic crystals (E to I), and liquid crystals (J to L) . From [9]. Reprinted with permission from AAAS.

Figure 1.2 shows three examples of chiral aggregates. Figure 1.2(a) shows an example of a helical aggregate constituted by porphyrins, whose typical dimensions are in the range some tens of nm to some μm [33–35]. Figure 1.2(c) shows a cartoon of the cholesteric phase, which is a liquid crystal phase exhibited by chiral polymers at high density and is characterized by the pitch of supramolecular helix with the dimensions of some micrometers. Figure 1.2(b) is a typical example of hierarchical self-assembly: At lower level, crown-ether phthalocyanines self-assemble in helical aggregates which organize themselves into a superhelix structure. At higher level, these superhelices self-assemble into chiral fibers with dimension of tens of micrometers [36, 37]. Therefore, in this field different length scales are involved and the transmission of chirality from the molecular level of the building block to the macro- or supra-molecular level in the form of helical assembly is a general issue. A small chiral imbalance at the molecular level can be amplified in the helical structure. Understanding the mechanism of transmission of chirality at different length scales is of great significance in artificial systems and biopolymers and understanding how to control and tune it offers ample opportunities towards smart materials [31, 32].

1.1.1 Multiscale modelling

Self-assembly and chirality propagation are typical examples where a *multiscale approach* is needed [38, 39]. By definition, this entails the application of modelling techniques at two or more different lengths and/or times scales, which are different in their theoretical character. In fact a challenging task is often to bring together different scales. We can make a distinction between the *hierarchical approach* [40, 41], which involves running separate models with some sort of parametric coupling, and the *hybrid approach* [42, 43], in which models are

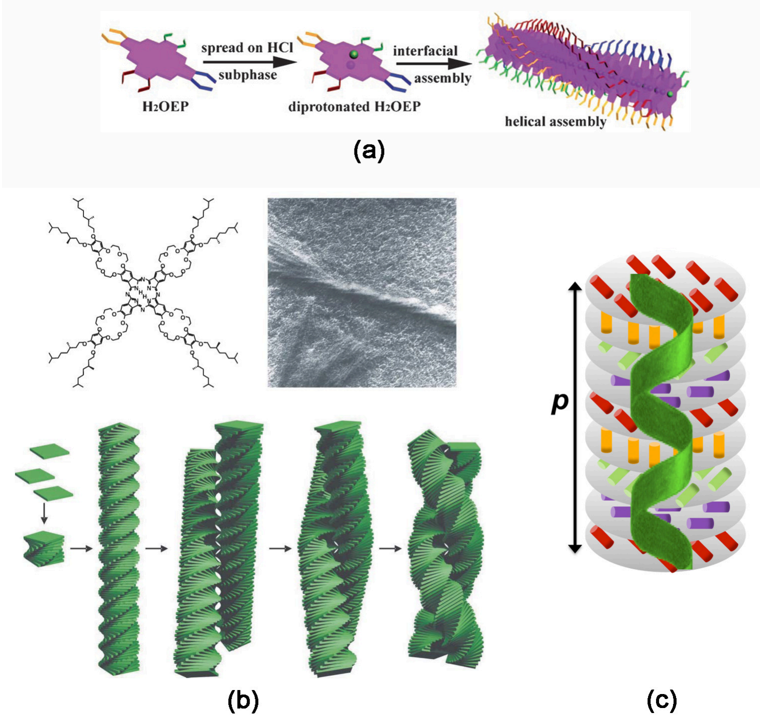

Figure 1.2: (a) Helical aggregate of porphyrins. Reproduced with permission from ref. [33]. Copyright 2008 Wiley-VCH Verlag GmbH&Co. KGaA, Weinheim. (b) Schematic representation of the hierarchical self-assembly of crown-ether phthalocyanine. Reproduced with permission from ref. [37]. Copyright 2003 Royal Society of Chemistry. (c) Schematic representation of the cholesteric phase.

run concurrently over different spatial regions of a simulation. The relationships between different categories of methods commonly used in the multiscale modelling hierarchy are shown in Figure 1.3. At lower level, quantum mechanical modelling methods, e.g. electronic DFT or *ab initio* methods, are used to study electronic structure of single molecules or condensed phases. At next level, molecular modelling is needed. The common methods are Molecular Dynamics (MD) and Monte Carlo (MC). At mesoscopic level, the system is still too small to be regarded as a continuum, yet too large to be simulated effectively using atomistic methods. Hence coarse-grained models and statistical mechanics methods are commonly used. Finally, when the length scale is of the order of some micrometers, continuum theory can be used. A common way of modelling such systems is the finite element method. In this Thesis, we connected the atomistic scale with mesoscale: An example is given by the cholesteric phase of DNA, where the chirality of the molecule is propagated to the chirality of the phase and the length scales involved are from Angstrom to μm (see below).

1.2 Liquid crystals

Matter exists in one of several states such as, for example, solid, liquid, or gas having different degree and type of positional and orientational order. These states can be transformed one

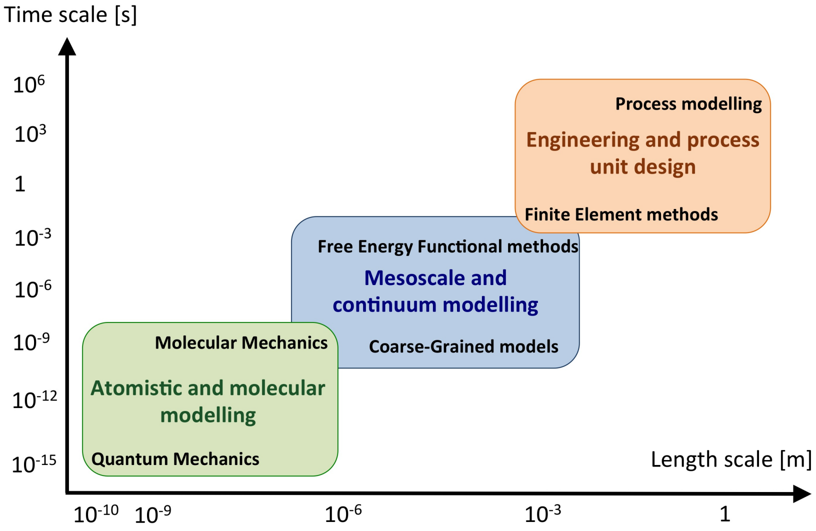

Figure 1.3: Scheme of the hierarchy of multiscale modelling techniques. Different ranges of temporal and spatial scales covered by different categories of methods are shown. Areas of overlap permit "mapping" from one scale to the next.

to another under appropriate conditions. The term *Liquid Crystal* (LC) indicates phases where the molecules present orientational order at long range, while there is only partial or missing transitional order. There are two classes of liquid crystals: *Thermotropics*, that exhibit phase transition as function of the temperature, and *lyotropics*, where the phase transition is controlled by the concentration of the molecules in a solvent (for example water).

The molecules that form liquid crystal phases are characterized by anisotropic shape, hence they have also anisotropic intermolecular interactions. Thermotropic liquid crystals are characterised by molecules with a rigid core, usually aromatic rings, and one or more flexible chains. Examples of lyotropic liquid crystals are micelles, membranes, and dense solutions of rigid or semi flexible polymers, i.e. DNA and virus.

There are different types of liquid crystalline phases, classified according to the dimensionality of the translational correlations of building units. The basic types are: Nematic (no translational correlations), smectic (1D correlation), columnar (2D) and various 3D-correlated structures, such as cubic phases.

1.2.1 Nematic and cholesteric phase

Uniaxial *nematics* (N) are optically uniaxial phases (see Figure 1.4). The unit vector $\hat{\mathbf{n}}$ along the optical axis is called director and the directions $\hat{\mathbf{n}}$ and $-\hat{\mathbf{n}}$ are equivalent. The symmetry point group of the N phase is $D_{\infty h}$.

A measure of the alignment of the molecules is given by the order parameter P_2, defined

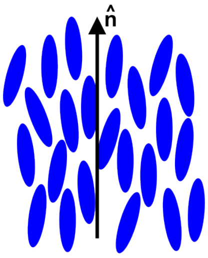

Figure 1.4: Schematic representation of nematic liquid crystal with director **n̂**.

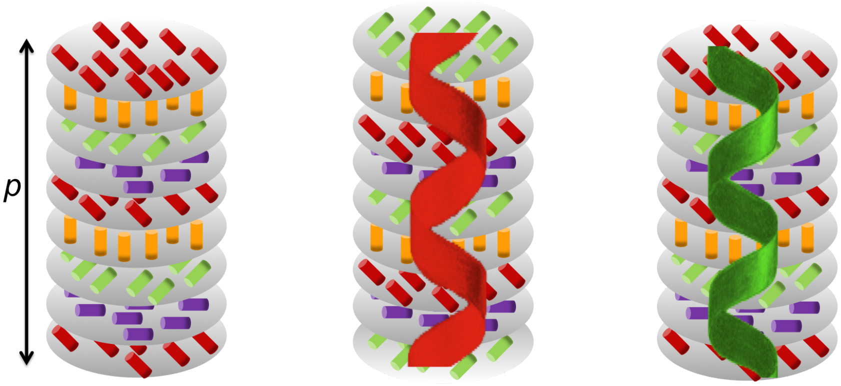

Figure 1.5: Schematic representation of cholesteric phase with the pitch p (left). Left- (center) and Right-handed (right) cholesteric phase.

as:

$$P_2 = \frac{1}{2}\left\langle 3\cos^2\theta - 1\right\rangle \tag{1.1}$$

where θ is the angle between the long molecular axis and the director. The order parameter, P_2, can assume all the values between $-1/2$ and 1. If the orientational distribution is isotropic, $P_2 = 0$, whereas unit values are assumed for a perfect alignment with long molecular axis perpendicular ($-1/2$) or parallel (1) to the director.

If the molecules are chiral, a chiral nematic phase can be formed, which is generally called *cholesteric* (N*). A cholesteric phase can also be obtained by doping an achiral nematic phase with chiral solutes [44–46]. N* phase is a spontaneously distorted N phase, where the director **n̂** rotates in a helical way around a perpendicular axis. Sign (handedness) and magnitude of the helical pitch p depend on the molecular structure of the system. Typical values of the pitch are orders of magnitude larger than the molecular size. They can range from hundreds of nanometers to microns. The pitch, or correspondingly the wavenumber $q = 2\pi/p$, is defined as positive or negative, according to the right- or left-handedness of the cholesteric helix, respectively (see Figure 1.5).

1.2.2 Smectic phases

Smectic phases are layered liquid crystal phases characterized by one-dimensional translational order along the normal to the layers. Within the layers, the molecules possess only orientational order. There are several kinds of smectic phases; the most common are:

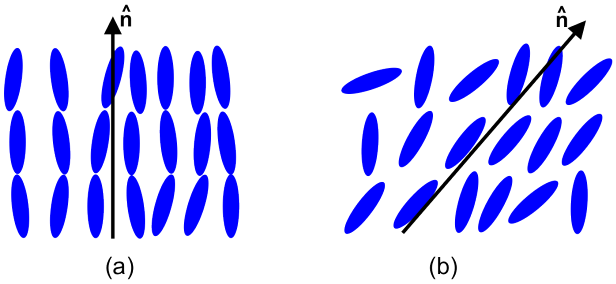

Figure 1.6: Schematic representation of smectic phases. The vector $\hat{\mathbf{n}}$ represents the director. (a) Smectic A, (b) smectic C.

- *Smectic A* (SmA): This is optically uniaxial and in each layer, the molecules are directionally ordered with their long axis normal to the plane of the layer. In other words, the director $\hat{\mathbf{n}}$ is along the normal to the layers [Figure 1.6(a)].
- *Smectic C* (SmC): This is a biaxial phase where the long molecular axes are tilted with respect to the layers' normal [Figure 1.6(b)]. In this case, the director is tilted with respect to the layer normal.
- *Smectic C** (SmC*): This is a chiral version of the SmC, which is formed when molecules are chiral. The director, which is tilted with respect to the layer normal, rotates in a helical way around the normal to the layers.

1.2.3 Columnar phase

The columnar phase is formed by molecules, that can be approximated as disks or rods, stacked one on the top of the other. The structure is often the highly packed hexagonal, but a number of variants have been identified: Orthorhombic, rectangular, tilted, etc.

In the hexagonal phase, the columns are arranged in lateral hexagonal order, but the structure is not that of a true crystal because there is only correlation in the plane. The molecules show a certain degree of disorder around their average position and they can rotate around their axis; the columns can slide one with respect to the other (Figure 1.7).

1.2.4 Onsager-like theory for isotropic-to-nematic transition

The first attempt to describe the isotropic-nematic transition (IN) was made by Lars Onsager [48], who studied the behaviour of a model system of N identical rigid rods of length L and diameter D, considering only hard core repulsions: The interaction potential between particles is zero and becomes infinite when the rods are at a distance equal or lesser than that of contact. In this kind of system the only thermodynamic variable is density.

The starting point of the Onsager theory is the virial expansion of the Helmholtz free energy [49]:

$$\frac{A}{Nk_BT} = \ln(\Lambda_{tr}^3\rho) - 1 + \mathcal{B}_2\rho + \frac{1}{2}\mathcal{B}_3\rho^2 + ... \tag{1.2}$$

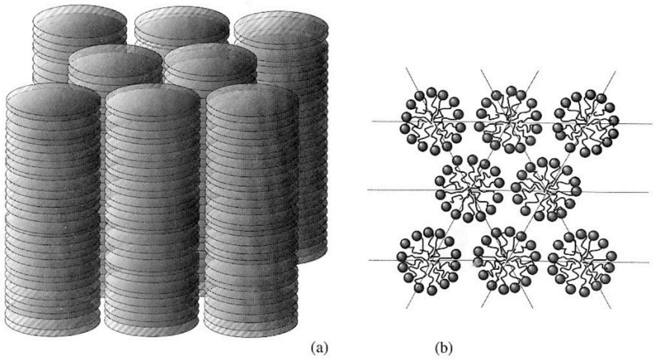

Figure 1.7: Schematic representation of hexagonal columnar phase formed by (a) discotic molecules and (b) cylindric micelles (in section). Reproduced with permission from ref. [47]. Copyright 2013 Springer Publishing Company.

where $\ln(\Lambda_{tr}^3 \rho) - 1$ represents the ideal contribution. Here, Λ_{tr} is the thermal de Broglie wavelength,

$$\Lambda_{tr} = h/\sqrt{2\pi m k_B T} \tag{1.3}$$

where T is the temperature, m is the mass of the rods, k_B is the Boltzmann constant and h is the Planck constant. The other terms represent the virial contribution of different order and $\rho = N/V$ is the density with V the total volume and N the number of molecules [1]. The coefficients $\mathcal{B}_i$, called virial coefficients, depend on interparticle interactions. If the interparticle potential can be expressed as a sum of pair contributions, the second virial contribution, $\mathcal{B}_2$, depends only on the interactions between two particles:

$$\mathcal{B}_2 = -\frac{b_1}{2} = -\frac{1}{2V}\int d\mathbf{R}_1 d\mathbf{R}_2 e_{12}^h(\mathbf{R}_{12}) \tag{1.4}$$

where $\mathbf{R}_1$ and $\mathbf{R}_2$ are the position of particle 1 and 2 and $\mathbf{R}_{12} = \mathbf{R}_1 - \mathbf{R}_2$ is a vector defining the relative position, $e_{12}^h(\mathbf{R}_{12})$ is the Mayer function. For the case of hard particles it is equal to -1 when the particles overlap and 0 when they do not, hence, the opposite of b_1 has the geometric meaning of excluded volume of particle 2 with respect to particle 1 (v_{excl}).

The third virial coefficient, $\mathcal{B}_3$, is related to the simultaneous interaction of three particles:

$$\mathcal{B}_3 = -\frac{2b_3}{3} = -\frac{1}{3V}\int d\mathbf{R}_1 d\mathbf{R}_2 d\mathbf{R}_3 e_{12}^h(\mathbf{R}_{12}) e_{13}^h(\mathbf{R}_{13}) e_{23}^h(\mathbf{R}_{23}) \tag{1.5}$$

Since the nematic phase is uniform, an orientational distribution function, $f(\beta)$, is introduced, where β is the angle between the molecular axis and the director $\hat{\mathbf{n}}$ and obeys the normalization condition $\frac{1}{2}\int f\beta d\cos\beta = 1$.The Helmholtz free energy could be expressed as

---

[1] Another quantity to express the concentration is generally the volume fraction ϕ defined as $\phi = v_0/v$ where v_0 is the volume of a molecule, v is volume per molecule $v = V/N = 1/\rho$; for the cylinders of length L and diameter D, the volume fraction becomes $\phi = \dfrac{1}{4v}\pi L D^2$.

[50]:

$$\begin{aligned}\frac{A}{Nk_BT} =& \ln(\Lambda^3\rho) - 1 + \frac{1}{2}\int d\cos\beta f(\beta)\ln f(\beta) \\ &- \frac{1}{128\pi^4}\rho\int d\mathbf{\Omega}d\mathbf{\Omega}'b_1(\mathbf{\Omega},\mathbf{\Omega}')f(\beta)f(\beta') + ...\end{aligned} \tag{1.6}$$

where $\mathbf{\Omega} = (\alpha, \beta, \gamma)$ and $\mathbf{\Omega}' = (\alpha', \beta', \gamma')$ are the Euler angles that define the rotation from 1 to LAB frame and from 2 to LAB frame, respectively. The first integral accounts for the decrease of orientational entropy due to orientational ordering, and the second integral is the second virial contribution. By increasing the aspect ratio L/D the other virial terms decrease; in the limit of $L/D \to \infty$, the expansion can be truncated at the second term.

The free energy, eq. (1.6), is a functional of the orientational distribution function. By truncating the free energy at the second virial term, we can write:

$$\frac{A[f]}{Nk_BT} \approx constant + \ln\rho + A_1[f] + \rho A_2[f] \tag{1.7}$$

Imposing the condition for minimum with this constraint, we can obtain the following self-consistent equation for the distribution function f:

$$\ln[f(\beta)] = \lambda - 1 - \frac{1}{64\pi^2}\rho\int d\alpha\, d\gamma\, d\mathbf{\Omega}'\, b_1(\mathbf{\Omega},\mathbf{\Omega}')\, f(\beta') \tag{1.8}$$

where λ is a Lagrange multiplier which is determined by normalization condition. The solution of eq. (1.8) gives the the equilibrium distribution function of the system.

It is difficult to solve the non-linear integral eq. (1.8) exactly. Onsager assumed a trial function of the form:

$$f = const \cosh\left(\alpha^N \cos\beta\right) \tag{1.9}$$

where α^N is a variational parameter.In the nematic phase, α^N becomes very large (≈ 20) and the function f is strongly peaked around $\beta = 0$ and $\beta = \pi$. A first-order phase transition from isotropic ($\alpha^N = 0$) to nematic ($\alpha^N \approx 20$) is obtained. At the coexistence in the nematic phase the volume fraction of rods is $\phi_N = 4.486DL$, in the isotropic phase $\phi_I = 3.34DL$. Hence the concentration at which the transition occurs decreases by increasing the aspect ratio L/D. This is an entropy-driven phase transition, whose driving force is the gain of transitional entropy when the orientational order appears.

Bibliography

(1) G. M. Whitesides and B. Grzybowski, *Science*, 2002, **295**, 2418–2421.

(2) I. Hamley, *Introduction to Soft Matter*, Wiley & Sons, 2007.

(3) S. C. Glotzer, *Science*, 2004, **306**, 419–420.

(4) Z. Nie, D. Fava, E. Kumacheva, S. Zou, G. C. Walker, and M. Rubinstein, *Nat. Mater.*, 2007, **6**, 609–614.

(5) Y.-S. Cho, G.-R.Yi, J.-M. Lim, S.-H. Kim, V. N. Manoharan, D. J. Pine, and S.-M. Yang, *J. Am. Chem. Soc.*, 2005, **127**, 15968–15975.

(6) V. Workum and J. Douglas, *Phys. Rev. E*, 2006, **73**, 031502.

(7) F. W. Starr and F. Sciortino, *J. Phys.: Condens. Matter*, 2006, **18**, L347–L353.

(8) C. Mirkin, R. Letsinger, R. Mucic, and J. Storhoff., *Nature*, 1996, **382**, 607–609.

(9) P. Damasceno, M. Engel, and S. C. Glotzer, *Science*, 2012, **337**, 453–457.

(10) J. de Graaf, R. van Roij, and M. Dijstra, *Phys. Rev. Lett.*, 2011, **107**, 155501.

(11) A. Khan, *Current Opinion in Colloid & Interface Science*, 1996, **1**, 614–623.

(12) P. van der Schoot and M. Cates, *Langmuir*, 1994, **10**, 670–679.

(13) D. M. Kuntz and L. M. Walker, *Soft Matter*, 2008, **4**, 286–293.

(14) J.-M. Jung and R. Mezzenga, *Langmuir*, 2010, **26**, 504–514.

(15) C. F. Lee, *Phys. Rev. E*, 2009, **80**, 031902.

(16) A. Ciferri, *Liq. Cryst.*, 2007, **34**, 693–696.

(17) A. Aggeli, M. Bell, L. M. Carrick, C. W. G. Fishwick, R. Harding, P. J. Mawer, S. E. Radford, A. E. Strong, and N. Boden, *J. Am. Chem. Soc.*, 2003, **125**, 9619–9628.

(18) C. Robinson, *Tetrahedron*, 1961, **13**, 219 –234.

(19) F. Livolant, A. M. Levelut, J. Doucet, and J. P. Benoit, *Nature*, 1989, **339**, 724–726.

(20) F. Livolant and A. Leforestier, *Prog. Polym. Sci.*, 1996, **21**, 1115–1164.

(21) K. Merchant and R. L. Rill, *Biophys. J.*, 1997, **73**, 3154–3163.

(22) F. Tombolato and A. Ferrarini, *J. Chem. Phys.*, 2005, **122**, 054908.

(23) F. Tombolato, A. Ferrarini, and E. Grelet, *Phys. Rev. Lett.*, 2006, **96**, 258302.

(24) E. Barry, D. Beller, and Z. Dogic, *Soft Matter*, 2009, **5**, 2563–2570.

(25) E. Grelet and S. Fraden, *Phys. Rev. Lett.*, 2003, **90**, 198302.

(26) S. Tomar, M. M. Green, and L. A. Day, *J. Am. Chem. Soc.*, 2007, **129**, 3367–3375.

(27) J. Lydon, *J. Mater. Chem.*, 2010, **20**, 10071–10099.

(28) K. Liu, Z. Nie, N. Zhao, W. Li, M. Rubinstein, and E. Kumacheva, *Science*, 2010, **329**, 197–200.

(29) A. Kuijk, D. V. Byelov, A. V. Petukhov, A. van Blaaderen, and A. Imhof, *Faraday Discuss.*, 2012, **159**, 181–199.

(30) A. Aggeli, I. A. Nyrkova, M. Bell, R. Harding, L. Carrick, T. C. B. McLeish, A. N. Semenov, and N. Boden, *Proc. Natl. Acad. Sci. USA*, 2001, **98**, 11857–11862.

(31) M. A. Mateos-Timoneda, M. Crego-Calama, and D. N. Reinhoudt, *Chem. Soc. Rev.*, 2004, **33**, 363–372.

(32) D. Pijper and B. L. Feringa, *Soft Matter*, 2008, **3**, 1349–1372.

(33) Y. Zhang, P. Chen, and M. Liu, *Chem. Eur. J.*, 2008, **14**, 1703–1803.

(34) L. Zhao, R. Xiang, R. Ma, X. Wang, Y. An, and L. Shi, *Langmuir*, 2011, **27**, 11554–11559.

(35) Y. Rong, P. Chen, and M. Liu, *Chem. Comm.*, 2013, **49**, 10498–10500.

(36) H. Engelkamp, S. Middelbeek, R. J. M., and Nolte, *Science*, 1999, **284**, 785–788.

(37) J. A. A. W. Elemans, A. E. Rowan, and R. J. M. Nolte, *J. Mater. Chem.*, 2003, **13**, 2661–2670.

(38) J. J. de Pablo and W. A. Curtin, *Mater. Res. Soc. Bull.*, 2007, **32**, 905–911.

(39) J. A. Elliott, *Int. Mater. Rev.*, 2011, **56**, 207–225.

(40) R. M. Nieminen, *Journal of Physics: Condensed Matter*, 2002, **14**, 2859–2876.

(41) H. J. C. Berendsen, *Simulating the physical world: hierarchical modeling from quantum mechanics to fluid dynamics*, Cambridge University Press, Cambridge, 2005.

(42) S. Ogata, E. Lidorikis, F. Shimojo, A. Nakano, P. Vashishta, and R. K. Kalia, *Comput. Phys. Commun.*, 2001, **138**, 143–154.

(43) N. Bernstein, J. R. Kermode, and G. Csányi, *Reports on Progress in Physics*, 2009, **72**, 026501.

(44) M. G. Friedel, *Ann. Phys.*, 1922, **18**, 273–474.

(45) S. Pieraccini, A. Ferrarini, and G. P. Spada, *Chirality*, 2008, **20**, 749–759.

(46) S. Pieraccini, S. Masiero, A. Ferrarini, and G. P. Spada, *Chem. Soc. Rev.*, 2011, **40**, 258–271.

(47) M. Kleman and O. D. Lavrentovich, *Soft Matter Physics: An Introduction*, Springer, 2001.

(48) L. Onsager, *Ann. N.Y. Acad. Sci.*, 1949, **51**, 627–659.

(49) D. A. McQuarrie, *Statistical Mechanics*, University Science Books, Sausalito, CA, 2000.

(50) G. J. Vroege and H. N. W. Lekkerkerker, *Rep. Prog. Phys.*, 1993, **55**, 1241–1309.

Part II

Self assembly of hard helical particles

The helix is a typical structural motif in nature: For example, polynucleotides, proteins and collagen fibers are all right-handed helices [1]. Rigid and semiflexible helical polymers can exhibit ordered structures but the relationship between these structure and the helical features remains unknown. One of the questions is whether there may be any kind of organization that is specific of the helical shape. To address this problem, we have investigated the phase diagram of hard rigid homochiral helices. Since the early Onsager work [2], there have been several demonstrations that purely hard-core repulsions are sufficient for the formation of ordered phases. Recent investigations have revealed the unexpected complexity of the ordered structures obtained by changing the shape of hard particles [3, 4]. The influence of chirality is still mostly unexplored.

We have focused on the LC phases formed by hard helices. We have performed a theoretical study using an Onsager-like theory, in parallel with Monte Carlo (MC) simulations carried out by other groups (Prof. Achille Giacometti, Università Ca' Foscari di Venezia; Dr. Giorgio Cinacchi, Universidad Autónoma de Madrid). The combined investigation is meant to compensate for the limits of each single approach. MC simulations of dense systems of several hundreds of particles have a high computational cost. On the other hand, calculations based on Onsager theory are much less demanding, but have some underlying assumption and approximations.

Homochiral helices are expected to form a cholesteric phase, which differs from the uniform nematic only because the local preferred orientational axis (the director) rotates in space around a perpendicular axis. MC simulation with usual periodic boundary conditions do not allow the emergence of an equilibrium cholesteric order, with a pitch much longer than the size of the simulation box. On the other hand, due to the length scale of the cholesteric pitch, which is orders of magnitude longer than that of inter-particle interactions, the phase chirality can be neglected if we are interested in the local phase properties and the location of the isotropic-to-cholesteric phase transition.

Therefore, at a first stage we have focussed on the effects of the particle shape on the isotropic to the uniform nematic (IN) phase transition. This study was aimed at investigating whether helical particles can be assimilated to rods, as generally done in interpreting experimental data [5]. From a theoretical stand point, we wanted to investigate whether Onsager theory can be extended to systems of helical non-convex particles (see Chapter 2).

Subsequently, using only an Onsager-like theory we have investigated in detail the relationship between the helical parameters of the particles and the chiral structure of the cholesteric phase. A first issues is the handedness of the cholesteric phase: Based on a toy model it has been proposed that the phase chirality is the same as that of the constituent helices when the helical inclination angle is small ($\alpha < \pi/4$), and opposite for large inclination angles ($\alpha > \pi/4$) [6]. We have performed a systematic investigation to verify this hypothesis. Then, we have studied how the tortuosity of particles affects the cholesteric pitch (see Chapter 3).

Finally, we have studied the full phase diagram of hard helices which reveals a zoo of phases with peculiarities that depend on the helical parameters. Especially interesting is the presence of a novel chiral phase, the *screw-like nematic phase* (N_s^*), originating from the specific helical shape of the particles (see Chapter 4).

Chapter 2

Hard helices: The isotropic-to-nematic phase transition

In this Chapter, we present a study of the isotropic-to-nematic (IN) phase transition in systems of hard helical particles, using Onsager theory and Monte Carlo computer simulations. This theory was previously applied with success to IN phase transition in systems of hard convex bodies, like spherocylinders. Here its performance for hard helices has been tested by comparison with MC simulations.

2.1 State of the art

While the first example of phase transition driven by purely steric interactions is undoubtly the fluid-to-crystal phase transition in hard spheres [7], the isotropic-to-nematic liquid crystal (IN) phase transition in hard slender rods predicted by Onsager [2] paved the way for an entirely new field. Although Onsager theory was originally motivated by the observation of a nematic liquid crystal phase in suspensions of inorganic and biological rod-like colloidal particles [8, 9], its influence over the years have proven to be much more profound.

The original Onsager theory accounted only for the second-virial coefficient contribution, thus (strictly) limiting its applicability to rod–like particle systems with large aspect ratios, but several improvements have been more recently proposed to overcome this drawback and include also higher order contributions. This prompted a number of approaches with different degrees of sophistication, as well as a series of computer simulations, [10–12], that can be applied and extended to many systems, either mono- or poly-disperse, both homo- and hetero-geneous.

So far, most theoretical and computational studies have focussed on convex hard particles (e.g. Ref. [10]), whilst concave particles have been given less attention. Besides simple dumbbells, these include bent-core [13–15], lens-like [16] and bowl-shaped [17] particles. Somewhat surprisingly, hard helices are not part of the above list, in spite of the several examples of this shape that can be found in natural and synthetic polymers. Rigid and semiflexible helical polymers (polynucleotides, polypeptides, viruses) have a well known propensity to form liquid crystal phases at high concentration [1, 18–20]. When examining and interpreting the experimental phase behaviour, helicoidal particles were generally assimilated to rods, thus neglecting peculiarities related to the actual shape (e.g. [5]).

2.2 Theory

2.2.1 Free energy of the isotropic and nematic phases

Let us consider a system of N identical helices in a volume V at temperature T. We denote by $v = V/N$ the volume per particle and $\phi = v_0/v$ the packing density, where v_0 is the volume of a particle.

The mutual interaction between a pair of hard helices (1 and 2) takes the form:

$$U(\mathbf{R}_{12}, \mathbf{\Omega}_{12}) = \begin{cases} \infty & \text{if 1,2 overlap} \\ 0 & \text{if 1,2 do not overlap} \end{cases} \tag{2.1}$$

where $\mathbf{R}_1$ and $\mathbf{R}_2$ are the positions of the center-of-mass for helices 1 and 2 respectively, $\mathbf{R}_{12} = \mathbf{R}_2 - \mathbf{R}_1$ is a vector defining the relative position of helix 2 with respect to helix 1 and $\mathbf{\Omega}_{12} = (\alpha_{12}, \beta_{12}, \gamma_{12})$ are the Euler angles that define the rotation from 1 to 2.

In the Onsager approach the free energy of the system is expressed as a functional of the single particle density function $\rho(\mathbf{R}, \mathbf{\Omega})$, where $\mathbf{R}$ is the particle position and $\mathbf{\Omega} = (\alpha, \beta, \gamma)$ are the Euler angles specifying the particle orientation, with the normalization condition $\int d\mathbf{R} d\mathbf{\Omega} \rho(\mathbf{R}, \mathbf{\Omega}) = N$. In an uniform and isotropic phase this function is independent of the molecular position and orientation and is simply given by $\rho_{\text{iso}} = 1/8\pi^2 v$, with $v = V/N$ being the available volume per molecule; in an uniform and an isotropic phase the density function only depends on the molecular orientation $\int d\mathbf{\Omega} \rho(\mathbf{\Omega}) = N/V$.

The free energy can then be expressed as:

$$A[\rho(\mathbf{\Omega})] = N k_B T \left[\ln \frac{\Lambda_{\text{tr}}^3}{V} \frac{\Theta_{\text{or}}}{T} + \ln N - 1 \right] + A^{\text{or}}[\rho(\mathbf{\Omega})] + A^{\text{ex}}[\rho(\mathbf{\Omega})] \tag{2.2}$$

The first term is the Helmholtz free energy of the ideal gas: Λ_{tr} is the de Broglie wavelength, eq. (1.3), and $\Theta_{\text{or}} = h^2/8\pi^2 k_B I$ is the rotational temperature, with k_B and h being the Boltzmann and the Planck constant, respectively, while m is the mass and I is the inertia moment of the particle. The second term in eq. (2.2) accounts for the decrease of orientational entropy due to orientational ordering:

$$\frac{A^{\text{or}}}{N k_B T} = k_B T V \int d\mathbf{\Omega} \rho(\mathbf{\Omega}) \ln \frac{\rho(\mathbf{\Omega})}{\rho_{iso}} \tag{2.3}$$

and the last term, A^{ex}, represents the excess free energy. Assuming that hardcore repulsions are treated according to the second virial approximation, the excess Helmholtz free energy can be expressed as:

$$\frac{A^{ex}}{k_B T} = \frac{V}{2} \int d\mathbf{R}_{12}\, d\mathbf{\Omega}_1\, d\mathbf{\Omega}_2\, \rho(\mathbf{\Omega}_1) \rho(\mathbf{\Omega}_2) u(\mathbf{R}_{12}, \mathbf{\Omega}_{12}) \tag{2.4}$$

where the function $u(\mathbf{R}_{12}, \mathbf{\Omega}_{12})$ is defined as:

$$u(\mathbf{R}_{12}, \mathbf{\Omega}_{12}) = -k_B T e^h_{12}(\mathbf{R}_{12}, \mathbf{\Omega}_{12}) \tag{2.5}$$

where e^h_{12} is the Mayer function, defined as [21] :

$$e^h_{12}(\mathbf{R}_{12}, \mathbf{\Omega}_{12}) = \exp\{-U_h(\mathbf{R}_{12}, \mathbf{\Omega}_{12})/k_B T\} - 1 \tag{2.6}$$

This function is related to the volume excluded to the 2 by the 1 helix:

$$v_{excl}(\mathbf{\Omega}_{12}) = -\int d\mathbf{R}_{12}\, e^h_{12}(\mathbf{R}_{12}, \mathbf{\Omega}_{12}) \tag{2.7}$$

Since the nematic phase is uniform and the density function depends only on the particle orientation and assuming helices as uniaxial particles, the single particle density in the uniaxial nematic phase can be reduced to [1]: $\rho = \rho(\beta) = f(\beta)/(4\pi^2 v)$, where β is the angle between the helix axis and the nematic director and $f(\beta)$ the orientational distribution function. The expression of the excess free energy A_{ex}, eq. (2.4), coupled with the Parsons-Lee (PL) correction [22–24], becomes:

$$\frac{A^{\text{ex}}}{Nk_B T} = \frac{G(\phi)}{2(4\pi^2)^2 v} \int d\mathbf{\Omega}_1\, f(\beta_1) \int d\mathbf{\Omega}_2\, f(\beta_2) v_{\text{excl}}(\mathbf{\Omega}_{12}) \tag{2.8}$$

Introducing the second virial coefficient:

$$B_2 = \frac{1}{2}\frac{1}{(4\pi^2)^2} \int d\mathbf{\Omega}_1\, f(\beta_1) \int d\mathbf{\Omega}_2\, f(\beta_2) v_{\text{excl}}(\mathbf{\Omega}_{12}). \tag{2.9}$$

the excess free energy eq. (2.8) becomes

$$A^{\text{ex}}[f]/Nk_B T = G(\phi) B_2[f]/v. \tag{2.10}$$

2.2.2 Parsons-Lee (PL) and Modified Parsons-Lee (MPL) approximations

The approximation proposed by Parsons [22] and subsequently used by Lee [23, 24] and others [25, 26] for hard sperocylinders (and ellipsoids) relies on the assumption that the excess free energy is proportional to that of a system of hard spheres (HS) at the same packing fraction (ϕ):

$$\frac{A^{\text{ex}}(\phi)}{Nk_B T B_2(\phi)} = \frac{A^{\text{ex}}_{HS}(\phi)}{Nk_B T B^{HS}_2(\phi)}. \tag{2.11}$$

Use of the Carnahan-Starling expression for the free energy of hard spheres [27], along with the relationships $B^{HS}_2 = 4v_{HS}$ and $\phi = v_{HS}/v$, where v_{HS} is the volume of a hard sphere, yields

$$G(\phi) = \frac{A^{\text{ex}}_{HS}(\phi)}{Nk_B T B^{HS}_2(\phi)} = \frac{1}{4}\frac{4-3\phi}{(1-\phi)^2} \tag{2.12}$$

In the original and subsequent works [23–26] the volume of the reference hard spheres was taken equal to that of the spherocylinders (or ellipsoids), $v_{HS} = v_0$. Good agreement between

---

[1] Note that a finite helix has C_2 point symmetry, yet we have verified that the helices examined here have nearly uniaxial order (with the helix axis as the ordering axis) in the uniaxial nematic phase.

theory and simulations was obtained in that case, but significant discrepancies were found for linear particles made of tangentially bonded hard spheres [28]. It has then been suggested that the assumption $v_{HS} = v_0$ may be inappropriate for hard non-convex bodies, since in this case the free volume available at a given number density is smaller than for convex particles having the same geometrical volume [29]. It was proposed that in this case the volume of the reference hard spheres should be replaced by an effective volume, v_{ef}, defined as the volume of the non-convex particle that is inaccessible to other particles. This effective volume is larger than the geometrical volume, and for linear hard spheres it has been evaluated in ref. [30]. This variant of the PL theory has been given the name of modified Parsons-Lee (MPL) theory [29].

2.2.3 Expansion in terms of orientational order parameters

In the nematic phase the orientational distribution function $f(\beta)$ is conveniently expanded on a basis of Legendre polynomials

$$f(\beta) = \frac{1}{2}\sum_{j=0}^{\infty}(4j+1)\,\langle P_{2j}\rangle\, P_{2j}(\cos\beta) \tag{2.13}$$

where $\langle P_{2j}\rangle$ are the nematic order parameters

$$\langle P_{2j}\rangle = \int_{-1}^{1} d(\cos\beta) f(\beta) P_{2j}(\cos\beta) \tag{2.14}$$

These range between -0.5 (helix perpendicular to the director) and 1 (helix parallel to the director) and vanish in the isotropic phase.

Upon substituting Eq. (2.13) in Eqs. (2.3)-(2.8) and exploiting the properties of Wigner rotation matrices [31], we can express the orientational and excess contributions to the Helmholtz free energy as a function of the order parameters:

$$\begin{aligned}\frac{A^{\text{id}}}{Nk_BT} &= \ln\left(\frac{\Lambda_{tr}^3\Omega_{or,x}^{1/2}\Omega_{or,y}^{1/2}\Omega_{or,z}^{1/2}}{\pi^{1/2}VT^{3/2}}\right) + \ln N - 1 \\ &\quad + \sum_{j=0}^{\infty}(4j+1)\,\langle P_{2j}\rangle \int_{-1}^{1} d(\cos\beta) P_{2j}(\cos\beta)\,\ln\left[\sum_{j'=0}^{\infty}(4j'+1)\langle P_{2j'}\rangle P_{2j'}(\cos\beta)\right]\end{aligned} \tag{2.15}$$

$$\frac{A^{\text{ex}}}{Nk_BT} = \frac{G(\phi)}{16\pi^2 v}\sum_{j=0}^{\infty}(4j+1)\,\langle P_{2j}\rangle^2 \int d\boldsymbol{\Omega}_{12}\, P_{2j}(\cos\beta_{12}) v_{\text{excl}}(\boldsymbol{\Omega}_{12}) \tag{2.16}$$

This leads to the following expressions for the pressure and the chemical potential:

$$\begin{aligned}\frac{P}{k_BT} = -\frac{1}{k_BT}\left(\frac{\partial A}{\partial V}\right)_{NT} &= \frac{1}{v} + \frac{1}{16\pi^2 v^2}\left(G(\phi) + \frac{\phi(5-3\phi)}{4(1-\phi)^3}\right) \\ &\quad \times \sum_{j=0}^{\infty}(4j+1)\langle P_{2j}\rangle^2 \int d\boldsymbol{\Omega}_{12}\, P_{2j}(\cos\beta_{12}) v_{\text{excl}}(\boldsymbol{\Omega}_{12})\end{aligned} \tag{2.17}$$

$$\begin{aligned}\frac{\mu}{k_B T} = \left(\frac{\partial A}{\partial N}\right)_{VT} = \ln \frac{\Lambda_{\mathrm{tr}}^3 \Omega_{\mathrm{or}}}{VT^2} &+ \ln N + \frac{1}{2} \sum_{j=0,1,2,\ldots} (4j+1)\langle P_{2j}\rangle \\ &\times \int d(\cos\beta) P_{2j}(\cos\beta) \ln\left[\sum_{j'=0,1,2,\ldots} (4j'+1)\langle P_{2j'}\rangle\, P_{2j'}(\cos\beta)\right] \\ &+ \frac{1}{8\pi^2 v}\left(G(\phi) + \frac{\phi(5-3\phi)}{8(1-\phi)^3}\right) \\ &\times \sum_{j=0,1,2,..} (4j+1)\langle P_{2j}\rangle^2 \int d\mathbf{\Omega}_{12}\, P_{2j}(\cos\beta_{12}) v_{\mathrm{excl}}(\mathbf{\Omega}_{12}).\end{aligned} \tag{2.18}$$

2.2.4 Computational details

For each system, the Helmholtz free energy given in eqs. (2.2), (2.15) and (2.16), is minimised at increasing values of the density $1/v$, and the order parameters of the stable phase at each density value obtained are then used to calculate the pressure according to eq. (2.17).

Evaluation of pair integrals

Integrals over all the relative positions and orientations of pairs of particles, appearing in eqs. (2.16), (2.17), and (2.18) are preliminarly evaluated and stored, to be used for the calculations at the various density values. These integrals have the general form:

$$\int_0^{2\pi} d\alpha_{12} \int_{-1}^{1} d(\cos\beta_{12}) P_{2j}(\beta_{12}) \int_0^{2\pi} d\gamma_{12} \int_0^{2\pi} d\phi_{12} \int_{-1}^{1} d(\cos\vartheta_{12}) (R_{12}^0)^3 \tag{2.19}$$

where $\mathbf{R}_{12}$, the vector position of helix 2 with respect to helix 1, is expressed in spherical coordinates, $\mathbf{R}_{12} \equiv \{R_{12}, \phi_{12}, \vartheta_{12}\}$ and R_{12}^0 is the closest approach distance, which is a function of the relative position and orientation of the two helices. Gauss-Legendre and Gauss-Chebyshev quadrature algorithms are used to evaluate these integrals [32]. Each integral in the form of eq. (6.38) requires the evaluation of the function within the integrals for a number of pair configurations of the order of 10^9. If a helix is represented as an assembly of M_s spheres, a number of operations proportional to M_s^2 is required for each configuration. It follows that the feasibility of calculations depends on the level of detail employed in modelling the molecular features.

Free energy minimisation

It is expedient to choose as variational parameters the coefficients u_j of the expansion

$$-\ln f(\beta) = \sum_{j=2,4,\ldots}^{\infty} u_j P_{2j} \cos(\beta), \tag{2.20}$$

rather than the order parameters. Eq. (2.20) is used in eq. (2.3) for the orientational contribution to the free energy, A^{or}, and is introduced into eq. (2.4) for the excess contribution, A^{ex}, through the order parameters, eq. (2.14). Thus, the Helmholtz free energy is expressed as a function of the u_j coefficients. This has a twofold advantage: The expansion eq. (2.20) converges faster than that of the density function eq. (2.13) and the parameters u_j are unconstrained, unlike order parameters.

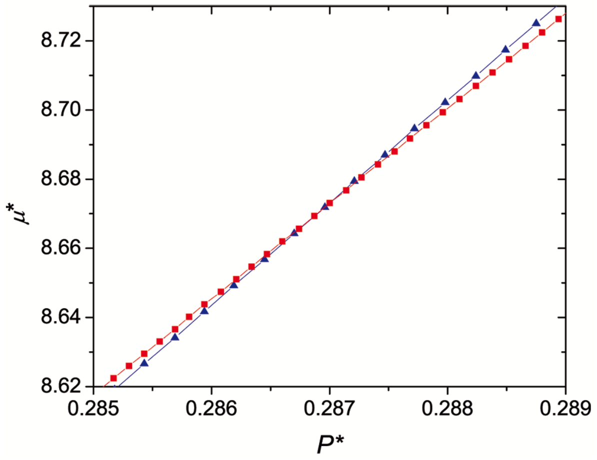

Figure 2.1: Determination of the isotropic-to-nematic coexistence for helices with $p = 8$ and $r = 0.2$. Red squares, nematic branch; blue triangles, isotropic branch.

Determination of isotropic-to-nematic phase coexistence

The volume fraction of coexisting isotropic and nematic phase, ϕ_I and ϕ_N respectively, is calculated by minimizing the free energy with respect to the variational parameters u_j, with the constraint of equal pressure and chemical potential:

$$\begin{aligned} P_I &= P_{N^*} \\ \mu_I &= \mu_{N^*} \end{aligned} \tag{2.21}$$

The following procedure is used: Two calculations are started, one at low density (isotropic) and the other at high density (nematic). Then, the density is increased from the lowest value and decreased from the highest value. At each step, after free energy minimization, the pressure and the chemical potential are calculated. The coexistence is identified by crossing of the curves for isotropic and the nematic branches in the plot of (P^*, μ^*) (see Figure 2.1).

2.3 Monte Carlo simulations

MC simulations [33, 34] on a system of N hard helices were carried out in the ensemble Isothermal-Isobaric (NPT). Cubic or orthorhombic computational boxes was used, with the usual periodic boundary conditions. Simulations were organised in cycles, each consisting of $2N$ attempted particle moves (a random translation and rotation) and a volume move [35]. Rotation trial moves were implemented either using the Barker-Watts [36] or the quaternions methods [37, 38], finding a good consistency between them. Volume moves were either performed scaling up or down the box in those cases where cubic boxes were used or attempting to change a randomly selected edge of the box in the other cases. Being concerned with the IN phase transition only, other possible conditions on boundary or/and on computational boxes, that could be necessary to properly account for other phases, are neglected.

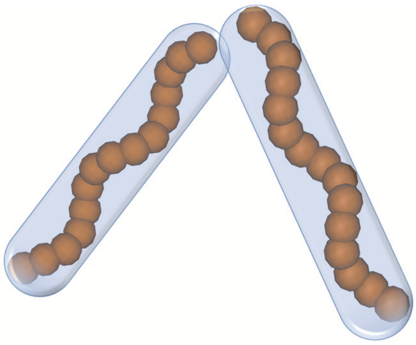

Figure 2.2: Cartoon of the overlap between the spherocylinders containing a pair of helices.

The overlap condition was computed by first inserting each helix into the smallest spherocylinder containing it and testing for overlap between two such spherocylinders (see Figure2.2). This is a relatively fast test as it amounts to finding the minimal distance between two segments. To this purpose, the algorithm proposed by Vega and Lago are used [39]. This method is approximatively four times faster than others previously used, essentially because it reduces to only four the number of regions to be checked for closest approach. Only in the event of overlap between two spherocylinders, the spheres forming the embedded helices were tested for overlapping. This procedure significantly reduced the computational cost of the overlap test, that is one of the bottlenecks of this type of simulations, and considerably increased their efficiency.

The IN phase transition was monitored using the main orientational order parameter, $\langle P_2 \rangle$, already discussed in the theoretical section. To this aim, the following tensor [40]

$$\mathbf{Q}_{\alpha\beta} = \frac{1}{N}\sum_{i=1}^{N}\frac{3}{2}\widehat{\mathbf{u}}_i^{\alpha}\widehat{\mathbf{u}}_i^{\beta} - \frac{1}{2}\delta_{\alpha\beta} \tag{2.22}$$

was evaluated, and the corresponding eigenvalues and eigenvectors computed. Here $\alpha, \beta = x, y, z$ and $\widehat{\mathbf{u}}_i^{\alpha}$ is the α component of the unit vector $\widehat{\mathbf{u}}_i$ describing the orientation of the $i-$th helix axis. The orientational order parameter $\langle P_2 \rangle$ was then identified with the largest eigenvalue of $\mathbf{Q}$. The difference between the other eigenvalues of $\mathbf{Q}$ was found to be smaller than 5%, in agreement with our assumption of uniaxial nematic order.

2.3.1 Computational details

NPT MC simulations were carried out using $N = 675$ or 867 hard helices with periodic boundary conditions. As a general rule, a series of simulations has been started from a diluted configuration and equilibrium has been reached upon compression. Typical equilibration runs consisted of 3×10^6 MC cycles and were followed by a production run of additional 3×10^6 MC cycles, during which averages of density and order parameter were calculated.

In most of the equilibration runs the maximum values for the displacement, rotation and volume moves were varied in the course of the run to reach a $30\% - 40\%$ of acceptance. This procedure is known to lead to a possible violation of the detailed balance condition [41], but they explicitly verified that this does not lead to any bias in the present case. During production runs, the overall acceptance ratio was adjusted to be $30\% - 40\%$ by a suitable choice of the maximum displacement, rotation and volume parameters, and these values were never altered during the run.

It is worth emphasizing that simulations for hard helices are considerably more demanding from the computational point of view than simulations of hard spherocylinders. Depending on the state point considered and the values used for the radius and pitch, the computational cost might be as high as 8 times that of the corresponding spherocylinders.

2.4 Helical particles

We have studied systems of identical helices, shown in Figure 2.3, obtained by deformation of a linear chain of 15 fused hard spheres of diameter D and contour length equal to L=10 D. A helix is made of N spheres, whose centers are located at the points defined by the parametric equations:

$$\begin{cases} x_i = r\cos(2\pi t_i) \\ y_i = r\sin(2\pi t_i) \\ z_i = p t_i \end{cases} \qquad 1 \leq i \leq N \tag{2.23}$$

where r is the radius and p is the pitch of the helix (see Fig. 2.3). Given the values of r, p and of the contour length L, the increment $\Delta t = t_{i+1} - t_i$ is determined by the equation:

$$\frac{L}{N-1} = 2\pi\Delta t\sqrt{r^2 + \left(\frac{p}{2\pi}\right)^2}. \tag{2.24}$$

The Euclidean length of the helix is defined as $\Lambda = z_N - z_1$, depends on the pitch and radius, and coincides with the contour length L only for $r = 0$. We can also define the inclination angle, α, as:

$$\alpha = \arcsin t_z = \arcsin\left(\frac{p}{\sqrt{p^2 + 4\pi^2 r^2}}\right) \tag{2.25}$$

where t_z is the component z of the tangent to the helix:

$$\begin{cases} t_x = \dot{x} = \dfrac{-2\pi r\sin(2\pi t_i)}{\sqrt{p^2 + 4\pi^2 r^2}} \\ t_y = \dot{y} = \dfrac{2\pi r\cos(2\pi t_i)}{\sqrt{p^2 + 4\pi^2 r^2}} \\ t_z = \dot{z} = \dfrac{p}{\sqrt{p^2 + 4\pi^2 r^2}} \end{cases} \tag{2.26}$$

2.4.1 Molecular volume and effective volume

We have considered helical particles with different structural parameters and for comparison a linear chain formed by m_s fused hard spheres (LHSC) of diameter D and center-to-center distance d_{cc} (see Figure 2.4). An important feature in MPL and PL approximation is the

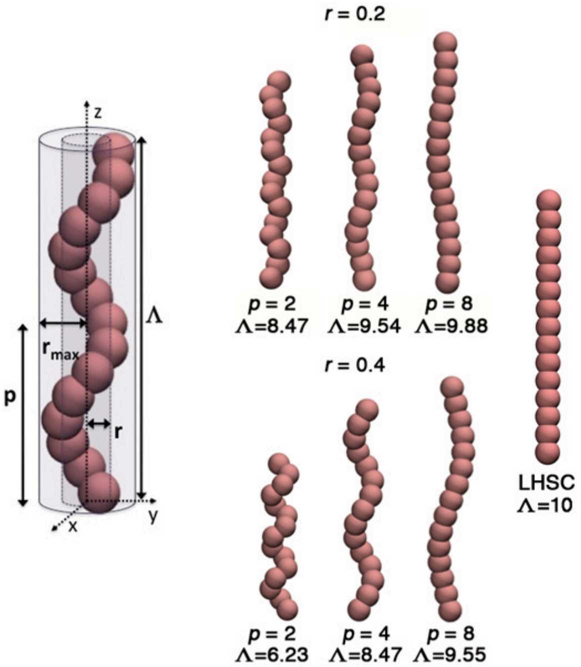

Figure 2.3: Left: Definition of helical parameters. Right: Helices of radius r and pitch p investigated here. Helices have the same contour length L but different Euclieдean lengths Λ (lengths are scaled with the the sphere diameter D). For comparison also the fully extended linear hard sphere chain (LHSC) is shown.

proper definition of the volume of the system under investigation. The volume v_0 of LHSC is given by

$$v_0 = \frac{\pi}{6}D^3\left[1+\frac{m_s-1}{2}\left(3\frac{d_{cc}}{D}-\left(\frac{d_{cc}}{D}\right)^3\right)\right] \tag{2.27}$$

The same expression holds for a helix of fused hard spheres, provided that there are only two-sphere overlaps and the correct value of the distance d_{cc} is used.[2] For a given length of the curve connecting the centers of a pair of subsequent spheres, this distance depends on the helix radius and pitch. Table 2.1 reports the (geometric) volume calculated for the all the helices shown in Figure 2.3.

A definition of the *effective* volume has been proposed for LHSCs, as the volume enclosed by the surface drawn by a sphere identical to those of the chain, rolling over the particle [30]. An example of this surface is shown in Figure 2.4. The effective volume of the LHSC is then given by the expression:

$$v_{\text{ef}}^{\text{LHSC}} = \frac{\pi}{6}D^3\left[1+(m_s-1)\left(3\frac{d_{cc}}{D}-\frac{1}{2}\left(\frac{d_{cc}}{D}\right)^3-3\sqrt{\left(1-\left(\frac{d_{cc}}{2D}\right)^2\right)}\arcsin\left(\frac{d_{cc}}{2D}\right)\right)\right] \tag{2.28}$$

We have adopted the same definition of the effective volume for fused hard sphere helices. However in this case, depending on the helix curvature, the effect of the rolling sphere can

---

[2] $d_{cc} = \sqrt{(x_{i+1}-x_i)^2+(y_{i+1}-y_i)^2+(z_{i+1}-z_i)^2}$ is the distance between centres of two subsequent spheres.

helix	d_{cc}	v_0
p= 2, r= 0.2	0.687	6.89
p= 2, r= 0.4	0.680	6.85
p= 4, r= 0.2	0.711	7.02
p= 4, r= 0.4	0.707	7.00
p= 8, r= 0.2	0.714	7.04
p= 8, r= 0.4	0.714	7.04
LHSC	0.714	7.04

Table 2.1: Volume v_0 of fused hard sphere helices of radius r and pitch p, calculated using Eq. (2.27). For comparison, also the value for LHSCs is reported.

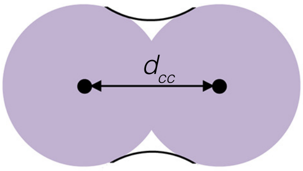

Figure 2.4: Surface defining the effective volume of a pair of fused hard spheres.

go beyond that of simply filling the voids between subsequent beads. We have calculated the effective volume (v_{ef}) of helices using the program MSMS [42]. The rolling sphere radius was taken equal to the radius of the fused hard spheres that form the helix. Table 2.2 reports the v_{ef} values obtained for the helices shown in Figure 2.3; for comparison we report in the table also the volume calculated according to eq. 2.28, using for each sphere the appropriate d_{cc} value ($v_{\mathrm{ef}}^{\mathrm{LHSC}}$). We can observe that $v_{\mathrm{ef}} = v_{\mathrm{ef}}^{\mathrm{LHSC}}$ for all helices with longer pitch; only for $p = 2$ there is some difference, more pronounced in the case with $r = 0.4$. This discrepancy can be understood considering that these helices have grooves narrower than the sphere diameter D (see Figure2.4).

helix	v_{ef}	$v_{\mathrm{ef}}^{\mathrm{LHSC}}$
p= 2, r= 0.2	7.24	7.20
p= 2, r= 0.4	7.78	7.15
p= 4, r= 0.2	7.37	7.37
p= 4, r= 0.4	7.34	7.34
p= 8, r= 0.2	7.39	7.39
p= 8, r= 0.4	7.39	7.39
LHSC	7.39	7.39

Table 2.2: Effective volume of fused hard sphere helices of radius r and pitch p, calculated either by the program MSMS [42] or using Eq. (2.28) with the d_{cc} distances reported in Table 2.1. For comparison, also the value for the LHSC is reported.

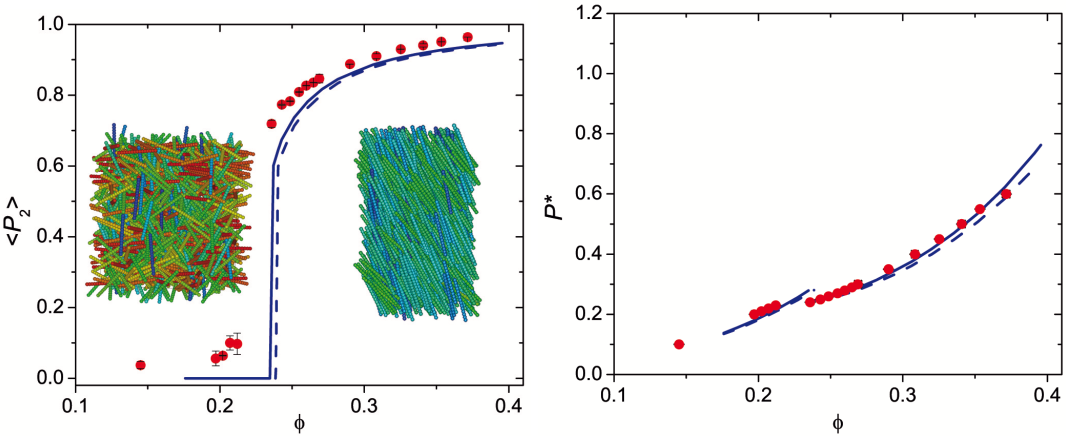

Figure 2.5: $\langle P_2 \rangle$ order parameter (Left) and reduced pressure P^* (Right) as a function of the volume fraction $\phi = v_0/v$ for the LHSC, from MC simulations (closed circles) and from Onsager theory with PL (dashed line) or MPL (solid line) approximation. Insets on the left panel, here and in following figures, depict representative snapshots obtained using QMGA software [44].

2.5 Results and Discussion

In presenting and discussing our results we will use reduced units, with the diameter D taken as the unit of length, and with reduced pressure $P^* = PD^3/k_BT$. For each system, the results from MC simulations were compared with those from Onsager theory with the PL and the MPL approximation, which differ in the definition of the packing fraction entering the scaling factor $G(\phi)$, eq. (2.12): $\phi = v_0/v$, with v_0 being the geometric volume of the helix (PL), and $\phi = v_{ef}/v$, where v_{ef} is the effective volume defined in 2.4.1 (MPL). Values of geometric and effective volume are reported in Tables 2.1 and 2.2, respectively. MC data will be reported with error bars, evaluated according to the reblocking algorithm described in ref. [43].

As a preliminary test, we have performed calculations for the the linear hard sphere chain (LHSC), for which Λ=L. Figure 2.5 shows order parameter $\langle P_2 \rangle$ and reduced pressure P^* calculated for the LHSC as a function of the packing fraction $\phi = v/v_0$. At $\phi \sim 0.24$ an IN phase transition occurs, characterized by a jump in the order parameter. On moving deeper in to the N phase $\langle P_2 \rangle$ takes higher values, larger than 0.8. The nonvanishing $\langle P_2 \rangle$ obtained in the isotropic phase from simulations can be attributed to finite-size effects, and this feature is also present in the isotropic phase for helices. Figure 2.5 shows good agreement between theory and simulations for LHSCs. The results obtained using the PL and the MPL approximation are also very close one to the other, as expected in view of the high superimpositions of the spheres, so that the cavities between them have tiny volumes. This agrees with ref. [29] where it was shown that for LHSCs the discrepancies between MC simulations and PL theory, and correspondingly also the improvements of the MPL scaling, decrease as the superposition between adjacent spheres increases.

Figures 2.6-2.8 show order parameters and pressures calculated for the helices with $r = 0.2$ and decreasing pitches $p = 8$, 4 and 2. In all these cases a IN transition is clearly visible, with

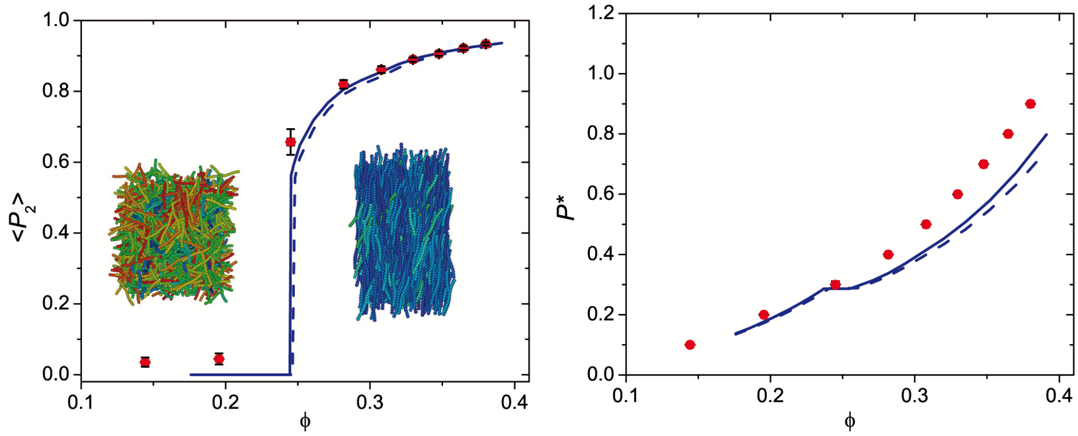

Figure 2.6: $\langle P_2 \rangle$ order parameter (Left) and reduced pressure P^* (Right) as a function of the volume fraction $\phi = v_0/v$ for the helix with p= 8 and r= 0.2, from MC simulations (closed circles) and from Onsager theory with PL (dashed line) or MPL (solid line) approximation.

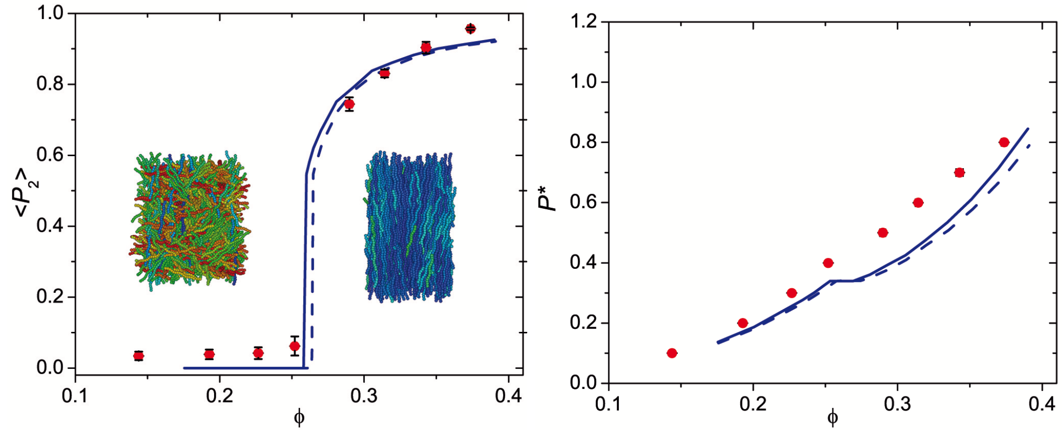

Figure 2.7: $\langle P_2 \rangle$ order parameter (Left) and reduced pressure P^* (Right) as a function of the volume fraction $\phi = v_0/v$ for the helix with p= 4 and r= 0.2, from MC simulations (closed circles) and from Onsager theory with PL (dashed line) or MPL (solid line) approximation.

its location in densities shifting from $\phi \sim 0.24$ to $\phi \sim 0.29$ with decreasing pitches from LHSC (infinite pitch) to the helix with shorter pitch ($p = 2$). This can be qualitatively understood in terms of the decrease of the Euclidean length (and hence the aspect ratio) with decreasing pitch. In all these cases, we find a good agreement between Onsager theory and numerical simulations in the location of the IN transition and in the density dependence of the $\langle P_2 \rangle$ order parameter. However pressure tends to be underestimated by theory, especially in the N phase, and this differences increase with increasing density and with decreasing pitch. The PL approximation does not appear to be adequate for these helical particles and use of the MPL variant leads only to a very slight improvement. The reason is that the non-convexity of the helices is not simply due to the voids between adjacent spheres (see Figure 2.4), so removal of these voids is not sufficient to account for the the real excluded volume.

The discrepancy with respect to LSHCs becomes even more pronounced for larger radii, as depicted in Figures 2.9-2.11 reporting the $\langle P_2 \rangle$ order parameter and the reduced pressure

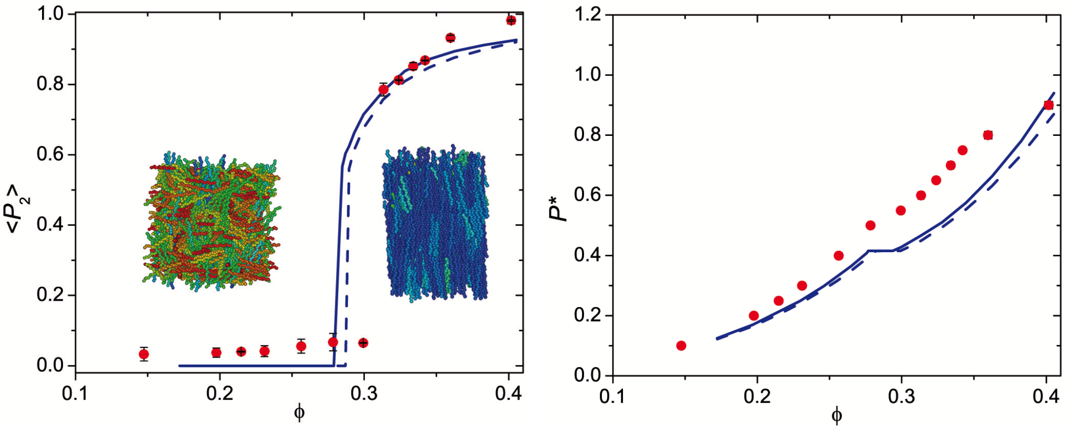

Figure 2.8: $\langle P_2 \rangle$ order parameter (Left) and reduced pressure P^* (Right) as a function of the packing fraction $\phi = v_0/v$ for the helix with $p = 2$ and $r = 0.2$, from MC simulations (closed circles) and from Onsager theory with PL (dashed line) or MPL (solid line) approximation.

calculated for helices with $r = 0.4$ and $p = 8$, 4 and 2. These helices are curlier than those with smaller r value (see Figure 2.3), so it is not surprising that the differences from the behaviour of LSHCs are even more pronounced. No clear N phase is observed in simulations for the helices with $p = 4$ and $p = 2$, although at sufficiently high packing fraction ($\phi \approx 0.35$) an anisotropic organization, with some signature of layered ordering, is visible. A complete characterization of these phases is delicate, mainly due to equilibration problems, and is presently under scrutiny. In the case of $p = 8$ (see Figure2.9), a nematic phase was detected between $\phi \sim 0.27$ and $\phi \sim 0.38$; interestingly, the IN transition occurs at higher density than for the helices with smaller radius and similar Euclidean length ($r = 0.2$ and $p = 4$). In all helices with $r = 0.4$ we have also found a marked deviation between theoretical and MC results. In contrast to simulations, a nematic phase is predicted by Onsager theory for all pitch values, with the IN transition occurring at increasing density as the pitch decreases. Of course, being the theory implemented only for isotropic and uniaxial nematic phases, other possible phases could not be investigated. In short, only for the most elongated system ($r = 0.4$ and $p = 8$), we find a reasonable agreement between theory and simulations in this case. For shorter pitches, a jump in the $\langle P_2 \rangle$ order parameter is obtained from simulations and theory at similar ϕ values, but the ordered phases appear to be different. As for pressure, differences between theory and simulations even appear in the isotropic phase for the helices with $p = 4$ and $p = 2$, with theoretical predictions lower than the MC results. For $p = 2$ the improvement deriving from the MPL approximation is more significant than in the other cases, due to the larger value of the effective volume determined for this system using the rolling sphere criterion (see Table 2.2 and 2.4.1).

An interesting last point, related to the above findings, is whether the IN phase transition for helices can be mapped on to that of rods in terms of simple parameters like the aspect ratio, as generally done in experimental work on helical systems [5]. Figure 2.12 collects the theoretical predictions of the IN phase transition as a function the Euclidean length Λ. For

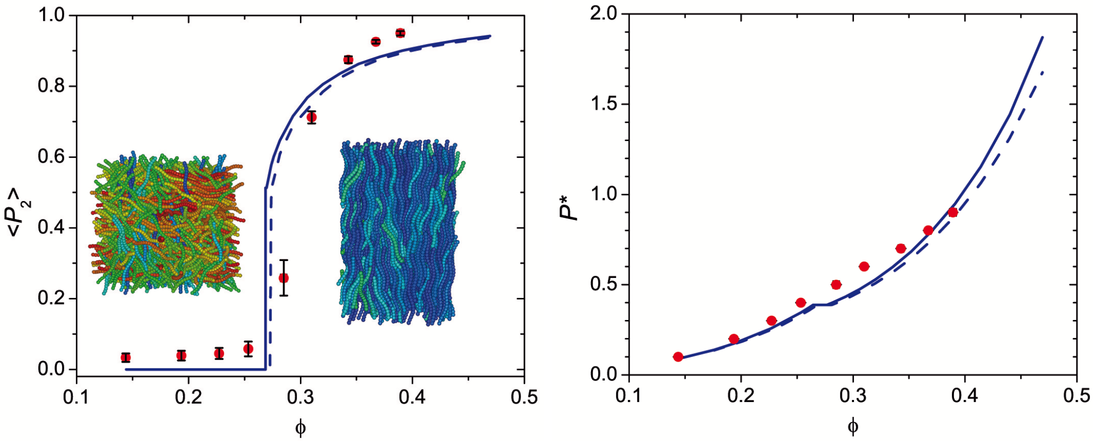

Figure 2.9: $\langle P_2 \rangle$ order parameter (Left) and reduced pressure P^* (Right) as a function of the volume fraction $\phi = v_0/v$ for the helix with $p = 8$ and $r = 0.4$, from MC simulations (closed circles) and from Onsager theory with PL (dashed line) or MPL (solid line) approximation.

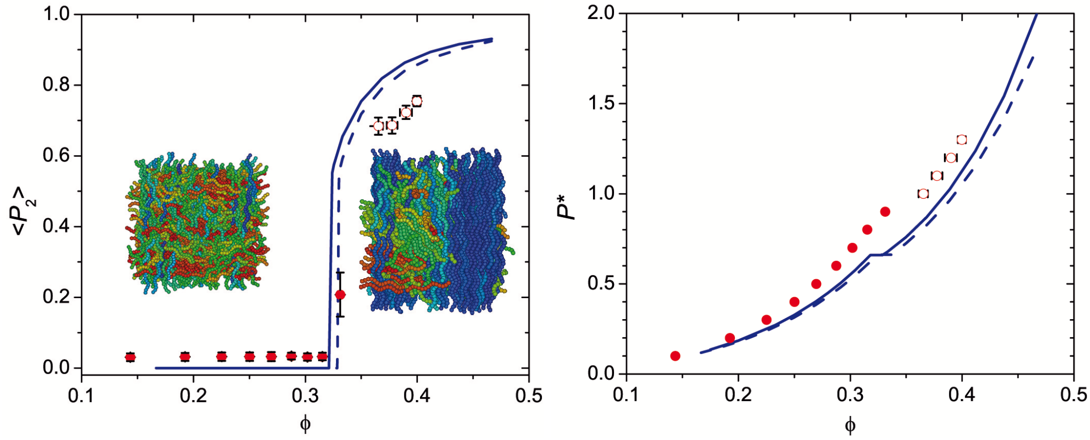

Figure 2.10: $\langle P_2 \rangle$ order parameter (Left) and reduced pressure P^* (Right) as a function of the volume fraction $\phi = v_0/v$ for the helix with $p = 4$ and $r = 0.4$, from MC simulations (circles) and from Onsager theory with PL (dashed line) or MPL (solid line) approximation. Open circles are used for metastable states not yet fully characterized.

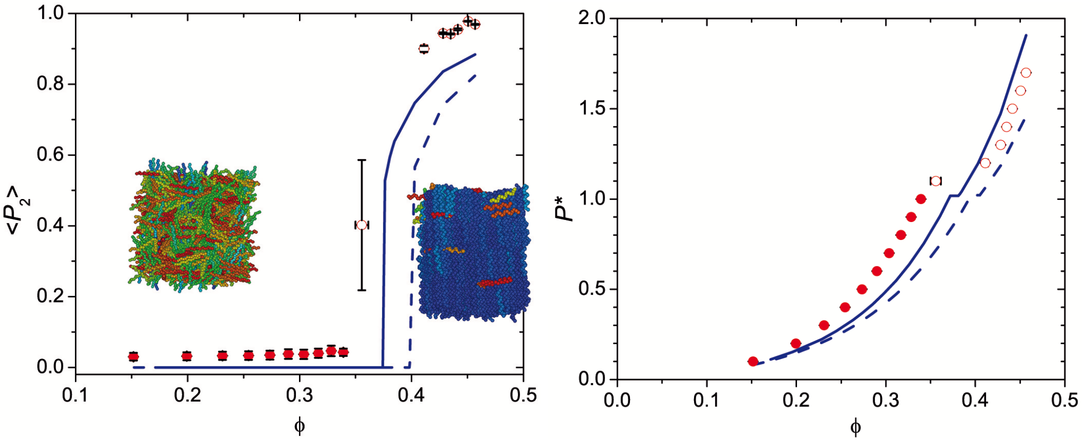

Figure 2.11: $\langle P_2 \rangle$ order parameter (Left) and reduced pressure P^* (Right) as a function of the volume fraction $\phi = v_0/v$ for the helix with $p = 2$ and $r = 0.4$, from MC simulations (circles) and from Onsager theory with PL (dashed line) or MPL (solid line) approximation. Open circles are used for metastable states not yet fully characterized.

comparison, the results obtained for LHSCs and those for spherocylinders are also reported. In the latter case the Onsager expression for the excluded volume was used [2]. Of course the contour length L, which is identical for all the helices, is not a significant parameter in relation to the IN phase transition. On the other hand, Figure 2.12 also suggests that the Euclidean length, although more meaningful, is not fully satisfactory either, since for the same aspect ratio Λ/D, the density at which the IN transition occurs has a non trivial dependence on the combination of the helical parameters r and p. As a general rule, we find the transition to move towards higher volume fraction with increasing degree of non-convexity. The fact that the location of the IN phase transition is not uniquely related to the aspect ratio may have implications for the analysis of experimental data for helical particles, as anticipated.

2.6 Conclusions

The main goal of this study was to rationalize the changes in the isotropic-to-nematic phase transition on going from straight rod-like to quite tortuous helical particles. We have found that the aspect ratio, which is usually taken as the key quantity for the IN transition, is not a suitable descriptor for helices, since there are specific effects of helical parameters. In particular, the IN transition is shifted to higher densities with decreasing Eucledian length Λ and for the same Λ values, is shifted to higher densities with increasing helical distortions.

The comparison with MC simulations has allowed us to evaluate the accuracy of Onsager theory in the case of non-convex particles. We have found that for high helicity Onsager theory departs from numerical simulations, even when a modified form of the Parsons-Lee rescaling is included to account for the non-convexity of particles. When compared to the MC simulations, Onsager theory generally underestimates pressure, with deviations that increase with increasing density and upon going from the isotropic to the nematic phase. This points

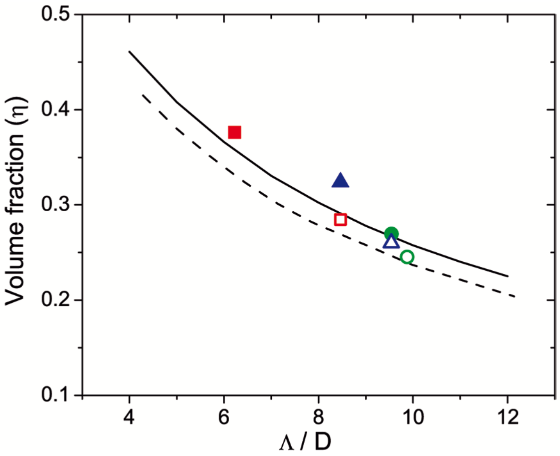

Figure 2.12: Volume fraction $\phi = v_0/v$ at the isotropic-nematic transition as a function of the Euclidean length (Λ), obtained from the Onsager theory with MPL approximation. Symbols refer to helices of different radius r (open for $r = 0.2$ and closed for $r = 0.4$) and pitch p (squares for $p = 2$, triangles for $p = 4$ and circles for $p = 8$), lines are for LHSCs (dashed) and spherocylinders (solid).

to the need of a more effective theory for hard non-convex particles, a field that remains largely unexplored. Besides the Onsager theory employed here, other theoretical approaches have been proposed, which include scaled-particle theory [45–47], the Vega and Lago theory that aims at incorporating a better description of the isotropic state [48], as well as Wertheim statistical mechanical treatment of associating fluids [49], which was successfully applied to bent-shaped particles in the isotropic phase [26]. Another approach envisages the extension of the Onsager theory beyond the second virial contribution.

Chapter 3

Hard helices: The cholesteric phase

This Chapter deals with the relationship between the helical shape of particles and the chiral properties of the cholesteric (N*) phase. Calculations based on Onsager-like theory are presented and a suitable descriptor is proposed to correlate the helix structure with the inverse cholesteric pitch and handedness.

3.1 Theoretical background

The existence of the cholesteric phase can be explained as the result of the trade-off between the intrinsic propensity to twist of the director, due to the chirality of intermolecular interactions, and a restoring torque which opposes this deformation. According to the continuum elastic theory, the Helmholtz free energy density, a, of the N* phase in the presence of long range twist deformations with pitch p_{N^*}, or wavenumber $q = 2\pi/p_{N^*}$, can be approximated by the truncated Taylor series expansion [50]:

$$a = a_u + k_2\, q + \frac{1}{2}\, K_{22}\, q^2 \tag{3.1}$$

where a_u is the free energy density of the un-deformed N phase, $k_2 = (\partial a/\partial q)_{q=0}$ is the *chiral strength*, and $K_{22} = (\partial^2 a/\partial q^2)_{q=0}$ is the *twist elastic constant*. The equilibrium wavenumber in the N* phase is then obtained by minimization of the free energy:

$$q = -\frac{k_2}{K_{22}}. \tag{3.2}$$

Chiral strength and twist elastic constant are material parameters whose value is determined by the chemical constitution of the system; in particular, k_2 vanishes in the absence of enantiomeric excess and has opposite sign for enantiomers. The twist elastic constants must be positive for the existence of a stable twisted nematic phase. On the contrary, there are no restrictiion for the sign of k_2: it is positive for a right-handed (R) N* phase, and negative for a left-handed (L) N* phase. Correspondingly, the wavenumber q is negative and positive, respectively. The prediction of k_2 and K_{22} for solutions of polyelectrolytes is a challenge: Suitable methods are needed, able to handle intermolecular interactions with different length-scales and to account for the response of the system to long range deformations, while

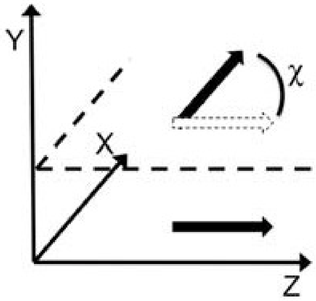

Figure 3.1: Definition of the angle χ between the director in a given position and that in the origin of the laboratory (LAB) frame. Black arrows indicate the director at different positions. $\{X, Y, Z\}$ are the axes of the LAB frame, with Z parallel to the director in the origin and Y parallel to the axis of the cholesteric helix.

including a molecular level representation. This is required since chiral properties depend on tiny effects, which are sensitive to structural details of the constituents. Here, the main points of the molecular theory, leading to expressions for the equilibrium properties of the N* phase in terms of intermolecular interactions, are outlined [51].

3.1.1 Free energy of the cholesteric phase

In the cholesteric (N*) phase, the density function can be expressed as $\rho[\mathbf{\Omega}, \chi(\mathbf{R})]$, where χ is the angle between the director at the position $\mathbf{R}$ and that in the origin of the LAB frame (see Figure 3.1) and $\mathbf{\Omega}$ are the Euler angles which define the molecular orientation in the LAB frame. Since the length scale of the twist deformation is orders of magnitude bigger than that of intermolecular interactions, the local phase properties are hardly distinguishable from those of the corresponding Nematic phase.

Thus, the free energy of the cholesteric phase can be expressed as the sum of an ideal contribution with the form of the first two terms of eq. (2.2),with the Euler angles $\mathbf{\Omega}$ expressing the molecular orientation with respect to the local director, along with an excess term which has the form

$$A^{ex} = \frac{G(\phi)}{V} \int d\mathbf{R}_2 d\mathbf{\Omega}_1 \mathbf{\Omega}_2 \rho(\mathbf{\Omega}_1) \rho[\mathbf{\Omega}_2, \chi(\mathbf{R}_2)] u(R_{12}, \mathbf{\Omega}_{12}) \tag{3.3}$$

having chosen a laboratory frame with the Z axis parallel to the local director at the position of the helix 1. Here, the factor $G(\phi) = (4 - 3\phi)/(4(1 - \phi)^2)$ is a correction introduced to account for higher virial contributions [22–24].

If a laboratory frame with the Y axis along the cholesteric axis is chosen, as in Figure 3.1 and 3.2, we can write

$$\chi(\mathbf{R}) = qY. \tag{3.4}$$

Therefore we can write $\rho = \rho(\mathbf{\Omega}, qY)$, the chiral stength and the twist elastic constant can be obtained as derivatives of excess free energy density with respect to the wavenumber q.

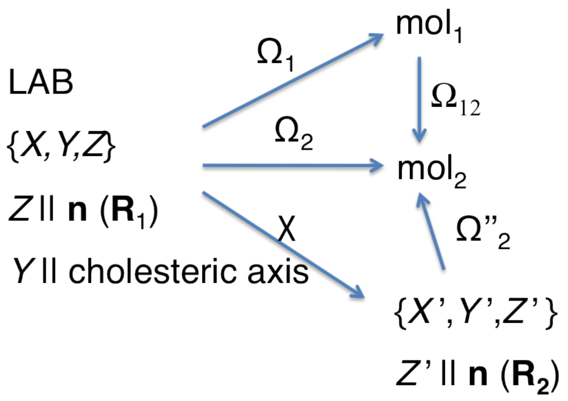

Figure 3.2: Scheme of the reference frames and of the transformations between them.

3.1.2 Orientational order parameters

The density distribution function, $\rho(\mathbf{\Omega}, \chi(\mathbf{R}))$, can be expressed by an expansion on a basis of Wigner rotation matrices, $D^j_{lm}(\mathbf{\Omega})$ [31]. In the Nematic (N) phase, the expansion has the same form as reported in eq. (2.13) which using Wigner rotation matrix formalism takes the following form:

$$\rho(\mathbf{\Omega}) = \frac{1}{8\pi^2 v} \sum_{j=0,2,4,\ldots} (2j+1) \, \langle D^j_{00} \rangle \, D^j_{00} \tag{3.5}$$

where the summation is restricted to the components of even rank j. The coefficients of the expansion, defined as:

$$\langle D^j_{00} \rangle = v \int d\mathbf{\Omega} \, \rho(\mathbf{\Omega}) D^j_{00}(\mathbf{\Omega}) \tag{3.6}$$

are the (orientational) order parameters of the N phase.

In the (N*), the expansion of the density function on a basis of Wigner rotation matrices takes the form:

$$\rho[\mathbf{\Omega}, \chi(\mathbf{R})] = \frac{1}{8\pi^2 v} \sum_{j=0,2,4,\ldots} (2j+1) \sum_{l=-j}^{j} \langle D^j_{l0}[\chi(\mathbf{R})] \rangle \, D^j_{l0}(\mathbf{\Omega}) \tag{3.7}$$

where $\langle D^j_{l0}[\chi(\mathbf{R})] \rangle$, defined by an expression analogous to eq. (3.6), are local order parameters. Using the addition theorem [31], their position dependence can be expressed as:

$$\langle D^j_{l0}[\chi(\mathbf{R})] \rangle = v \sum_{n=-j}^{j} D^j_{ln}(0, \chi, 0) \int d\mathbf{\Omega}'' \, \rho(\mathbf{\Omega}'') D^j_{l0}(\mathbf{\Omega}'') \tag{3.8}$$

where $\mathbf{\Omega}''$ are the Euler angles which define the molecular orientation in a local frame, $\{X', Y', Z'\}$, which is obtained from the LAB frame by a χ rotation around its Y axis (the LAB and the local frame have a common origin and $Y = Y'$, parallel to the cholesteric helix, but Z is parallel to the director in the origin, whereas Z' is parallel to the director at the position $\mathbf{R}$).

Since the length scale of the twist deformation is orders of magnitude bigger than that of intermolecular interactions, the density function, expressed with reference to the local director, is assumed to have the same form of that in the undeformed N phase; thus, using the relation $D^j(0,\chi,0) = d^j_{ln}(\chi)$, where $d^j_{ln}(\chi)$ are reduced Wigner rotation matrices [31], eq. (3.8) can be rewritten as:

$$\langle D^j_{l0}[\chi(\mathbf{R})]\rangle = d^j_{l0}(\chi)\,\langle D^j_{00}\rangle \tag{3.9}$$

where $\langle D^j_{00}\rangle$ coincides with the order parameter in N phase. The density function eq. (3.7) then becomes

$$\rho[\mathbf{\Omega},\chi(\mathbf{R})] = \frac{1}{8\pi^2 v}\sum_{j=0,2,4,..}(2j+1)\,\langle D^j_{00}\rangle\sum_{l=-j}^{j} d^j_{l0}[\chi(\mathbf{R})]D^j_{l0}(\mathbf{\Omega}) \tag{3.10}$$

3.1.3 Molecular expressions for the chiral strength k_2 and the twist elastic constant K_{22}

Under the assumption that the cholesteric pitch is much longer than the molecular size (see above), eqs. (2.15) and (2.16) are also appropriate for the Helmholtz free energy of N* phase, provided that the order parameters appearing in them bear a dependence on the position, as in eq. (3.9). Using the transformations shown in Figures 3.1 and 3.2, the Helmholtz free energy can be expressed in terms of the cholesteric wavenumber q, as shown in eq. (3.3). Thus, molecular expressions for the chiral strength, k_2, and for the elastic constant, K_{22}, are obtained as derivatives of the Helmholtz free energy density, $a = A/V$, i.e. $k_2 = (\partial a/\partial q)_{q=0}$ and $K_{22} = (\partial^2 a/\partial q^2)_{q=0}$:

$$\begin{aligned} k_2 =& \frac{1}{3\sqrt{2}}\frac{1}{8\pi^2 v^2}G(\phi)\sum_{j_A=0,2,4}(2j_A+1)\,\langle D^{j_A}_{00}\rangle\sum_{j_B=0,2,4}(2j_B+1)\sqrt{\frac{(j_B+1)!}{(j_B-1)!}} \\ &\times C^2(j_A,j_B,1;0,1,1)\,\langle D^{j_B}_{00}\rangle\int d\mathbf{\Omega}_{12}\int d\mathbf{R}_{12}\,\mathrm{Im}\left\{D^{j_B}_{10}T^{11}\right\}u(\mathbf{R}_{12},\mathbf{\Omega}_{12}) \end{aligned} \tag{3.11}$$

and

$$K_{22} = [K_{22}]_{T^{00}} + [K_{22}]_{T^{20}} + \sum_{p=1,2}[K_{22}]_{T^{2p}} \tag{3.12}$$

with

$$\begin{aligned} [K_{22}]_{T^{00}} =& \frac{G(\phi)}{8}\left(\frac{1}{8\pi^2 v}\right)^2\sum_{j_A=2,4,..}(2j_A+1)\,\langle D^{j_A}_{00}\rangle\sum_{j_B=2,4,..}(2j_B+1)\,\langle D^{j_b}_{00}\rangle\,\delta_{j_A,j_B}\left(-\frac{16\pi^2}{\sqrt{3}}\right) \\ &\times j_B(j_B+1)C^2(j_A,j_B,0;0,0,0)\int d\mathbf{R}_{12}\int d\mathbf{\Omega}_{12}D^{j_B}_{00}(\mathbf{\Omega}_{12})T^{00}u(\mathbf{R}_{12},\mathbf{\Omega}_{12}) \end{aligned} \tag{3.13}$$

$$\begin{aligned} [K_{22}]_{T^{2p}} =& \frac{1}{8}G(\phi)\left(\frac{1}{8\pi^2 v}\right)^2\sum_{j_A=2,4,..}(2j_A+1)\,\langle D^{j_A}_{00}\rangle\sum_{j_B=2,4,..}(2j_B+1)\,\langle D^{j_b}_{00}\rangle\,\frac{8\pi^2}{5} \\ &\times\left\{\frac{2}{\sqrt{6}}j_B(j_B+1)C(j_A,j_B,2;0,0,0) - \sqrt{\frac{(j_B+1)!)}{(j_B-1)!}}C(j_A,j_B,2;0,2,2)\right\} \\ &\times 2C(j_A,j_B,2;0,p,p)\int d\mathbf{R}_{12}\int d\mathbf{\Omega}_{12}\,\mathrm{Re}\{D^{j_B}_{10}(\mathbf{\Omega}_{12})T^{2p}_{12}\}u(\mathbf{R}_{12},\mathbf{\Omega}_{12}) \end{aligned} \tag{3.14}$$

$$
\begin{aligned}
[K_{22}]_{T^{20}} = & \frac{1}{8}G(\phi)\left(\frac{1}{8\pi^2 v}\right)^2 \sum_{j_A=2,4,..}(2j_A+1)\langle D_{00}^{j_A}\rangle \sum_{j_B=2,4,..}(2j_B+1)\langle D_{00}^{j_b}\rangle \frac{8\pi^2}{5} \\
& \times \left\{ \frac{2}{\sqrt{6}} j_B(j_B+1)C(j_A,j_B,2;0,0,0) - \sqrt{\frac{(j_B+2)!)}{(j_B-2)!}}C(j_A,j_B,2;0,2,2) \right\} \\
& \times 2C(j_A,j_B,2;0,0,0)\int d\mathbf{R}_{12}\int d\mathbf{\Omega}_{12} D_{00}^{j_B}(\mathbf{\Omega}_{12})T^{20}u(\mathbf{R}_{12},\mathbf{\Omega}_{12})
\end{aligned}
\tag{3.15}
$$

In the above expressions, $C(j_A, j_B, j; 0, m, m)$ are Clebsch–Gordan coefficients [31], while Im$\{\}$ and Re$\{\}$ denote the imaginary and real part of the functions within brackets, respectively. The symbol T^{1p} is used for irreducible spherical components of the first rank tensor $\mathbf{R}_{12}$, while T^{00} and T^{2p} are used for zeroth and second rank irreducible spherical components of the tensor $\mathbf{R}_{12} \otimes \mathbf{R}_{12}$ [31]. Their explicit expressions in terms of spherical coordinates $\mathbf{R}_{12} = (R_{12}, \phi_{12}, \theta_{12})$ are:

$$T^{0,0} = -\frac{1}{\sqrt{3}}R_{12}^2 \tag{3.16a}$$

$$T^{1,\pm 1} = \mp\left(\frac{1}{2}\right)^{1/2} R_{12}\sin\theta_{12}(\cos\phi_{12} \pm \imath\sin\phi_{12}) \tag{3.16b}$$

$$T^{2,0} = \frac{1}{\sqrt{6}}R_{12}^2(1+3\cos^2\theta_{12}) \tag{3.16c}$$

$$T^{2,\pm 1} = \mp R_{12}^2\sin\theta_{12}\cos\theta_{12}(\cos\phi_{12} \pm \imath\sin\phi_{12}) \tag{3.16d}$$

$$T^{2,\pm 2} = R_{12}^2\sin^2\theta_{12}\left[\frac{1}{2}(\cos\phi_{12}^2 - \sin^2\phi_{12}) \pm \imath\cos\phi_{12}\sin\phi_{12})\right] \tag{3.16e}$$

If we introduce the quantities

$$h_{ii} = -\int d\Omega_{12}\int d\mathbf{R}_{12}\ \mathrm{Im}\left\{D_{10}^{i}\left(\Omega_{12}\right)T^{11}\right\}\ u\left(\mathbf{R}_{12},\Omega_{12}\right) \tag{3.17}$$

eq. (3.11) can be rewritten as:

$$
\begin{aligned}
k_2 = & -\frac{1}{3\sqrt{2}}\frac{1}{8\pi^2 v^2}G(\phi)\sum_{j_A=0,2,4}(2j_A+1)\langle D_{00}^{j_A}\rangle \\
& \times \sum_{j_B=0,2,4,\ldots}(2j_B+1)\sqrt{\frac{(j_B+1)!}{(j_B-1)!}}C^2(j_A,j_B,1;0,1,1)\langle D_{00}^{j_B}\rangle\, h_{j_B j_B}
\end{aligned}
\tag{3.18}
$$

The orientational order parameters of the helices in the N phase are obtained by minimization of the free energy, eqs. (2.15) and (2.16); under the assumptions specified above, these are also the order parameters of the helices with respect to the local director in the N* phase. The cholesteric pitch is calculated as

$$p_{N^*} = -\frac{2\pi K_{22}}{k_2}. \tag{3.19}$$

Since both chiral strength and twist elastic constant are proportional to the Parsons-Lee factor, the pitch is independent of it.

3.2 Computational details

For free energy minimization the same procedure described in 2.2.4 was used.

3.2.1 Evaluation of pair integrals

Calculations require the evaluation of six-fold integrals with the general form:

$$\int d\mathbf{R}_{12} \int d\mathbf{\Omega}_{12} u(\mathbf{R}_{12}, \mathbf{\Omega}_{12}) \Xi(\mathbf{R}_{12}, \mathbf{\Omega}_{12}) \tag{3.20}$$

where $\mathbf{\Omega}_{12} = (\alpha_{12}, \beta_{12}, \gamma_{12})$ are Euler angles for the rotation from the molecular frame of helix 1 to that of helix 2 and $\Xi(\mathbf{R}_{12}, \mathbf{\Omega}_{12})$ denotes a generic function, whose specific form depends upon the property we are dealing with:

$$\Xi(\mathbf{R}_{12}, \mathbf{\Omega}_{12}) = \begin{cases} \mathrm{Im}\{D^{j_B}_{10}(\mathbf{\Omega}_{12}) T^{11}\} \rightarrow k_2 \\ \mathrm{Re}\{D^{j_B}_{10}(\mathbf{\Omega}_{12}) T^{2p}\} \rightarrow K_{22} \\ \qquad\qquad\qquad D^{j_1}_{00} \rightarrow \text{order parameters}, P, \mu \end{cases} \tag{3.21}$$

Using spherical coordinates $R^0_{12} = \{R_{12}, \phi_{12}, \theta_{12}\}$ the explicit form of integral eq. (3.20) is:

$$\begin{aligned} &\int_0^{2\pi} d\phi_{12} \int_0^{\pi} d\theta_{12} \sin\theta_{12} \int_0^{2\pi} d\alpha_{12} \int_0^{\pi} d\beta_{12} \sin\beta_{12} \int_0^{2\pi} d\gamma_{12} \\ &\times u(R_{12}, \phi_{12}, \theta_{12}, \alpha_{12}, \beta_{12}, \gamma_{12}) \Xi(R_{12}, \phi_{12}, \theta_{12}, \alpha_{12}, \beta_{12}, \gamma_{12}) \int_0^{\infty} dR_{12} R_{12}^2 \end{aligned} \tag{3.22}$$

Gauss-Legendre and Gauss-Chebyshev quadrature algorithms are used to evaluate these integrals, exclusive of the integral on γ_{12} which is evaluated using Romberg quadrature [32]. The cost of the calculation can be very high since a large number of pair configurations has to be sampled. In particular, high accuracy is required for k_2, because this is a small quantity, resulting from the sum of integrals which are large in value and opposite in sign.

3.3 Results and discussion

In presenting and discussing our results we will use reduced units, with the diameter D taken as the unit of length: $h^*_{ii} = h_{ii}/D^4$, $k^*_2 = k_2 D^2/k_B T$, $K^*_{22} = K_{22} D^3//k_B T$, and $p^*_{N^*} = pN^*/D$.

3.3.1 Helices with constant contour length

Calculations were performed for the cholesteric phase formed by the right-handed helices shown in Figure 2.3. Table 3.1 reports for all of them the inclination angle ψ, defined by eq. (2.25) and the h_{ii} contributions to the chiral strength, defined by eq. (3.17). The second rank contribution, h_{22}, which in general is the largest, has a simple meaning that clearly appears if the expression under the integral in eq. (3.17) is rewritten as:

$$(\hat{\mathbf{u}}_1 \cdot \hat{\mathbf{u}}_2)(\hat{\mathbf{u}}_1 \wedge \hat{\mathbf{u}}_2) \cdot \mathbf{R}_{12} = \frac{1}{2} (\hat{\mathbf{w}}_{12} \cdot \mathbf{R}_{12}) \sin(2\beta_{12}) \tag{3.23}$$

where $\mathbf{R}_{12}$ is the inter helix vector, $\hat{\mathbf{u}}_1$ and $\hat{\mathbf{u}}_2$ are unit vectors parallel to the helix axes, β_{12} is the angle between them and $\hat{\mathbf{w}}_{12} = \hat{\mathbf{u}}_1 \wedge \hat{\mathbf{u}}_2 / |\hat{\mathbf{u}}_1 \wedge \hat{\mathbf{u}}_2|$. Thus, the expression under the integral is equal to zero when the two helices are perpendicular to each other (β_{12} is a multiple of $\pi/2$), and is positive/negative for a right-handed (**R**)/left-handed (**L**) relative

		h_{22}^*	h_{44}^*	h_{66}^*	ψ (°)
$r = 0.2$	$p = 2$	-15.1573	9.041	1.432	57.858
	$p = 4$	-78.457	0.722	5.577	72.559
	$p = 8$	-66.101	- 12.598	-2.765	81.073
$r = 0.4$	$p = 2$	-2.425	8.419	-0.751	38.512
	$p = 4$	-147.348	28.968	9.549	57.858
	$p = 8$	-212.318	-23.4329	1.700	72.559

Table 3.1: Reduced h_{ii}^* values, eq.(3.17), and inclination angle, ψ, calculated for the helices reported in Figure 2.3, having different pitch p and radius r. Lengths are scaled with the sphere diameter D.

configuration. The maxima in absolute value correspond to β_{12} equal to odd multiples of $\pi/4$. The integral is evaluated for all pair configurations. For achiral particles, e.g. for cylinders, the number of (R) and (L) configurations is identical, and the integral vanishes; however, in the case of helices there is an unbalance and a net value is obtained. If the two chiral molecules are replaced by their mirror images (enantiomers) the integral changes its sign.

We can see in Table 3.1 that negative h_{22} values have been obtained for all helices with $\psi > \pi/4$; higher rank contributions may be positive or negative, but are generally smaller. For one case ($p = 2$, $r = 0.4$) the inclination ψ is sligthly lower than $\pi/4$; h_{22} is negative, but small, and h_{44} is larger and positive. We can also see that, for the same inclination, significantly higher h_{22} values are obtained for helices with larger pitch and radius. This can be easily understood considering that larger picth and radius imply deeper groves and more marked deviations for a cylindrical shape.

Table 3.2 shows the predictions for the cholesteric phase formed by the helices under investigations: Chiral strength k_2^*, twist elastic constant K_{22}^*, $\langle P_2 \rangle_{\mathrm{NI}}$ order parameter and cholesteric pitch. All quantities are calculated at the N*I transition. We can see a clear correlation between the chiral strength and the h_{22}^* values just commented: Positive k_2^* is predicted for all helices but the one with $p = 2$, $r = 0.4$, for which a small negative k_2^* is obtained. Higher chiral strengths are predicted for the helices with $r = 0.4$, which are more curled, with the exception of those having case $p = 2$. In this case strong interlocking of pair of adjacent helices is not possible, due to the small size of the helix pitch compared to the sphere diameter. The twist elastic constants are much lesss sensitive than chiral strengths to changes in the helix structure and follow the trend of the $\langle P_2 \rangle$ order parameters (see Chapter 2 for the discussion of the transition properties). Thus, the calculated $p_{N^*}^*$ values reflect the chiral strenghts, with a left-handed twist in all but one case. The cholesteric pitch predicted for the helices with $r = 0.4$ and p sufficiently larger than the sphere diameter, which is only 100 times the molecular dimensions, is particularly small. Indeed, typical experimental values for lyotropic liquid crystals are at least one order of magnitude higher [18, 20, 52, 53].

		$k_2^* \times 10^{16}$	K_{22}^* (10^8)	$\langle P_2 \rangle_{\mathrm{IN}}$	$p^*_{N^*}$	Λ
$r = 0.2$	$p = 2$	1.368	4.862	0.64	-2224.8	8.47
	$p = 4$	11.180	5.035	0.66	-268.00	9.54
	$p = 8$	8.278	5.052	0.68	-398.48	9.88
$r = 0.4$	$p = 2$	-0.967	3.863	0.60	2507.8	6.23
	$p = 4$	28.049	4.326	0.61	-96.89	8.47
	$p = 8$	31.414	4.522	0.61	-90.42	9.55

Table 3.2: Reduced chiral strength k_2^* and twist elastic constant K_{22}^*, $\langle P_2 \rangle_{\mathrm{IN}}$ order parameter and reduced cholesteric pitch $p^*_{N^*}$ calculated at the IN phase transition for the helices reported in Figure 2.3, having different pitch p and radius r. Λ is the Eucledian length. p, r and Λ are scaled with the sphere diameter D.

3.3.2 Helices with constant Euclidean length

To analyse in a systematic way the relationship between inclination angle and cholesteric handedness we have considered a set of helices with the same aspect ratio ($\Lambda = 16$), radius equal to $r = 0.6$ and pitch $p$equal to 2, 4, 6, 8, 10 and 12. Again, the sphere diameter D is taken as the unit lenght. So, along this series the inclination angle changes only as a function of the pitch. The helices are shown in Figure 3.3 and Table 3.3 reports their inclination angles, which gradually increase from $\sim 28°$ to $\sim 75°$. Figure 3.4 shows the calculated h_{22}^* values as a function of the inclination angle. Since, as just discussed, the twist elastic constant is expected to be similar for all the helices in Figure 3.3, the changes in h_{22}^* can be related to those in the cholesteric organization. A non monotonic dependence on the inclination angle (i.e. the helix pitch, here) clearly appears: h_{22} is negative for $\psi >\sim 40°$ and takes the highest absolute values around $\psi \sim 65°$. This means that helices having $p > 2$ are predicted to form left-handed cholesteric phases and the tightest pitches are expected for $p = 8$. For $\psi <\sim 40°$, h_{22} becomes positive, but is low, which can be understood for the reason discussed in the previous section. So, the helix with $p = 2$ is expected to form a long-pitch, right-handed cholesteric phase.

For the sake of comparison we show in Figure 3.4 also the h_{22}^* values obtained for the some of the helices examined in the previous section ($\Lambda = 10$). They are smaller than those for the helices in Figure 3.3 but, for helices with the same ψ value, it is mainly a matter of size. If we compare, for instance, the cases $r = 0.4$, $p = 8$ and $r = 0.6$, $p = 12$, the scale factor is $\approx 1.5^4$, as expected simply for scaling reasons from eq. (3.17).

3.4 Conclusions

Our calculations for hard helices with different r, p values show that the helix parameters, while crucial for the chiral strength k_2, have a comparatively weaker effect on the molecular order parameter and on the twist elastic constant K_{22}, which are mainly determined by the

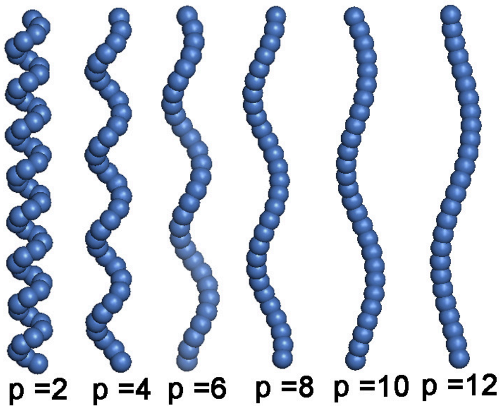

Figure 3.3: Helices of radius, $r = 0.6$, and pitch p equal to 2, 4, 6, 8, 10 and 12.

helices	ψ (°)
$p = 2$	27.9467
$p = 4$	46.6962
$p = 6$	57.8581
$p = 8$	64.7684
$p = 10$	69.344
$p = 12$	72.5594

Table 3.3: Inclination angle for helices of same $\Lambda = 16$ and radius, $r = 0.6$.

ic

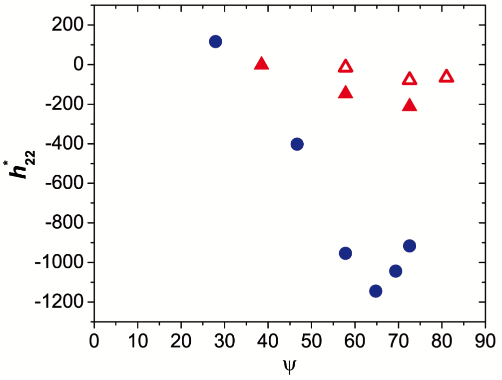

Figure 3.4: Cholesteric parameter, h^*_{22}, as a function of the inclination angle. Blue circles: Helices with Eucledian length $\Lambda = 16D$ and radius equal to 0.6. Closed triangles: Helices with $\Lambda = 10$, $r = 0.4$, and $p = 2, 4$ and 8. Empty triangles: Helices with $\Lambda = 10$, $r = 0.2$, and $p = 2, 4$ and 8.

anisotropy of particles. So, we can propose a chiral descriptor, h_{22} defined by eq. (3.17), which correlates with the inverse cholesteric pitch.

Our systematic investigation confirms the expectation, based on geometry considerations [54], that the cholesteric organization has a non-monotonic dependence upon the helix parameters. In particular calculations confirm the change of cholesteric handedness for inclination angles $\psi \sim 40^\circ$: Right-handed helices with $\psi > 40^\circ$ are found to form L cholesterics, those with $\psi < 40^\circ$ lead to R cholesterics. For left-handed helices the opposite would occur. Helices having $\psi \sim 65^\circ$ are the most effective in twisting the nematic director. This is a general trend for helices with purely hard core interactions, provided that the helix pitch is longer than the characteristic size of particles (in our case, for $p \sim D$). When the two lenght scales become comparable more specific effects may appear, which require an ad hoc analysis.

Interestingly, for strongly curled helices we predict very tight cholesteric pitches, of the order of one hundred times the characteristic size of particles. There are no evidences of such strong distortions in real systems: Typical values of the cholesteric pitch for lyotropic liquid crystals are at least one order of magnitude higher [55]. One reason is that in real systems there are also other interactions, which can compete with steric repulsions [56–58]. Moreover helical particles, whether they be polymers or colloids, are generally endowed by some flexibility, and this has the effect of reducing the net chirality [55]. One last point has to be remarked: The results reported here were obtained for the hypotentical N^* phase that beyond a certain packing fraction becomes more stable than the isotropic phase. However, under the same conditions there might be other competing phases, which have not been considered here. Actually, as will be shown in the next chapter, for strongly curled helices Monte Carlo simulations show a direct transition from the isotropic to another chiral nematic phase with screw-like order.

Chapter 4

Hard helices: The screw-like nematic phase

This Chapter deals with the phase diagram of hard helices. We present convincing theoretical evidence of the existence of a new chiral nematic phase, which we have called screw-like nematic (N_s^*), originating from the specific helical shape. The main features of the entropy-driven nematic-to-screw-like-nematic phase transition are analyzed as a function of the helical parameters.

4.1 Phase Diagram

The same model of helices in Chapter 2 were studied and MC isobaric-isothermal (NPT) simulations [37] were performed using the same methodology described in section 2.4.

Figure 4.1 shows the MC results for $r = 0.2$ and $r = 0.4$ and the same values of $p = 4$ and 8. In the P^*–volume fraction plane, points labeled I, N, Sm correspond to the isotropic, ordinary nematic and smectic phases, respectively, as identified by the usual nematic $\langle P_2 \rangle$ and smectic $\tau_1 = |\langle \exp\left(i2\pi Z/d\right)\rangle|$ (d being the layer spacing, and Z being the position along the $\widehat{\mathbf{n}}$ axis) order parameters [59], as well as appropriate correlation functions. Note that, unlike the case of spherocylinders [60], the high-density phase diagram of helices is not known, and constitutes an interesting property on its own right. Points identified by C in Figure 4.1 correspond to compact phases and are associated with highly ordered configuration compatible with solid-like ordering. Finally, points identified by N_s^* in Figure 4.1 correspond to the new nematic phase with screw-like order. These are the central results of this Chapter.

4.2 Screw-like nematic phase

Similarly to the cholesteric, the screw-like nematic phase is still nematic in that helices are homogeneously distributed and mobile with their principal axis $\widehat{\mathbf{u}}$ preferentially oriented along $\widehat{\mathbf{n}}$. Differently from the cholesteric, in this new organization it is their C_2 ($\widehat{\mathbf{w}}$) axes that become long-range correlated and preferentially oriented along a second director $\widehat{\mathbf{c}}$, that

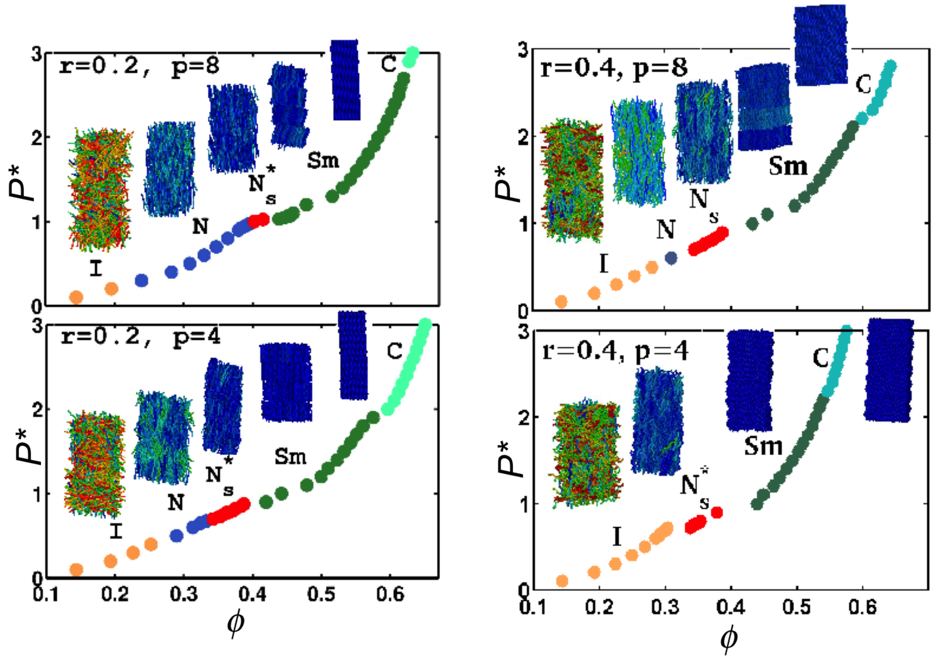

Figure 4.1: P^* as a function of ϕ for systems with $r = 0.2, 0.4$ and $p = 4, 8$. Representative snapshots of each phase (I=isotropic, N=nematic, N_s^*=screw-like, Sm=smectic, C=compact) are also given in each panel. Here different colors represent different orientations of the helix axis $\hat{\mathbf{u}}$ with respect to the direction $\hat{\mathbf{n}}$.

in turn spirals around $\hat{\mathbf{n}}$ with a pitch that coincides with that of the particle (Figure 4.2(a)). This phase appears at the high density end of the nematic phase, when helices are well aligned, and is characterized by the helices C_2 axes spiraling around the nematic director with periodicity equal to the particle pitch. This coupling between translational and rotational degrees of freedom allows a more efficient packing and hence an increase of the translational entropy counterbalancing the loss of orientational entropy. and denote it by N_s^*.

There have been some previous clues of the existence of this phase. Barry *et al* [61] observed a screw-like nematic organization in suspensions of helical shaped flagella with a pitch of the order of the nanometer, using polarising and differential interference contrast microscopy, combined with experiments on single-particle dynamics. This unknown organization was identified as the conical phase [62–64]. Manna *et al* [65] presented a study of the transition from the conventional nematic phase to a nematic phase with screw-like order based on symmetry considerations, and suggested that in principle this could also be exhibited by DNA. We have fully characterizes the microscopic order exhibited by the screw-like nematic phase and analyzes its stability relative to the isotropic and to the conventional nematic phase, as a function of the helix parameters, the radius r and the pitch p. Formation of the screw-like nematic phase will be explained in terms of a coupling between translational and rotational degrees of freedom occouring whenever there is a sufficiently high interlock of the grooves belonging to neighboring helices. The screw-like nematic organization is then adopted in order to maximize the translational entropy and hence balance the loss in

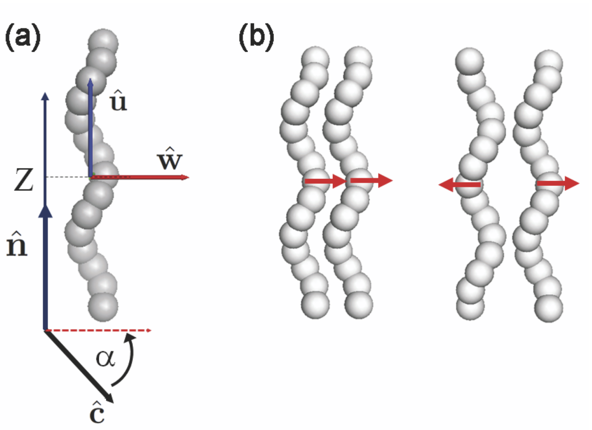

Figure 4.2: (a) Model helix made of 15 partially fused hard spheres of diameter D, our unit of length, and contour length L=10D. Shown are the molecular axes ($\widehat{\mathbf{w}}, \widehat{\mathbf{u}}$), the phase directors ($\widehat{\mathbf{c}}, \widehat{\mathbf{n}}$) and the laboratory axes (X,Z). (b) Pairs of helices instantaneously in phase and anti-phase; arrows show the twofold symmetry axes (C_2).

orientational entropy associated with the periodic alignment of the C_2 axes.

As an intuitive physical picture, consider a pair of helices that are locally in phase contrasted with the case where they are in antiphase, as schematically illustrated in Figure 4.2 (b). Clearly, in the latter case both helices can freerly rotate about their principal axis, effectively behaving as cylinders, whereas this is no longer true for the in phase configuration, where one of the two helices has to perform a specific additional translation along its principal axis, in order to also rotate about it. This new phase require a special set of correlation functions and order parameters to be fully characterized. One key orientational correlation function is

$$g_{1,\parallel}^{\widehat{\mathbf{w}}}(R_\parallel) \quad = \quad \langle \widehat{\mathbf{w}}_i \cdot \widehat{\mathbf{w}}_j \rangle (R_\parallel), \tag{4.1}$$

where $\widehat{\mathbf{w}}_i$ is a unit vector along the C_2 axis of helix i while $R_\parallel = \mathbf{R}_{ij} \cdot \widehat{\mathbf{n}}$ is the projection along $\widehat{\mathbf{n}}$ of the interparticle separation between a pairs of helices i and j. Thus $g_{1,\parallel}^{\widehat{\mathbf{w}}}(R_\parallel)$ probes the polar correlation between the C_2 axes of two helices as a function of their distance projected along the main director. Figure 4.3 shows this correlation function calculated for helices with $r = 0.2$ (a) and 0.4 (b) and pitches $p = 3$ and 6, at different values of volume fraction $\phi = \rho v_0$, with ρ the density of the sample and v_0 the volume of a helical particle (see Chapter 2). For both radii, a sinusoidal structure with a periodicity equal to p is clearly visible. It persists with a constant amplitude at long interparticle distances. This behaviour reflects the helical correlation of particle C_2 axes along $\widehat{\mathbf{n}}$ and is the signature of the screw-like order. The results reported for $p = 3$ in Figure 4.3(a) illustrate the onset of this order with increasing density: for $\phi \simeq 0.27$ $g_{1,\parallel}^{\widehat{\mathbf{w}}}(R_\parallel)$ is equal to zero everywhere, showing the lack of transversal correlation between helices, but at $\phi \simeq 0.36$ a small amplitude oscillation can be distinguished, which continuously grows up with increasing density, toward the condition of perfect ordering, where $g_{1,\parallel}^{\widehat{\mathbf{w}}}(R_\parallel)$ would oscillate between ±1.

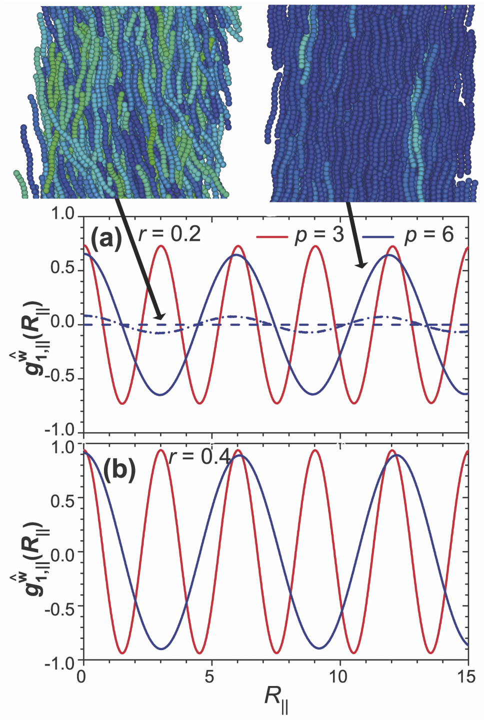

Figure 4.3: The correlation function $g^{\widehat{\mathbf{w}}}_{1,\|}(R_\|)$. (a) $r = 0.2$ and $p = 3$ (red) at $\phi \simeq 0.38$, and $p = 6$ (blue) at $\phi \simeq 0.40$ (solid), $\phi \simeq 0.36$ (dashed dotted) and $\phi \simeq 0.27$ (dashed). (b) $r = 0.4$ and $p = 3$ at $\phi \simeq 0.41$ and $p = 6$ at $\phi \simeq 0.40$.

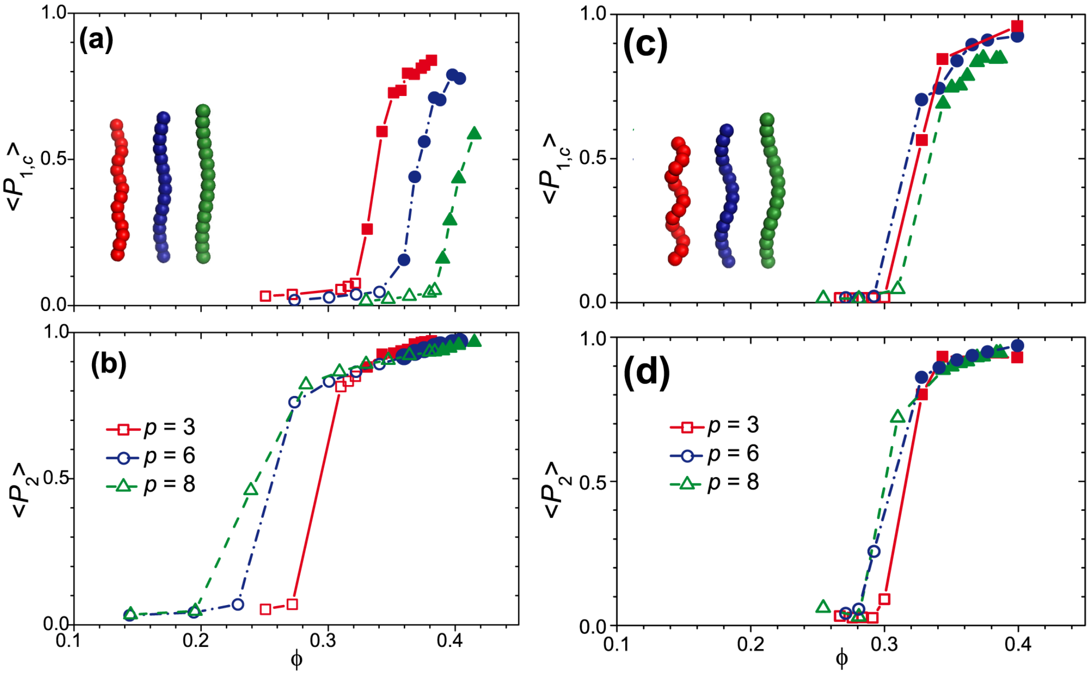

Figure 4.4: The order parameters $\langle P_2 \rangle$ and $\langle P_{1,c} \rangle$ as a function of the volume fraction ϕ, in the case $r = 0.2$ (a,b) and $r = 0.4$ (c,d) and different values of the pitches $p = 3; 6; 8$. Solid symbols are used for N_s^* phase.

Based on the symmetry of the particles and of the phase [66], we have found that the lowest rank order parameter characterizing the N_s^* phase is given by

$$\langle P_{1,c} \rangle = \langle \widehat{\mathbf{w}} \cdot \widehat{\mathbf{c}} \rangle \,, \tag{4.2}$$

that distinguishes the N_s^* from the standard N phase, as both are characterized by a non-zero value of $\langle P_2 \rangle$.

In Figure 4.4 (a,b) both $\langle P_2 \rangle$ and $\langle P_{1,c} \rangle$ are depicted as a function of ϕ at increasing value of pitches ($p = 3; 6; 8$) in the case of $r = 0.2$. Note that values with $p \leq 2$ are particular cases as very limited interlocking of spheres belonging to neighboring helices can occur under these conditions. As pitch increases, the location of the isotropic-to-nematic transition moves to lower ϕ, as indicated by the $\langle P_2 \rangle$ behaviour, in agreement with results reported earlier (see Chapter 2); this can be understood in terms of an increase of the aspect ratio that tends to stabilize the N phase. The location of the N to N_s^* phase transition instead moves to larger ϕ for increasing pitch, with a significant pitch dependence. The onset of a N_s^* phase always occurs at high values of $\langle P_2 \rangle$, with the behaviour of the $\langle P_{1,c} \rangle$ in the neighborhood of the N to N_s^* phase transition suggestive of a second-order character. This is at variance with the first-order character of the isotropic-to-nematic transition. and can be ascribed to the fact that the nematic order has first to set in and reach a very high degree before the C_2 axes start twisting around $\widehat{\mathbf{n}}$ and become long-range correlated to enhance translational entropy. The situation is markedly different for the cases with $r = 0.4$, depicted in Figure 4.4(c,d). While there is a similar trend, albeit much less pronounced, of the isotropic-to-nematic transition approximatively shifting toward larger volume fraction for decreasing pitch, a direct transition from the isotropic to the N_s^* phase is here observed, with no signature of the ordinary N phase, as indicated by the simultaneous raise of both $\langle P_2 \rangle$ and $\langle P_{1,c} \rangle$.

4.3 Onsager-like theory

The onset of the N_s^* phase has been further rationalized by an Onsager theory [2]. Since numerical simulations show that the N_s^* phase forms at very high values of $\langle P_2 \rangle$, we have assumed perfectly parallel helices ($\langle P_2 \rangle = 1$). The single-particle density can be expressed as a function of $\alpha' = \widehat{\mathbf{w}} \cdot \widehat{\mathbf{c}}$, the azimuthal angle between the C_2 helix axis $\widehat{\mathbf{w}}$ and the local $\widehat{\mathbf{c}}$ director; thus $f(\alpha')$ is the local orientational distribution function. In the N phase the latter is a constant, $f = 1/2\pi$, being the normalization condition $\int_0^{2\pi} d\alpha' f(\alpha') = 1$. The Helmholtz free energy is expressed as a functional of the single-particle density $A[f(\alpha, Z)]$, with Z the position of a particle along $\widehat{\mathbf{n}}$ and $\alpha = \alpha' + 2\pi Z/p$ (Figure 4.2(a)). Its orientational contribution

$$\frac{\beta A^{or}}{N} = \int_0^{2\pi} d\alpha' f(\alpha') \ln \left[2\pi f(\alpha') \right] \tag{4.3}$$

represents the entropic cost for the loss of freedom in the azimuthal angle rotation. Here $\beta = 1/(k_B T)$ with k_B the Boltzmann constant. In the Onsager's spirit, the second–virial

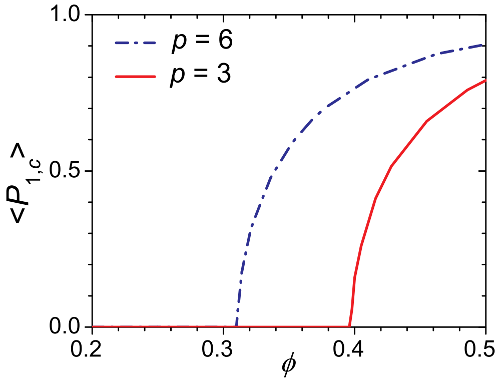

Figure 4.5: Order parameter $\langle P_{1,c} \rangle$ as a function of the volume fraction ϕ, calculated for helices with $r = 0.4$ and pitch $p = 3$ and 6 using Onsager theory.

approximation is used for the excess free energy:

$$\begin{aligned}\frac{\beta A^{ex}}{N} &= \frac{\rho}{2} \frac{4-3\phi}{4(1-\phi)^2} \int_0^{2\pi} d\alpha_1 f(\alpha_1|0) \\ &\quad \int dZ_{12} \int_0^{2\pi} d\alpha_2 f(\alpha_2|Z_{12}) a_{excl}(Z_{12}, \alpha_1, \alpha_2)\end{aligned} \tag{4.4}$$

where particle positions and orientations are expressed with respect to the same (laboratory) reference frame, having its origin at the position of the center of the particle 1 and the X axis parallel to the $\hat{\mathbf{c}}$ director at this position. The vector $\mathbf{R}_{12} = (X_{12}, Y_{12}, Z_{12})$ defines the position of particle 2 in this frame, and α_i is the angle between the C_2 axis of particle i and the X axis. The factor $(4-3\phi)/(4(1-\phi)^2)$ is a correction introduced to account for higher virial contributions [22–24]. The function a_{excl}, defined as:

$$a_{excl}(Z_{12}, \alpha_1, \alpha_2) = -\int dX_{12} \int dY_{12} e_{12}(\mathbf{R}_{12}, \alpha_1, \alpha_2), \tag{4.5}$$

with e_{12} the Mayer function[67], is the section of the volume excluded to particle 2 by particle 1 cut by a plane normal to $\hat{\mathbf{n}}$ at $Z = Z_{12}$[68].

The local equilibrium orientational distribution $f(\alpha|0) \equiv f(\alpha')$, obtained by minimization of the free energy functional, is found to be uniform up to a certain density, at which there is a second-order transition to a N_s^* phase: a peak at $\alpha' = 0$, which corresponds to a preferential alignment of the helix C_2 axes along the local $\hat{\mathbf{c}}$ director, is incipient, whose height then grows with increasing density. Figure 4.5 shows the dependence on ϕ of the order parameter $\langle P_{1,c} \rangle = \int_0^{2\pi} d\alpha' f(\alpha') \cos(\alpha')$ for helices with r =0.4 and p=3 and 6. We can see that screw-like order gradually increases with ϕ and the phase transition is shifted to higher density on moving from p=6 to p=3. This is in qualitative agreement with the trend shown in Figure 4.1 The Onsager approach provides insights into the nature of the N-N_s^* phase transition but the assumption of perfect nematic ordering prevents a direct comparison with present simulation results.

4.4 Conclusions

We have found that systems of hard helical particles exhibit a rich phase diagram with some phases that are specific of their shape. In particular, we have focused on the second-order transition from the ordinary nematic to a screw-like-nematic phase, which occurs at high density. This chiral nematic organization is different from the cholesteric in several respects. First, screw-like order is specific of helical molecules, whereas the cholesteric order only requires molecular chirality. Both cholesteric and screw-like nematic phase are characterized by a helical distortion, but in the former it is the main director that rotates around a perpendicular axis with a periodicity longer than 0.1 μm, whereas in the latter a secondary director rotates around the main director with a typical periodicity equal to the pitch of the molecular helix. In addition, screw-like order, unlike cholesteric order, is locally polar. It would be interesting to address the compatibility of these two types of order that, in principle, could coexist. Addressing this issue in simulations, however, would require a specialized approach to identify the cholesteric phase whose pitch is typically much longer than accessible box sizes (see Chapter 2).

The features of the screw-like-nematic phase proposed in this study provide an explanation for the experimental findings on helical flagella [61], where the phase modulation is in the μm range, and hence observable by polarized optical microscopy. A similar observation in DNA and other helical polymers, as proposed in Ref. [65], would be more experimentally challenging.

Bibliography

(1) I. W. Hamley, *Soft Matter*, 2010, **6**, 1863–1871.

(2) L. Onsager, *Ann. N.Y. Acad. Sci.*, 1949, **51**, 627–659.

(3) P. Damasceno, M. Engel, and S. C. Glotzer, *Science*, 2012, **337**, 453–457.

(4) J. de Graaf, R. van Roij, and M. Dijstra, *Phys. Rev. Lett.*, 2011, **107**, 155501.

(5) M. Nakata, G. Zanchetta, B. Chapman, C. Jones, J. Cross, R. Pindak, T. Bellini, and N. Clark, *Science*, 2007, **318**, 1276–1279.

(6) A. Cherstvy, *J. Phys. Chem. B*, 2008, **112**, 12585–12595.

(7) M. N. Rosenbluth and A. W. Rosenbluth, *J. Chem. Phys.*, 1954, **22**, 881.

(8) H. Zocher, *Z. Anorg. Chem.*, 1925, **157**, 91.

(9) F. C. Bawden, *Nature*, 1936, **138**, 1051.

(10) M. P. Allen, G. T. Evans, D. Frenkel, and B. Mulder, *Adv. Chem. Phys.*, 1993, **86**, 1.

(11) G. J. Vroege and H. N. W. Lekkerkerker, *Rep. Prog. Phys.*, 1993, **55**, 1241–1309.

(12) P. Tarazona, J. A. Cuesta, and Y. Martinez-Raton, *Lec. Notes in Physics*, 2009, **247**, 753.

(13) P. Camp, M. P. Allen, and A. J. Masters, *J. Chem. Phys.*, 1999, **111**, 9871.

(14) P. K. Maiti, Y. Lansac, M. A. Glaser, and N. A. Clark, *Phys. Rev. Lett.*, 2002, **88**, 065504.

(15) P. K. Maiti, Y. Lansac, M. A. Glaser, and N. A. Clark, *Phys. Rev. Lett.*, 2004, **92**, 025501.

(16) G. Cinacchi and J. van Duijneveldt, *J. Phys. Chem. Lett.*, 2010, **1**, 787.

(17) M. Marechal and M. Dijkstra, *Phys. Rev. E*, 2010, **82**, 031405.

(18) C. Robinson, *Trans. Faraday Soc.*, 1956, **52**, 571.

(19) R. Oldenbourg, X. Wen, R. B. Meyer, and D. L. D. Caspar, *Phys. Rev. Lett.*, 1988, **61**, 1851.

(20) F. Livolant and A. Leforestier, *Prog. Polym. Sci.*, 1996, **21**, 1115–1164.

(21) J. L. Barrat and J. P. Hansen, *Basic Concepts for Simple and Complex Liquids*, Cambridge University Press, Cambridge, 2003.

(22) J. Parsons, *Phys. Rev. A*, 1979, **19**, 1225.

(23) S. Lee, *J. Chem. Phys.*, 1987, **87**, 4972.

(24) S. Lee, *J. Chem. Phys.*, 1988, **89**, 7036.

(25) S. C. McGrother, D. C. Williamson, and G. Jackson, *J. Chem. Phys.*, 1996, **104**, 6755.

(26) P. Camp, C. P. Mason, M. P. Allen, A. A. Khare, and D. A. Kofke, *J. Chem. Phys.*, 1996, **105**, 2837.

(27) F. Carnahan and E. Starling, *J. Chem. Phys.*, 1969, **53**, 471.

(28) D. C. Williamson and G. Jackson, *J. Chem. Phys.*, 1998, **108**, 10294.

(29) S. Varga and I. Szalai, *Mol. Phys.*, 2000, **98**, 693–698.

(30) J. L. F. Abascal and S. Lago, *J. Mol. Liq.*, 1985, **30**, 133–137.

(31) A. D. Varshalovich, N. A. Moskalev, and V. Kersonskii, *Quantum Theory of Angular Momentum*, World Scientific, New York, 1995.

(32) W. H. Press, B. P. Flannery, S. A. Teukolsky, and W. T. Vettering, *Numerical Recipes*, Cambridge University Press, Cambridge, 1986.

(33) W. W. Wood and J. D. Jacobson, *J. Chem. Phys*, 1957, **27**, 1207.

(34) H. F. King, *J. Chem. Phys*, 1972, **57**, 1837.

(35) E. Frezza, A. Ferrarini, H. B. Kolli, A. Giacometti, and G. Cinacchi, *J. Chem. Phys.*, 2013, **138**, 164906.

(36) J. A. Barker and R. O. Watts, *Chem. Phys. Lett*, 1969, **3**, 144.

(37) M. P. Allen and D. J. Tildesley, *Computer simulation of Liquids*, Clarendon Press, Oxford, 1987.

(38) D. Frenkel and B. Smit, *Understanding Molecular Simulation: From Algorithms to Applications*, Academica, San Diego, 2002.

(39) C. Vega and S. Lago, *Computers Chem.*, 1994, **18**, 55–59.

(40) J. Veillard-Baron, *Mol. Phys*, 1974, **28**, 809–818.

(41) M. A. Miller, L. M. Amon, and W. P. Reinhardt, *Chem. Phys Letts.*, 2000, **31**, 278–284.

(42) M. F. Sanner, A. J. Olson, and J. C. Spehner, *Biopolymers*, 1996, **38**, 305–320.

(43) H. Flyvbjerg and H. G. Petersening, *J. Chem. Phys*, 1972, **57**, 1837.

(44) A. T. Gabriel, T. Meyer, and G. Germano, *J. Chem. Theor. Comp.*, 2008, **4**, 468–476.

(45) M. A. Cotter, *J. Chem. Phys.*, 1977, **66**, 1098.

(46) T. Boublik, C. Vega, and M. Diazpena, *J. Chem. Phys.*, 1990, **93**, 730.

(47) T. Jiang and J. Wu, *J. Chem. Phys.*, 2007, **127**, 034902.

(48) C. Vega and S. Lago, *J. Chem. Phys*, 1994, **100**, 6727.

(49) M. S. Wertheim, *J. Chem. Phys.*, 1986, **85**, 2929.

(50) G. W. Vertogen and W. de Jeu, *Thermotropic Liquid Crystals. Fundamentals*, Springer, Berlin, 1998.

(51) F. Tombolato and A. Ferrarini, *J. Chem. Phys.*, 2005, **122**, 054908.

(52) C. Robinson, *Tetrahedron*, 1961, **13**, 219 –234.

(53) E. Grelet and S. Fraden, *Phys. Rev. Lett.*, 2003, **90**, 198302.

(54) J. P. Straley, *Phys. Rev. A*, 1976, **14**, 1835.

(55) N. Katsonis, E. Lacaze, and A. Ferrarini, *J. Mater. Chem.*, 2012, **22**, 7088–7097.

(56) E. Grelet and S. Fraden, *Phys. Rev. Lett.*, 2003, **90**, 198302.

(57) E. Barry, D. Beller, and Z. Dogic, *Soft Matter*, 2009, **5**, 2563–2570.

(58) G. Proni, G. Gottarelli, P. Mariani, and G. Spada, *Chem.-Eur. J.*, 2000, **6**, 3249–3253.

(59) P. G. de Gennes and J. Prost, *The Physics of Liquid Crystals*, Clarendon Press, Oxford, 1993.

(60) P. Bolhuis and D. Frenkel, *J. Chem. Phys.*, 1997, **106**, 666.

(61) E. Barry, Z. Hensel, Z. Dogic, M. Shribak, and R. Oldenbourg, *Phys. Rev. Lett.*, 2006, **96**, 018305.

(62) R. D. Kamien, *J. Phys. II (France)*, 1992, **6**, 461–475.

(63) R. B. Mayer, *App. Phys. Lett.*, 1969, **14**, 208.

(64) R. B. Mayer, *App. Phys. Lett.*, 1968, **12**, 281.

(65) F. Manna, R. Lorman, B. Podgornik, and B. Zeks, *Phys. Rev. E*, 2007, **75**, 030901.

(66) C. Zannoni, in *The Molecular physics of liquid crystals*, ed. G. R. Luckhurst and G. W. Gray, Academic Press, 1979.

(67) D. A. McQuarrie, *Statistical Mechanics*, University Science Books, Sausalito, CA, 2000.

(68) G. Cinacchi, L. Mederos, and E. Velasco, *J. Chem. Phys.*, 2004, **121**, 3854.

Part III

Self-assembly of oligonucleotides

THE chirality of nucleic acids (NAs) has been the object of recent interest, for different reasons. It has been proposed that the chirality of local interactions, which determine the geometry and stability of DNA-DNA crossovers, affects the physical properties, and then the global topological state, of supercoiled DNA [1]. The local chirality has been claimed to play a key role also for the organisation of DNA inside bacteriophages [2]. The molecular chirality is responsible for the helical twist of the director, the local axis of molecular alignment, on a micrometer length-scale in the cholesteric phase N*: It is well known that, above a given concentration, a left-handed N* phase is formed by solutions of double stranded B-DNA, with a number of base pairs (bp) ≈130 (hereafter denoted as l-DNA) [3–5]. Recently, it was found that even concentrated solutions of oligomers of double stranded (ds) NAs, with 6 to 20 base pairs, exhibit the N* phase [6, 7]. This behaviour, observed even in the absence of multivalent ions, was ascribed to end-to-end stacking interactions between short duplexes; these would promote the formation of long linear aggregates having a length-to-width ratio sufficiently high to induce nematic ordering. Surprisingly, both left- and right-handed cholesteric phases were found, depending on the sequence, the length and the nature of oligomer ends [8]. This result is quite remarkable, since the same handedness would be expected for perfect, right-handed helices with the same periodicity and the same charge distribution. Several reasons might underlie the observed behaviour: structural differences between the linear aggregates, like those deriving from the intrinsic curvature of duplexes or from defects in the molecular helix at the junction between oligomers; influence of the sequence on the flexibility of oligomers and of their aggregates, or on the interactions of duplexes with counterions and salts. However, the effects of these various factors on helix-helix interactions are unknown.

The molecular origin of the cholesteric organisation of solutions of dsNA duplexes is controversial. Simple packing effects between hard, perfect helices, would lead to a right-handed cholesteric phase for *l*-DNA, in contrast to the experimental findings [9]. Yet, electrostatics is expected to play a role in the interactions between NA duplexes, which are highly charged polyelectrolytes. Sophisticated models were developed, which have provided new insights into the subtle effects of interactions between helical charge distributions [10]; in contrast to experiment, right-handed N* organization was predicted for *l*-DNA, but the effects of various factors on the phase chirality were highlighted [11]. The sensitivity of the cholesteric pitch to the charge periodicity was also demonstrated by further studies, where a model system of hard cylinders decorated with a helical distribution of charges, experiencing screened Coulomb interactions, was considered, and a statistical theory was used to connect pair interactions and orientational distribution function in the liquid crystal phase [12]. In particular, the handedness of the cholesteric phase was found to oscillate from left to right as a function of the charge periodicity [13]. Another approach was developed, taking into account both the shape and the charge helicity of duplexes; handedness, magnitude and temperature dependence of the cholesteric pitch in agreement with experimental data were obtained for *l*-DNA, modeled as a perfect helix [14].

To shed light on the relation between cholesteric organization and sequence of dsNA oligomers, at first we have undertaken a computational investigation using the same approach as in ref. [14]. The structural differences induced by the sequence were taken into account by ad hoc modelling (Chapter 5). At this stage, aggregates of fixed length were considered and the coupling of order and aggregation was fully neglected. Subsequently we have developed a theoretical model for the cholesteric phase formed by DNA oligomers, which integrates the theory for cholesteric order [14, 15] with that for linear aggregation in the nematic phase [16, 17] (Chapter 6).

Chapter 5

LC phases of oligonucleotides: Molecular structure and cholesteric handedness

In this Chapter, we have investigated the relation between the sequence of oligonucleotides and their organisation in the cholesteric phase, N*, using a molecular theory and coarse-grained modelling, based on sequence dependent structural data.

5.1 Theoretical background

We considered a system of N identical duplexes in a volume V at temperature T. We started from the molecular theory described in Chapter 3 and we introduced electrostatic interactions. It is assumed that the mutual interaction between pairs of duplexes (1 and 2) can be described as the superposition of steric repulsions and ion mediated electrostatic interactions. The expression for the Helmholtz free energy of the system is derived on the basis of the following assumptions: (i) hardcore repulsions are treated according to the second virial approximation; (ii) electrostatic interaction are introduced in a mean field way, with a pair distribution function determined by hard-core repulsions. We started from the excess Helmholtz free energy of the N phase of a solution of N rigid rod-like polyelectrolytes reported eq. (2.4), but in this case the function $u(\mathbf{R}_{AB}, \mathbf{\Omega}_{AB})$ is defined as:

$$u(\mathbf{R}_{AB}, \mathbf{\Omega}_{AB}) = -k_B T e^h_{AB}(\mathbf{R}_{AB}, \mathbf{\Omega}_{AB}) + g^h(\mathbf{R}_{AB}, \mathbf{\Omega}_{AB}) U^{el}(\mathbf{R}_{AB}, \mathbf{\Omega}_{AB}) \tag{5.1}$$

Here $U^{el}(\mathbf{R}_{AB}, \mathbf{\Omega}_{AB})$ is the electrostatic interactions and g^h is the hard particle pair distribution function, which is approximated as:

$$g^h(\mathbf{R}_{AB}, \mathbf{\Omega}_{AB}) = \begin{cases} 0 & \text{if A,B overlap} \\ 1 & \text{if A,B do not overlap} \end{cases} \tag{5.2}$$

Electrostatic interactions are expressed as the sum of interactions between point charges in 1 (a) and in 2 (b):

$$U^{el}(R_{12}) = \sum_{a=1}^{M_1}\sum_{b=1}^{M_2} U^{el}_{ab}(r_{ab}) \tag{5.3}$$

where M_1 (M_2) is the number of point charges in 1 (2) and r_{ab} is the distance between a pair of charges. A hybrid form is assumed for the interaction potential, U^{el}_{ab} , between the charges ζ_a and ζ_b (in electron units); it which coincides with the screened Coulomb potential beyond a certain reference distance (r^0_{ab}) and is equal to the Coulomb potential at the contact distance (σ_{ab}) between the spheres (see below) bearing the two charges:

$$U^{el}(r_{ab}) = \begin{cases} \dfrac{e^2\zeta_a\zeta_b}{4\pi\epsilon_0\epsilon' r_{ab}} & r_{ab} = \sigma_{ab} \\ \dfrac{e^2\zeta_a\zeta_b}{4\pi\epsilon_0\epsilon' r_{ab}}\exp(-\kappa_D r_{ab}) & r_{ab} \geq r^0_{ab} \\ U(\sigma_{ab}) + \dfrac{U^{el}_{ab}(r^0_{ab}) - U^{el}_{ab}(\sigma_{ab})}{r^0_{ab} - \sigma_{ab}}(r_{ab} - \sigma_{ab}) & \sigma_{ab} > r_{ab} > r^0_{ab} \end{cases} \tag{5.4}$$

where e is the electron charge (in absolute value), ϵ is the dielectric constant of the solvent, ϵ' is an effective dielectric constant within duplexes, ϵ_0 is the permittivity of vacuum and κ_D^{-1} is the Debye screening length. This is defined as: $\kappa_D = (2Ie^2N_A/\epsilon\epsilon_0 k_B T)^{1/2}$, with the Boltzmann constant k_B, the temperature T, the Avogadro number N_A and the ionic strength $I = (10^{-3}/2N_A)\sum\limits_{\alpha} z^2_\alpha \rho^0_\alpha$; here z_α is the valence of α ions and ρ^0_α is their concentration in bulk solution. In our calculations the reference distance r^0_{ab} was taken equal to the contact distance, σ_{ab}, increased by 0.2 nm and the effective dielectric constant was given the value ϵ'=2 [14].

5.1.1 Molecular expressions for Helmholtz free energy, pressure and chemical potential

In this study, we neglected Parsons-Lee rescaling because we are only interested on general trend and the main point is the introduction of electrostatics interactions. The expressions for the equilibrium properties of the N* phase in terms of intermolecular interactions are the same as reported in subsection 3.1.3, eqq. (3.11)-(3.15), but in this case the pre factor $G(\phi)$ is not included. The following expressions are obtained for the ideal and the excess contribution to the Helmholtz free energy of the N* phase:

$$\begin{aligned} \frac{A^{id}}{Nk_BT} = \ln\left(\frac{\Lambda^3_{tr}\Omega^{1/2}_{or,x}\Omega^{1/2}_{or,y}\Omega^{1/2}_{or,z}}{\pi^{1/2}VT^{3/2}}\right) + \ln N - 1 + \frac{1}{8\pi^2}\sum_{j=0,2,4}(2j+1)\,\langle D^j_{00}\rangle^2 \\ \times \int d\mathbf{\Omega}\, D^j_{00}(\mathbf{\Omega})\ln\left\{\sum_{j'=0,2,4}(2j'+1)\,\langle D^{j'}_{00}\rangle\, D^{j'}_{00}(\mathbf{\Omega})\right\} \end{aligned} \tag{5.5}$$

$$\frac{A^{ex}}{Nk_BT} = \frac{N}{16\pi^2 V}\sum_{j_A=0,2,4}(2j_A+1)\,\langle D^{j_A}_{00}\rangle^2 \int d\mathbf{R}_{12}d\mathbf{\Omega}\, D^{j_A}_{00}(\mathbf{\Omega}_{12})\frac{u(\mathbf{R}_{12},\mathbf{\Omega}_{12})}{k_BT} \tag{5.6}$$

These lead to the following expressions for the pressure and the chemical potential:

$$P = \frac{Nk_BT}{V} + \frac{N^2}{16\pi^2V^2}\sum_{j_A=0,2,4,..}(2j_A+1)\,\langle D^{j_A}_{00}\rangle^2 \int d\mathbf{R}_{AB}d\mathbf{\Omega}_{AB}D^{j_A}_{00}(\mathbf{\Omega}_{AB})u(\mathbf{R}_{AB},\mathbf{\Omega}_{AB}) \tag{5.7}$$

$$
\begin{aligned}
\mu = \ln\left(\frac{\Lambda_{tr}^{3}\Omega_{or,x}^{1/2}\Omega_{or,y}^{1/2}\Omega_{or,z}^{1/2}}{\pi^{1/2}VT^{3/2}}\right) + \ln N + \frac{1}{8\pi^2}\sum_{j=0,2,4}(2j+1)\left\langle D_{00}^{j}\right\rangle \int d\mathbf{\Omega} D_{00}^{j} \\
\frac{Nk_BT}{V} + \frac{N^2}{16\pi^2V^2}\sum_{j_A=0,2,4,..}(2j_A+1)\left\langle D_{00}^{j_A}\right\rangle^2 \int d\mathbf{R}_{AB}d\mathbf{\Omega}_{AB}D_{00}^{j_A}(\mathbf{\Omega}_{AB})u(\mathbf{R}_{AB},\mathbf{\Omega}_{AB})
\end{aligned}
\tag{5.8}
$$

5.2 Modelling of oligomers and their linear aggregation

We have studied the NA dodecamers with self-complementary sequences listed in Table 5.1, for which detailed structural data are available. They were found to form either left- or right-handed N* phases [8]. The crystal structures of these duplexes exhibit significant differences from each other, both in the geometry of individual oligomers and in their organization; such differences can be ascribed to the sequence and to the end-to-end interactions. DD, as all oligonucleotides in the B form, crystallizes as infinitely long columns, stabilized by end-to-end interactions [18, 19]. However it exhibits significant departures from the classical B-helix geometry: Each base has a propeller twist and the overall helix axis is slightly curved; moreover oligomers, rather than stacked on top of one another, are staggered with each molecule overlapping by three base pairs with its neighbours, above and below [18]. Detailed structural data are not available for all-AT dodecamers, but only for octamers and examers [20, 21]. Unlike DD, these exhibit a geometry close to the classical B-helix: Nearly straight, without any obvious bend and with small spread in their structural parameters. They assemble in columns in which the terminal base pairs are stacked, but do not form a pseudocontinuous helix [19, 22]. Unlike DNA, RNA duplexes are usually found in the A form, which has significant consequences: The helix is thicker than that formed by B-DNA duplexes, and bases are tilted with respect to the helix axis. Stacked DD-RNA dodecamers were found in crystals, complexed with RNaseIII [23]. Using structural information from X-rays, we built models of linear aggregates. For DD and DD-RNA, the crystal coordinates of dodecamers were used and the end-to-end stacking geometry found in crystals was assumed [18, 24]. The atomic coordinates of all-AT dodecamers were generated using the structural parameters available in 3DNA [25–27]; the twist in the virtual base step was adjusted according to the crystal data reported in ref. [19].

Sequence	Acronym	PDB entry	Chol. hand.	c_{IN} (mg mL^{-1})
AATAAATTTATT	all-AT	-	L	600
CGCGAATTCGCG	DD	1BNA [18]	R	730
CGCGAAUUCGCG	DD-RNA	1YYO [23]	R	900

Table 5.1: Sequence of DNA dodecamers under investigation, with the corresponding acronyms and PDB entries. In the fourth and fifth column: Experimental handedness in the cholesteric phase and concentration (c_{IN}) at the IN transition.

These models of linear aggregates were used to calculate the properties of the N* phase, according to the theory outlined above. Calculations require that the interaction between

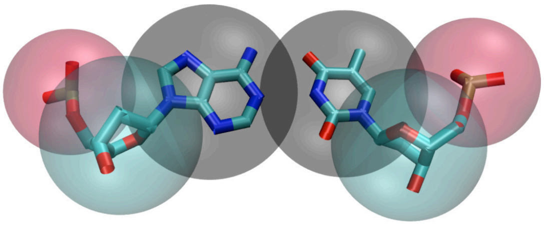

Figure 5.1: CG representation, superimposed on the stick model of a base pair. Gray: nucleobase; cyan: sugar; pink: phosphate.

Group	Sphere radius (nm)
Phosphate	0.3
Sugar	0.35
Nucleobase	0.4

Table 5.2: Geometric parameters of the CG model.

pairs of linear aggregates are evaluated at all possible relative positions and orientations. As a compromise between the requirements of retaining the structural features, needed for the prediction of chiral properties, and reducing the number of interaction centers, necessary to keep calculations affordable, the coarse-grained (CG) representation shown in Figure 5.1 was adopted: Each base pair was represented by three spheres of suitable size, one for the nucleobase, another for the sugar and the third for the phosphate group. The centre of each sphere was located in the centre of mass of the group of atoms which it represents and the radius is evaluated on the basis of the size of each group; the values obtained in this way are reported in Table 5.2; so the CG model preserved the sequence-specific structural features of each aggregate. Figure 5.2 shows the CG models of linear aggregates, made of five dodecamers of all-AT, DD and DD-RNA. We can clearly see that they differ in length, diameter and overall shape. The structure of the all-AT aggregate is close to that of a perfect helix, whereas significant deviations appear in the case of DD and DD-RNA. These structural differences could be responsible for the formation of N^* phases with opposite handedness; there are experimental evidences [5, 28, 29] and theoretical predictions [13, 30] of oppositely-handed cholesteric phases induced by helices which, albeit homochiral, have different structural parameters. Especially intriguing is the presence of a supra-helical arrangement, in the case of DD and DD-RNA, which introduces a higher level of chirality; the existence of a supra-helical twist was proposed as the origin of the chiral organization in the N^* phase formed by suspensions of rod-like viruses [31].

For the electrostatic interactions, we used the model described in subsection 5.1, with screened Coulomb repulsions between renormalized charges. The point charges appearing in eq. (5.4) are effective charges, partially compensated by counterions. According to the Manning condensation theory [32], the fraction of uncompensated charge is given by

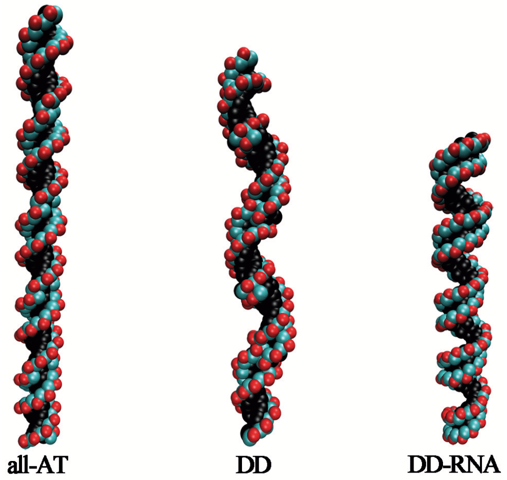

Figure 5.2: CG model of linear aggregates made of five dsNA dodecamers.

$\delta = 1/|z|\xi$, with z equal to the counterion valence and the parameter $\xi(>1)$ defined as $\xi = e^2/(4\pi\epsilon\epsilon_0 bk_BT)$, where b is the average charge spacing along the helix axis (the other symbols have been defined above). For dsNAs, the value $b = (0.34/2)$ nm (two phosphate groups with charge -1e at distance 0.34 nm) can be assumed; thus, in the presence of monovalent counterions in water at 25 °C, ξ=4.2 and δ=0.24 are obtained. In our calculations, effective charges equal to $-\delta e$ were set at the positions of the centers of mass of phosphate groups [14] .

5.2.1 Computational details

For free energy minimization, we used the same procedure described in 2.2.4. To evaluate the integrals of free energy density, chiral strength and twist elastic constant, we used the same quadrature algorithms reported in subsection 3.2.1. However, since non-chiral properties (K_{22} and IN transition), which depend on the anisotropy, rather than on the chirality of intermolecular interactions, have a weaker sensitivity to molecular details [14], we used a simpler representation of aggregates to determine the IN phase coexistence (henceforth denoted as reduced CG): Each base pair was represented by a single bead, with its centre on the axis of the aggregate and the radius sufficiently large to contain the phosphate groups. Thus, linear aggregates of dodecamers were modelled as columns of stacked beads. For the all-AT and the DD-RNA dodecamers this simple representation was found to provide a good approximation of non chiral phase properties, with a significant gain in computer time. For the DD dodecamer a slightly different model was needed, which was built by setting the centre of each bead at the position of the centre of mass of a base pair, rather than along the common stacking axis, so that the supra-helical structure of the aggregate was retained (see Figure 5.3).

Figure 5.3: Reduced CG representation of a linear aggregate of DD dodecamers.

5.3 Results and discussion

5.3.1 IN phase transition

The IN phase coexistence was determined by minimizing the Helmholtz free energy of a systems of linear aggregates, under the conditions of mechanical and chemical equilibrium between the I and N phases. Calculations were carried out for aggregates experiencing excluded volume interactions; the sequence dependence would not be dramatically modified by inclusion of electrostatic repulsions, since these could be simply accounted for by a larger effective diameter of the linear aggregates [33].

Linear aggregates of nine dodecamers (108 bp) were assumed, a value deemed reasonable for the systems under investigation [6]. Figure 5.4 shows the NA volume fraction, ϕ, calculated at the IN coexistence, as a function of the aspect ratio L/D, with L being the length of an aggregate and D its effective diameter. For all-AT and DD-RNA dodecamers, this coincides with the diameter of the beads in reduced CG representation; the results obtained for these systems practically coincide with those for spherocylinders having aspect ratio equal to L/D. In the case of DD aggregates, the effective diameter was defined as that of the spherocylinder with the same length L and the same second virial coefficient [33] as the aggregate.

Figure 5.4 shows a strong dependence on sequence of the volume fraction at the IN transition: This is predicted to occur at increasing concentration on going from all-AT to DD-RNA, through DD dodecamers. This behaviour can be correlated with the decreasing aspect ratio, L/D, of the linear aggregates, in agreement with the Onsager theory [34]. The theoretical prediction are in line with the experimental increase of the concentration at the IN transition (c_{IN}) along the series of dodecamers, reported in Table 5.1; for the sake of comparison, the corresponding value for *l*-DNA (150 bp) is 160 mg/mL. The influence of sequence on the aspect ratio was generally ignored [6]; our calculations, with a realistic account of the molecular shape, suggest that this aspect should be taken into account when experimental and theoretical phase boundaries are compared.

5.3.2 Phase chirality

To evaluate the effect of the molecular structure on the cholesteric handedness we have calculated the chiral strength, k_2, for all-AT, DD and DD-RNA dodecamers: (i) assuming only excluded volume interactions between aggregates; (ii) introducing also screened electrostatic interactions. Despite the structural differences, we obtained for all the systems under examination the same result, which is identical to that previously obtained for *l*-DNA [14]:

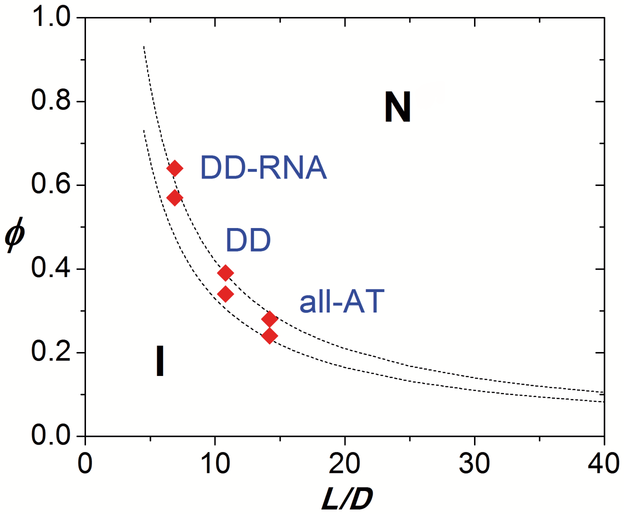

Figure 5.4: Volume fraction, ϕ, at the IN coexistence, calculated for linear aggregates of nine dodecamers, of length L and effective diameter D (diamonds). For comparison, the coexistence lines calculated for hard rods of length L and diameter D are shown (dashed lines) [35].

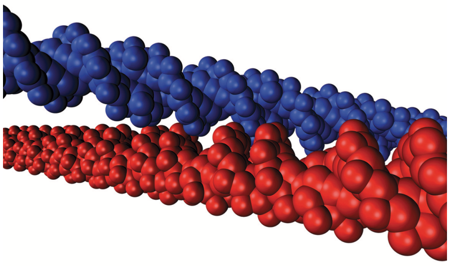

Figure 5.5: Configuration of a pair of all-AT aggregates with a right-handed crossover.

Excluded volume interactions yield negative k_2 (R cholesteric twist), but a change to positive k_2 (L twist) is obtained when electrostatic interactions are switched on. The reason is that the right-handed organization allows the best packing of the right-handed dsNA helices, whereas electrostatic repulsions are minimized by the left-handed arrangement. Figure 5.5 shows a typical configuration of a pair duplexes at a close distance, with the backbone of one helix fitting into the groove of the other. A resemblance with the right DNA-DNA crossovers, which are often found in crystals of oligonucleotides, can be appreciated [1]. Thus, according to our calculations, the cholesteric handedness would be dictated by the short-scale chirality, which is the same for all dsNA aggregates, rather than by the specific features of each individual sequence, like the intrinsic curvature of dodecamers, the end-to-end arrangement, the A- or B-form of duplexes, or the possible presence of supra-helicity.

Our calculations, while ruling out a direct effect of the sequence on the chirality of intermolecular interactions, suggest that a possible reason for the differences in handedness, experimentally observed between dodecamers, might be a different role of steric and electrostatic interactions. Interestingly, this role changes with the concentration of oligonucleotides, as shown in Figure 5.6, which shows the chiral strength, k_2, along with the individual steric and electrostatic contribution, calculated for a cholesteric phase formed by aggregates of nine all-AT dodecamers, as a function of their concentration (at $T = 293$ K). The two contributions to k_2 have opposite sign and different dependence on concentration: The net result is that k_2, which is positive at lower NA density (electrostatic dominates), lowers with increasing concentration and eventually changes its sign (excluded volume dominates). A dependence of both contributions on the square of concentration derives from the excluded volume approximation and the mean-field form of the electrostatic term. Some further increase of both terms with concentration is due to the increase of order parameters. Another significant, though often disregarded, consequence of the increase of concentration is the raise of ionic strength, which implies an increase of charge screening, and then a decrease of the relative weight of the electrostatic term. As a result, the relative magnitude of the steric and the electrostatic contribution changes with increasing concentration, in favour of the former. In Figure 5.6 we have reported also the ionic strength, calculated for salt-free solutions with monovalent counterions according to the expression $I = (c/M_{bp})\delta$, where c is the oligomer concentration, M_{bp} is the molar mass of a base pair and δ is the fraction of uncompensated charge. In our calculations was taken equal to 0.24 [14], according to a simple estimate based on the Manning condensation theory [32].

The results shown in Figure 5.6 point to a change of cholesteric handedness, from left-handed to right-handed, on increasing concentration of all-AT oligomers. Experimentally this change of handedness was not observed for this system, which undergoes a transition to a columnar phase at a concentration lower that 1000 mg/mL [6]. In fact, our calculations were performed for a hypothetical cholesteric phase of all-AT aggregates, without checking its stability against that of more ordered phases. Interestingly, a change of handedness was reported, from L below about 650 mg/ml, to R above this value, for one of the sequences exhibiting the N^* phase over a broad range [8]. We did not perform calculations for such a sequence, for the lack of structural information. However the trend shown in Figure 5.6, which depends mainly on the surface charge density, rather than on specific details, must be a general behaviour for all NA sequences.

As a final remark, we want to stress that the results reported in Figure 5.6 cannot be taken too strictly in quantitative sense, due to the several limits of the available model: The most questionable issues are the neglect of the concentration dependence of aggregation, the adoption of the second virial approximation, which is certainly inadequate at high concentration, and the simple modelling of electrostatics. In our opinion a suitable description of the interactions between polyelectrolytes at very high concentration is a crucial issue for the systems under investigation, as discussed below.

5.3.3 Proposed origin of chirality inversion

As a result of our study, we propose that the sequence of dsNA dodecamers affects the cholesteric handedness in an indirect way, by controlling the concentration at which the

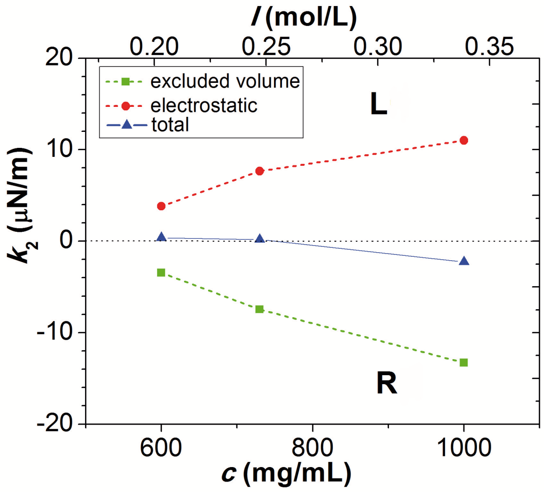

Figure 5.6: Chiral strength k_2 calculated for the cholesteric phase formed by aggregates of nine all-AT dodecamers (solid); also the steric and the electrostatic contributions are shown (short dashes). The ionic strength I is determined on the basis of the concentration of free monovalent counterions.

IN transition occurs. At lower concentration, the system would behave as expected for a polyelectrolyte solution where, in addition to steric repulsions, electrostatic interactions play a role. Under these conditions, dsNA dodecamers would form a left-handed N* phase. At extremely high concentration, a more unusual regime would emerge, where the behaviour of the system can be simply described in terms of excluded volume interactions. In this case a right-handed N* phase would be formed. Inspection of the experimental data of cholesteric handedness and concentration at the IN transition, shows that the change of handedness can be located around 650 mg/ml [8]. It is worth noticing that the range 600-800 mg/mL is close to the typical concentrations in highly hydrated crystals of oligonucleotide duplexes [22]. This regime of very high density, at which the spacing between the surface of duplexes may reach a few water layers, remains poorly understood. Studies of osmotic pressure as a function of the inter-axial distance, for solutions of dsDNA, revealed a change of DNA-DNA interactions below about 3 nm (i.e. concentrations higher than about 450 mg/mL) [36]. The electric double layer theory, that holds at longer distances, cannot explain the experimental behaviour when helices are in close proximity: In the case of multivalent ions even a turn from repulsive to attractive interactions is observed [37], whereas in the presence of monovalent ions steeply increasing repulsions, independent of the ionic strength, were detected, those nature is controversial. Hydration forces, associated with the energetic cost of removing bound water from molecular surfaces, were invoked [36]. Alternatively, it was proposed that very short range repulsions would derive from image charge forces, originating from the difference of dielectric constant between water and DNA core [10]. It was also claimed that the peculiar behaviour at very short distances could be accounted for by a proper description of ion mediated forces between polyelectrolytes, without the need that other kinds of interactions come into play [38]. We think that the puzzling behaviour of the N* handedness found for oligonucleotides may be another evidence of the breakdown of the double layer theory for dsNAs at very short distances. Our results reported here suggest that the forces between helices at very high concentrations have the same dependence on mutual orientation as steric repulsions. Further investigation is needed to ascertain the real nature of these interactions and we believe that the study of the cholesteric organization can provide new insights on this topic.

5.4 Conclusions

According to our calculations neither the changes in shape, nor those in the helicity of the charge distribution, due to the different sequence, are able to induce the inversion of cholesteric handedness observed experimentally for NA dodecamers. On the other hand, these changes may have profound effects on the location of the IN phase transition. Unfortunately at the present stage we are not able to provide an exhaustive account of the relationship and of the behaviour of systematic investigation. However, on the basis of our results we propose that the sequence determines the cholesteric handedness by dictating the stability region of the N* phase: The switch from left- to right-handed would reflect a general change of interactions occurring under very high concentration. The extreme sensitivity of chirality to subtleties on the molecular scale, combined with the chirality amplification, promoted by the liquid crystal elasticity, would bring to the micrometer scale a change otherwise difficult to highlight. The high concentration regime appears as particularly intriguing: These are conditions hard to characterise, both experimentally and theoretically, but extremely interesting, since highly dense NAs are usually found within cells and viruses. For the latter, inter-axial distances between 2.4 and 2.8 nm are reported [39], which are close to the values in the N* phases studied.

Chapter 6

LC phases of oligonucleotides: Coupling of order and aggregation

In this Chapter, we present a theoretical model for the cholesteric phase formed by self-assembling helical particles, which integrates the theory for cholesteric order presented in Chapter 3 with that for linear aggregation in the nematic phase [16]. The model is applied to the liquid crystal phases formed by DNA oligomer considering two sequences reported in Chapter 5.

6.1 Theory

6.1.1 Free energy of the system

The system under investigation is a cholesteric phase formed by a polydisperse mixture of linear aggregates. Each aggregate is formed by l monomers ($1 \leq l \leq \infty$); the total number of monomers is N, v_0 is the volume of a monomer and V the total volume. Therefore $\rho = N/V$ is the number density and $\phi = \rho v_0$ is the volume fraction of monomers. The Helmholtz free energy of the system is written as [16, 17]:

$$\begin{aligned} \frac{A}{k_B T V} &= \sum_{l=1}^{\infty} \nu(l)\{\ln[v_0 \nu(l)] - 1\} + \frac{G(\phi)}{2} \sum_{\substack{l=1 \\ l'=1}}^{\infty} \nu(l)\nu(l')\overline{v}^{excl}(ll') \\ &\quad - \frac{\Delta A_b}{k_B T} \sum_{l=1}^{\infty}(l-1)\nu(l) + \sum_{l=1}^{\infty} \nu(l)\sigma_0(l) \end{aligned} \tag{6.1}$$

where k_B denotes the Boltzmann constant and T the temperature. The first term in eq. (6.1) The first term in eq. (6.1) represents the ideal gas contribution; $\nu(l)$ is the chain length distribution of aggregates of scaled length l, which is normalized such that $\sum_{l=1}^{\infty} l\nu(l) = \rho$. The second term accounts for excluded volume interactions between aggregates; $\overline{v}^{excl}(ll')$ is the excluded volume of a pair of aggregates of scaled lengths l and l', integrated over all their relative orientations as defined below, and $G(\phi)$ is the Parsons-Lee factor (see eq. (2.12)) [40–42]. The third term accounts for the stacking free energy which is parametrized in terms of the free energy gain associated to the formation of a bond between a pair of duplexes, $-\Delta A_b$ [16]. The last term is the orientational entropy and $\sigma_o(l)$ is the loss of entropy due to orientational order for an aggregate of scaled length l in the cholesteric phase [43]. We considered the second limit. Eq. (6.1) is reduced to eq. (2.2).

6.1.2 Orientational distribution function

As already discuss in Chapter 3, due to the large scale of the cholesteric pitch compared to the molecular size, the orientational distribution of aggregates with respect to the local director can be assumed to be the same as in the corresponding nematic phase with uniform director. Thus, this is expressed as $f_l(\hat{\mathbf{u}} \cdot \hat{\mathbf{n}}(\mathbf{R}))$, where $\hat{\mathbf{u}}$ is a unit vector parallel to the axis of the aggregates and $\hat{\mathbf{n}}(\mathbf{R})$ is a unit vector parallel to the director at the position $\mathbf{R}$.

6.1.3 Excluded volume contribution

The excluded volume term in eq. (6.1), relative to a pair of aggregates of scaled lengths l and l', is given by:

$$\overline{v}^{excl}(ll') = -\frac{1}{V}\int d\mathbf{R}_1 d\mathbf{R}_2 d\boldsymbol{\Omega}_1 d\boldsymbol{\Omega}_2\, e_{12}^{ll'}(\mathbf{R}_{12}, \boldsymbol{\Omega}_{12}) f_l(\hat{\mathbf{u}}_1 \cdot \hat{\mathbf{n}}(\mathbf{R}_1) f_{l'}(\hat{\mathbf{u}}_2 \cdot \hat{\mathbf{n}}(\mathbf{R}_2)) \tag{6.2}$$

where $\mathbf{R}_i$ is the vector position of the i aggregate, $\mathbf{R}_{12} = \mathbf{R}_2 - \mathbf{R}_1$ is the relative position and $\boldsymbol{\Omega}_{12}$ the relative orientation of 2 with respect to 1, and $e_{12}^{ll'}$ is the Mayer function defined in eq. (2.6).The reference frames and transformations are summarized in Figure 6.1.

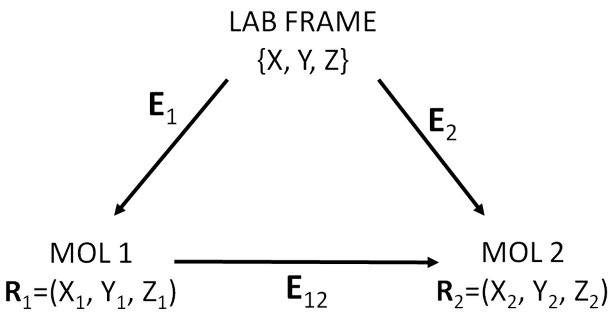

Figure 6.1: Definition of reference frames and transformations.

Starting from eq. (6.2) which contains the director, $\hat{\mathbf{n}}$, as a function of its position, the elastic contributions to the free energy can de derived using a Taylor expansion of the orientational distribution function with respect to the position. This derivation is more general than that presented in Chapter 3, because it can be used for any form of the orientational distribution function:

$$\begin{aligned} f_l(\hat{\mathbf{u}}\hat{\mathbf{n}}(\mathbf{R}+\delta\mathbf{R})) &\approx f_l(\hat{\mathbf{u}} \cdot \hat{\mathbf{n}}(\mathbf{R})) + \delta R_J \nabla_J f_l(\hat{\mathbf{u}} \cdot \hat{\mathbf{n}}(\mathbf{R})) + \frac{1}{2}\delta R_I\, \delta R_J\, \nabla_I \nabla_J f_l(\hat{\mathbf{u}} \cdot \hat{\mathbf{n}}(\mathbf{R})) \\ &\approx f_l(\hat{\mathbf{u}} \cdot \hat{\mathbf{n}}(\mathbf{R})) + \delta R_J\, \dot{f}_{l_K} \nabla_J (\hat{\mathbf{u}} \cdot \hat{\mathbf{n}}(\mathbf{R}))_K + \frac{1}{2}\delta R_I \delta R_J \nabla_I \dot{f}_{l_K} \nabla_J (\hat{\mathbf{u}} \cdot \hat{\mathbf{n}}(\mathbf{R}))_K \end{aligned} \tag{6.3}$$

where the Einstein convention is used for summations over repeated indices. Here $\dot{\mathbf{f}}_l$ is the vector of the first derivatives of the function f_l with respect to its argument, $\dot{f}_{l\,X} = \partial f_l(\ldots)/\partial(\ldots)_X$, calculated in $\mathbf{R}$. Using eq. (6.3) to express the orientational distribution function of particle 2 as a function of the director at the position of particle 1, eq. (6.2) can be rewritten as:

$$\begin{aligned}
\overline{v}^{excl}(ll') = &-\frac{1}{V}\int d\mathbf{R}_1 d\mathbf{R}_{12} d\mathbf{\Omega}_1 d\mathbf{\Omega}_2\, e_{12}^{ll'}(\mathbf{R}_{12},\mathbf{\Omega}_{12}) f_l\left(\mathbf{u_1}\cdot\hat{\mathbf{n}}(\mathbf{R}_1)\right) f_{l'}\left(\mathbf{u_2}\cdot\hat{\mathbf{n}}(\mathbf{R}_1)\right) \\
&-\frac{1}{V}\int d\mathbf{R}_1 d\mathbf{R}_{12} d\mathbf{\Omega}_1 d\mathbf{\Omega}_2\, e_{12}^{ll'}(\mathbf{R}_{12},\mathbf{\Omega}_{12}) f_l\left(\mathbf{u_1}\cdot\hat{\mathbf{n}}(\mathbf{R}_1)\right) R_{12,J}\, \dot{f}_{l'\,K} \nabla_J \left(\mathbf{u_2}\cdot\hat{\mathbf{n}}(\mathbf{R}_1)\right)_K \\
&\int d\mathbf{R}_{12} d\mathbf{\Omega}_1 d\mathbf{\Omega}_2\, e_{12}^{ll'}(\mathbf{R}_{12},\mathbf{\Omega}_{12}) R_{12,I} R_{12,J} \dot{f}_{l\,M} \nabla_I \left(\mathbf{u_1}\cdot\hat{\mathbf{n}}(\mathbf{R})\right)_M \dot{f}_{l'\,K} \nabla_J \left(\mathbf{u_2}\cdot\hat{\mathbf{n}}(\mathbf{R})\right)_K
\end{aligned} \tag{6.4}$$

The last term has been obtained by integrating by parts and neglecting the surface term, which is not relevant if we are interested in bulk properties. In a local frame with the Z-axis parallel to the local director and the Y-axis parallel to the axis of the cholesteric helix, the director field is a function of only the Y coordinate, according to:

$$\hat{\mathbf{n}}(\mathbf{R}) = \cos(qY)\hat{\mathbf{Z}} + \sin(qY)\hat{\mathbf{X}} \tag{6.5}$$

where q is the helix wavenumber. For small displacements on the length scale of the helical pitch, we can approximate:

$$\hat{\mathbf{n}}(\mathbf{R}) \approx \hat{\mathbf{Z}} + qY\hat{\mathbf{X}}, \tag{6.6}$$

and using this expression eq. (6.4) can be written in the form:

$$\overline{v}^{excl}(ll') = \overline{v}_0^{excl}(ll') + q\overline{v}_1^{excl}(ll') + \frac{q^2}{2}\overline{v}_2^{excl}(ll') \tag{6.7}$$

where the first term represents the contribution of the undeformed Nematic phase:

$$\overline{v}_0^{excl,ll'} = \int d\mathbf{\Omega}_1 d\mathbf{\Omega}_2\, M_0\left(\mathbf{\Omega}_1,\mathbf{\Omega}_2\right)\, f_l\left(\mathbf{u_1}\cdot\hat{\mathbf{Z}}\right) f_{l'}\left(\mathbf{u_2}\cdot\hat{\mathbf{Z}}\right); \tag{6.8}$$

the second is a chiral contribution:

$$\overline{v}_1^{excl,ll'} = \int d\mathbf{\Omega}_1 d\mathbf{\Omega}_2\, M_1\left(\mathbf{\Omega}_1,\mathbf{\Omega}_2\right) f_l\left(\mathbf{u_1}\cdot\hat{\mathbf{Z}}\right)\left[\dot{\mathbf{f}}_{l'}\left(\mathbf{u_2}\cdot\hat{\mathbf{Z}}\right)\cdot\mathbf{u_2}\cdot\hat{\mathbf{X}}\right], \tag{6.9}$$

and the latter term accounts for the elastic restoring torque:

$$\overline{v}_2^{excl}(ll') = -\int d\mathbf{\Omega}_1 d\mathbf{\Omega}_2\, M_2\left(\mathbf{\Omega}_1,\mathbf{\Omega}_2\right)\left[\dot{\mathbf{f}}_l\left(\hat{\mathbf{u}}_1\cdot\hat{\mathbf{Z}}\right)\cdot\hat{\mathbf{u}}_1\cdot\hat{\mathbf{X}}\right]\left[\dot{\mathbf{f}}_{l'}\left(\hat{\mathbf{u}}_2\cdot\hat{\mathbf{Z}}\right)\cdot\hat{\mathbf{u}}_2\cdot\hat{\mathbf{X}}\right] \tag{6.10}$$

These expressions contain the moments M_k:

$$M_k^{ll'}\left(\mathbf{\Omega}_1,\mathbf{\Omega}_2\right) = \int_{v^{excl}(ll')} d\mathbf{R}_{12}\, Y_{12}^k \tag{6.11}$$

where the integral is over v^{excl}, the volume excluded to 2 in the orientation $\mathbf{\Omega}_2$ by 1 in the orientation $\mathbf{\Omega}_1$.

6.1.4 Free energy of the cholesteric phase

Using the results reported in the previous sections, the free energy eq. (6.1) can be expressed in the same form of eq. (3.1) as:

$$\frac{A}{V} = \frac{A_u}{V} + qk_2 + \frac{q^2}{2}K_{22} \tag{6.12}$$

where $\frac{A_u}{V}$ is the free energy density of the undeformed nematic phase:

$$\begin{aligned}\frac{A_u}{Vk_BT} &= \sum_{l=1}^{\infty}\nu(l)\{\ln[v_0\nu(l)]-1\} + \frac{G(\phi)}{2}\sum_{\substack{l=1\\l'=1}}^{\infty}\nu(l)\nu(l')\overline{v}_0^{excl}(ll') \\ &- \frac{\Delta A_b}{k_BT}\sum_{l=1}^{\infty}(l-1)\nu(l) + \sum_{l=1}^{\infty}\nu(l)\sigma_0(l);\end{aligned} \tag{6.13}$$

k_2 is the chiral strength:

$$k_2 = \frac{k_BTG(\phi)}{2}\sum_{\substack{l=1\\l'=1}}^{\infty}\nu(l)\nu(l')\overline{v}_1^{excl}(ll'), \tag{6.14}$$

and K_{22} is the twist elastic constant:

$$K_{22} = \frac{k_BTG(\phi)}{2}\sum_{\substack{l=1\\l'=1}}^{\infty}\nu(l)\nu(l')\overline{v}_2^{excl}(ll') \tag{6.15}$$

Then the cholesteric wavenumber is given by:

$$q = -\frac{k_2}{K_{22}} = -\frac{\sum\limits_{\substack{l=1\\l'=1}}^{\infty}\nu(l)\nu(l')\overline{v}_1^{excl}(ll')}{\sum\limits_{\substack{l=1\\l'=1}}^{\infty}\nu(l)\nu(l')\overline{v}_2^{excl}(ll')} \tag{6.16}$$

Unlike the twist elastic constant and the chiral strength, it does not explicit depend on temperature and density. However these parameters affect the length distribution of aggregates and the orientational distribution function in the expressions for $\overline{v}_1^{excl}(ll')$ and $\overline{v}_2^{excl}(ll')$.

The free energy eq. (6.1) is a functional of the orientational distribution function, $f_l(\hat{\mathbf{u}}\cdot\hat{\mathbf{n}}(\mathbf{R})$, and the chain length distribution of aggregates, $\nu(l)$. At a given monomer density,ρ, the equilibrium state is obtained by functional minimization of the free energy.

6.2 Computational procedure

It is convenient to assume for the orientational distribution function and the chain length distribution a given functional form, in terms of a number of parameters which are used as variational parameters in the minimization of the free energy.

As proposed in Ref.[16], we have assumed that the chain length distribution $\nu(l)$ is exponential with an average chain length M:

$$\nu(l) = \rho M^{-(l+1)}(M-1)^{l-1} \tag{6.17}$$

where

$$M = \frac{\sum_{l=1}^{\infty} l\nu(l)}{\sum_{l=1}^{\infty} \nu(l)} \tag{6.18}$$

For the orientational distribution function, we have assumed the simple Onsager form [34]:

$$f_l(\cos\beta_i) = \frac{\alpha_l^N}{8\pi^2 \sinh \alpha_l^N} \cosh(\alpha_l^N \cos\beta_i) \tag{6.19}$$

where α_l^N is a parameter related to the degree of orientational order ($\alpha_l^N > 0$ for calamitics and $\alpha_l^N = 0$ in the isotropic phase), which is taken as a variational parameter for the free energy minimization. This distribution function is normalized as $\int_{-1}^{1} d(\cos\beta_i)\, f_l(\beta_i) \simeq 1/4\pi^2$. The parameter α_l^N is uniquely related to the order parameter $\langle P_2\rangle_l$, defined as:

$$\langle P_2\rangle_l \equiv 4\pi^2 \int_{-1}^{1} d(\cos\beta_i)\, f_l(\beta_i) P_2(\cos\beta_i) \approx 1 - 3/\alpha^N \tag{6.20}$$

where P_2 is the second-order Legendre polynomial and the approximate holds in the limit $\alpha^N \to \infty$.

For simplicity, in calculations the length dependence of the parameter controlling the orientational distribution function, eq. (6.19), was neglected: $\alpha_l^N = \alpha^N$ [16].

6.2.1 Length dependence of excluded volume contributions

To obtain a manageable form of the free energy, the chiral strength and the twist elastic constant, it is convenient to express the excluded volume contributions appearing in eq. (6.13),(6.14), (6.15) in polynomial forms with respect to the scaled length l. Assuming the same form as for cylinders [34], the contribution in eq. (6.13) in the isotropic phase is written as:

$$\overline{v}_0^{excl}(ll') = 2B_I X_0^2\, l\, l' + 2v_0 k_I \frac{l+l'}{2} \tag{6.21}$$

where X_0 is the aspect ratio of the monomers and B_I (with the dimension of a volume) and k_I are determined by the geometry of the particles (length and diameter in the case of cylinders). In the nematic phase, using the form of the orientational distribution function, eq. (6.19), we can write:

$$\overline{v}_0^{excl}(ll', \alpha^N) = 2B_N(\alpha^N) X_0^2 l\, l' + 2v_0 k_N(\alpha^N) \frac{l+l'}{2} \tag{6.22}$$

where B_N and k_N are function of the parameter α^N which controls the width of the angular distribution.

For the excluded volume contributions appearing in eq. (6.14) and (6.15) there is no analytical expression. A polynomial form has been obtained by fitting the values of $\overline{v}_1^{excl}(ll', \alpha^N)$ and $\overline{v}_2^{excl}(ll', \alpha^N)$ calculated for different scaled lengths. The results will be reported in the Section 6.5.

6.2.2 Expressions for the free energy A_u

Assuming the chain length distribution reported in eq. (6.17) and using eq. (6.21), the free energy eq. (6.13) in the isotropic phase becomes:

$$\begin{aligned}\frac{\beta A_u^I}{V} &= -\rho\frac{\Delta A_b}{k_B T}(1-M^{-1}) + G(\phi)\left[B_I X_0^2 + \frac{v_0 k_I}{M}\right]\rho^2 + \\ &+ \frac{\rho}{M}\left[\ln\left(\frac{v_0\rho}{M}\right) - 1\right] + \rho\frac{M-1}{M}\ln(M-1) - \rho\ln M. \qquad (6.23)\end{aligned}$$

If we use (6.22), we obtain the free energy in the nematic phase:

$$\begin{aligned}\frac{\beta A_0^N}{V} &= \hat{\sigma}_o - \rho\frac{\Delta A_b}{k_B T}(1-M^{-1}) + G(\phi)\left[B_N(\alpha^N) X_0^2 + \frac{v_0 k_N(\alpha^N)}{M}\right]\rho^2 + \\ &+ \frac{\rho}{M}\left(\ln\left[\frac{v_0\rho}{M}\right] - 1\right) - \rho\ln M + \rho\ln(M-1)\frac{M-1}{M} \qquad (6.24)\end{aligned}$$

where $\hat{\sigma}_o \equiv \sum_l \sigma_o(l)\nu(l)$.

6.2.3 Determination of isotropic-to-nematic phase coexistence

The phase coexistence is determined by minimizing the free energy A_u with respect to the parameter α^N, eq. (6.19) and to the average chain length M, under the conditions of mechanical and chemical equilibrium between the two phases. The following set of equations have to be satisfied:

$$\begin{aligned}\frac{\partial A_u^I(\rho_I, M_I)}{\partial M_I} &= 0 \\ \frac{\partial A_u^N(\rho_I, M_N, \alpha^N)}{\partial M_N} &= 0 \\ \frac{\partial A_u^N(\rho_I, M_N, \alpha^N)}{\partial \alpha^N} &= 0 \\ P_I(\rho_I, M_I) &= P_N(\rho_N, M_N, \alpha^N) \\ \mu_I(\rho_I, M_I) &= \mu_N(\rho_N, M_N, \alpha^N)\end{aligned} \qquad (6.25)$$

where the indices I and N refer to the isotropic and nematic phase, respectively.

6.3 Computational details

Introducing the expression of the orientational distribution function, eq. (6.19), into eqs. (6.8)-(6.10) we obtain:

$$\begin{aligned}\overline{v}_0^{excl}(ll') = \frac{\alpha^{N2}}{64\pi^4(\sinh\alpha^N)^2}&\int_{-1}^{1} d(\cos\beta_1)\, \cosh(\alpha^N\cos\beta_1)\\ &\times\int_{-1}^{1} d(\cos\beta_2)\, \cosh(\alpha^N\cos\beta_2)\\ &\times\int_0^{2\pi} d\alpha_1 \int_0^{2\pi} d\alpha_2 \int_0^{2\pi} d\gamma_1 \int_0^{2\pi} d\gamma_2\, M_0^{ll'}(\boldsymbol{\Omega}_1, \boldsymbol{\Omega}_2)\end{aligned} \tag{6.26}$$

$$\begin{aligned}\overline{v}_1^{excl}(ll') = \frac{\alpha^{N3}}{64\pi^4(\sinh\alpha^N)^2}&\int_{-1}^{1} d(\cos\beta_1)\, \cosh(\alpha^N\cos\beta_1)\\ &\times\int_{-1}^{1} d(\cos\beta_2)\, \sinh(\alpha^N\cos\beta_2)\\ &\times\int_0^{2\pi} d\alpha_1 \int_0^{2\pi} d\alpha_2\cos\alpha_2 \int_0^{2\pi} d\gamma_1 \int_0^{2\pi} d\gamma_2\, M_1^{ll'}(\boldsymbol{\Omega}_1, \boldsymbol{\Omega}_2)\end{aligned} \tag{6.27}$$

$$\begin{aligned}\overline{v}_2^{excl}(ll') = -\frac{\alpha^{N4}}{64\pi^4(\sinh\alpha^N)^2}&\int_{-1}^{1} d(\cos\beta_1)\, \sinh(\alpha^N\cos\beta_1)\\ &\times\int_{-1}^{1} d(\cos\beta_2)\, \sinh(\alpha^N\cos\beta_2)\\ &\times\int_0^{2\pi} d\alpha_1\cos\alpha_1 \int_0^{2\pi} d\alpha_2\cos\alpha_2 \int_0^{2\pi} d\gamma_1 \int_0^{2\pi} d\gamma_2\, M_2^{ll'}(\boldsymbol{\Omega}_1, \boldsymbol{\Omega}_2)\end{aligned} \tag{6.28}$$

The computational cost of the sixfold integrals in eqs. (6.26)-(6.28) scales with the product of the number of interaction sites in each of the two aggregates, and can become unfeasibly high for longer aggregates. To put then in more manageable form, it is convenient to make the change of variables $\boldsymbol{\Omega}_2 \to \boldsymbol{\Omega}_{12}$. Then, eq. (6.26) takes the following form:

$$\overline{v}_0^{excl}(ll') = \frac{1}{8\pi^2}\int_0^{2\pi} d\alpha_{12}\int_{-1}^{1} d(\cos\beta_{12})\int_0^{2\pi} d\gamma_{12} M_0^{ll'}(\boldsymbol{\Omega}_{12}) \tag{6.29}$$

in the isotropic phase, whereas in the liquid crystal phase it becomes:

$$\begin{aligned}\overline{v}_0^{excl}(ll') =& \frac{\alpha^{N2}}{32\pi^3(\sinh\alpha^N)^2}\int_0^{2\pi} d\alpha_{12}\int_{-1}^{1} d(\cos\beta_{12})\int_0^{2\pi} d\gamma_{12} M_0^{ll'}(\boldsymbol{\Omega}_{12})\\ &\times\int_{-1}^{1} d(\cos\beta_1)\cosh(\alpha^N\cos\beta_1)\int_0^{2\pi} d\gamma_1\cosh(\alpha^N g)\end{aligned} \tag{6.30}$$

where

$$\begin{aligned}g(\alpha_{12},\beta_{12},\gamma_1,\beta_1) =& -\cos\gamma_1\sin\beta_1\sin\beta_{12}\cos\alpha_{12}\\ &+\sin\beta_1\sin\gamma_1\sin\beta_{12}\sin\alpha_{12}+\cos\beta_1\cos\beta_{12}\end{aligned}. \tag{6.31}$$

and

$$\begin{aligned}M_0^{l,l'}(\boldsymbol{\Omega}_{12}) =& \int_{v^{excl}(ll')} d\mathbf{R}_{12}\\ =&(1/3)\int_{-1}^{1} d(\cos\theta_{12})\int_0^{2\pi} d\phi_{12}\,(R_{12}^0)^3.\end{aligned} \tag{6.32}$$

Here spherical coordinates are used, $\mathbf{R}_{12} \equiv \{R_{12}, \phi_{12}, \vartheta_{12}\}$, and R^0_{12} is the closest approach distance of the two aggregates. Likewise, eqs. (6.27) and (6.28) become:

$$\begin{aligned} \overline{v}_1^{excl}(ll') =& \frac{\alpha^{N3}}{64\pi^4(\sinh\alpha^N)^2}\int_0^{2\pi} d\alpha_{12} \int_{-1}^{1} d(\cos\beta_{12}) \int_0^{2\pi} d\gamma_{12} M_1^{ll'}(\mathbf{\Omega}_{12}) \\ & \times \int_0^{2\pi} d\alpha_1 \int_{-1}^{1} d(\cos\beta_1)\cosh(\alpha^N\cos\beta_1) \int_0^{2\pi} d\gamma_1 h \sinh(\alpha^N g) \end{aligned} \tag{6.33}$$

$$\begin{aligned} \overline{v}_2^{excl}(ll') =& -\frac{\alpha^{N4}}{64\pi^4(\sinh\alpha^N)^2}\int_0^{2\pi} d\alpha_{12} \int_{-1}^{1} d(\cos\beta_{12}) \int_0^{2\pi} d\gamma_{12}\, M_2^{ll'}(\mathbf{\Omega}_{12}) \\ & \times \int_0^{2\pi} d\alpha_1 \cos\alpha_1 \int_{-1}^{1} d(\cos\beta_1)\sinh(\alpha^N\cos\beta_1) \int_0^{2\pi} d\gamma_1 h \sinh(\alpha^N g) \end{aligned} \tag{6.34}$$

where

$$\begin{aligned} h(\alpha_{12}, \beta_{12}, \gamma_1, \alpha_1, \beta_1) =& \sin\beta_{12}\cos\alpha_{12}(\cos\alpha_1\cos\beta_1\cos\gamma_1 - \sin\alpha_1\sin\gamma_1) \\ & - \sin\beta_{12}\sin\alpha_{12}(\cos\alpha_1\cos\beta_1\sin\gamma_1 + \sin\alpha_1\cos\gamma_1) \\ & + \cos\beta_{12}\cos\alpha_1\sin\beta_1. \end{aligned} \tag{6.35}$$

$$\begin{aligned} M_1^{l,l'}(\mathbf{\Omega}_{12}) =& \int_{v^{excl}(ll')} d\mathbf{R}_{12}(R_{12,x}e_x^Y + R_{12,y}e_y^Y + R_{12,z}e_z^Y) \\ =& (1/4)\int_{-1}^{1} d(\cos\theta_{12}) \int_0^{2\pi} d\phi_{12}\,(R^0_{12})^4 \\ & [\sin\theta_{12}\cos\phi_{12}(\sin\alpha_1\cos\beta_1\cos\gamma_1 + \cos\alpha_1\sin\gamma_1) \\ & + \sin\theta_{12}\sin\phi_{12}(-\sin\alpha_1\cos\beta_1\sin\gamma_1 + \cos\alpha_1\cos\gamma_1) \\ & + \cos\theta_{12}\sin\alpha_1\sin\beta_1] \end{aligned} \tag{6.36}$$

$$\begin{aligned} M_2^{l,l'}(\mathbf{\Omega}_{12}) =& \int_{v^{excl}(ll')} d\mathbf{R}_{12}(R_{12,x}e_x^Y + R_{12,y}e_y^Y + R_{12,z}e_z^Y)^2 \\ =& (1/5)\int_{-1}^{1} d(\cos\theta_{12}) \int_0^{2\pi} d\phi_{12}\,(R^0_{12})^5 \\ & [\sin^2\theta_{12}\cos^2\phi_{12}(\sin\alpha_1\cos\beta_1\cos\gamma_1 + \cos\alpha_1\sin\gamma_1)^2 \\ & + \sin^2\theta_{12}\sin^2\phi_{12}(-\sin\alpha_1\cos\beta_1\sin\gamma_1 + \cos\alpha_1\cos\gamma_1)^2 \\ & + \cos^2\theta_{12}\sin^2\alpha_1\sin^2\beta_1 + 2\sin^2\theta_{12}\cos\phi_{12}\sin\phi_{12} \\ & \times (\sin\alpha_1\cos\beta_1\cos\gamma_1 + \cos\alpha_1\sin\gamma_1)(-\sin\alpha_1\cos\beta_1\sin\gamma_1 + \cos\alpha_1\cos\gamma_1) \\ & + 2\sin\theta_{12}\cos\phi_{12}\cos\theta_{12}(\sin\alpha_1\cos\beta_1\cos\gamma_1 + \cos\alpha_1\sin\gamma_1)\sin\alpha_1\sin\beta_1 \\ & + 2\sin\theta_{12}\sin\phi_{12}\cos\theta_{12}(-\sin\alpha_1\cos\beta_1\sin\gamma_1 + \cos\alpha_1\cos\gamma_1)\sin\alpha_1\sin\beta_1] \end{aligned} \tag{6.37}$$

The integrals in eqs. (6.30), (6.33) and (6.34) are the sum of terms, each having have the general form:

$$\int_0^{2\pi} d\alpha_{12} \int_{-1}^{1} d(\cos\beta_{12})\Xi(\alpha_{12}, \beta_{12}; \alpha_l^N, \alpha^N)H(\alpha_{12}, \beta_{12}) \tag{6.38}$$

where Ξ represents a threefold integral over the $\{\alpha_1, \beta_1, \gamma_1\}$ angles and contains the whole dependence on the α_l^N, α^N parameters, whereas

$$H(\alpha_{12}, \beta_{12}) = \int_0^{2\pi} d\gamma_{12} \int_0^{2\pi} d\phi_{12} \int_{-1}^{1} d(\cos\vartheta_{12})F(\alpha_{12}, \beta_{12}, \gamma_{12}, \phi_{12}, \vartheta_{12}) \tag{6.39}$$

Calculation of the Ξ integrals is fast, so can be easily repeated for different values of α_l^N, α^N ; the H integrals, implying the evaluation of the interactions between aggregates, are much more demanding and their cost increases with the lengths of the aggregates. The two kinds of contributions can be computed separately for different values of the α_{12}, β_{12} angles, and are then collected. The Gauss quadrature algorithm [44], with integration points and weights determined by the zeros of the Legendre polynomials (for θ_{12}, β_{12} and β_1) and the Chebyshev polynomials (for α_{12}, ϕ_{12}, α_1) has been used. Integration over the γ_{12} and γ_1 angles has been performed using the Romberg method [44], which allows a non-uniform spacing of abscissas.

6.4 Linear aggregates of dsDNA

Calculations were performed for DD and all-AT dodecamers with the self-complementary sequences listed in Table 5.1. We used the same models of linear aggregates and CG representation described in Section 5.2. The geometric and energetic parameters needed for calculations are reported below.

6.4.1 Geometric parameters

The geometric parameters present in the theory are the aspect ratio, X_0, and the volume of the monomers, v_0. The definition of these parameters is not obvious in the case of complex molecular structures, like those of DNA dodecamers.

We adopted the following procedure. We have calculated the volume and excluded volume for aggregates of DD and all-AT dodecamers and we have mapped the results into those for an equivalent cylinder. We have considered aggregates of $l = 10$, v_{10}; the volume was calculated using the procedure outlined in subsection 2.4.1 with a rolling sphere radius equal to the size of a half base pair ($r_{probe} = 1$ nm). The excluded volume was evaluated by integrating over all relative orientations of two aggregates. The geometric parameters of the equivalent cylinder, aspect ratio and diameter, D, were then determined by solving the following system of equation:

$$\begin{cases} v_{10} = \dfrac{\pi}{4} D^3 l X_0 \\ v_0^{excl}(ll') = \dfrac{\pi^2}{8} D^3 + \left(3\dfrac{\pi}{8} + \dfrac{\pi^2}{8}\right) 2l^2 X_0 D^3 + \dfrac{\pi}{2} l^3 X_0^2 D^3 \end{cases} \tag{6.40}$$

The volume of the monomer is equal to $v_0 = v_{10}/10$. Table 6.1 shows the values of v_0, X_0 and D obtained for all-AT and DD.

6.4.2 Stacking free energy

As reported in ref. [17], we assumed the following expression for ΔA_b

$$\ln[\Delta A_b] = \frac{1}{\beta}\left(\ln\frac{2D^3}{v_0} + \ln(2) - 17.6769 + 4559/T\right) \tag{6.41}$$

Sequence	v_0	X_0	D
all-AT	12.7234	2.3043	1.91568
DD	11.5864	1.94406	1.96509

Table 6.1: Volume, v_0, aspect ratio, X_0 and diameter, D, evaluated for monomers of all-AT and DD dodecamers.

6.5 Results and discussion

6.5.1 Excluded volume contributions: Dependence on the scaled length and ordering

We have calculated the excluded volume contributions to the free energy, , $\overline{v}_0^{excl}$, chiral strength, $\overline{v}_1^{excl}$, and the twist elastic constant, $\overline{v}_2^{excl}$, for aggregates of different scaled lengths and different values of α^N, using eq. (6.29), (6.30) (6.33) and (6.34), respectively. For each contribution, a simultaneous fit to data was performed using an expansion of the functions of α^N that appear in each of them (k_N, B_N, in eq. (6.22) and other functions introduced below) in powers of $\alpha^{N^{-1/2}}$ [16]. In the following we will discuss the results obtained for $\overline{v}_1^{excl}$ and $\overline{v}_2^{excl}$.

Figure 6.2 shows $\overline{v}_1^{excl}(ll)$ for all-AT and DD. The values of $\overline{v}_1^{excl}(ll)$ are negative and increase with increasing scaled length and increasing α^N, i.e. increasing order. At given α_N and scaled length, the contribution for DD is greater than for all-AT, which can be ascribed to the different chirality of aggregates. The following equation was used for fitting:

$$\overline{v}_1^{excl}(ll')(\alpha^N) = \kappa_1(\alpha^N)v_0\frac{l+l'}{2} + \mathcal{A}_1(\alpha^N). \tag{6.42}$$

where κ_1 and $\mathcal{A}_1$ are functions of the parameter α^N. The linear dependence on aggregate length reflects the local character of chiral interactions between pairs of aggregates. Actually, figure 6.2 shows that for DD there are larger deviations from this linear dependence.

Figure 6.3 shows the excluded volume contribution to the twist elastic constant .We can observe that $\overline{v}_2^{excl}$ increases with increasing both l and α_N, and the l dependence is highly non-linear. In this case, the following form was used for fitting:

$$\overline{v}_2^{excl}(ll')(\alpha^N) = ll'\left[\mathcal{B}_2(\alpha^N)X_0^2 ll' + \kappa_2(\alpha^N)v_0\frac{l+l'}{2} + \mathcal{A}_2(\alpha^N)\right] \tag{6.43}$$

where $\mathcal{B}_2$, κ_2 and $\mathcal{A}_2$ are functions of the parameter α^N. For the same α_N and l, the contribution evaluated for all-AT is nearly twice as big as that for DD: This can traced back to the higher aspect ratio of all-AT (see Table 6.1).

6.5.2 Temperature and concentration dependence of the average chain length

An important parameter in the coupling of order and self-assembly is the *average aspect ratio*, MX_0. Minimization of free energy with respect to M yields, after dropping terms in $\mathcal{O}(1/M^2)$

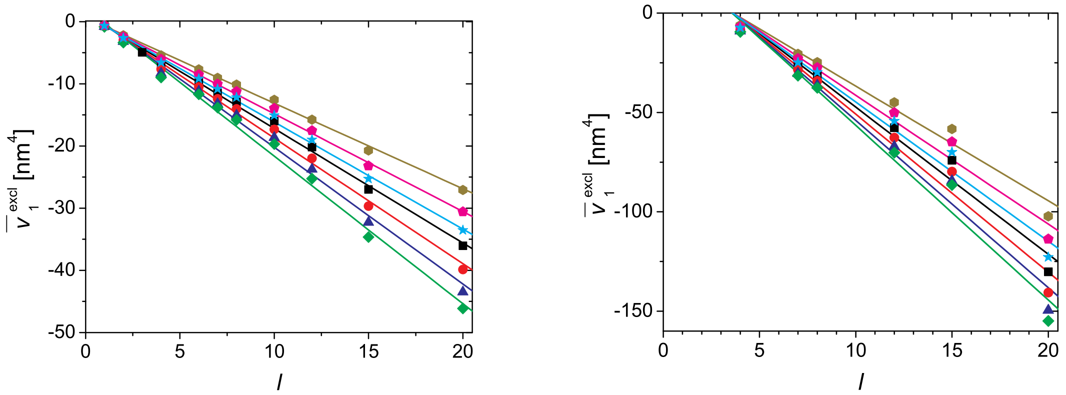

Figure 6.2: Average excluded volume contribution to the chiral strength, $\overline{v}_1^{excl}$, calculated for all-AT (left) and DD (right) aggregates for different values of α^N as a function of the scaled length, l . Solid lines represent fitting curves The following values of α^N were used: 20 (green), 15 (blue), 12 (red), 10 (black), 9 (cyan), 8 (magenta), 7 (dark yellow).

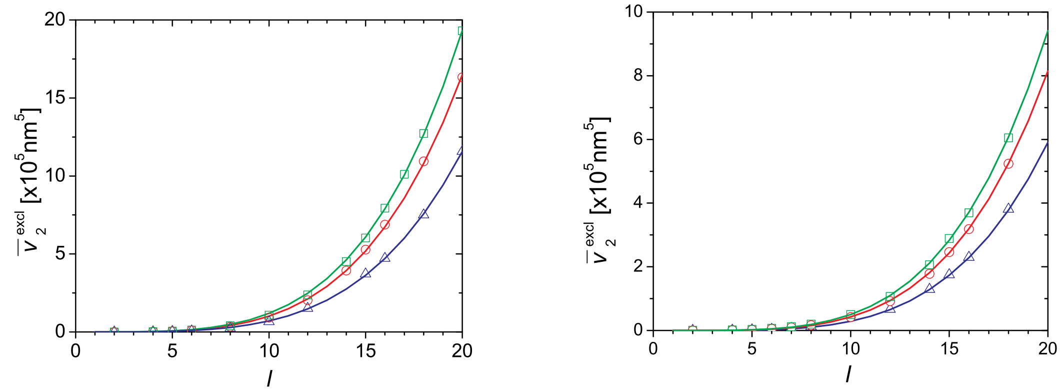

Figure 6.3: Average excluded volume contribution to the twist elastic constant, $\overline{v}_2^{excl}$, calculated for aggregates of all-AT (left) and DD dodecamers (right) with different values of α^N, as a function of the scaled length, l. Solid lines represent fitting curves. The following values of α^N were used: 30 (green), 20 (red), 10 (blue).

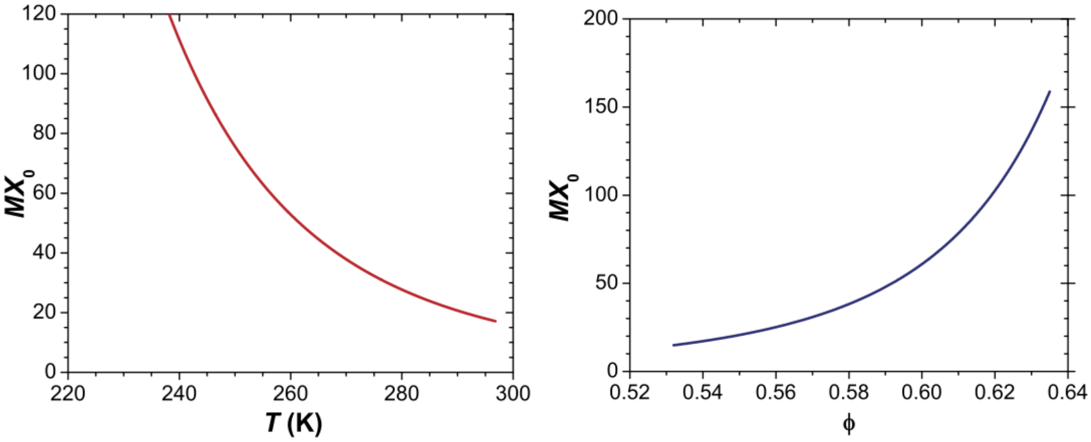

Figure 6.4: Average aspect ratio MX_0 obtained for all-AT in the nematic as a function of the temperature, T, at $\phi = 0.55$, (left), and as a function of the volume fraction, ϕ, at $T = 280$ K (right).

[16]:

$$M = \frac{1}{2}\left(1 + \sqrt{1 + \alpha^N \phi \exp\left(k_N(\alpha^N)\phi G(\phi) + \frac{\Delta A_b}{k_B T}\right)}\right) \tag{6.44}$$

Thus, the average chain length is expected to increase with increasing volume fraction and decreasing temperature. Figure 6.4 shows the dependence of the average aspect ratio, MX_0, upon the temperature (at fixed volume fraction) and upon the volume fraction (at fixed temperature), obtained for all-AT in the nematic phase. The average number of dodecamers is found to range from about 10 to more than 60 at low temperature and high volume fraction. Similar results were obtained for DD.

6.5.3 Isotropic-to-nematic phase coexistence

Figure 6.5 shows the isotropic-nematic coexistence region in the MX_0-ϕ plane, obtained for DD and all-AT. In both cases, a clear re-entrant behaviour is observed. Similar results were found for polymerizing superquadric particles and other model of short DNA duplexes [16, 17]. We can observe that the coexistence regions are quite similar for the two systems.

Figure 6.6 and 6.7 show the chiral strength and the twist elastic constant calculated in the nematic phase along the coexistence curve for all-AT and DD, as a function of volume fraction and temperature, respectively. We can observe a non-monotonic dependence of both k_2 and K_{22} which reflects the reentrance in the phase diagram. The trend of K_{22} can be explained considering that $\overline{v}_2^{excl}$ is strongly increasing function of the scaled length, thus of MX_0: Starting from low volume fraction and temperature, K_{22} first decreases and then increases, as as also MX_0 does. The steep increase at high volume fraction (high temperature) is also determined the dependence on ρ^2 in eq. (6.15).

Understanding the behaviour of k_2 is not as obvious. This is determined by the local character of the chiral hard-core interactions between a pair of molecules, which originates a linear dependence of $\overline{v}_1^{excl}$ on the scaled length. Just to illustrate this situation, we can compare

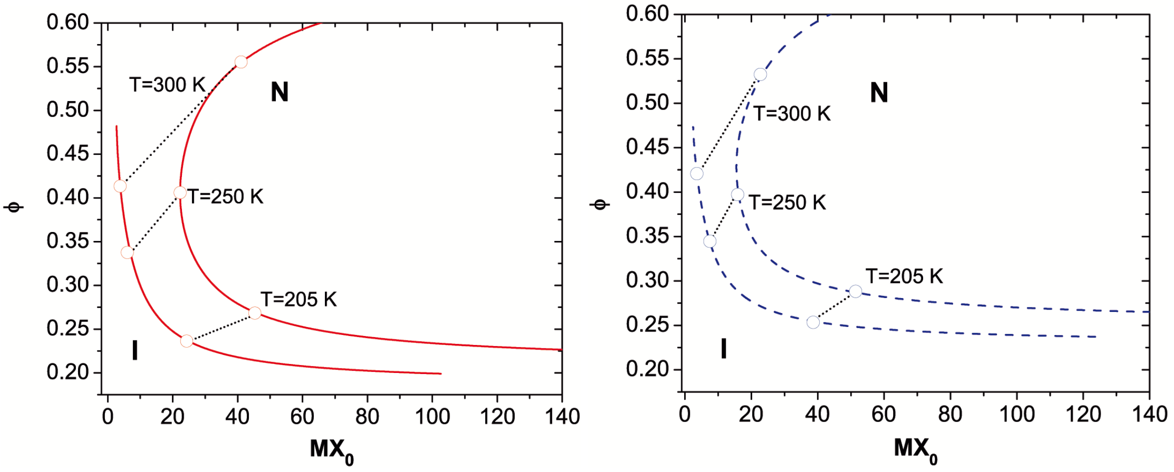

Figure 6.5: IN coexistence in the average aspect ratio MX_0 *vs* volume fraction ϕ plane, for all-AT (red solid line, left) and DD (blue dashed line, right) dodecamer aggregates. Short dot lines represent tie lines at different temperatures.

the limit cases of a system of N monomers and one of 2 polymer with $l = N/2$. The chiral interactions are proportional to N^2 in the first case, and to N in the latter. Hence, somehow counterintuitively, the magnitude of k_2 increases/decreases with decreasing/increasing the average aggregation length (see Figure 6.6).

Figure 6.8 shows the cholesteric pitch calculated for aggregates of all-AT and DD as a function of the volume fraction and the temperature, respectively. Experimental values of the pitch for the cholesteric phase formed by DNA oligomers are of the order of magnitude of a micron or smaller [8]. The results shown in Figure 6.8 are much longer and beyond the range detectable by standard optical techniques. In the case of DD, cholesteric pitches comparable with the experimental values are predicted in limited intervals of ϕ and T. Indeed in Figure 6.8 we can see some differences between all-AT and DD. In Chapter 5 we have already shown that the duplex structure influences the properties of the cholesteric phase. Here we have found that differences are amplified by the coupling of cholesteric order and self-assembly. The non-monotonic behaviour of the pitch is especially interesting and, since the pitch is an experimentally accessible quantity, in principle could be used to confirm the predicted re-entrance in the phase diagram. Unfortunately, the predicted re-entrance of all-AT and DD is located in a range of temperature and concentration which cannot be explored by experimental measurements. However, our results suggest that the re-entrance might be detectable for other geometry and the shape of aggregates.

6.5.4 Comparison with experiments

For a better comparisons with experimental data, it is convent to analyze results at fixed volume fraction or temperature, rather than along the coexistence.

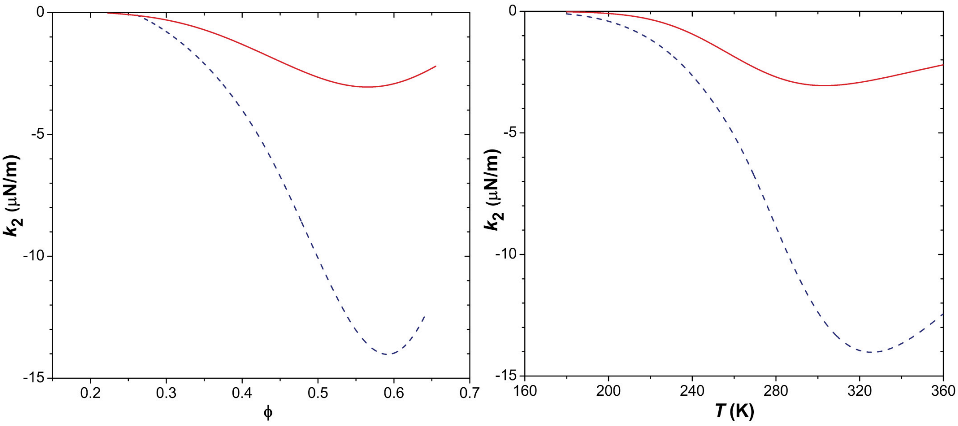

Figure 6.6: Chiral strength, k_2, along the coexistence curve, as a function of the volume fraction ϕ (left) and of the temperature (right) for aggregates of all-AT (red solid line) and DD (blue dashed line).

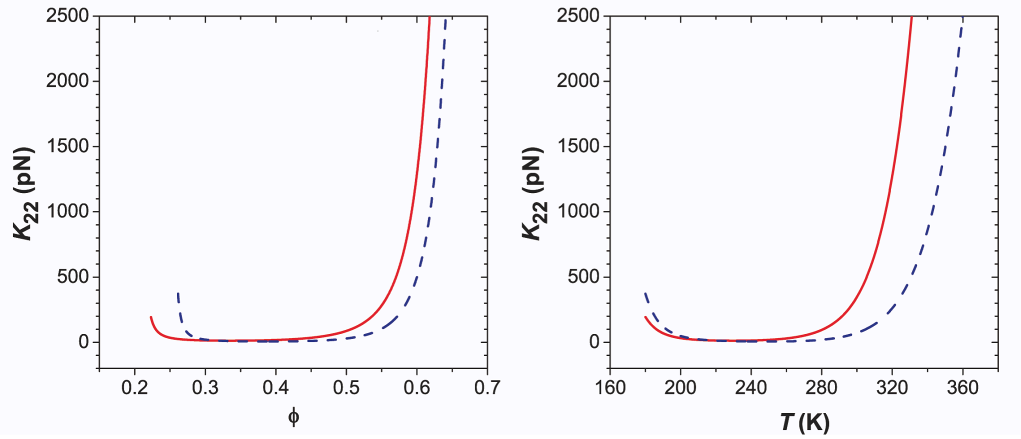

Figure 6.7: Twist elastic constant, K_{22}, along the coexistence curve, as a function of the volume fraction ϕ (left) and of the temperature (right) for aggregates of all-AT (red solid line) and DD (blue dashed line).

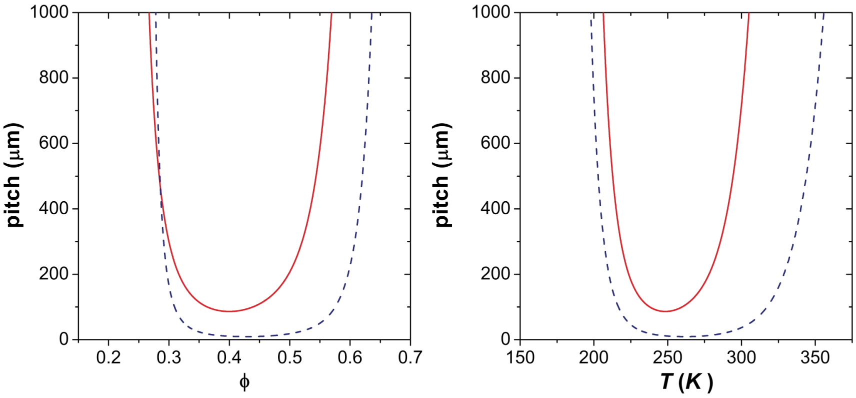

Figure 6.8: Cholesteric pitch , along the coexistence curve, as a function of the volume fraction ϕ (left) and of the temperature (right) for aggregates of all-AT (red solid line) and DD (blue dashed line).

Concentration dependence

Figure 6.9 and 6.10 show the chiral strength k_2 as a function of the average aspect ratio, MX_0, and volume fraction, ϕ, respectively, obtained for all-AT and DD dodecamers at different temperature. In the case of allAT, k_2 decreases in modulus with increasing ϕ. This is related to the increase of average chain length M according to eq. (6.44). The relation between k_2 and M has already been discuss in subsection 6.5.3. Analogous results are obtained for DD, with some deviation from this general trend only for M smaller than ≈ 15, which again can be explained by considering the interplay of length dependence of the $\overline{v}_1^{excl}$ and statistical distribution of lengths. We can see that the oligomer structure has a strong effect on the chiral strength: k_2 is much larger for DD than for all-AT duplexes, which can be ascribed to the higher structural chirality of the DD aggregates (see Figure 5.2).

Figures 6.12 shows the twist elastic constants $K_{22}$of all-AT and DD at as a function of the volume fraction. K_{22} is a function that strongly increases with increasing volume fraction and decreasing temperature. Again, this behaviour is amenable to the increase in the average chain length with increasing density (see Figure 6.11). The larger average chain length (M) is also the reason for the larger K_{22} values predicted for all-AT compared to DD dodecamers.

Experimental values of the twist elastic constant are not available for DNA duplexes, but typical values for cholesteric solutions of polymers are around some pN [45, 46]. The results obtained for all-AT are all much higher, whereas for DD values of some micrometers were obtained at volume fractions lower than ≈ 0.50, especially at the highest temperatures. The reason for this discrepancy between theory and experiment must be the neglect of the flexibility of aggregates, which are treated here as rigid particles. The persistence length of linear aggregates of dodecamers is not known; however, taking as reference long DNA, for which a persistence length of about 50 nm ($\approx$ 150 base pairs) has been reported [47], we expect that beyond $l \approx 10$, K_{22} can be strongly overestimated if flexibility is neglected.

Figure 6.13 shows the dependence of the pitch upon concentration for all-AT and DD dodecamers. In both cases the pitch increases with concentration, which is mainly due to the increase of the twist elastic constant. With increasing concentration there is also a decrease of the chiral strength, but this is a minor effect if compared to the huge change of K_{22}. As already obtained for aggregates of fixed length (see Chapter 5), a positive pitch (pitch > 0), i.e. R cholesteric organization, is predicted for both sequences. For all-AT this is the opposite of what found experimentally; moreover, the magnitude of the pitch is orders of magnitude longer than the measured values [8]. On the contrary, for DD the positive pitch is in agreement with the R handedness found in experiments. Moreover, for $\phi < 0.6$, which corresponds to the experimental range, the predicted pitch is relatively closer to the measured values: it is about 10 times longer, an overestimate that is probably due to the modelling of aggregates as stiff polymers. As discussed above, the introduction of some flexibility would lead to a reduction of the twist elastic constant, thus an increase of the cholesteric pitch. The pitch increases with concentration, as generally found in experiments [8]. Actually, in the case of DD the experimental trend is not so clear, probably because of the limited range explored.

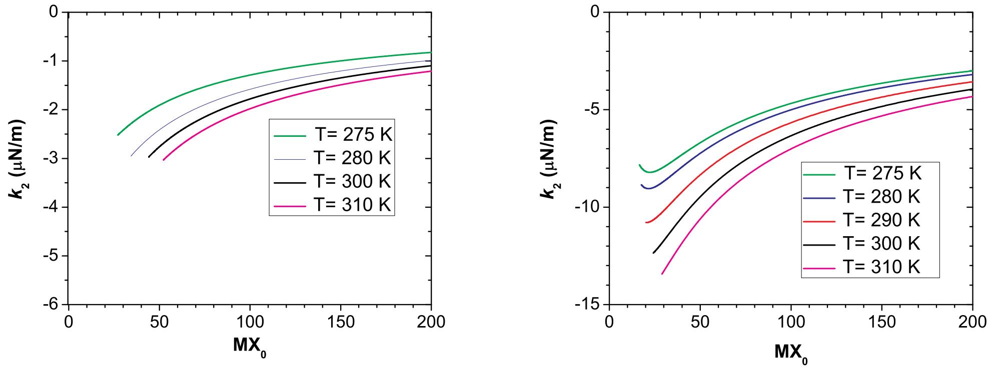

Figure 6.9: Chiral strength k_2 calculated for aggregates of all-AT (left) and DD (right), as a function of the average aspect ratio MX_0. Curves refer to different temperatures and start at the isotropic-to-nematic transition.

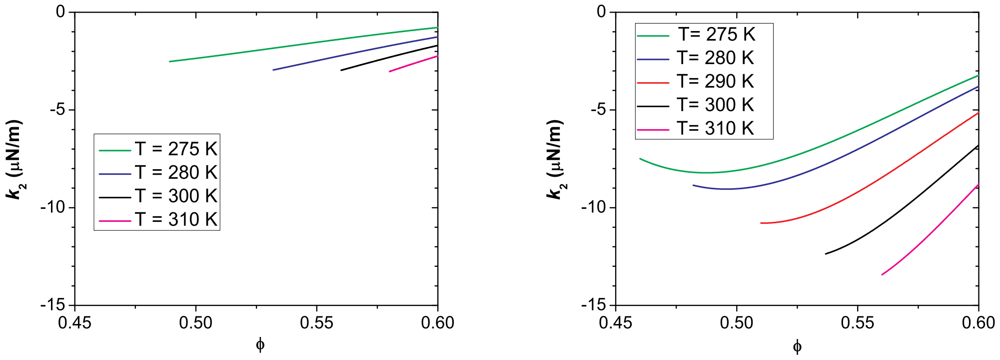

Figure 6.10: Chiral strength k_2 calculated for aggregates of all-AT (left) and DD (right), as a function of the volume fraction, ϕ. Curves refer to different temperature and start at the isotropic-to-nematic transition.

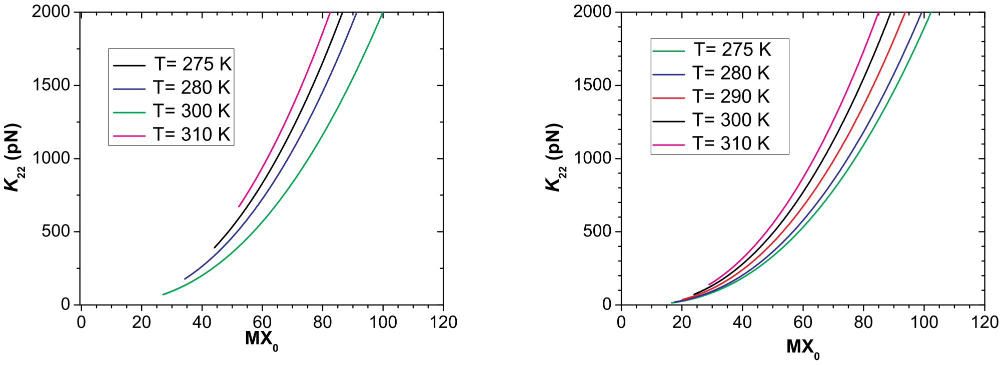

Figure 6.11: Twist elastic constant K_{22} calculated for aggregates of all-AT (left) and DD dodecamers (right), as a function of the average aspect ratio, MX_0. Curves refer to different temperature and start at the isotropic-to-nematic transition.

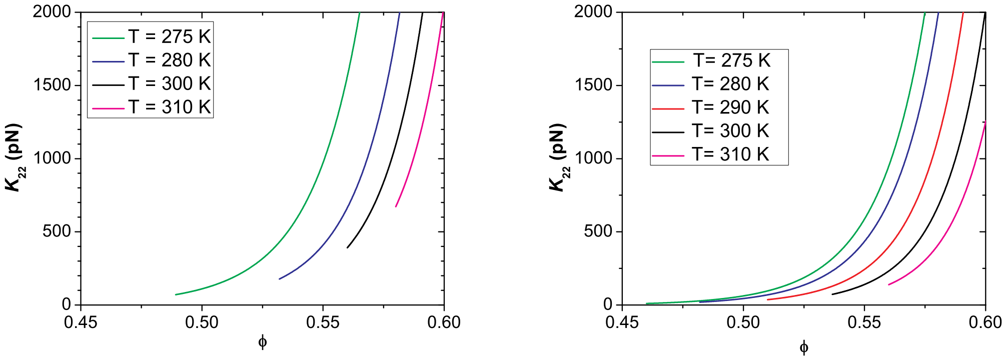

Figure 6.12: Twist elastic constant K_{22} calculated for aggregates of all-AT (left) and DD (right) dodecamers, as a function of the volume fraction, ϕ. Curves refer to different temperature and start at the isotropic-to-nematic transition

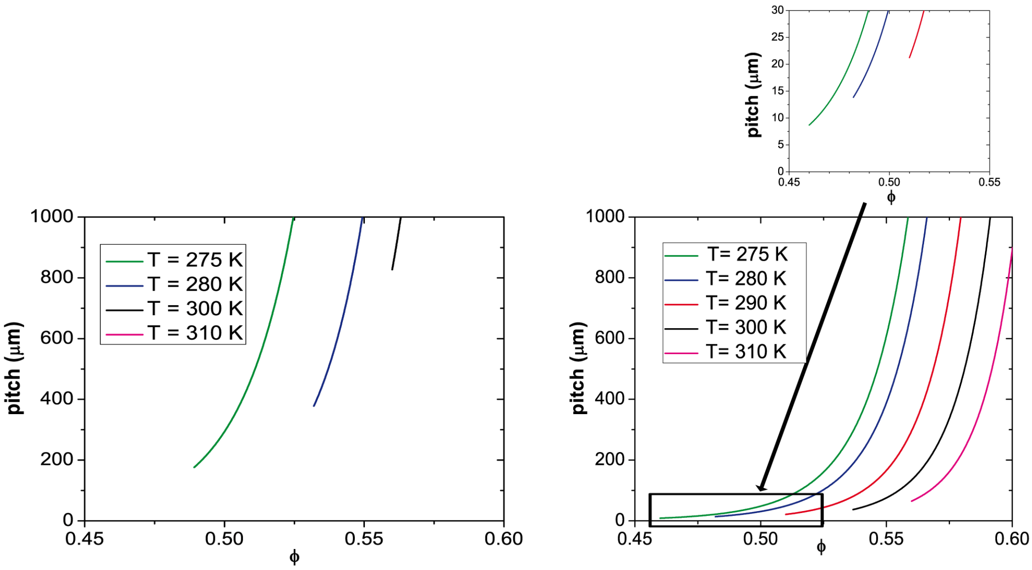

Figure 6.13: Cholesteric pitch calculated for aggregates of all-AT (left) and DD dodecamers (right), as a function of the volume fraction, ϕ.Curves refer to different temperatures and start at the isotropic-to-nematic transition.

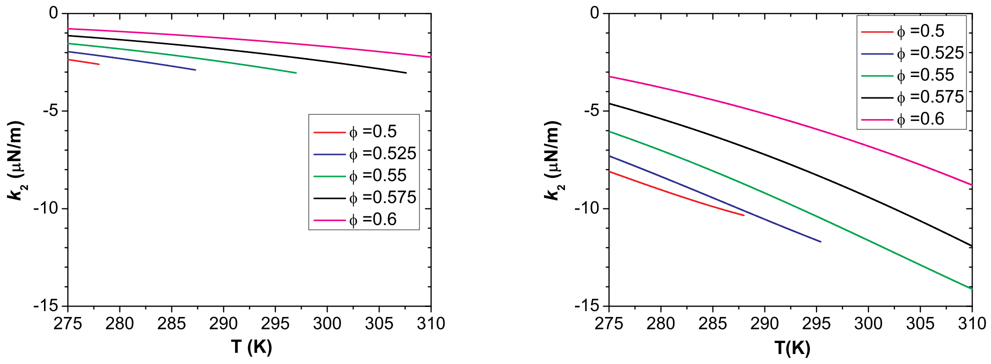

Figure 6.14: Chiral strength k_2 calculated for aggregates of all-AT (left) and DD dodecamers (right) as a function of the temperature, T. Curves refer to different values of volume fraction, ϕ and begin at the temperature of the isotropic-to-nematic transition.

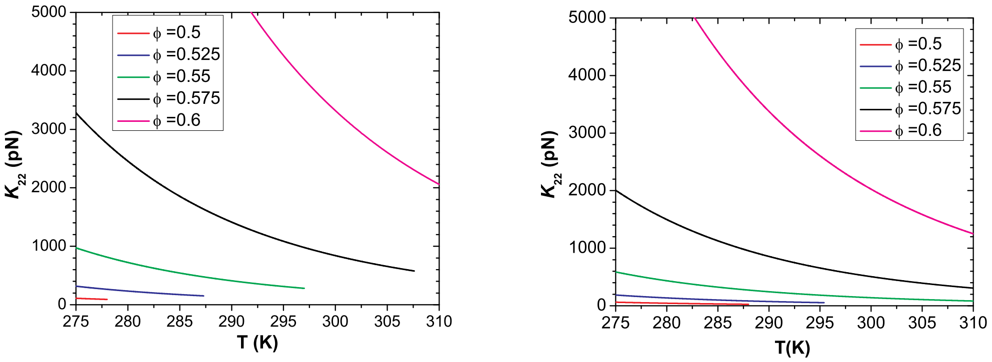

Figure 6.15: Twist elastic constant, K_{22}, calculated for aggregates of all-AT (left) and DD dodecamers (right), as a function of the temperature, T. Curves refer to different values of volume fraction, ϕ and start at the isotropic-to-nematic transition.

Temperature dependence

Figures 6.14 and 6.15 show the temperature dependence of the chirality strength and of the twist elastic constant, calculated for all-AT and DD dodecamers. We can see that, with increasing temperature, k_2 increases in magnitude and K_{22} decreases, in line with the decrease of the average chain length (see Figure 6.4). K_{22}, exhibiting the more dramatic changes, determines the temperature dependence of the pitch: We can see in Figure 6.16 that this is predicted to decrease with increasing temperature, as generally found in experiment [8].

6.6 Conclusions

We have developed and implemented a theoretical framework for the study of the cholesteric phase formed by self-assembling chiral monomers with purely steric interactions. This is

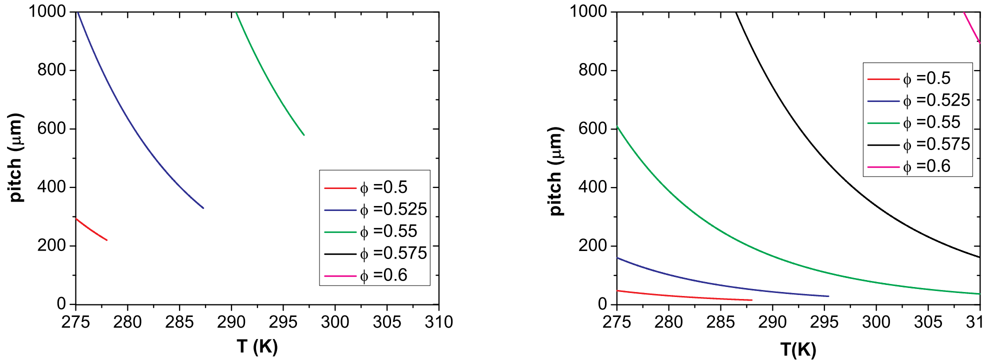

Figure 6.16: Cholesteric pitch obtained for aggregates of all-AT (left) and DD dodecamers (right) as a function of the temperature, T. Curves refer to different values of volume fraction, ϕ and start at the isotropic-to-nematic transition.

obtained by integrating the theory for cholesteric order with that for linear aggregation in the nematic phase. This is the first approach that, taking into account the interplay of aggregation and orientational order, allows us to analyze the temperature and concentration dependence of the cholesteric properties.

Here the theory has been applied to DNA dodecamers, for which experimental data are available [8]. In particular, we have focused on two self-complementary sequences denoted as all-AT and DD, which form duplexes with different geometry (see Chapter 5), and we have been able to determine how the structural features affect the cholesteric properties. We have found that the liquid crystal organization promotes aggregation: The average chain length jumps from very few units to around ten units at the isotropic-to-nematic phase transition, and then steadily increases with the orientational order, reaching values close to one hundred at high ordering. The material properties that control the cholesteric structure are the chiral strength, k_2, and the twist elastic constant, K_{22}, which are differently affected by the molecular structure: The latter is mainly determined by the aspect ratio, whereas the former depends on the molecular chirality. The systems under investigation differ in both: DD is thicker and shorter than all-AT and has more pronounced chirality (see Figure 5.2). We have found that aggregation amplifies the differences between the two systems: under analogous conditions, higher twist elastic constant are predicted for all-AT, due to the higher aspect ratio of its aggregates. On the other hand, DD aggregates lead to higher chiral strength, which results from the combination of the intrinsic chirality of duplexes with a chiral superstructure. The final result is that a much smaller cholesteric pitch is predicted for DD. Yet, it is about ten times higher than the experimental value. The reason of this discrepancy can be ascribed to the neglect of flexibility. K_{22} scales with the fourth power of the length for stiff rod-like particles, but the introduction of a persistence length would prevent the increase beyond a certain value. For all-AT a pitch that is orders of magnitude longer than typical experimental values is obtained, mainly because of the huge elastic constant, amenable to the high aspect ratio of all-AT aggregates. Flexibility is expected to play an even higher role for this system.

The coupling of aggregation to order does not affect the cholesteric handedness: For both all-AT and DD we predict a right-handed cholesteric phase. This is in agreement with experiment for DD, but not for all-AT [8]. As discussed in Chapter 5, purely steric interactions are probably insufficient to explain the behaviour of all-AT duplexes.

Bibliography

(1) Y. Timsit and P. Varnai, *PLoS One*, 2010, **5**, e936.

(2) D. Marenduzzo, E. Orlandini, A. Stasiak, D. W. Sumners, L. Tubiana, and C. Micheletti, *Proc. Natl. Acad. Sci. U.S.A.*, 2009, **106**, 22269–22274.

(3) F. Livolant and A. Leforestier, *Prog. Polym. Sci.*, 1996, **21**, 1115–1164.

(4) D. H. Van Winkle, M. W. Davidson, W. X. Chen, and R. L. Rill, *Macromolecules*, 1990, **23**, 4140–4148.

(5) G. Proni, G. Gottarelli, P. Mariani, and G. Spada, *Chem.-Eur. J.*, 2000, **6**, 3249–3253.

(6) M. Nakata, G. Zanchetta, B. Chapman, C. Jones, J. Cross, R. Pindak, T. Bellini, and N. Clark, *Science*, 2007, **318**, 1276–1279.

(7) G. Zanchetta, T. Bellini, M. Nakata, and N. A. Clark, *J. Am. Chem. Soc.*, 2008, **130**, 12864–12865.

(8) G. Zanchetta, F. Giavazzi, M. Nakata, R. Cerbino, N. A. Clark, and T. Bellini, *P. Natl. Acad. Sci. USA*, 2010, **107**, 17497–17502.

(9) J. P. Straley, *Phys. Rev. A*, 1976, **14**, 1835.

(10) A. Kornyshev, D. Lee, S. Leikin, and A. Wynveen, *Rev. Mod. Phys.*, 2007, **79**, 943–994.

(11) A. Cherstvy, *J. Chem. Phys.*, 2005, **123**, 116101.

(12) H. H. Wensink and G. Jackson, *J. Chem. Phys.*, 2009, **130**, 234911.

(13) H. H. Wensink and G. Jackson, *J. Phys.: Condens. Matter*, 2011, **23**, 194107.

(14) F. Tombolato and A. Ferrarini, *J. Chem. Phys.*, 2005, **122**, 054908.

(15) E. Frezza, F. Tombolato, and A. Ferrarini, *Soft Matter*, 2011, **7**, 9291–9296.

(16) C. De Michele, T. Bellini, and F. Sciortino, *Macromolecules*, 2012, **45**, 1090–1106.

(17) C. De Michele, L. Rovigatti, T. Bellini, and F. Sciortino, *Soft Matter*, 2012, **8**, 8388–8398.

(18) R. Wing, T. Drew, H. andTakano, C. Broka, S. Tanaka, K. Itakura, and R. Dickerson, *Nature (London)*, 1980, **287**, 755–758.

(19) L. Campos, N. Valls, L. Urpí, C. Gouyette, T. Sanmartín, M. Richter, E. Alechaga, A. Santaolalla, R. Baldini, M. Creixell, R. Ciurans, P. Skokan, J. Pous, and J. A. Subirana, *Biophysic. J.*, 2006, **91**, 892–903.

(20) N. Valls, A. Santaolalla, J. L. Campos, and J. A. Subirana, *J. Biomol.*, 2007, **24**, 547–551.

(21) N. Valls, M. Richter, and J. A. Subirana, *Acta Crystallogr., Sect. D: Biol. Crystallogr.*, 2005, **61**, 1587–1593.

(22) J. L. Campos, *Personal Communication*.

(23) J. E. Gan, B. P. Tropea, D. L. Austin, D. S. Court, and X. J. Waugh, *Structure.*, 2005, **13**, 1435 –1442.

(24) H. M. Berman, W. K. Olson, D. L. Beveridge, J. Westbrook, A. Gelbin, T. Demeny, S.-H. Hsieh, A. R. Srinivasa, and B. Schneider, *Biophys. J.*, 1992, **63**, 751–759.

(25) X.-J. Lu and W. K. Olson, *Nucleic Acids Res.*, 2003, **31**, 5108–5121.

(26) X.-J. Lu and W. K. Olson, *Nat. Protoc.*, 2008, **8**, 1213–1227.

(27) G. Zheng, X.-J. Lu, and W. K. Olson, *Nucleic Acids Res.*, 2009, **37**, W240–W246.

(28) E. Barry, D. Beller, and Z. Dogic, *Soft Matter*, 2009, **5**, 2563–2570.

(29) S. Pieraccini, A. Ferrarini, K. Fuji, G. Gottarelli, S. Lena, K. Tsubaki, and G. P. Spada, *Chem.-Eur. J.*, 2006, **12**, 1121–1126.

(30) A. B. Harris, R. D. Kamien, and T. C. Lubensky, *Rev. Mod. Phys.*, 1999, **71**, 1745–1757.

(31) E. Grelet and S. Fraden, *Phys. Rev. Lett.*, 2003, **90**, 198302.

(32) G. Manning, *J. Chem. Phys.*, 1969, **5**, 924–933.

(33) G. J. Vroege and H. N. W. Lekkerkerker, *Rep. Prog. Phys.*, 1993, **55**, 1241–1309.

(34) L. Onsager, *Ann. N.Y. Acad. Sci.*, 1949, **51**, 627–659.

(35) H. N. W. Lekkerkerker, P. Coulon, and R. J. Van Der Haegen, *J. Chem. Phys.*, 1984, **28**, 1259–1265.

(36) S. Leikin, V. Parsegian, D. Rau, and R. P. Rand, *Ann.Rev.Phys. Chem.*, 1993, **44**, 369–395.

(37) G. Wong and L. Pollack, *Ann.Rev.Phys.Chem.*, 2010, **61**, 171–189.

(38) A. Lyubartsev and L. Nordenskiöld, *J. Phys. Chem.*, 1995, **99**, 10373–10382.

(39) W. C. Earnshaw and S. C. Harrison, *Nature*, 1977, **268**, 598–602.

(40) J. Parsons, *Phys. Rev. A*, 1979, **19**, 1225.

(41) S. Lee, *J. Chem. Phys.*, 1987, **87**, 4972.

(42) S. Lee, *J. Chem. Phys.*, 1988, **89**, 7036.

(43) T. Odijk, *Macromolecules*, 1986, **19**, 2313–2329.

(44) W. H. Press, B. P. Flannery, S. A. Teukolsky, and W. T. Vettering, *Numerical Recipes*, Cambridge University Press, Cambridge, 1986.

(45) N. Katsonis, E. Lacaze, and A. Ferrarini, *J. Mater. Chem.*, 2012, **22**, 7088–7097.

(46) S. Zhou, Y. A. Nastishin, M. M. Omelchenko, L. Tortora, V. G. Nazarenko, O. P. Boiko, T. Ostapenko, T. Hu, C. C. Almasan, S. N. Sprunt, J. T. Gleeson, and O. D. Lavrentovich, *Phys. Rev. Lett.*, 2012, **109**, 037801.

(47) P. J. Hagerman, *Ann. Rev. Biophys. Biophys. Chem.*, 1988, **17**, 265–286.

Part IV

Self assembly of porphyrin-peptide conjugates

PEPTIDES and porphyrins are excellent building blocks for the self-assembly of supramolecular nanoarchitectures [1–5]. Their conjugation appears promising for the design of new nanostructured materials for photo-electronic applications and chirality may play a role in controlling self-assembling. Porphyrins are not chiral, but is well known that they can be lead to chiral structures, not only by chiral substituents, but also by chiral seeds present in the environment or by physical agents [4]. Ionic porphyrins preferentially self-assemble in J-aggregates, characterised by a head-to-tail arrangement of the monomeric units, which exhibit a characteristic UV-Vis spectrum, with a bathochromic shift: In the presence of chiral seeds they exhibit also a specific Circular Dichroism (CD) signal [6]. The behaviour of non-ionic porphyrins has been less investigated. Also in this case the chemical nature and the size of the substituents are important, but the control of the aggregate structure is awkward and mixtures of different aggregates are often found [7].

We have studied the behaviour of conjugates between 5-(4′-carboxyphenyl)-10,15,20-triphenylporphyrin (TPP) and the peptide [Leu^{21}] Magainin (GIGKFLHSAKKFGKAFVGEIL NS) in water solutions. These systems have been synthesized and characterized in the group of Professor Gobbo (Università degli Studi di Padova). The behaviour of this system in aqueous solution suggested the formation of aggregates, which was then confirmed by UV-Vis spectroscopy and Dynamic Light Scattering. Very interesting results were obtained by Circular Dichroism (CD) measurements. To get insights into this behaviour we have performed Molecular Dynamics simulations using two different models, all atom (see Chapter 8) and coarse-grained (see Chapter 9). In the next Chapter 7, some concepts of CD that will be useful to introduce and the experimental results will be recalled and the the state of the art of the aggregation of porphyrins in solution will be summarized.

Chapter 7

Porphyrin-peptide conjugates

7.1 Circular dichroism

Circular dichroism (CD) is defined as the difference

$$\Delta A = A^L - A^R \tag{7.1}$$

where A^L and A^R are the absorbances of left and right circularly polarized light, respectively [8]. For historical reasons, CD is also measured as ellipticity Θ (in angular units), [1], related to ΔA by the following relation $\Theta(\text{mdeg}) = \Delta A 3298$. In analogy with Beer-Lambert law, one can define a molar quantity, called molar circular dichroism, as:

$$\Delta\epsilon = \epsilon^L - \epsilon^R = \frac{\Delta A}{cb} \tag{7.2}$$

where c is the concentration expressed in molL^{-1} and b is the path length expressed in cm. CD is different from zero only for chiral molecules or for molecules in a chiral environment, and the signal has opposite sign for enantiomers.

The intensity of CD is related to the rotational strength, $\mathcal{R}$, according to Rosenfeld equation [8]:

$$\mathcal{R}_{ba} = \text{Im}(\langle\Psi_a|\,\tilde{\mu}\,|\Psi_b\rangle \cdot \langle\Psi_b|\,\tilde{\text{m}}\,|\Psi_a\rangle) = \text{Im}(\boldsymbol{\mu}_{ba} \cdot \mathbf{m}_{ba}) \tag{7.3}$$

where Im means the imaginary part of the quantity in parentheses, $\tilde{\mu}$ is the electric dipole operator, $\tilde{\text{m}}$ is the magnetic dipole operator, Ψ_a and Ψ_b represent wavefunctions of the a and b states respectively, $\boldsymbol{\mu}_{ba}$ and $\mathbf{m}_{ba}$ are the electric dipole and magnetic dipole transition moment, respectively.

7.1.1 CD of dimers and aggregates

CD can be detected also for achiral chromophores arranged in a chiral way. Hence, when two, or more, chromophores are close in space and have a proper mutual orientation, the interaction between their transition dipoles is responsible for large rotational strengths and

---

[1] The ellipticity is defined as $\arctan(I_{minor}/I_{major})$, where I_{minor} and I_{major} are the light intensities measured through polarizers parallel to the minor and major axes of the optical ellipse.

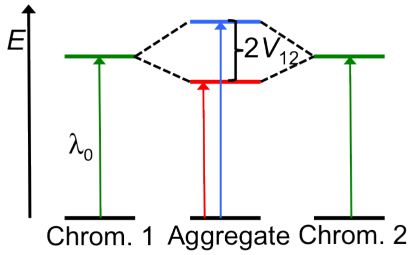

Figure 7.1: Splitting of two degenerate excited states of exciton-coupled chomophores.

the most significant contribution to CD arises when two (or more) chromophores with strong electric-dipole allowed transition couple to each other (exciton coupling) [9–11]. As a consequence of this coupling the two otherwise degenerate excited states of equal chromophores split into two levels separated by a quantity $2V_{12}$, called Davydov splitting (see Figure 7.1). The potential V_{12} for the interaction between electric transition dipoles cab be approximated in a Coulomb dipole-dipole form:

$$V_{12} = \frac{\mu_{ba(1)}\mu_{ba(2)}}{R_{12}^3}[\hat{\mathbf{u}}_1 \cdot \hat{\mathbf{u}}_2 - 3(\hat{\mathbf{u}}_1 \cdot \hat{\mathbf{u}}_{12})(\hat{\mathbf{u}}_2 \cdot \hat{\mathbf{u}}_{12})] \tag{7.4}$$

where $\mu_{ba(1)}$, $\mu_{ba(2)}$, R_{12} are the intensities and mutual distance of the two transition dipoles , $\hat{\mathbf{u}}_i$ are unit vectors parallel to the dipoles. The splitting of excited state reflects in a split or broadened absorption band, centered around the wavelength transition λ_0 of the isolated chromophore. A bisignate CD couplet is generated around λ_0 and allied with two opposite non-vanishing rotational strengths:

$$\mathcal{R}_{1,2} \propto \pm \mathbf{R}_{12} \cdot \boldsymbol{\mu}_{ba(1)} \wedge \boldsymbol{\mu}_{ba(2)} \tag{7.5}$$

where the ± signs refer to symmetric and antisymmetric linear combinations of the excited states of the two isolated chromophores. Therefore, the resulting CD couplet is determined by the expression:

$$\Delta\epsilon(\lambda) \propto \pm\Gamma(\lambda, \lambda_0)V_{12}\,\mathbf{r}_{12} \cdot \boldsymbol{\mu}_{ba(1)} \wedge \boldsymbol{\mu}_{ba(2)} \tag{7.6}$$

where Γ is a factor that takes into account the dispersive couplet line shape. CD depends only on the quadruple product $V_{12}\,\mathbf{R}_{12} \cdot \boldsymbol{\mu}_1 \wedge \boldsymbol{\mu}_2$, hence the CD couplet intensity is directly proportional to the fourth power of the transition dipole strength and inversely proportional to the square of the interchromophoric distance. This quantity is extremely sensitive to the relative geometry of the two chromophores. It will be zero if any two of the three vectors ($\boldsymbol{\mu}_{ba(1)}$, $\boldsymbol{\mu}_{ba(2)}$, $\mathbf{R}_{12}$) are parallel or if all three vectors lie in the same plane. The sign of the couplet is related to the mutual orientation of the transition dipoles through the vector product : Upon looking through the centers of the two dipoles, a positive sign is defined when a clockwise rotation by an acute angle brings the dipole in the front onto that in the back. Therefore, a right-handed configuration corresponds to a positive CD couplet and vice-versa.

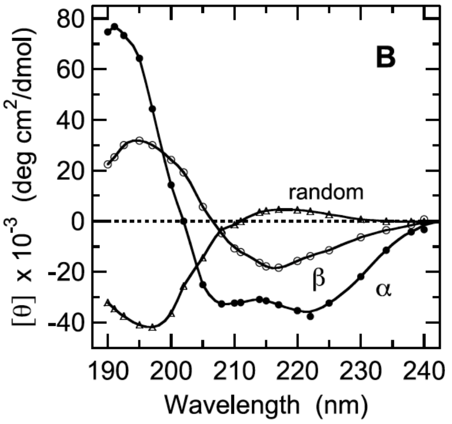

Figure 7.2: CD spectra of polylysine under conditions that cause the polypeptide to adopt α-helix (filled circles), β-sheet (open circles), or random coil (triangles) structures. Reproduced with permission from ref. [8]. Copyright 2009 Springer Publishing Company.

The measurement of the exciton couplet represents a sensitive method for determining the absolute sense of twist between electric transition moments of interacting chromophores and allows for nonempirical assignments of absolute configurations, provided there is no conformational ambiguity. The configurational analysis based on CD exciton coupling, known also as the exciton chirality method, has been applied to absolute configurational assignments of a wide variety of compounds.

7.1.2 Applications

CD is widely used to study biological systems, such as proteins, polypeptides and nucleic acids, and to investigate self-assembly and chiral molecules [8, 12]. Here. in particular, we will recall the main feature of CD of peptide and porphyrins which have been studied in this Thesis.

Circular dichroism of peptide

The CD of proteins between 190 and 230 nm arises primarily from coupled transitions of multiple peptide groups. CD is very sensitive to the secondary structure of polypeptides and proteins because the coupling depends strongly on the relative positions and orientations of peptide groups. The utility of circular dichroism (CD) in studying the conformation of polypeptides and proteins depends upon the possibility of correlating specific structures with characteristic CD spectra [12–15]. Distinctive spectra (see Figure 7.2) have been described for pure conformations such as the α-helix, β-sheets , β-turns, and also for the 'random' coil. A common application of CD is the measurement of the extent or the rate of protein folding and unfolding [16–19].

The α-helix is the dominant secondary structure in many proteins and has been extensively studied. The CD spectra of α-helices are characterized by a positive peak at 192 nm and two negative peaks near 205 and 222 nm. The magnitude of the CD signals does vary with variations in the helical geometry and has been concluded to depend on helix content.

The β-sheets are the second form of regular secondary structure and these may be parallel or antiparallel and of different length and widths. The general characteristics of β-sheets CD may be taken to be a negative band at about 215 nm and a positive band of comparable magnitude near 195 nm [13].

β-turn is known as the element of protein secondary structure, consisting of at most three residues, that approximately reverses the direction of the polypeptide chain. Approximately a quarter of the residues in globular proteins fall into this structural group. CD spectra of β-turn are characterized by a positive peak at 205 nm, a negative weak peak near 225 nm and a strong negative band between 180 nm and 190 nm.

In an attempt to avoid the somewhat misleading implications of the label “random coil”, Woody has coined the denomination “unordered conformation” [20]. However, when we refer to random coils, we are generally grouping the parts of the folded protein that do not fit into one of the previously discussed categories, which means that may be ordered structures included. The net CD of these parts of the protein has a strong negative CD signal just below 200 nm, a positive band at about 218 nm in many systems, and perhaps a very weak negative band at 235 nm.

Circular dichroism of porphyrins

CD has been used to characterize monoporphyrins and their aggregates. For example, CD spectra are used to detect the presence of chiral guests (with achiral monoporphyrin host) or for enantiomeric differentiation of chiral porphyrin hosts. In the case of two or more interacting porphyrins, the exciton chirality method can be used for absolute configurational assignments and for the determination of the geometry of chiral porphyrin assemblies.

It is known that porphyrins tend to exhibit $\pi - \pi$ stacking leading to stable dimers observed in solution and in crystal structures [21–24]. Several studies have been performed on dimers of porphyrins and metalloporphyrins linked with flexible chains containing a chiral substituent and their absolute configuration has been determined using the exciton chirality method [25]. It has been found that the CD spectra change a function of the length of the linker between the porphyrins [26]. Figure 7.3 (c) shows an example of CD spectrum obtained for bisporphyrin L-lysine derivative, where the two amino groups of $X(NH_2)$ and $Y(CH_2CH_2CH_2CH_2NH_2)$ moieties are derivatized by 5-(carboxyphenyl)-10,15,20-triphenylporphyrin (TPP) The negative CD couplet ($\lambda = 422$ nm, $\Delta\epsilon = -111$) is due to energetically favored intramolecular $\pi - \pi$ stacked conformations with negative twist [Figure 7.3 (b)].

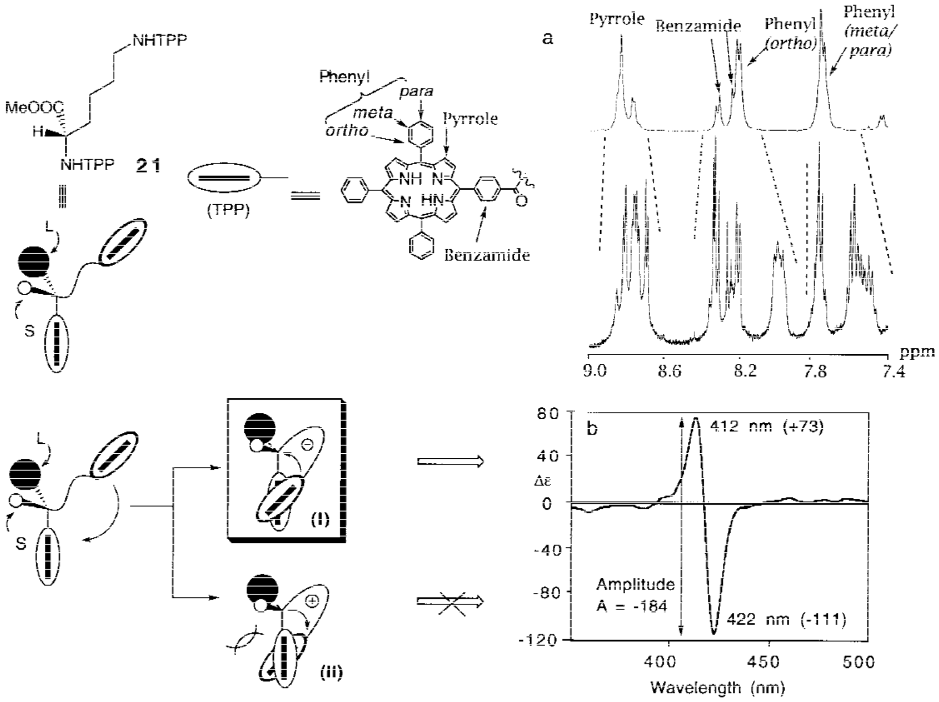

Figure 7.3: Bisporphyrin L-lysine derivative, **21**, in its sterically favored (I) and unfavorable (II) conformations. TPP= 5-(carboxyphenyl)-10,15,20-triphenylporphyrin. a: ^{1}H NMR of **21** in $CDCl_3$ (lower). b: CD spectrum in hexane. Reproduced with permission from ref. [25]. Copyright 2000 Wiley-Liss, Inc.

7.2 Aggregation of porphyrins in solution

Porphyrin aggregates can be dived into two significant groups with different aggregation behaviour: Ionic porphyrins with anionic or cationic peripheral group and non-ionic porphyrins that are water insoluble. The aggregates formed by ionic porphyrins depend of the strategy used to remove the electrostatic repulsion between the peripheral groups.

In general, there are two main arrangements: Face-to-face (*H*-) and end-to-end (*J*). In solution these exhibit distinct changes in the absorption band as compared to the monomeric species. J-aggregates exhibit a bathochromic shift, i.e., a change of spectral band position to a longer wavelength in the absorption, reflectance, transmittance, or emission spectrum . H-aggregates exhibit a blue-shift in the spectrum. As explained in subsection 7.1.1, the excitonic state of the dye aggregate splits into two levels through the interaction of transition dipoles. A transition to the upper state in H aggregates having parallel transition moments and to a lower state in head-to-tail arrangement (J aggregate) with perpendicular transition moments leads to blue and red shifts, respectively [27].

Most studies deal with anionic porphyrins and metalloporphyrin assemblies. A remarkable example of chiral aggregates is given by TPPS (tetrakis-sulfonium porphyrin) which have been studied by different research group. TPPS is able to self-assemble into J-aggregates, depending on the concentration, pH and ionic strength of its solution. Within these aggregates,

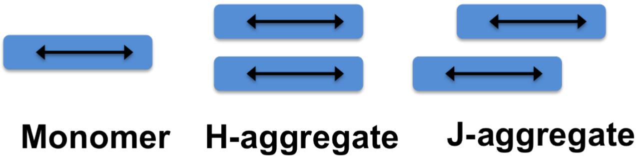

Figure 7.4: Schematic structure of different kinds of porphyrin aggregates.

porphyrins are staked head-to-tail and are stabilized by electrostatic, hydrogen-bonding, and dispersive interactions, and a variety of interesting structural features have been described, going from nano- up to microsized rod [28–30], nanotubes [31–33] and fractal clusters [34–38]. Purrello and co-workers have studied supramolecular chiral memory in porphyrin assemblies, in particular they focused on achiral tetra-cationic (H_2T_4 and its planar metallo derivatives, MeT_4) and tetra-anionic porphyrins (H_2TPPS) shown in Figure 7.5. Their aggregates in pure water do not exhibit a CD signal in the region of absorbance of the porphyrins [39–41]. However, addition of CuT_4 and H_2TTPS to an aqueous solution containing a chiral templane (such as an amino acid or covalent/noncovalent amino acid polymers, like poly-L or D-glutamate or phenylalanine) leads to chiral assemblies. Figure 7.5 shows an example of CD spectra obtained in the presence of L- and D- phenylalanine [42]. These ternary supramolecular species are remarkably stable, which allows them to "memorize" the chiral information imprinted by the templane and to retain it even if the matrix is "disrupted" by pH-induced conformational transitions or the amino acid is removed.

The aggregation type for non-ionic porphyrins seems to be a function of the nature and size of their peripheral substituents, and in this case the control of the formation of a particular aggregate is complex, since mixtures of different aggregate types are often found [43]. Non-ionic porphyrins can arrange in J aggregates similar to those found by anionic porphyrins in water solutions, such as TPPS [44].

In literature there are only few examples of conjugates of apolar porphyrins and the results are difficult to understand and strongly dependent on the substituent of the porphryin. In these studies, the substituent is usually an aminoacid or an alkyl chain or a glucosylated steroid, and CD spectra were obtained by changing substitutuents and solvent composition. Venanzi and co-workers have studied two glocosylated steroid-modified porphyrins with various ring substitutions, Figure 7.6 shows an example of FBMGSP and FBDSGPFigure 7.7 shows their CD spectra for different solvent composition of water and dimethylsiloxane (DMSO). Significant differences can be detected, which suggest a different morphologies for the aggregates.

7.3 Porphyrin-peptide conjugates studied in this thesis

In this Thesis, we have studied the aggregation of porphyrin conjugate made of [Leu^{21}]Magainin (MAG) linked to TPP trough an amide group, which will be called TPP-MAG (see Figure 7.8

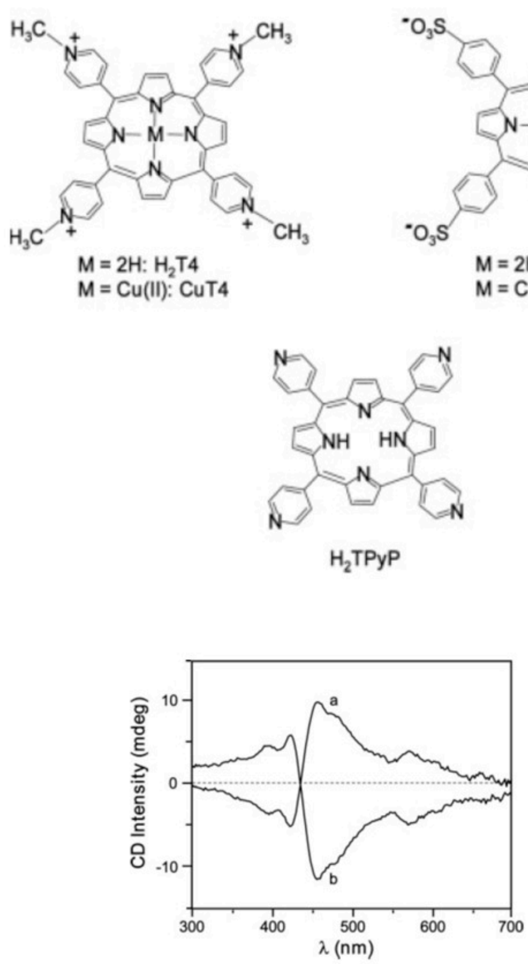

Figure 7.5: Top: Schematic structure of H_2T_4, CuT_4, H_2TPPS, CuTPPS, H_2TPyP. Reproduced with permission from ref. [42]. Copyright 2007 Wiley-Liss, Inc. Bottom: CD spectra of aqueous solutions of CuT4 (2 μM) and H2TPPS (2 μM) in the presence of (a) l-phenylalanine (8 μM) and (b) D-phenylalanine (8 μM). Reproduced with permission from ref. [42]. Copyright 2007 Wiley-Liss, Inc.

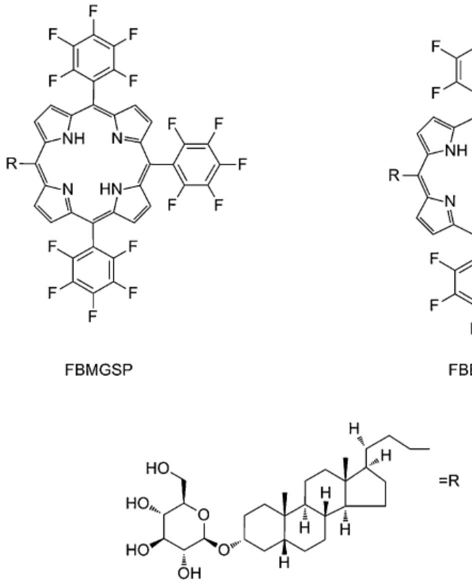

Figure 7.6: Chemical structure of FBDGS and FBMGSP. Reproduced with permission from ref. [45]. Copyright 2012 Royal Society of Chemistry.

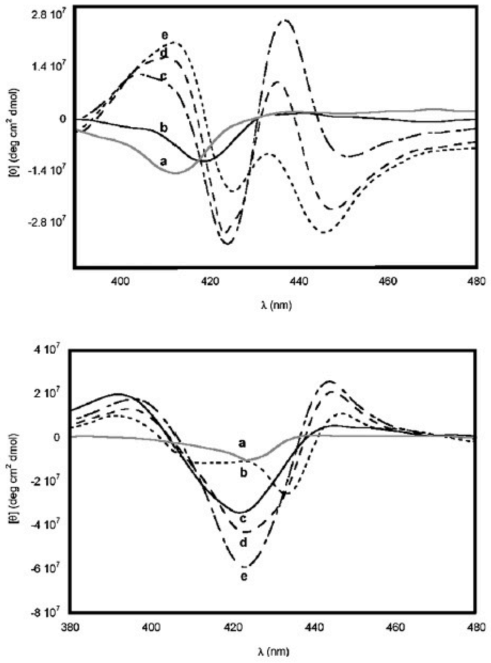

Figure 7.7: CD spectra of FBDGS (top) and FBMGSP (bottom) in water-dimethylsiloxane (DMSO) mixture. Reproduced with permission from ref. [45]. Copyright 2012 Royal Society of Chemistry.

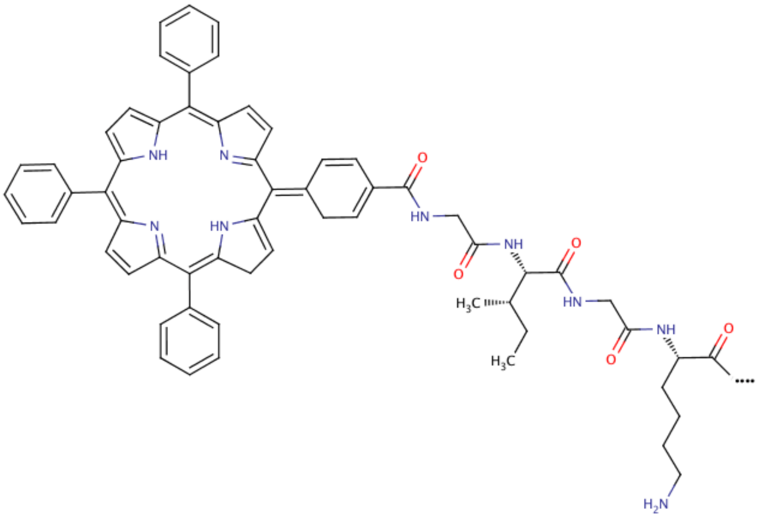

Figure 7.8: Structure of the N-terminal end of the porphyrin-peptide conjugate (TPP-MAG).

and Table 7.1).MAG is an amphipatic polypeptide and Figure 7.9 shows the helical wheel [2] representation of MAG [46]: Hydrophobic aminoacids are mainly located on one side and hydrophilic aminoacids on the other.

TPP-MAG has been synthesized and characterized in the group of Professor Marina Gobbo (Università degli Studi di Padova). Figure 7.10 (a) shows UV-Vis spectra obtained for different water/methanol mixtures. A severe broadening and a strong hypochromic effect of the Soret band can be clearly observed (Figure 7.10). The red shifted UV-Vis absorption suggests the formation of J-type aggregates. The formation of aggregates has then been confirmed by Dynamic Light Scattering measurements. The CD spectrum of the peptide (Figure 7.11 (a)) indicates a conformational change from random coil to helical structure upon conjugation (see subsection 7.1.2). The CD spectrum in the porphyrin region of the conjugate shows a typical and strong Cotton effect, which disappears on moving from water to organic solvent, suggesting the formation of ordered chiral aggregates. This kind of Cotton effect is observed when two porphyrins are close to each other in a chiral environment or when they self-assemble in a chiral structure. The sign of the Cotton effect (see Figure 7.11 (b)) suggests a preferential right-handed *twist* between porphyrins [25]. The origin of this behaviour is unknown, as unknown is the role of the peptide: The experimental findings do not allow us to discriminate between different mechanisms, like simple pairing of porphyrins driven by the side chains or formation of higher order aggregates; also unknown is the reason for the mutual chiral arrangement of porphyrins. To get insight in this behaviour, we have performed molecular dynamics simulation on TPP-MAG and in addition on TPP-GIGKF (see Table 7.1)

---

[2] It is a type of visual representation used to illustrate alpha helices.

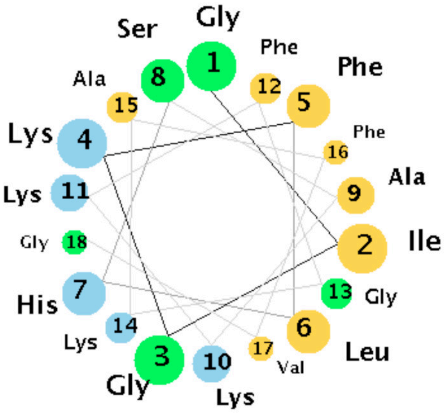

Figure 7.9: Helical wheel representation of MAG [46]. The amino acid side chains are projected down the alpha axis, orthogonal to the paper plane. As an ideal alpha helix consists of 3.6 residues per complete turn, the angle between two residues is chosen to be 100 degrees and thus there exists a periodicity after five turns and 18 residues. Colors refer to different types of aminoacids. Yellow: Non polar. Green: Polar or uncharged. Blue: Basic.

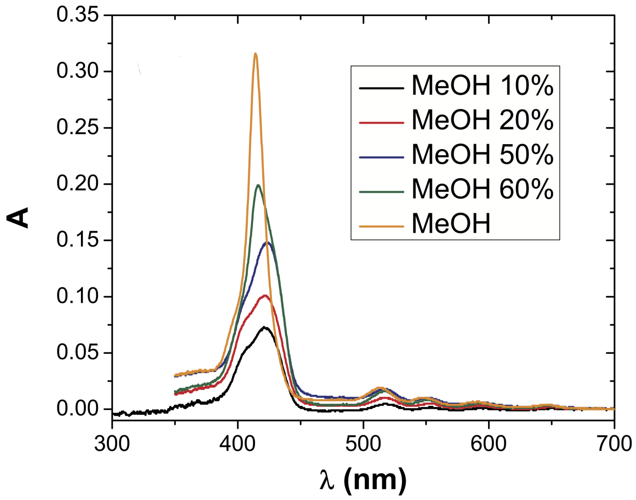

Figure 7.10: UV-Vis spectra of TPP-MAG obtained for water/methanol mixtures of different composition (% volume).

Acronym	Peptide sequence
TPP-MAG	GIGKFLHSAKKFGKAFVGEILNS
TPP-GIGKF	GIGKF

Table 7.1: Peptide sequence of the conjugates investigated in this Thesis.

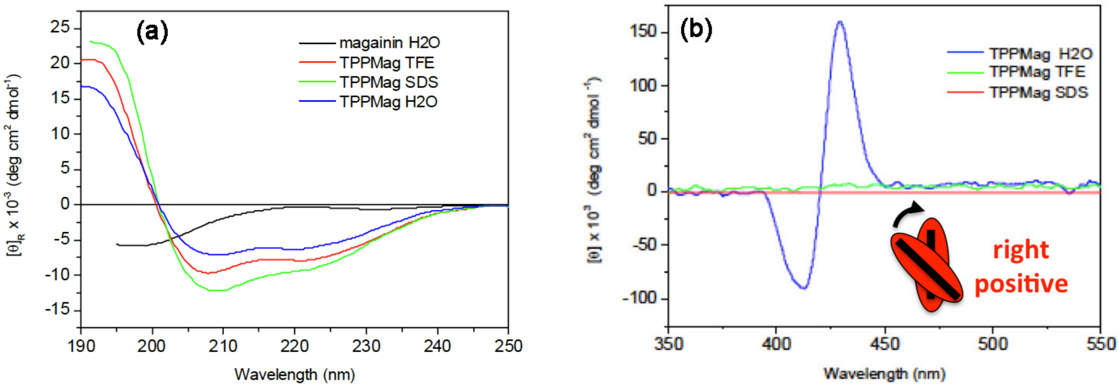

Figure 7.11: CD spectra of TPP-MAG in the peptide (a) and in the porphyrin region (b) detected in water and organic solvents (2,2,2-trifluoroethanol, TFE, and sodium dodecyl sulfate, SDS). The cartoon refers to the definition of the sign of the Cotton effect.

7.3.1 Methods

We performed Molecular Dynamics (MD) simulations (see Appendix B for details) using two different models: All Atom (AA) and Coarse-Grained (CG). Simulations of single conjugates in explicit and implicit solvent were carried out to study the interaction between porphyrin and peptide. Then extensive studies of aggregates of the conjugates were performed. The details of the systems and the results will be described in the Chapters 8 (AA) and 9 (CG). To analyse the trajectories, we used standard tools available in the software packages. In addition we developed home-made codes, to extract from trajectories information on the chirality of the systems. In particular, suitable quantities, defined in the following, were identified to characterize the chiral and structural properties of aggregates.

As a first chiral descriptor, we used the twist angle (τ) between a pair of adjacent porphyrins. We define a local frame of reference (LOC frame) with the origin in the center of mass of porphyrin, the XY plane equal to the average porphyrin plane and the X-axis parallel to the line connecting the center of mass with the carbonyl carbon of the amide (see Figure 7.12). The twist angle is the smaller angle between the directions of the X-axes of adjacent porphyrins. The sign is positive for a clockwise rotation, and negative for anti-clockwise rotation. $0^\circ < \tau < 90^\circ$ and $0^\circ > \tau > -90^\circ$ correspond to a right-handed (R) and to a left-handed (L) arrangement, respectively (see Figure 7.13). This is the same convention adopted in the chirality exciton method.

Another chiral descriptor (Y) is defined as

$$Y = \sum_{i}^{N-1} \frac{\boldsymbol{\mu}_{ba(i)}\boldsymbol{\mu}_{ba(i+1)}}{R^3_{ii+1}} \left[\hat{\mathbf{u}}_i \cdot \hat{\mathbf{u}}_{i+1} - 3(\hat{\mathbf{u}}_i \cdot \hat{\mathbf{u}}_{ii+1})(\hat{\mathbf{u}}_{i+1} \cdot \hat{\mathbf{u}}_{ii+1})\right] \mathbf{R}_{ii+1} \cdot \boldsymbol{\mu}_{ba(i)} \wedge \boldsymbol{\mu}_{ba(i+1)} \tag{7.7}$$

where i and $i+1$ are adjacent porphyrins, and the sum runs over all possible pairs of adjacent porphyrins ($N-1$). This descriptor is closely related to the observable in CD experiments, eq. (7.6).

An important structural feature is the orientation of a peptide chain with respect to the

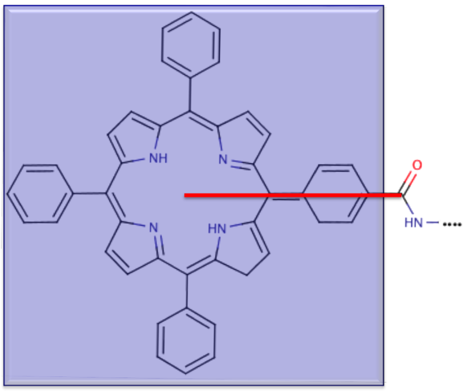

Figure 7.12: Definition of the twist angle (τ).

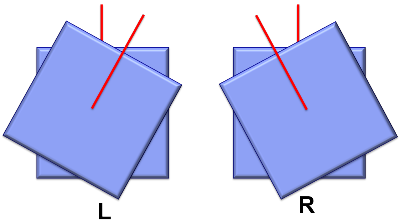

Figure 7.13: Definition of left (L) and right (R) twist.

porphyrin to which it is linked. To define the orientation of the peptide, a vector **c** is used, which connects the C_α of the first isoleucine to the C_α of the second phenylalanine. The orientation of this vector is specified by two polar angles (θ, ϕ) in the LOC frame (see Figure 7.14).

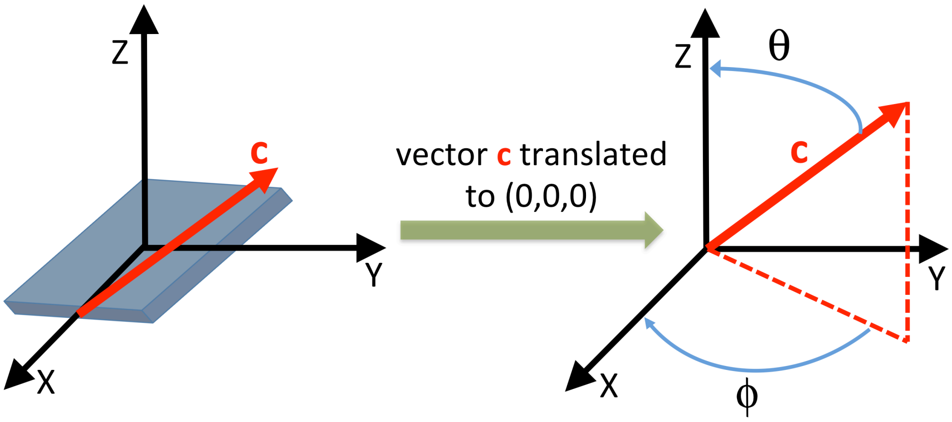

Figure 7.14: Definition of the angles, θ and ϕ, that specify the orientation of the vector **c** (parallel to the peptide chain) in the LOC frame (XYZ). The blue plate represents the porphyrin plane.

Chapter 8

Porphyrin-peptide conjugates: All Atom simulations

In this Chapter, we present the computational details and the results obtained by all atom (AA) simulations of aggregates of TPP-MAG and TPP-GIGKF.

8.1 Computational details

MD simulations were performed with AMBER force fields (see below) for the peptide chains reported in Table 7.1 and complemented with force field parameters derived for the porphyrin in [47] and the link between the porphyrin [48] and the polypeptide (a methylamide group) and with DFT calculations to parameterize the atomic charges of the porphryin and the linker. Both explicit and implicit solve were used.

8.1.1 Charge derivation

We use the RESP procedure, which is part of the AMBER10 package [49], to derive atomic charges. Calculations were performed for a fragment consisting of TPP and the methylamide group (Figure 8.1). Atomic coordinates of the the fragment were obtained by geometry optimization using the DFT method, with B3LYP functional and 6-31G** basis set [50]. RESP atomic charges were evaluated by fitting of the electrostatic potential, calculated by DFT at the B3LYP 6-31G** level. Following the approach proposed in the original RESP paper by Cornell et al. [51], we carried out RESP fits in two stages. In the first stage all atoms were allowed to vary and then in the second one all equivalent hydrogen atoms were constrained to have equal charge and refit.

8.1.2 Explicit solvent

Molecular dynamics simulations were performed with AMBER FF03 force field [52]. The choice of the water model may be crucial to study the solvation and to compare the results with experimental data. We took into account the following features: (i) the computational

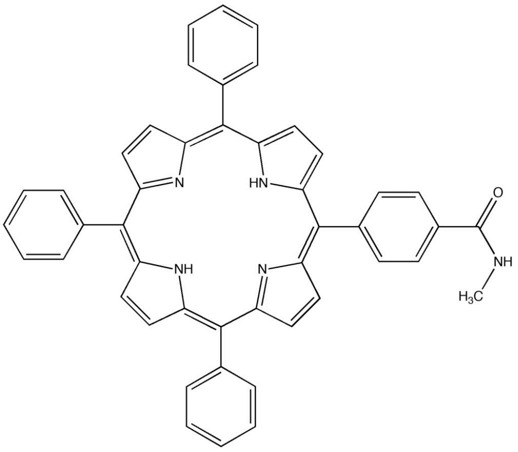

Figure 8.1: Fragment consisting of TPP linked to methylamide group.

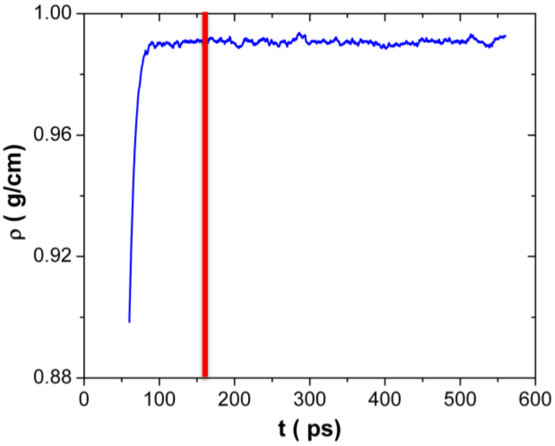

Figure 8.2: Density of the sample ρ along the trajectory during pre-equilibration of TPP-MAG in explicit water. The red line shows the configuration selected to start the equilibration run in the NVT ensemble.

cost (for example, the TIP5P model [53] is very good, but is 2.5 times more expensive than TIP3P [54] in terms of simulation time [55]); (ii) a good description of bulk properties of liquid water at 298 K; (iii) literature data on the use of the model in combination with the adopted force field. We focused on three site water models and we decided for TIP3P. Therefore, the structure was soaked in a TIP3P water octahedral box with a margin of 14 Å (75.434, 75.434, 75.434 Å) and was then neutralized by adding counterions (4 Cl^-) [54]. Periodic boundary conditions (PBC) were used. The cut-off distance for non-bonded interactions was 12 Å. Both for preparative rounds and production run, bond constraints were applied to bonds involving H atoms using the SHAKE algorithm [56]. Electrostatic long range interactions were evaluated with the particle-mesh Ewald method (PME) [57] with a cubic spline approximation, a tolerance of 10^{-5} and a grid of size 90. Temperature of the entire system was regulated by Langevin thermostat with the collision frequence $\gamma = 2.0\ \mathrm{ps}^{-1}$ [58]. The time step was set to 1 fs for minimisitation and heating, instead for equilibration and production runs the time step was set to 2 fs.

We performed a miminization of 5000 steps: We used for the first 2500 steps the steepest descent algorithm and for the last steps the conjugate gradient algorithm. Then we heated the system up over 60 ps from 1 K to 310 K. We performed a pre-equilbration run of 500 ps in the NPT ensemble. Pressure of the system was controlled by the Berendsen barostat [59] with time constant $\tau_P = 4$ps and compressibility equal to $4.6 \cdot 10^{-5}$ bar^{-1}. Figure 8.2 shows the density of the system along the trajectory during pre-equilibration. We calculated the average density of the system $\langle \rho_{\mathrm{NPT}} \rangle$ without considering the first 100 ps. From the trajectory, we extracted a snapshot where the density was near to the average value. This was used as the starting configuration for the subsequent constant volume simulation (NVT) [60].

8.1.3 Implicit solvent

Implicit models tend to be orders of magnitude faster for large simulations, hence they can be very useful to simulate aggregates. Our MD simulations were performed with AMBER ff96 force field [61] and solvent model ig5 (OBC) [62] because it is the best overall force field/solvatation pairs [63]. We used both analytical linearized Poisson-Boltzmann approximation and Generalized Born solvation models for the monomers. For simulation of aggregates, we used analytical linearized Poisson-Boltzmann approximation. The length of the trajectories varies with system under investigation (see below). The other parameters of the simulation are the same described in subsection 8.1.2.

8.2 Results and analysis

We performed both single-molecule simulations and simulations of aggregates of different lengths. The first were carried out both in explicit and in implicit solvent , the latter only in implicit solvent. In particular, we focused on dimers, trimers and tetramers of TPP-MAG and pentamer and decamer of TPP-GIGKF. To analyse our simulations of aggregates, we used different tools.

8.2.1 Simulations of single TPP-MAG

The length of trajectories is 10 ns in explicit solvent and 50 ns in implicit solvent. In both cases, the starting configuration was taken with the peptide in either extended or helical conformation. Figure 8.3 shows snapshots obtained in explicit and implicit solvent. Similar results were obtained in both cases. Irrespective of the starting configuration, we found a general trend: The peptide chain folds on the porphyrin platform into a helical conformation, stabilised by properly positioned phenylalanine side chains. The peptide exhibits the analogous behaviour to that observed when it is bound to the surface of a membrane [64].

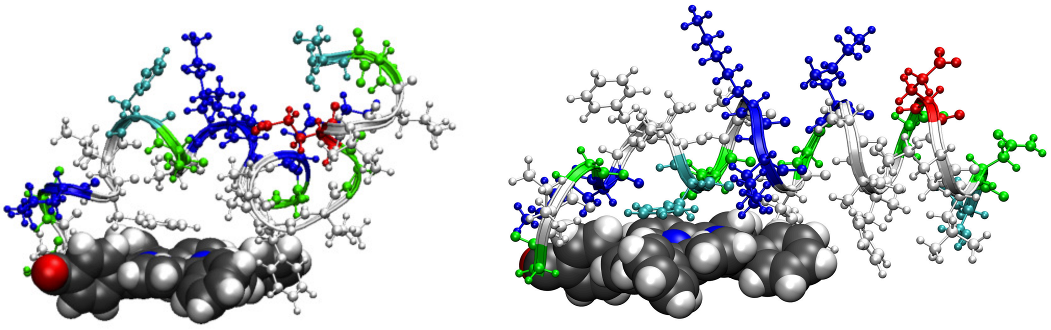

Figure 8.3: Final snapshots from the simulations of TPP-MAG in explicit (left) and implicit solvent (right). Colors code amino acid properties. White: Non polar. Green: Polar. Red : Acidic. Blue: Basic.

8.2.2 Simulations of TPP-MAG aggregates (complete peptide chain)

MD simulations of dimers and trimers from different initial conformations of the chain were carried out: Helical (H), globular (G) and extended (E). Using implicit solvent, we cannot use periodic boundary conditions and due to the cut-off of interactions, if the distance between the conjugates under investigation is larger than the cut-off distance, there is the possibility that the molecules separate each other. To prevent this situation which would separation of porphyrin, we used two different kinds of approach:

I we put the porphyrins at certain relative distance (usually equal to half length of the peptide) and we constrained the atomic coordinates of the nitrogen atoms inside porphyrin;

II we restraint the distance between the centres of mass of the porphyrins; this distance is gradually reduced and the restrains are step by step released. The restraint is a well with a square bottom with parabolic sides out to a defined distance, and then linear sides beyond that.

III we stack the porphyrins close each other with different twist angles of the porphyrins without using any constraints or restraints

We imposed both constrains (I) and restraints (II) during heating and equilibration, in this way the conjugates are close each other and these can interact. In approach II, during equilibration we slowly relaxed the constraints and then we run simulations. For dimers we used approaches I and II. For trimers, the starting configuration was characterized by different twist angles between the porphyrins (called *a*,*b*,*c*,*d*) and we used approach type II where in this case the restraints are imposed between the first and the third molecule and approach III. Table 8.1 summarizes the different simulations (A,B,C,D) we carried out for dimers and trimers.

Figure 8.4 show the final snapshots of simulations of dimers. Depending of the starting structure and the approach used during equilibration, the final structure changes. However,

Aggregate	A	B	C	D
Dimer	I-G	I-E	II-H	II-E
Trimer	II-E*a*	II-E*b*	III-E*c*	II-E*d*

Table 8.1: Summary of simulations. The first letter (I, II, III) refers to the approach used. The second letter G, E and H refers to the chain conformation (globular, extended and helical). The letters *a*, *b*, *c* and *d* refer to different twist angles between porphyrins.

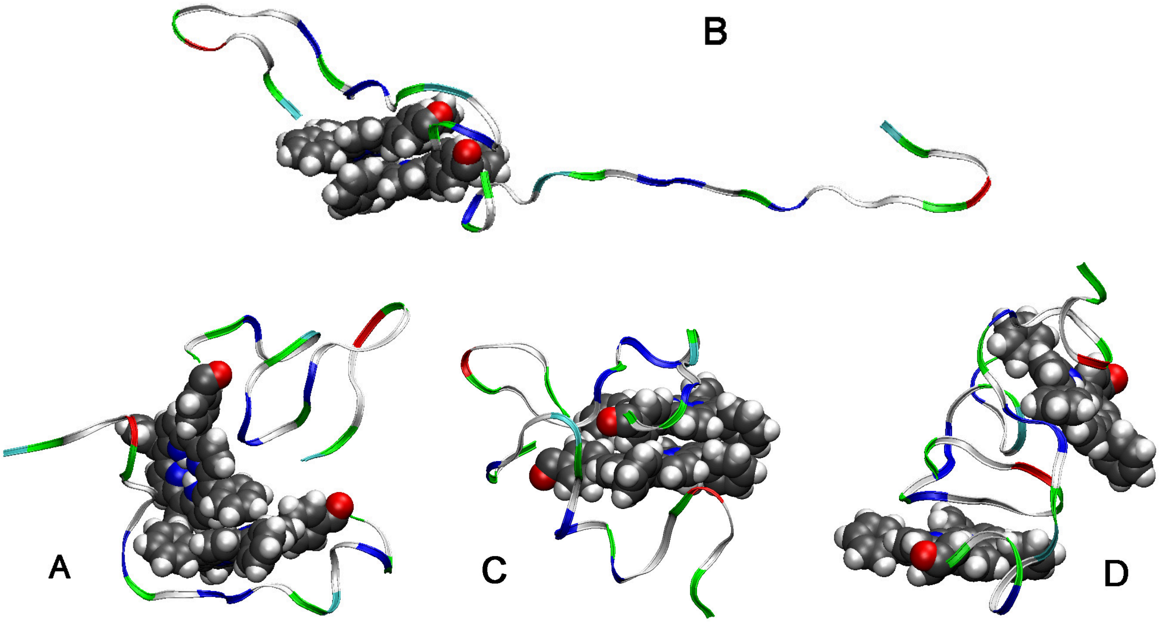

Figure 8.4: Final snapshots from simulations of TPP-MAG dimers in implicit solvent. Colors code amino acid properties. White: Non polar. Green: Polar. Red : Acidic. Blue: Basic.

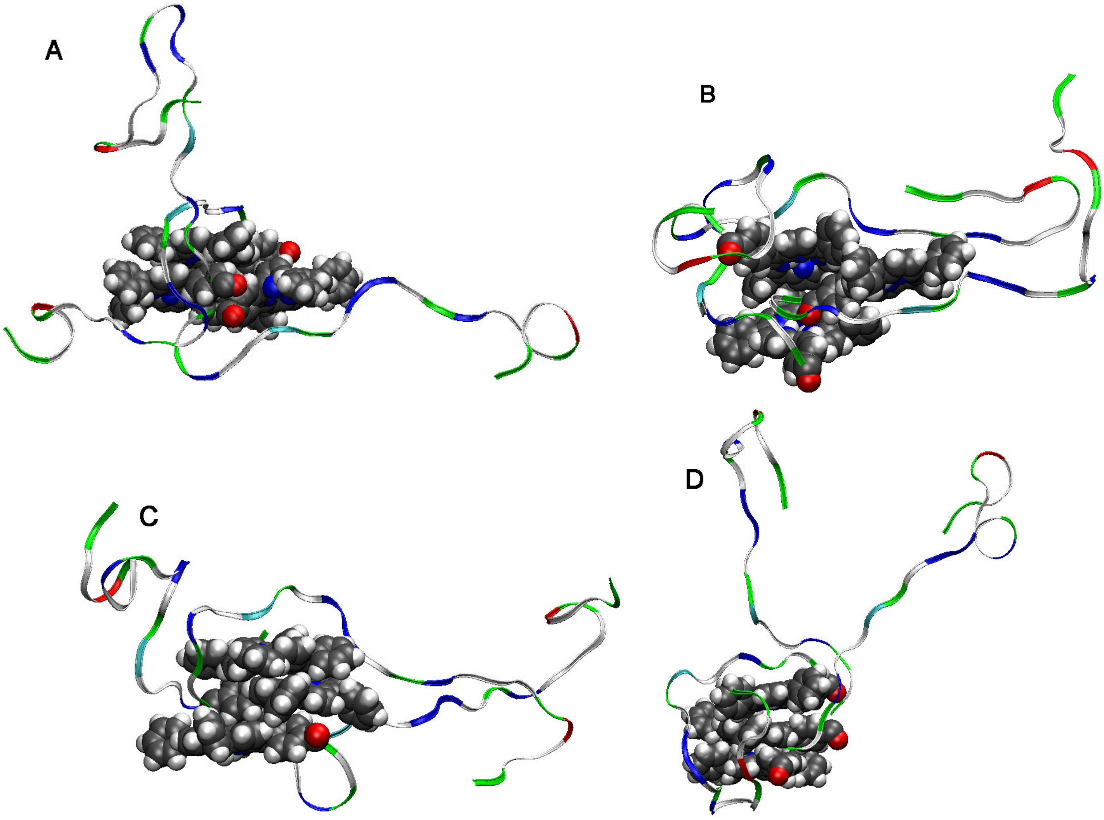

Figure 8.5: Final snapshots from the simulations of TPP-MAG trimers in implicit solvent. Colors code amino acid properties. White: Non polar. Green: Polar. Red : Acidic. Blue: Basic.

there is a tendency of the porphyrins to interact each other. By analysis of the trajectories using energy criteria, two important and competitive aspects for the self-assembly of the porphyrins arise: Porphyrin stacking and equilibration of peptide chain.

Figure 8.5 shows the final snapshot of the trajectories of trimers. The porphyrins in the aggregate are not perfectly stacked, but they are slightly shifted one relative to other. The peptide chains tend to interact with each other, but also the hydrophobic aminoacids strongly interact with the porphyrins to try to excluded them from water.

Using the available tools in AMBER which analysed the different contributions to potential energy, in particular we focused on three terms: (i) porphyrin-porphyrin interaction, (ii) peptide-peptide interaction, (iii) porphyrin-peptide interaction. We found that they are very close each other, hence there is a competition between them.

8.2.3 Simulations of TPP-GIGKF aggregates

The dynamics of the aggregate is very slow and the structures are trapped in local minima, therefore the final structure was found to depend on the starting configuration. However, there were indications of face-to-face interactions between the porphyrins and the interactions between hydrophobic groups seemed to be important. For this reason we decided to run simulations of aggregates with a shorter peptide (GIGKF). Simulations with different initial

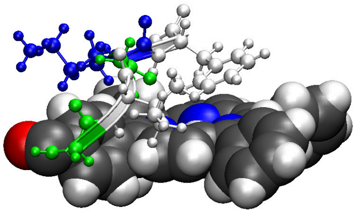

Figure 8.6: Final snapshot from simulation of a single TPP-GIGKF in implicit solvent. Colors code amino acid properties. White: non polar. Green: Polar. Red : Acidic. Blue: Basic.

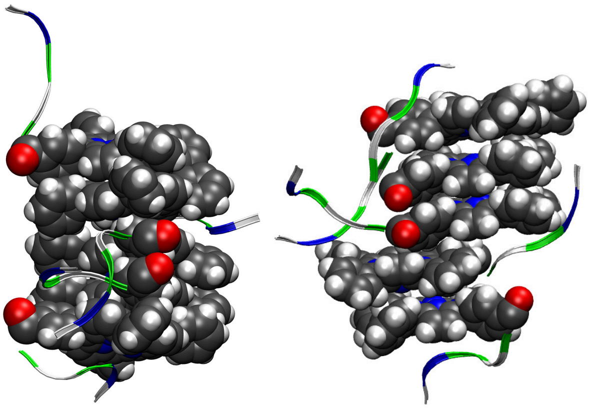

Figure 8.7: Final snapshots from trajectories of pentamers of TPP-GIGKF in implicit solvent. Simulations started from different pentamer configurations: Right-handed (left) and left-handed(right).

configurations (i.e. different twist angles) were run; the length of trajectories is around 25 ns. We built a aggregates of porphyrins stacked each other with different twist angles. In this subsection, we will focused on the results obtained for pentamers and decamers.

As starting, we performed simulations of monomer, and we found the same trend obtained with the complete chain: The phenylalanine interacts with the porphyrin, hence the chain is folded on the porphyin (see Figure 8.6).

Pentamers

We performed MD simulations of two aggregates starting with right-handed and left-handed twist between the porphyrins. Figure 8.7 shows the snapshots of the two trajectories. Figures 8.9, 8.10, 8.11, 8.12, 8.13 and 8.14 show the dihedral angle χ_1, χ_2, ϕ_1, ψ_1, ϕ_2, and ψ_2 (see Figure 8.8 for their definition) respectively, for the central porphyrin (Molecule 3) of both aggregates. We found similar distributions for the other conjugates inside the aggregates. The dihedral angles do not change significantly along both trajectories and no signficants different between the two trajectories were observed to explain the experimental preference of right-handed aggregates in water solution.

Figures 8.15 and 8.16 show the the twist angle for each adjacent pairs of the aggregates along the trajectory. We can observed the global handedness of the aggregate does not change along the trajectory, in other words the porprhyins cannot easily rotate along the trajectory.

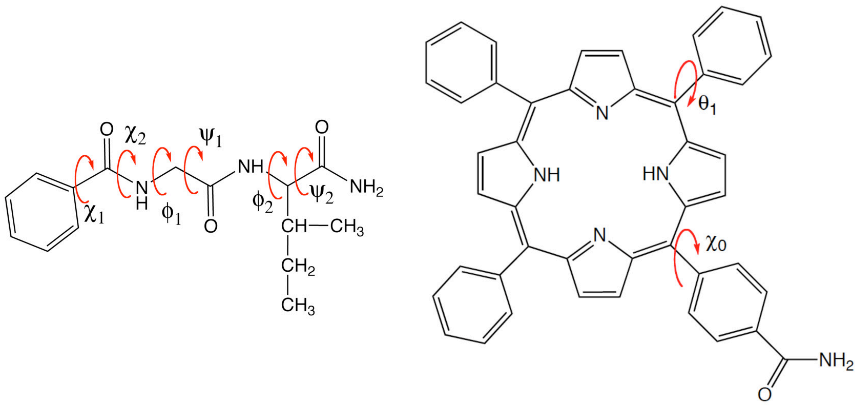

Figure 8.8: Labeling of dihedral angles in the porphyrin (right) and in the N-terminal end of TPP-MAG (left).

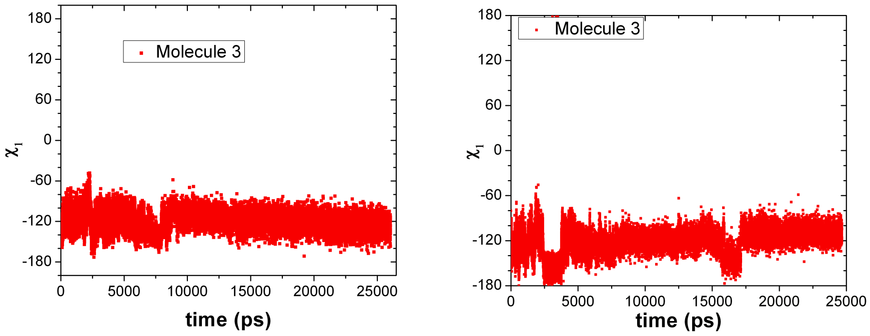

Figure 8.9: Dihedral angle χ_1 for the central conjugate of a pentamer, along trajectories starting from a right-handed (left) and a left-handed configuration (right).

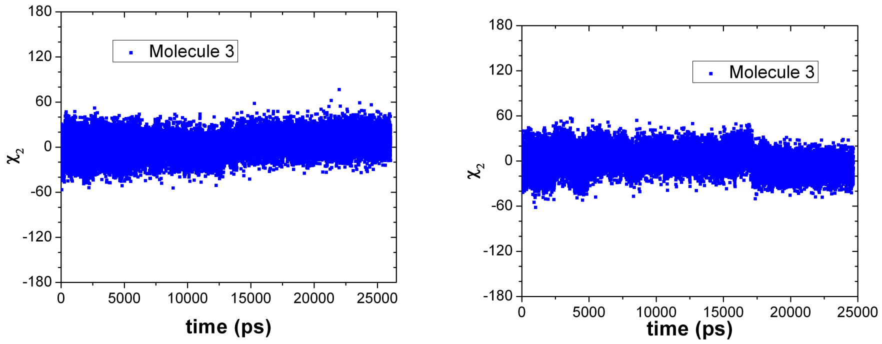

Figure 8.10: Dihedral angle $\chi_2$for the central conjugate of a pentamer, along trajectories starting from a right-handed (left) and a left-handed configuration (right).

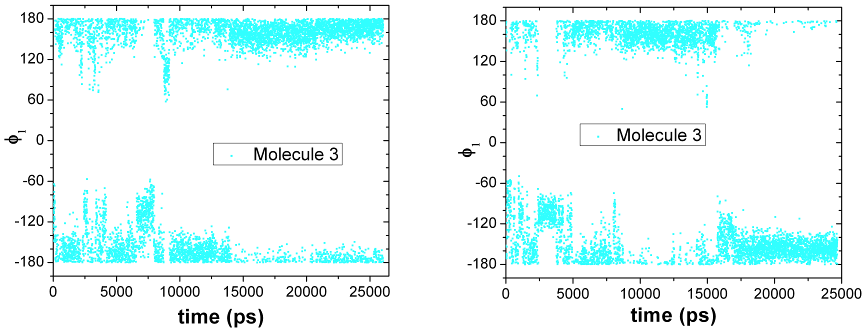

Figure 8.11: Dihedral angle ϕ_2 for the central conjugate of a pentamer, along trajectories starting from a right-handed (left) and a left-handed configuration (right).

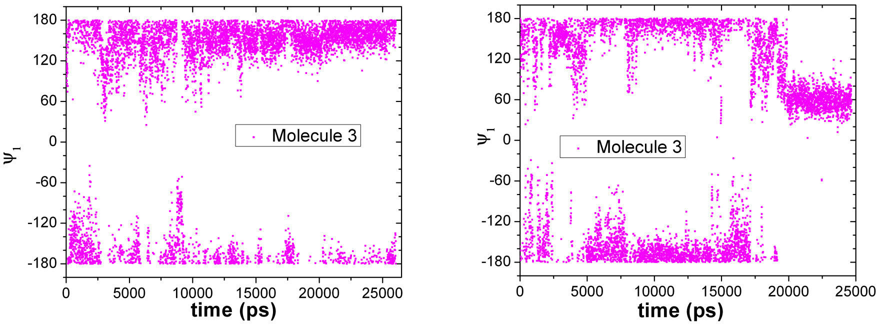

Figure 8.12: Dihedral angle ψ_1 for the central conjugate of a pentamer, along trajectories starting from a right-handed (left) and a left-handed configuration (right).

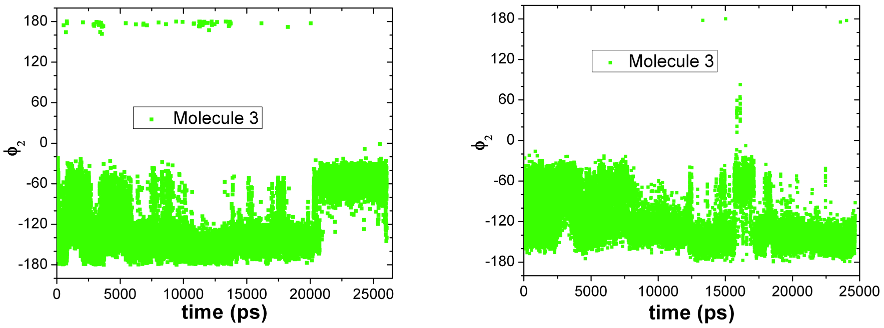

Figure 8.13: Dihedral angle ϕ_2 for the central conjugate of a pentamer, along trajectories starting from a right-handed (left) and a left-handed configuration (right).

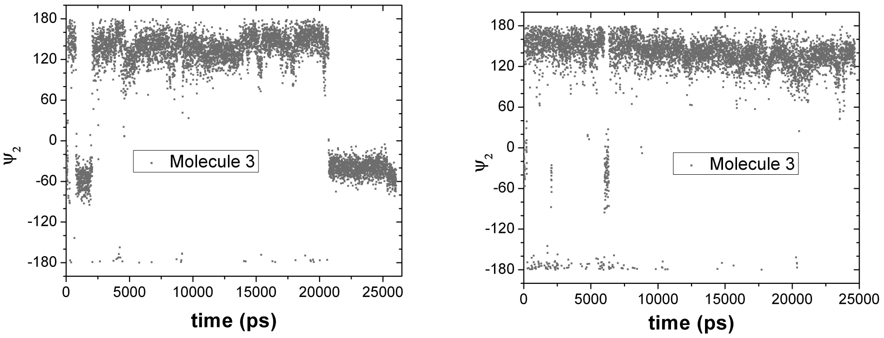

Figure 8.14: Dihedral angle ψ_2 for the central conjugate of a pentamer, along trajectories starting from a right-handed (left) and a left-handed configuration (right).

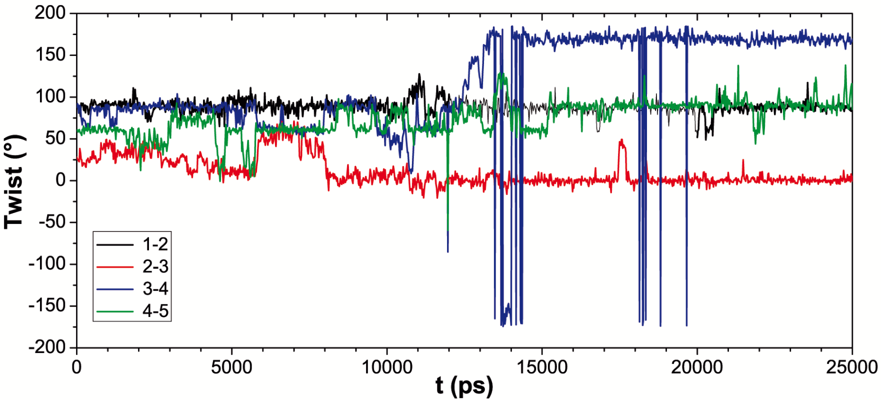

Figure 8.15: Twist angle, τ, between adjacent porphyrins of a pentamer, along a trajectory starting from a right-handed configuration.

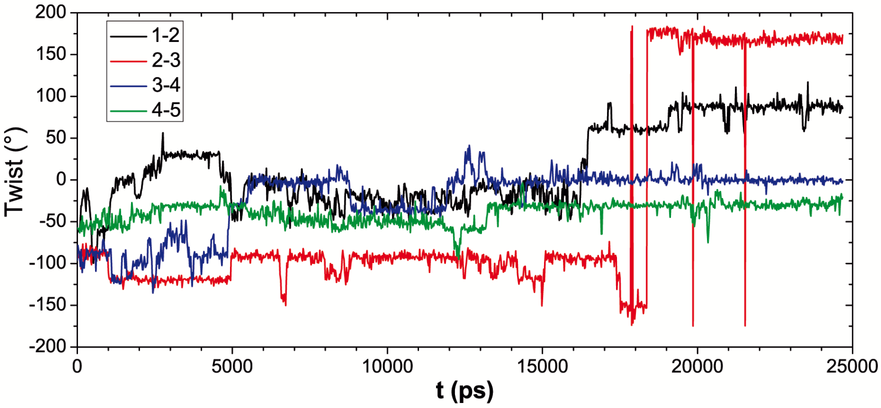

Figure 8.16: Twist angle, τ, between adjacent porphyrins of a pentamer, along a trajectory starting from a left-handed configuration.

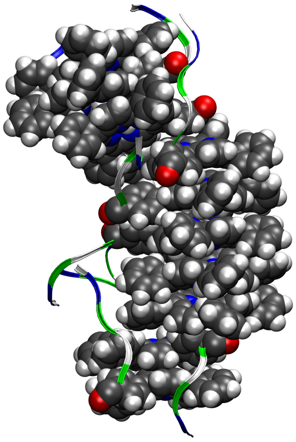

Figure 8.17: Final snapshots from trajectories of a decamer of TPP-GIGKF in implicit solvent. Simulations started from right-handed configuration.

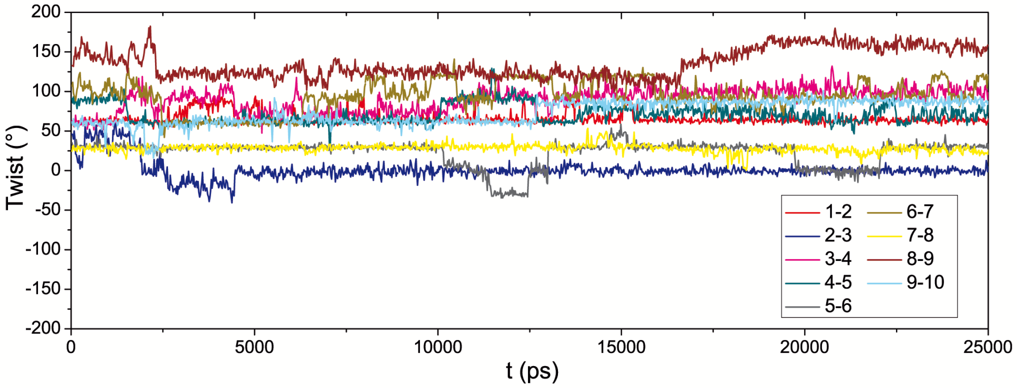

Figure 8.18: Twist angle, τ, between adjacent porphyrins of a decamer, along a trajectory starting from a right-handed configuration.

Therefore, using this strategy, we are not able to sample in a good way the conformational space and the final results strongly depend on the starting conditions and the procedure adopted.

Decamers

We performed MD simulations of two aggregates with opposite starting handedness. We found the same trend obtained for pentamers. In the following we considered only the decamer starting with right-handed twist between adjacent porphyrins. Figure 8.17 shows the final snapshot of the trajectory: The porphyrins tend to shift and form shorter aggregates that do not interact and are linked each other thank to the chain. Figures 8.18 show the the twist angle as function of the time of trajectory. The twist angles do not change along the trajectory and the global handedness of the aggregate does not change, as we found for the pentamers.

8.3 Conclusions

Simulations of a single TPP-MAG in water show that the peptide chain folds on porphyrin, interacting with it through its hydrophobic amino acids and exposing to solvent the polar ones. In the presence of two or more conjugates, there are also face-to-face interactions between porphyrins. Both kinds of interactions contribute to the stabilization of aggregates. However, the time scale of atomistic simulations was found to be insufficient to fully characterize the behaviour of TPP-MAG and TPP-GIGKF in water. The final structure of the aggregates was found to depend on the starting configuration and no clear preferential arrangement could be inferred.

Chapter 9

Porphyrin-peptide conjugates: Coarse-grained simulations

In this Chapter, we introduce the MARTINI force field and we describe the procedure adopted to define the parameters for the porphyrin conjugate. Then, we present and discuss the results of Molecular Dynamics simulations of aggregates of porphyrin-peptide conjugates based on the MARTINI force field.

9.1 Martini Force Field

MARTINI is a *coarse-grained (CG) force field* for simulations of biomolecules, which has been developed by Marrink and coworkers [65]. It was originally developed for lipids, and then has been extended to proteins [66], fullerenes [67], carbohydrates [68] and polystyrene [69].

9.1.1 Model

The MARTINI model is based on a four-to-one mapping, [65], i.e. four heavy atoms are represented by a single interaction site *bead*, with the exception of ring-like fragments. In the model there are four main types of interaction sites: Polar (P), nonpolar (N), apolar (C) and charged (Q). Each of them has a number of subtypes, which allow for a more accurate representation of the chemical nature of the underlying atomic structure. Within a main type, subtypes are distinguished either by a letter denoting the hydrogen-bonding capabilities (d=donor, a= acceptor, da= both, 0 = none) or by a number indicating the degree of polarity (from 1, low polarity, to 5, high polarity).

In general, four *bonded interactions* are considered. Bonds are described by a weak harmonic potential, $V_{bond}(R)$, acting between a pair of beads (*i*,*j*):

$$V_{bond}(R_{ij}) = \frac{1}{2}K_{bond}(R_{ij} - R_{bond})^2 \tag{9.1}$$

with an equilibrium distance $R_{bond} = \sigma = 0.47$ nm and a force constant equal to K_{bond}. A weak harmonic potential on the angles (θ_{ijk}) defined by triplets of adjacent beads (i, j, k) is

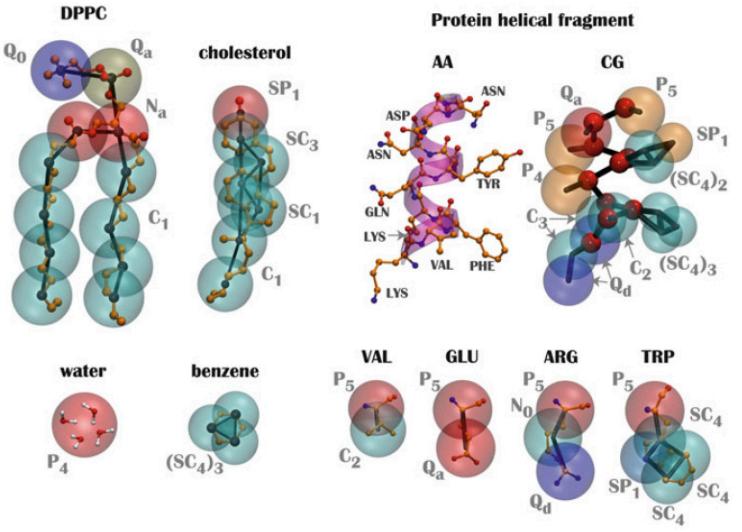

Figure 9.1: Martini model for DPPC, cholesterol, water, benzene, a protein helical fragment and a few amino acids (valine, glutamic acid, arginine, and tryptophan). Reproduced with permission from ref. [70]. Copyright 2013 Springer Publishing Company.

introduced to account for the chain stiffness:

$$V_{angle}(\theta_{ijk}) = \frac{1}{2}K_{angle}\left(\cos\theta_{ijk} - \cos\theta_0\right)^2 \tag{9.2}$$

where K_{angle} and θ_0 are the force constant and equilibrium angle, respectively. A proper potential is used for the dihedrals (ϕ_{ijkl}) between the planes containing the (i,j,k) and (j,k,l) triplets of adjacent beads

$$V_d(\phi_{ijkl}) = K_d[1 + \cos(\phi_{ijkl} - \phi_d)] \tag{9.3}$$

where ϕ_d is the equilibrium angle and K_d is the force constant. An improper dihedral angle potential is used for some geometries, to prevent out of plane distortions:

$$V_{id}(\phi) = K_{id}(\phi_{ijkl} - \phi_{id})^2 \tag{9.4}$$

where $\phi ijkl$ denotes the dihedral between the planes defined by the (i,j,k) and (j,k,l) beads, ϕ_{id} is the equilibrium angle and K_{id} is the force constant .

In order to preserve the geometry of small *ring compounds*, 2 or 3 to 1 mapping of ring atoms onto CG beads is used. This is a special bead type, labeled labelled as "S" [65]. For ring particles the effective interaction size and strength are smaller than for normal beads. Bonds and angles can be replaced by an appropriate set of constraints, to preserve the rigidity of the rings and to avoid fast oscillations arising from very high force constants.

A Lennard-Jones (LJ) 12-6 potential energy function is used to describe the *nonbonded interaction* between a pair of particles (i,j):

$$V_{LJ}(r_{ij}) = 4\epsilon_{ij}\left[\left(\frac{\sigma_{ij}}{r_{ij}}\right)^{12} - \left(\frac{\sigma_{ij}}{r_{ij}}\right)^{6}\right] \tag{9.5}$$

where r_{ij} is the inter-particle distance, σ_{ij} represents the distance at which the potential vanishes and ϵ_{ij} is the depth of the potential well. A constant effective size, $\sigma = 0.47$ nm, is assumed, with only a few exceptions. For charged (Q-type) and the most apolar types (C_1 and C_2), the range of repulsion is extended by setting $\sigma = 0.62$ nm. LJ interactions are absent between bonded particles and within rings, but are present between second nearest neighbours.

Charged groups (type Q) bear full charges (q_i) interacting via a Coulombic potential energy function:

$$U_{el}(r_{ij}) = \frac{q_i q_j}{4\pi\epsilon_0\epsilon_r r_{ij}} \tag{9.6}$$

with relative dielectric constant $\epsilon_r = 15$ for explicit screening. The nonbonded potential energy functions are used in their shifted form, in which both energy and force vanish at the cut-off distance r_{cut} = 1.2 nm. The LJ potential is shifted from $r_{shift} = 0.9$ nm to r_{cut}. The electrostatic potential is shifted from $r_{shift} = 0.0$ nm to r_{cut}.

In MARTINI a CG model is used also for the solvent Four water molecules are represented as a single bead of type P_4. The dynamics is determined by the masses to the CG beads. For reasons of computational efficiency, standard masses m = 72 amu are typically used for all beads, with the exception of those in rings, for which the m=45 amu [70].

9.1.2 Extensions of MARTINI model to protein

Monticelli and co-workers extended the MARTINI model to proteins [66]. Apolar amino acids (Leu, Pro, Ile, Val, Cys and Met) are represented by C-type beads, polar uncharged amino acids (Thr, Ser, Asn and Gln) by P-type beads, and amino acids with small negatively charged side chains (Glu and Asp) by Q-type beads. The positively charged amino acids Arg and Lys are modelled by a combination of a Q-type and an uncharged beads. The bulkier ring-based chains are modelled by three (His, Phe and Tyr) or four (Trp) beads of S-type. The Gly and Ala residues are only represented by backbone beads. Backbone parameters are independent on the kind of residue, but depend on the secondary structure of he peptide (or protein), and cannot change during a simulation. Backbone-backbone-side chain and backbone-side chain-side chain bond angles and force constants are independent of both secondary structure and kind of amino acid. Figure 9.2 summarizes the MARTINI representation of amino acids.

9.1.3 Coarse Graining recipe

To define the MARTINI parameters of a new system, Marrink and coworkers proposed a three-step recipe [70].

Step 1. Mapping of AA structure onto CG representation The first step consists of dividing the molecular system into small chemical building blocks, using a 4-1 or 2-1 mapping.The mapping of CG bead types to chemical building blocks subsequently serves a guide toward the assignment of CG particle types. Because most molecules cannot be entirely mapped onto

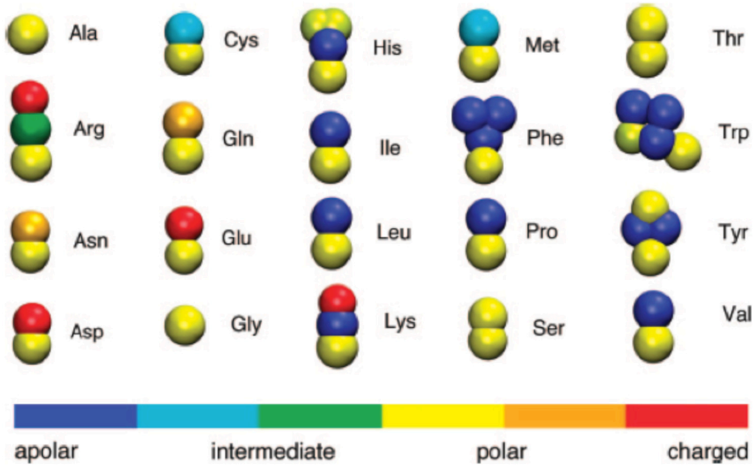

Figure 9.2: MARTINI representation of amino acids. Colors represent different bead types. Reprinted with permission from [66]. Copyright 2008 American Chemical Society.

groups of four heavy atoms, however, some groups will represent a smaller or larger number of atoms. To model compounds containing rings, a more fine grained mapping procedure can be used. In those case, the special class of S-particle is appropriate.

Step 2. Selecting bonded interactions For most molecules the use of a standard bond length and force constant of $K_{bond} = 1250\,\mathrm{kJ\,mol^{-1}\,nm^2}$. seems to work well, but for ring structures much smaller bond lengths are required. For rigid rings, the harmonic bond and angle potentials are better replaced by a constraint [66, 71]. For linear chainlike molecules, a standard force constant of $K_{angle} = 25\,\mathrm{kJ\,mol^{-1}\,nm^2}$ with an equilibrium bond angle $\theta_0 = 180°$ is the best initial choice. For complex molecules multiple ways exist for defining the bonded interactions. Not all of the possible ways are likely to be stable with the preferred time step of 30-40 fs.

Step 3. Optimization A powerful way to improve the model is by comparison to AA level simulations. Structural comparison is especially useful for optimization of the bonded interactions. The angle distribution function for a CG triplet can be directly compared to the distribution function obtained from the AA simulations of the centres of mass of the corresponding atoms. The optimal value for the equilibrium angle and force constant can be extracted. Comparison of thermodynamic behaviour is a crucial test for the assignment of particle types. The balance of forces determining the partitioning behaviour can be very subtle: the partitioning free energy is directly obtained from the equilibrium densities of CG particles in the water and organic solvent). The comparison to AA simulations and experimental data should be the deciding factor in choosing parameters.

9.2 Parametrization of force field for the porphyrin

9.2.1 Atomistic simulations

We performed all-atom (AA) simulation of the TPP-GIGKF conjugate in water using the same FF and explicit water described in Chapter 8. The length of the trajectory was 500 ns.

9.2.2 Coarse-Grained simulations

The optimization of bonded interactions was based on the comparison between AA and CG simulations. The temperature (300 K) and pressure (1bar) in atomistic and CG systems were identical. In CG simulations, a cutoff of 1.2 nm was used in the calculation of nonbonded interactions. A time step of 30 fs was used, and the neighbor list for nonbonded interactions was updated every 200 fs. These conditions is the standard one used in the parametrization of MARTINI. Simulations in the NPT ensemble were carried out with Berendsen thermostat ($\tau_T = 1$) and Berendsen pressure coupling ($\tau_P = 4$).

The parametrization of nonbonded interaction was based on the determination of octanol/water partition coefficient. We calculated the octanol/water partition coefficient using thermodynamics integration. The thermodynamic integration is a way to calculate free energy difference between two states A and B of a system from MD simulations as the work necessary to change the system from A to B over a reversible path. The thermodynamic integration (TI) formula [72–74] is:

$$\Delta F_{AB} = \int_{\lambda_A}^{\lambda_B} \left\langle \frac{\partial H(\lambda)}{\partial \lambda} \right\rangle_{\lambda'} d\lambda' \tag{9.7}$$

where H, the Hamiltonian, is made a function of a coupling parameter λ: $\lambda = 0$ for coupled system and $\lambda = 1$ for uncoupled system. One approach to solve eq. (9.7) is to evaluate the ensemble average at a number of discrete λ-points by performing separate simulation for each chosen λ-point. The integral can then be determined numerically.

Using this method, we can calculate the solvation free energy and from the calculated solvation free energy, the partition coefficient $\log P$ was evaluated according the following relation [75]:

$$\log P = -0.434 \frac{\Delta F_{\text{solv wat/oct}}}{RT} \tag{9.8}$$

where $\Delta F_{\text{solv wat/oct}}$ is the change in free energy passing from a low dielectric solvent (octanol) to water, R is the gas constant, T is the absolute temperature.

A stochastic integrator [76] was used to integrate the equations of motion in this study. The integrator was used to prevent an accumulation of translational and rotational kinetic energy in the compound being mutated as it became uncoupled from the rest of the system. The simulations were carried out at a constant temperature of 300 K by means of the stochastic velocity rescale thermostat by Bussi et al. [77] (0.1 ps relaxation time, with porphyrin and water coupled separately) and a constant pressure of 1 bar by means of the Parrinello-Rahman barostat [78].

We equilibrated an octanol box and than we equilibrate the system for 200 ns. We also equilibrate the system in water for 200 ns. The transformations during the free energy calculations from an interacting ($\lambda = 0$) to a non interacting molecule ($\lambda = 1$) were performed using a minimum of 16 λ points. The number of λ-points were increased near the minimum of the derivative. We started to collect the data after 20 ps. We integrated numerically the curves, $dH/d\lambda$ as, using trapezoidal rule to obtain solvation free energy.

All atomistic and coarse-grained simulations were performed using GROMACS MD package.

9.2.3 Mapping

Figure 9.3 shows the MARTINI model proposed for TPP covalently linked to glycine.

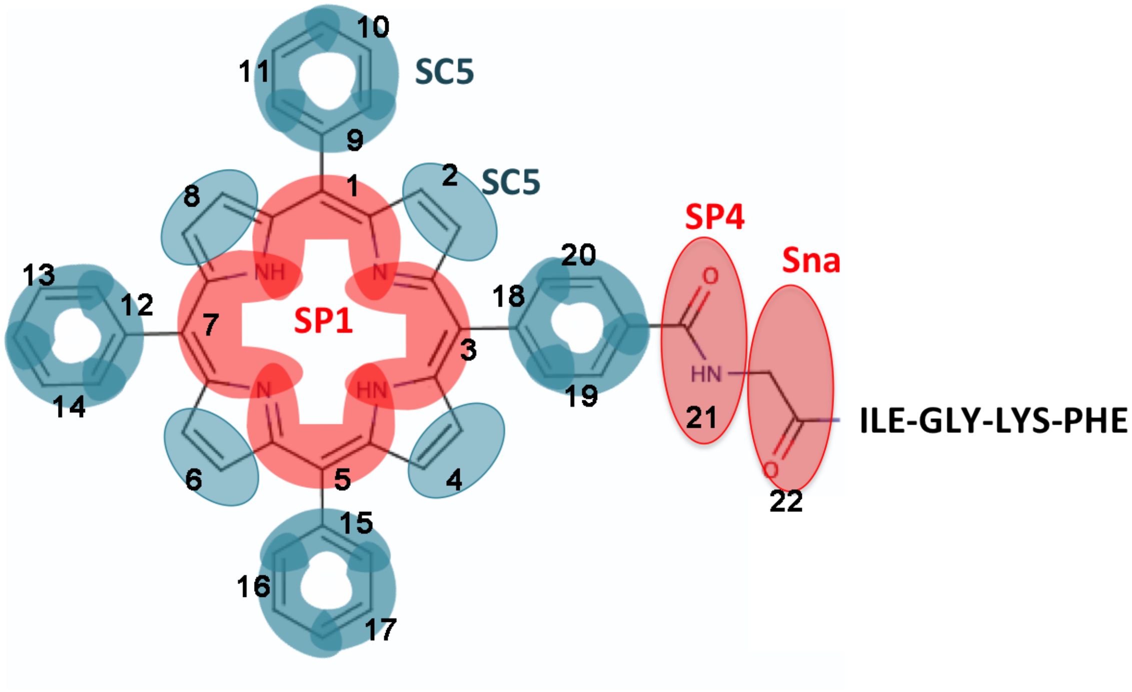

Figure 9.3: MARTINI model of TPP covalently linked to glycine.

9.2.4 Nonbondend interaction: Partition coefficient

We calculated the *n*octanol/water partition coefficient of meso tethahydroxyphenylporphyrin (see Figure 9.4). We decided to study this porphyrin, because experimental data are reported in literature ($\log P = 4.8$) [79, 80]. To perform calculations, we changed 4 beads of the phenyl from SC5 to SP1 to take in account the presence of hydroxy group.

Figure 9.5 shows the derivative $dH/d\lambda$ as a function of λ. We can observe a minimum at $\lambda = 0.5$ for both curves. Integrating numerically the curves, we can obtain the solvation free energy in water ($\Delta F_{wat} = 246.02 \pm 0.06$) and octanol ($\Delta F_{oct} = 278.69 \pm 0.05$). Using

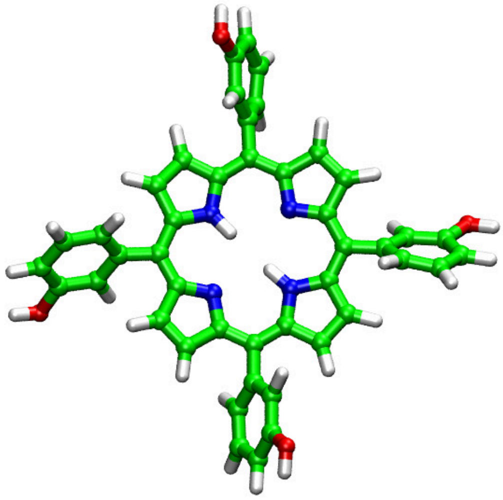

Figure 9.4: Chemical structure of meso tethahydroxyphenylporphyrin.

eq. (9.8), the calculated water/octanol partition function $\log P$ is equal to 5.69 ± 0.01. $\Delta F = (-32.67 \pm 0.08)$ J and $\log P = 5.69 \pm 0.01$

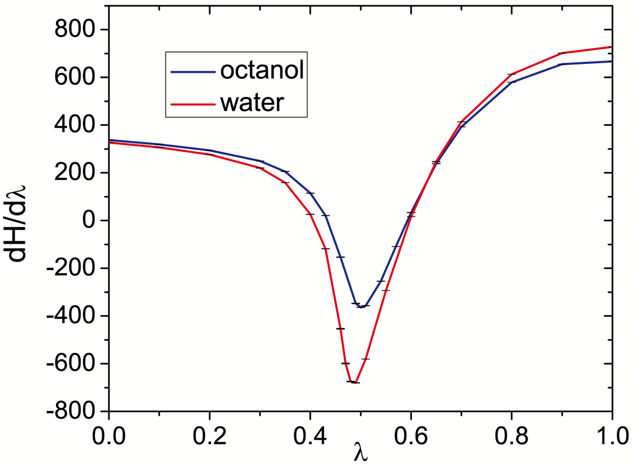

Figure 9.5: Derivate, $dH/d\lambda$ as a function of coupled parameter λ obtained in water and octanol.

9.2.5 Bonded interactions

We have used distributions of distances, angles and dihedral from atomistic simulation to parametrize the bonded interactions. We converted the AA trajectory into the corresponding CG trajectory. This is the trajectory of centers of mass (COMs) of groups of atoms, according to the mapping. From the CG trajectory, we extracted the distributions of the bond lengths, bond angles, and dihedral angles between COMs. We chose appropriate equilibrium lengths and angles, corresponding to the average distance and angle between COMs. The force constants were chosen to reproduce the width of the distributions. In our model, only some torsional angles have been introduced. In MARTINI spirit, we constrained the bonds of the phenyl groups and we introduced elastic network between the beads 1-5 and 3-7.

Figure 9.6 shows some representative examples of the distance, angle and dihedral distributions obtained by AA trajectory converted into COMs one and CG trajectory. The matching between CG distance, angle and proper and improper dihedral is good.

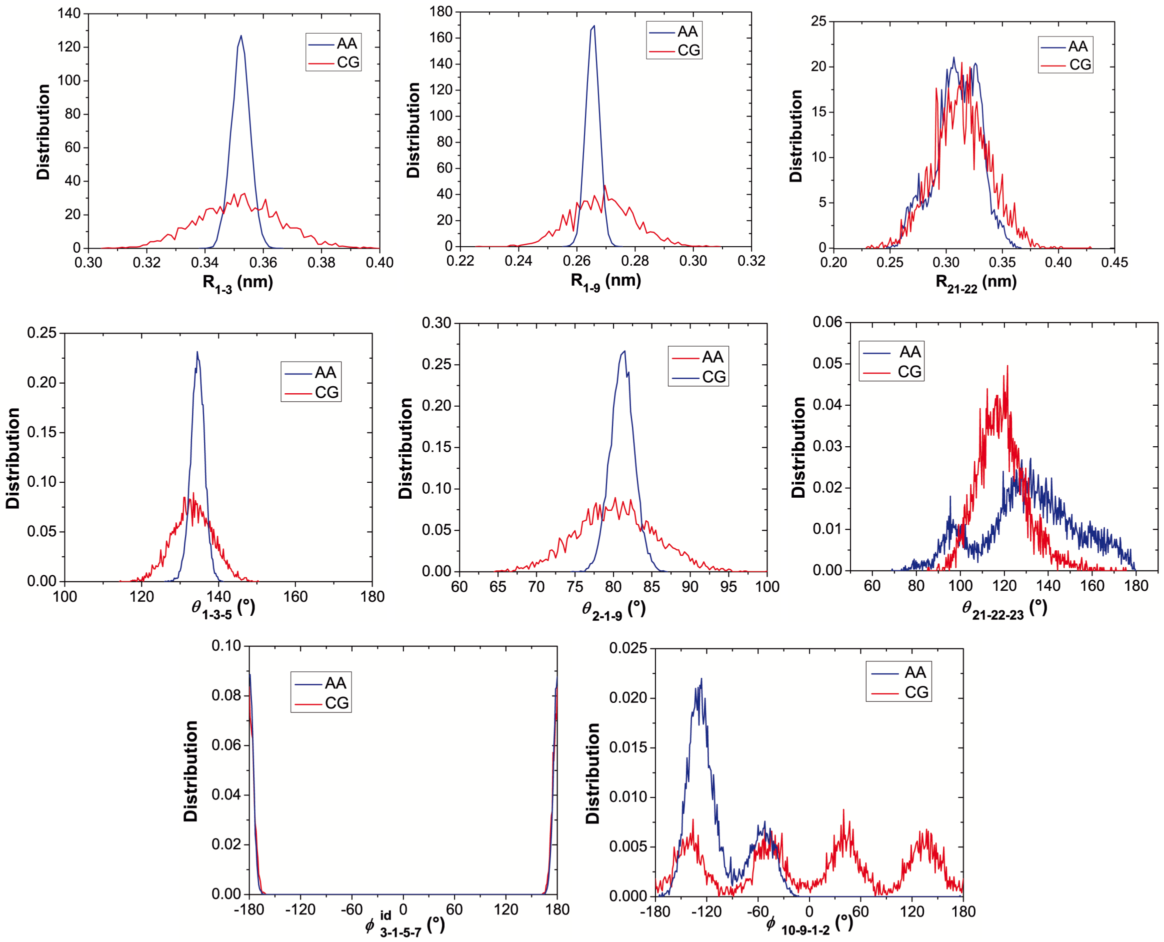

Figure 9.6: Distribution of bonded interactions obtained from CG and AA simulation of TPP-GIGKF mapped to CG. Top: Bonded distance (R). Middle: Bond angles (θ). Bottom: Proper (ϕ) and improper (ϕ^{id}) dihedrals.

9.3 Results and discussion

9.3.1 Computational details

In CG simulations, a cutoff of 1.2 nm was used in the calculation of nonbonded interactions. A time step of 20 fs for shorter chain and of 15ns for the complete chain was used , and the neighbor list for nonbonded interactions was updated every 200 fs. Simulations in the NPT ensemble were carried out in NPT ensemble. The simulations were carried out at a constant temperature of 300 K. We equilibrate the system in water for 500 ns using Berendsen thermostat ($\tau_T = 1$) and Berendsen pressure coupling ($\tau_P = 4$). he simulations were carried out with stochastic velocity rescale thermostat [77] ($\tau_T = 1$) and Parrinello-Rahman barostat ($\tau_P = 4$) [78]. A compressibility of 4.5×10^{-5} bar^{-1} was used. Length of the trajectories is some μs.

To build the aggregate structure, we stacked the porphyrins one on the other and each porphyrin is rotated by $\pm\pi/2$ or π with respect to the previous one. To determine the appropriate distance, we performed a simulation of twenty bare porphyrin (see Figure 9.7) in vacuum and we calculated the mean distance between the COMs of adjacent porphyrin.

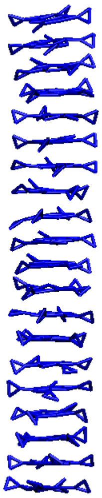

Figure 9.7: Aggregate of bare TPP.

9.3.2 Simulations of TPP-GIGKF aggregates

We performed simulations of TPP-GIGKF aggregates of different lengths (tetramer, octamer and dodecamer) with different starting configurations. The length of each trajectory is 2 μs. A general trend was found, irrespective the starting configuration: Stable face-to-face aggregates were formed, characterized by some relative shift between adjacent porphyrins. In Figure 9.8, the final structures of CG simulations are compared with those of the AA simulation reported in Chapter 8 . We can see that the structures of aggregates are similar in the two cases, which can be taken as a indication that CG parameterization retains the chemical specificity. An important advantage of the CG force field is that we can run much longer trajectories.

Figure 9.9 shows the twist angle calculated along the trajectory in a simulation of a dodecamer. We can clearly see jumps between preferred twist angles and correlations between nearest neighbours and next-nearest neighbours. The simulations evidence a special role of phenylalanine-phenylalanine (F-F) and F-TPP ring interactions, which compete in guiding the aggregate structure. Figure 9.10 shows the Y parameter defined in eq. (7.7), along trajectories of a tetramer, an octamer and a dodecamer. It fluctuates between negative and positive value, but its mean value of Y, $\langle Y \rangle$, is positive, although small (see Table 9.1).

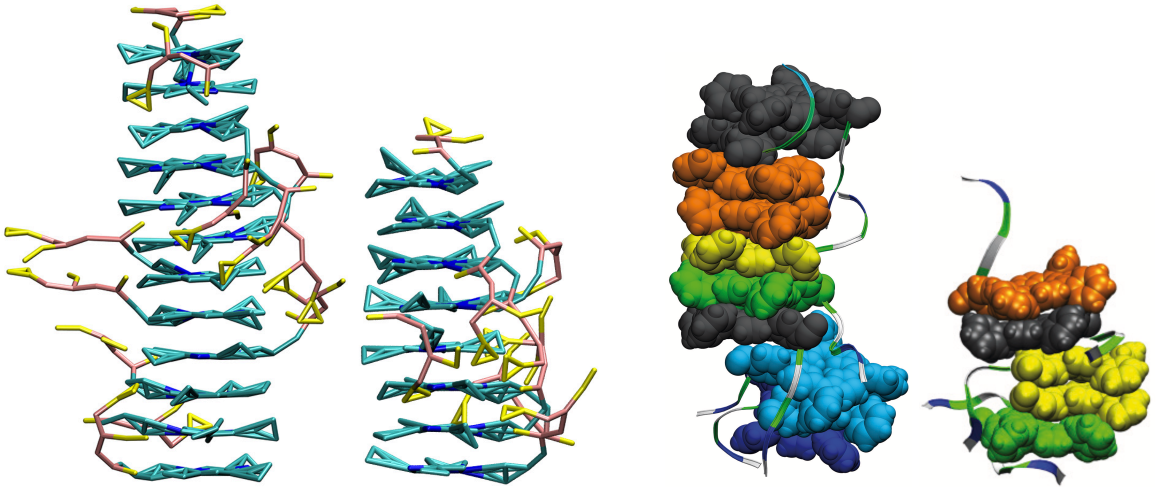

Figure 9.8: Final snapshots from CG simulations of a dodecamer and an octamer (left) and AA simulations of a decamer and a pentamer (right). Colors code amino acids properties. White: non polar. Green: Polar. Red : Acidic. Blue : Basic.

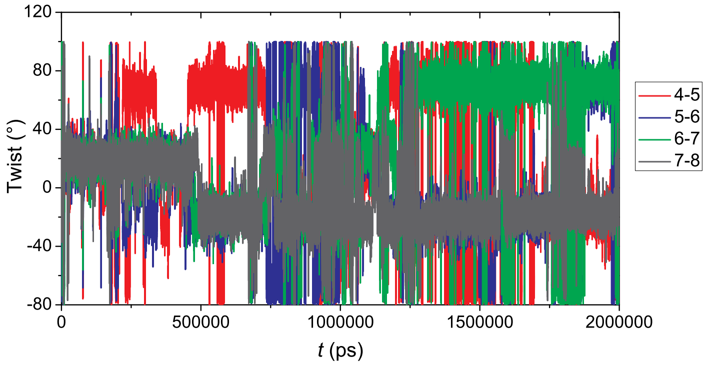

Figure 9.9: Twist angle, τ, between adjacent porphyrins of a dodecamer along a trajectory.

Number of units	$\langle Y \rangle$
4	1.92×10^{-3}
8	1.19×10^{-3}
12	3.0×10^{-3}

Table 9.1: Mean value of the Y parameter calculated for a tetramer, an octamer and a dodecamer of TPP-GIGKF.

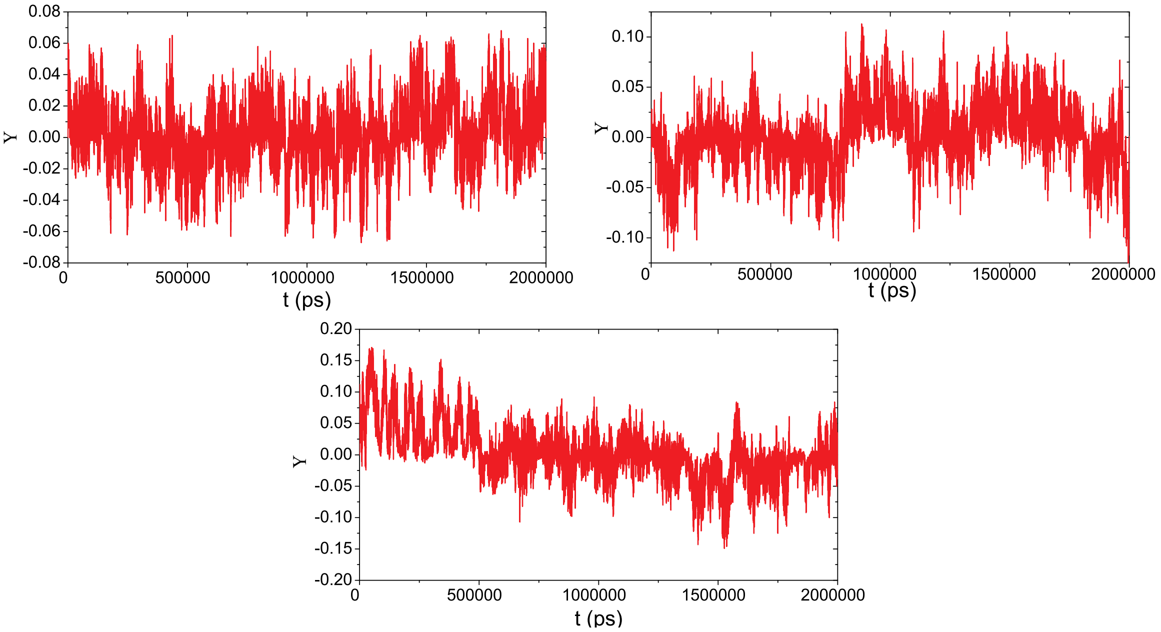

Figure 9.10: Y parameter calculated along the trajectories of a tetramer (left), an octamer (right) and a dodecamer (bottom) of TPP-GIGKF.

9.3.3 Simulations of TPP-MAG aggregates

We performed simulations of dodecamers of TPP-MAG conjugates with different starting conformations. In these porphyrins were rotated one with respect to the other by $+\pi/2$ (A), $-\pi/2$ (B) and π (C). The length of trajectories is 1-2 μs. Linear aggregates were stable along the trajectories, although there was a dynamic formation of shorter oligomers linked by peptides. Figure 9.11 shows the final snapshots. We can observe that porphyrins are not perfectly stacked on the top of the other, but are slightly shifted. The snapshots look different, both for the arrangement of the porphyrins and the orientation of peptides.

To study the chirality of aggregates, we determined the distribution of τ twist angles and the Y parameter, as well as the angles (ϕ, θ) that define the orientation of peptide chains. Figures 9.12 -9.14 show the distribution probability of the twist angles obtained from simulations A, B, C respectively. For A and C these distributions are mainly peaked in the positive region, from 0 to $\pi/2$, and in A there are generally narrower than in C. This means that there is a preferential R chirality. Instead, for B the twist angle distributions are broad and located in positive and negative regions. In this case, there is no clear preferential chirality.

Figure 9.10 shows the Y parameter along the trajectories. It is mainly positive for A and C, whereas for B it fluctuates between positive and negative values. Accordingly, its mean value, $\langle Y \rangle$ is positive for A and C and negative for B (see Table 9.2). This result is in agreement with the twist angle distributions reported above. The values of $\langle Y \rangle$ are larger than those obtained for shorter chains.

More insight into the structural details is provided by the analysis of angles (ϕ, θ) (defined in subsequent 7.3.1). Figures 9.16 - 9.17 show the contour plots of the (θ, ϕ) distributions

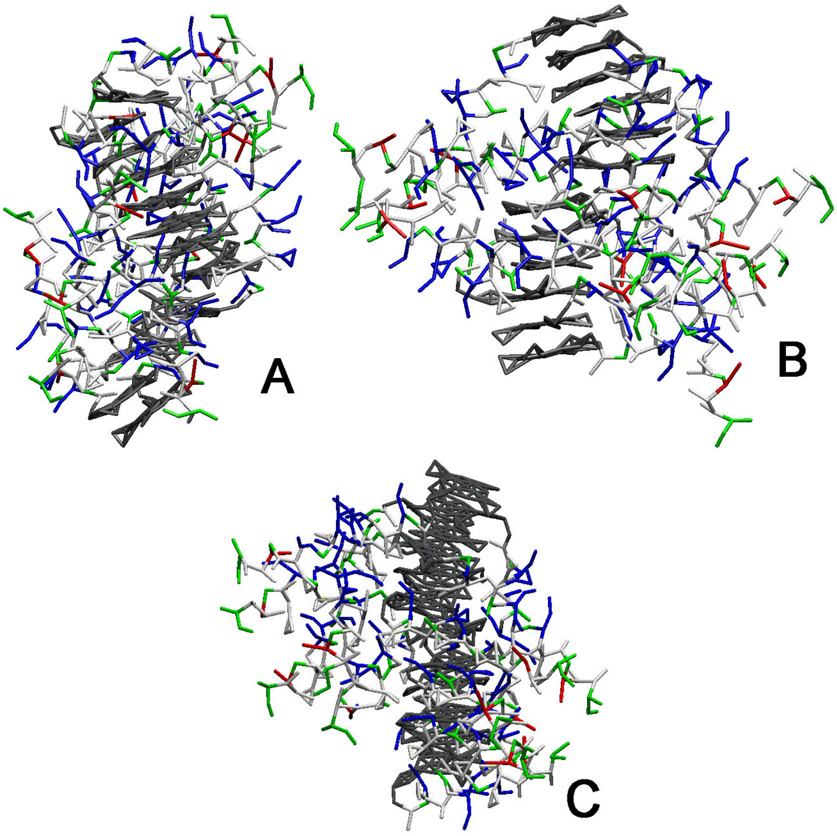

Figure 9.11: Final snapshots of A, B and C trajectories. Colors code amino acids properties. White: non polar. Green: Polar. Red : Acidic. Blue : Basic.

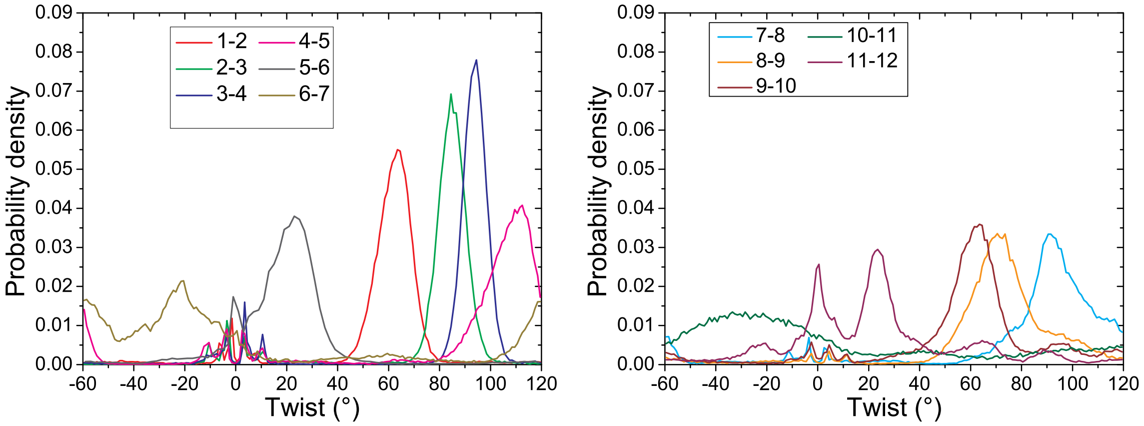

Figure 9.12: Probability distribution of the twist angle, τ, between adjacent porphyrins in a dodecamer of TPP-MAG (A simulation).

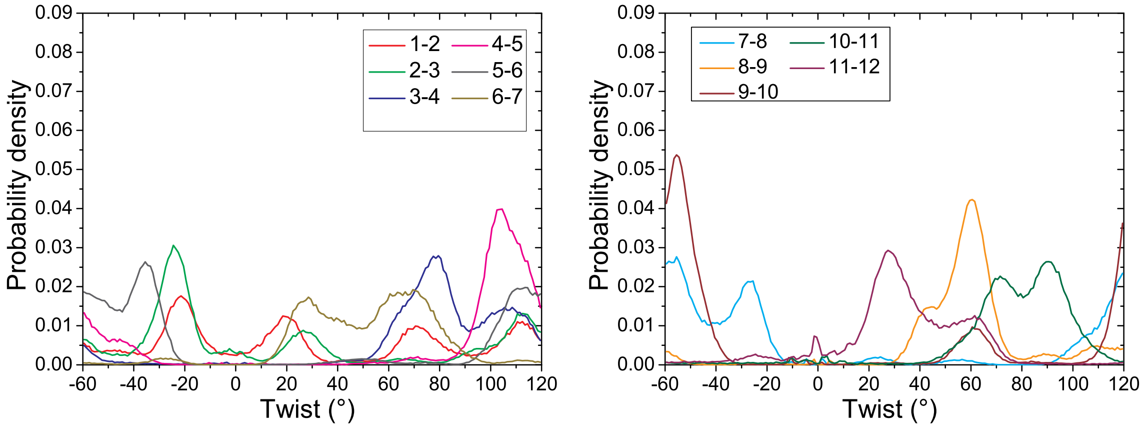

Figure 9.13: Probability distribution of the twist angle, τ, between adjacent porphyrins in a dodecamer of TPP-MAG (B simulation).

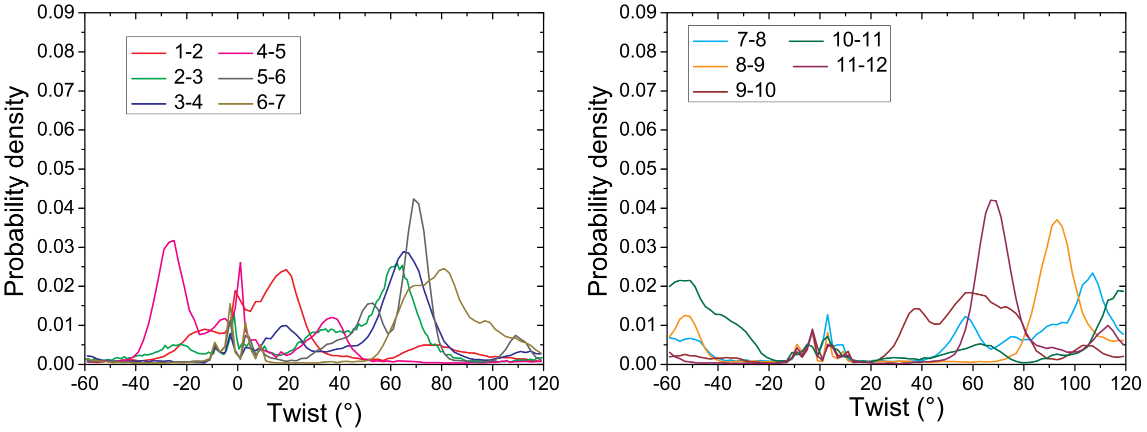

Figure 9.14: Probability distribution of the twist angle, τ, between adjacent porphyrins in a dodecamer of TPP-MAG (C simulation).

angle	$\langle Y \rangle$
$+\pi/2$	3.745×10^{-2}
$-\pi/2$	-1.366×10^{-2}
π	1.847×10^{-2}

Table 9.2: Mean value of Y parameter calculated for a dodecamer of TPP-MAG along A (top), B (middle), and C (bottom) trajectories

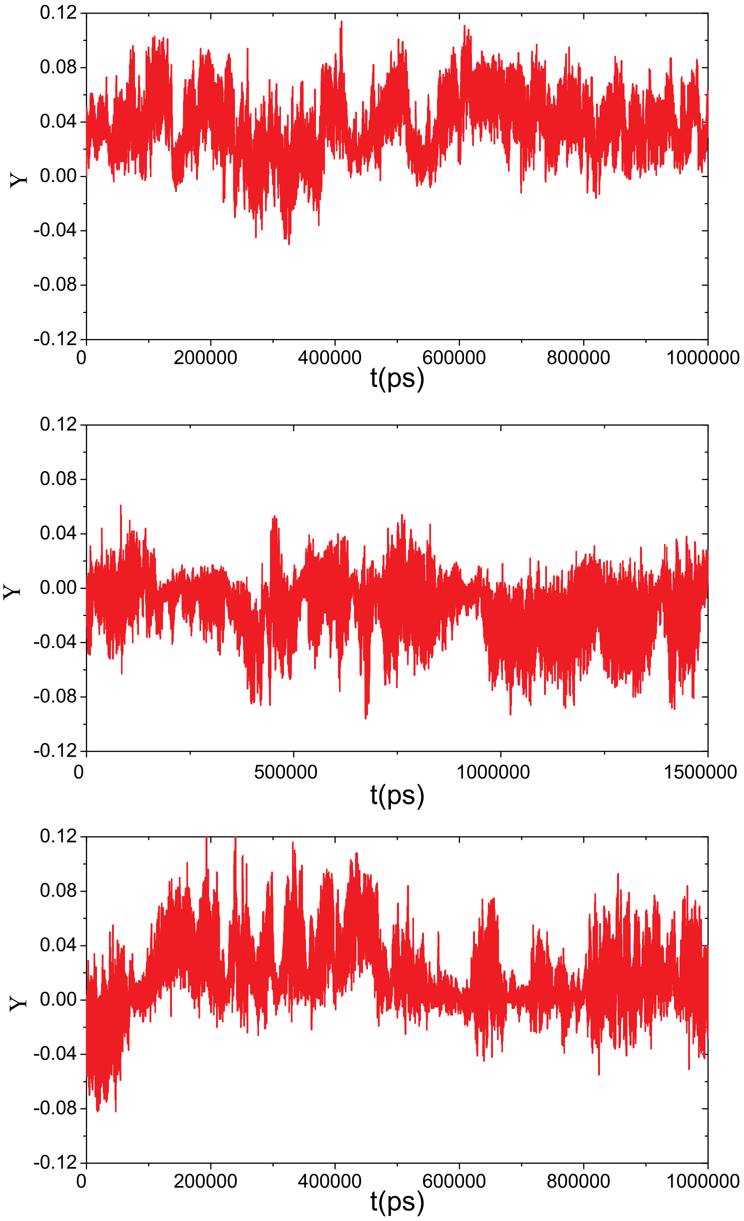

Figure 9.15: Y parameter calculated for a dodecamer of TPP-MAG along A (top), B (middle), and C (bottom) trajectories.

calculated for the six central conjugates (4-9) in A, B, C simulations. In case B (L aggregate), different contour plots are obtained for the units in the aggregate: Positive and negative values of ϕ have approximately the same probability. Therefore, there is no evidence of preferential orientation of the peptides; this can be related to the lack of a net handedness int the τ twist angle distributions (see Figure 9.13). On the contrary, in both A and C simulations (R aggregates), the peptide chains are found to have a preferential orientation, although there are some differences between the two cases. In C the peptides lie near to the porphyrin plane ($\theta \approx 90°$) with $\approx 90° < \phi <\approx 120°$ or $\approx -90° > \phi >\approx -120°$, but the latter configuration is less probable. In A, the situation is similar, but the probability of positive and negative ϕ values inserted (see Figure 9.19). In fact, in A and C the relative orientation of porphyrins is different: In the former the angle between the X-axes of the LOC frames (see subsection 7.3.1) of adjacent porphyrins is smaller than $\pi/2$, whereas in the latter this angle is π and $3/2\pi$. This angle should not be confused with the twist angle τ, which is defined as the smaller angle between the X directions of the LOC frames.

Figure 9.20 shows the comparison between the final snapshots of A, B and C simulations. One can notice that the surface exposed to the solvent is lower in case A. In this case, the proper orientation of the peptide chains allows hydrophobic amino acids, in particular phenylalanines (F), to interact with each other and with porphyrins, so creating a shell that excludes solvent from contact with hydrophobic groups. In Figure 9.21 we can distinguish that there are groups of two or three chains which strongly interact with each other . In simulation C, the peptide chains of adjacent units are nearly located at opposite sides and there are strong interactions between the chains of next-near neighbour. In this case phenylalanines tend to preferentially interact with the nearby phenyls of TPPs (see Figure 9.21). In B, the structure of aggregate is more disordered and the peptides seem to be unable to simultaneously interact with each other and with porphyrins.

9.4 Conclusions

We have derived a MARTINI model for TPP covalently linked to glycine and we have verified that the coarse grained model of TPP-MAG retains the atomistic structure of the system.We have then carried out MD simulations of aggregates of TPP-GIGKF (with shorter peptide) and TPP-MAG (full length peptide) in water. Use of the CG model has allowed us to reach the μs timescale and to overcome the sampling limits found in AA simulations (see Chapter 8). The chirality of aggregates has been quantified by suitable descriptors.

We have found that rod-like aggregates of TPP-GIGKF are stable along the trajectory, although single porphyrins can easily rotate around the axis perpendicular to their molecular plane. In the aggregates porphyrins stack on top of each other, with a slight relative shift of their centers of mass and a net, yet not strong preference for a right-handed configuration. The chiral peptide chains are responsible for this breaking of chiral symmetry. In the case of TPP-MAG the longer tails affect the structure of aggregates, which are less regular and mobile

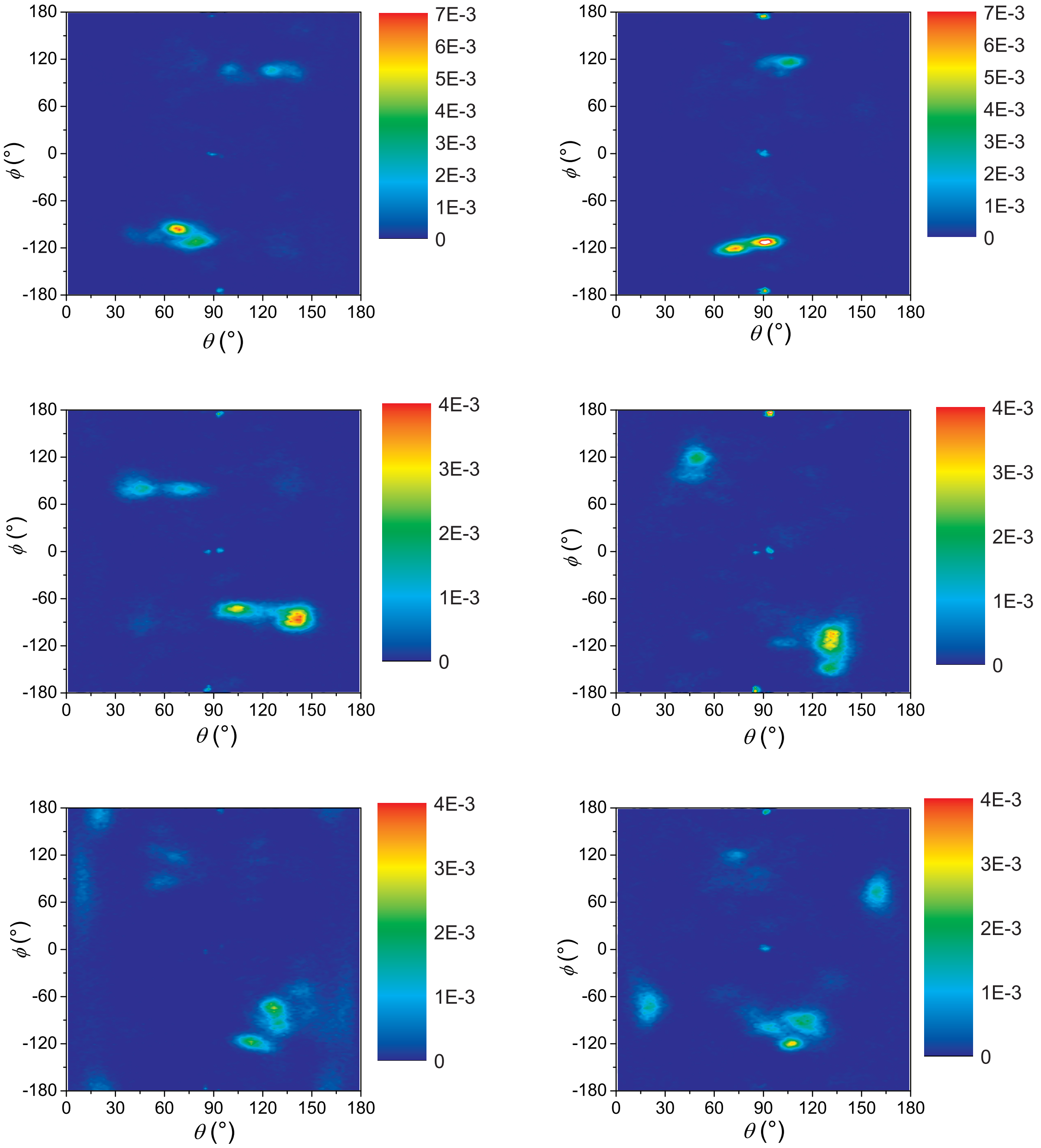

Figure 9.16: Contour plots of the distribution of θ, ϕ angles (see subsequent 7.3.1) from the A trajectory of central (4-9) TPP-MAG conjugates .

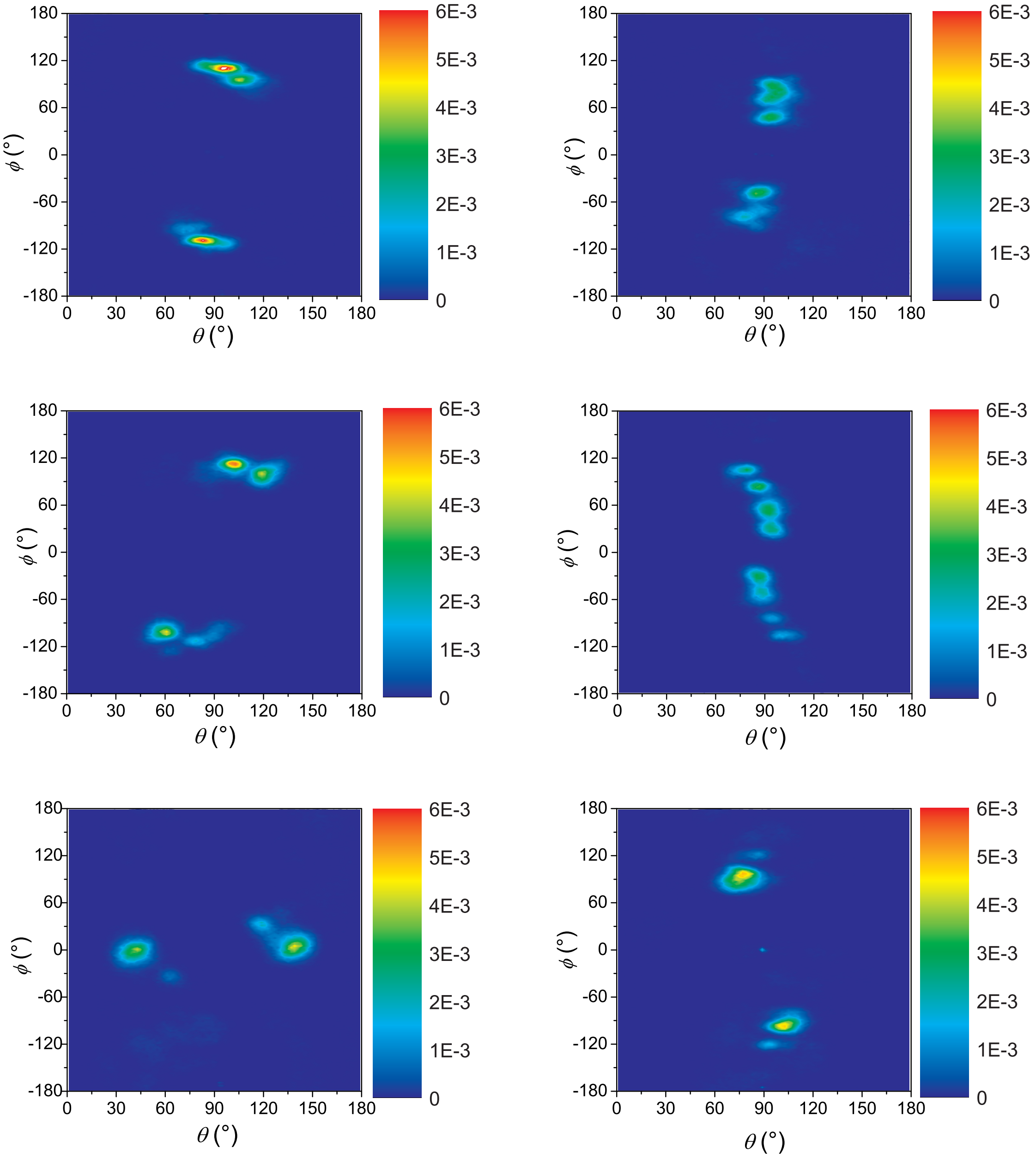

Figure 9.17: Contour plots of the distribution of θ, ϕ angles (see subsequent 7.3.1) from the B trajectory of central (4-9) TPP-MAG conjugates .

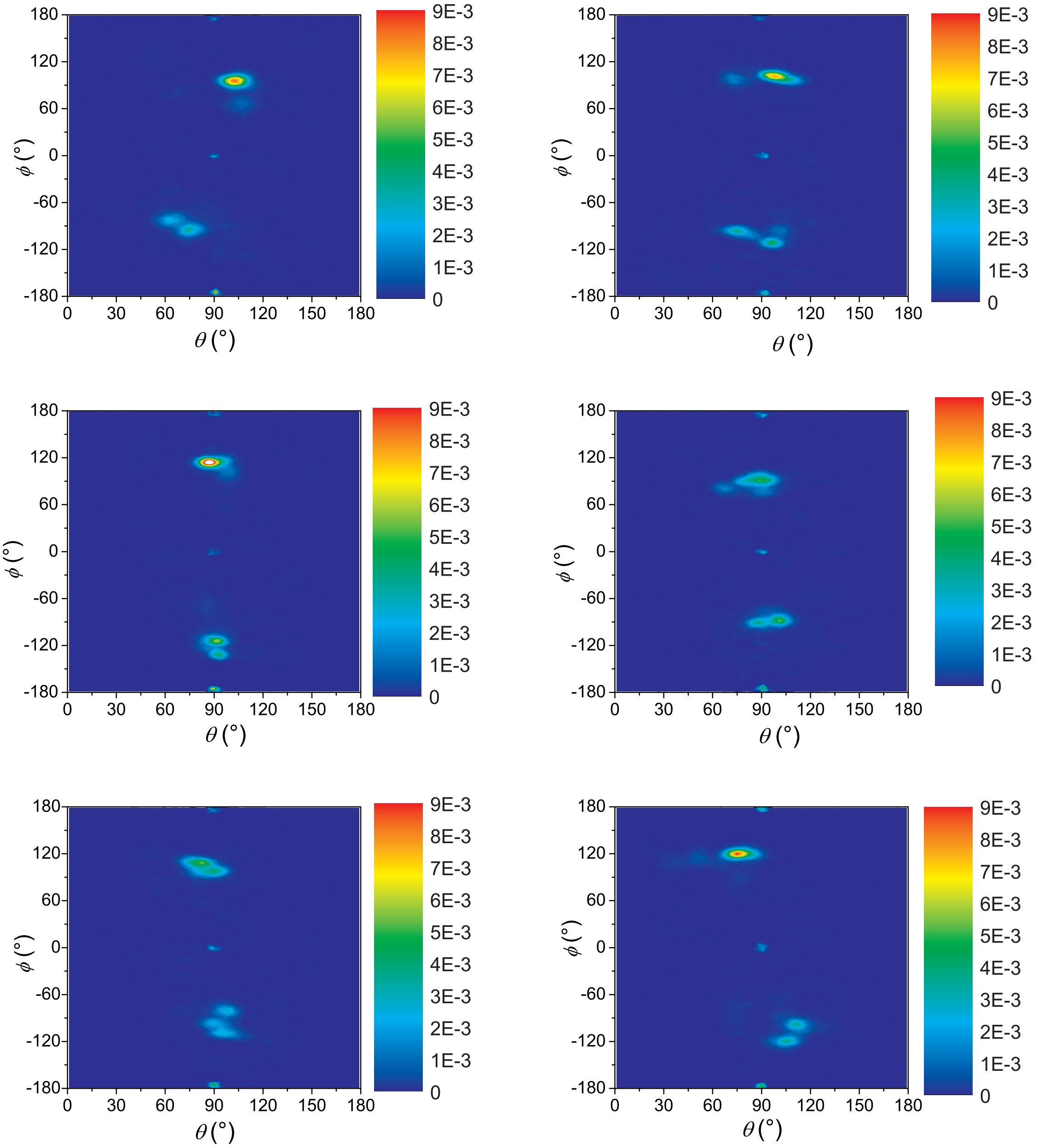

Figure 9.18: Contour plots of the distribution of θ, ϕ angles (see subsequent 7.3.1) from the C trajectory of central (4-9) TPP-MAG conjugates .

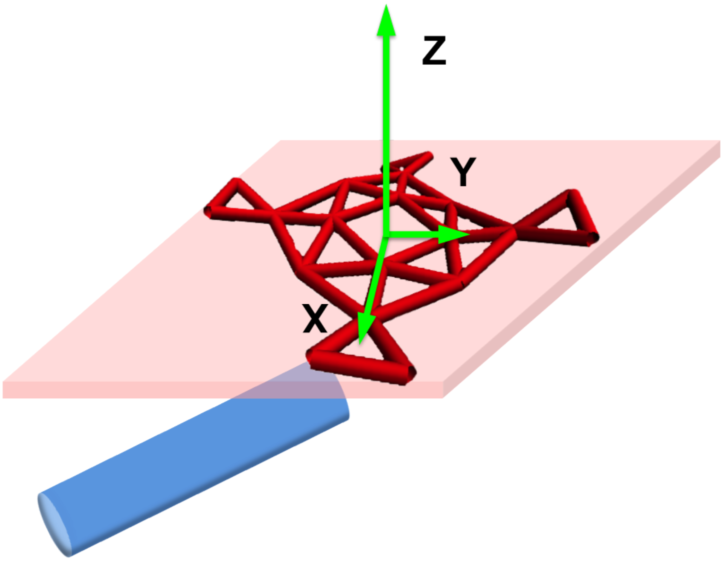

Figure 9.19: Schematic representation of a single TPP-MAG conjugate inside a right-handed aggregate.

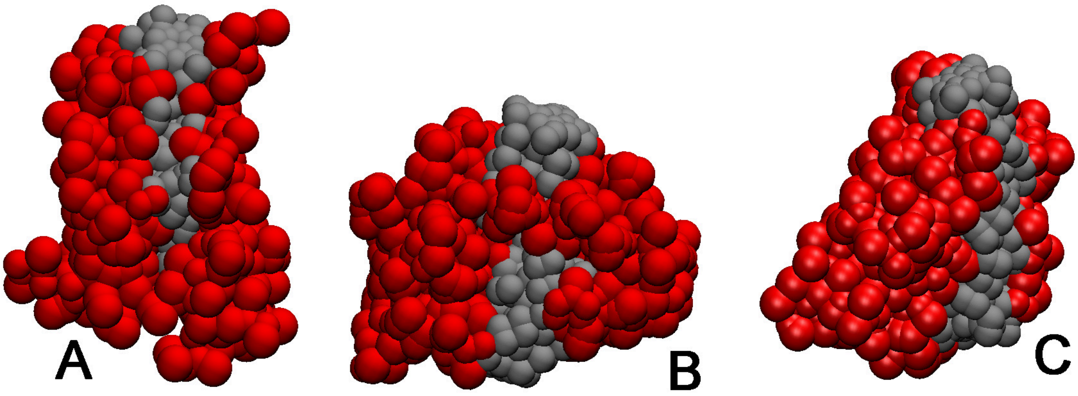

Figure 9.20: Final snapshots of A, B and C. trajectories Red spheres: Peptide. Gray spheres: Porphyrin.

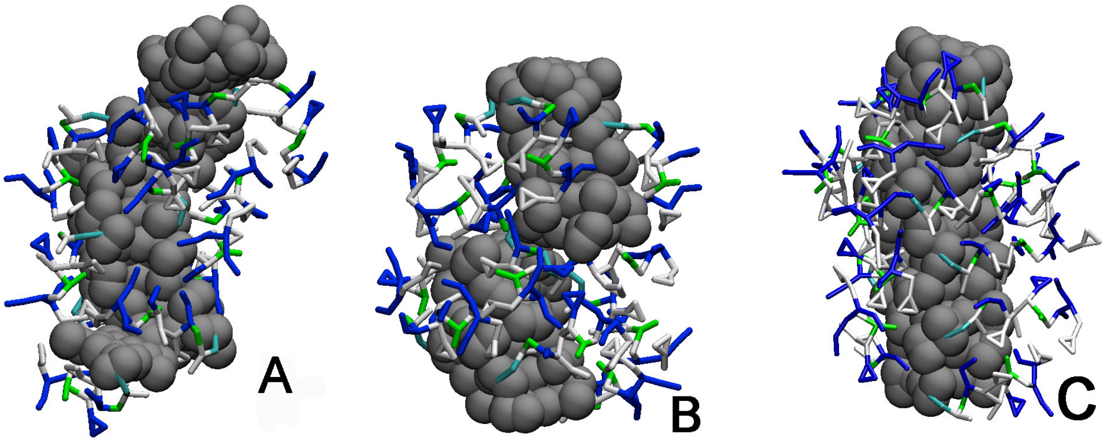

Figure 9.21: Final snapshots of A, B, C trajectories. For the sake of clarity only the first part of peptide is shown (GIGKFLHSAKKF). Colors code amino acids properties. White: non polar. Green: Polar. Red : Acidic. Blue : Basic.

than those formed by TPP-GIGKF. The simulations evidence strong interactions between hydrophobic amino acids of different chains and of these aminoacids with porphyrins. A special role is played by phenylalanine (F): F-F and F-TPP interactions compete in guiding the structure of aggregates. Although both right- and left-handed relative configurations of pairs of porphyrins are found, the former prevail. This is in agreement with the exciton couplet observed in circular dichroism experiments. The right-handed configuration allows the peptide chains to have a proper orientation to optimize the interactions of the hydrophopic aminoacids with each other and with porphyrins, while excluding water.

Bibliography

(1) L. Ziserman, H.-Y. Lee, S. R. Raghavan, A. Mor, and D. Danino, *J. Am. Chem. Soc.*, 2011, **133**, 2511–2517.

(2) T. B. Schuster, D. de Bruyn Ouboter, C. G. Palivan, and W. Meier, *Langmuir*, 2011, **27**, 4578–4584.

(3) A. Lakshmanan, S. Xhang, and C. Hauser, *Trends Biotechnol.*, 2012, **30**, 155–165.

(4) A. D'Urso, M. Fragalà, and R. Purrello, *Chem. Comm.*, 2012, **4**, 8165–8176.

(5) M. De Napoli, S. Nardis, R. Paolesse, M. G. H. Vicente, R. Lauceri, and R. Purrello, *J. Am. Chem. Soc.*, 2004, **126**, 5934–5935.

(6) M. A. Casticiano, A. Romeo, G. De Luca, V. Villari, L. Monsù Scolaro, and N. Micali, *J. Am. Chem. Soc.*, 2010, **133**, 765–767.

(7) G. De Miguel, M. T. Martin-Romero, J. Pedrosa, E. Muñoz, M. Pérez-Morales, T. H. Richardson, and L. Camacho, *Phys. Chem. Chem. Phys.*, 2008, **10**, 1569–1576.

(8) W. W. Parson, *Modern Optical Spectroscopy*, Springer, 2007.

(9) S. F. Mason, *Molecular Optical Activity and the Chiral Discrimination*, Cambridge University Press, Cambridge, 1982.

(10) N. Harada and K. Nakanishi, *Circular Dichroic Spectroscopy - Exciton Coupling in Organic Stereochemistry*, Oxford University Press, Oxford, 1983.

(11) N. Berova, L. Di Bari, and G. Pescitelli, *Chem. Soc. Rev.*, 2007, **36**, 914–931.

(12) N. Berova, K. Nakanishi, and R. W. Woody, *Circular Dichroism: Principles and Applications*, Wiley, 2000.

(13) N. Greenfield and G. Fasman, *Biochemistry*, 1969, **8**, 4108–4116.

(14) V. P. Saxena and D. B. Wetlaufer, *Proc. Natl. Acad. Sci. USA*, 1971, **68**, 969–972.

(15) W. C. J. Johnson, *Methods Enzymol.*, 1992, **210**, 426–447.

(16) G. D. Ramsay and M. R. Eftink, *Methods Enzymol.*, 1994, **240**, 615–645.

(17) R. W. Woody, *Methods Enzymol.*, 1995, **246**, 34–71.

(18) K. W. Plaxco and C. M. Dobson, *Curr. Opin. Struct. Biol.*, 1996, **6**, 630–636.

(19) T. Pan and T. R. Sosnick, *Nat. Struct. Biol.*, 1997, **4**, 931–938.

(20) R. W. Woody, *Adv. Biophys. Chem.*, 1992, **2**, 37–79.

(21) J.-H. Fuhrhop, C. Demoulin, C. Boettcher, J. Köning, and U. Siggel, *J. Am. Chem. Soc.*, 1992, **114**, 4159–4165.

(22) W. Scheidt and Y. Lee, *Struct. Bond.*, 1987, **64**, 1–70.

(23) C. Hunter, P. Leighton, and J. Sanders, *J. Chem. Soc. Perkin. Trans.*, 1989, **1**, 547–552.

(24) C. Hunter and J. Sanders, *J. Am. Chem. Soc.*, 1990, **112**, 5525–5534.

(25) X. Huang, K. Nakanishi, and N. Berova, *Chirality*, 2000, **12**, 237–255.

(26) I. Guryanov, A. Moretto, S. Campestrini, Q. Broxterman, B. Kaptein, C. Peggion, F. Formaggio, and C. Toniolo, *Biopolymers*, 2006, **82**, 482–490.

(27) M. Kasha, H. Rawls, and M. El-Bayoumi, *Pure Appl. Chem.*, 1965, **11**, 371–392.

(28) A. D. Schwab, D. E. Smith, C. S. Rich, E. R. Young, W. F. Smith, and J. C. de Paula, *J. Phys. Chem. B*, 2003, **107**, 11339–11345.

(29) R. Rotomskis, R. Augulis, V. Snitka, R. Valiokas, and B. Liedberg, *J. Phys. Chem. B*, 2004, **108**, 2833–2838.

(30) N. Micali, V. Villani, M. A. Castriciano, A. Romeo, and L. M. Scolaro, *J. Phys. Chem. B*, 2006, **110**, 8289–8295.

(31) S. Gandini, E. Gelamo, R. Itri, and M. Tabak, *Biophys. J.*, 2003, **85**, 1259–1268.

(32) Z. Wang, C. J. Medforth, and J. Shelnutt, *J. Am. Chem. Soc.*, 2004, **126**, 15954–15955.

(33) Z. Wang, C. J. Medforth, and J. Shelnutt, *J. Am. Chem. Soc.*, 2004, **126**, 16720–16721.

(34) N. Micali, F. Mallamace, A. Romeo, R. Purrello, and L. M. Scolaro, *J. Phys. Chem. B*, 2000, **104**, 5897–5904.

(35) N. Micali, F. Mallamace, A. Romeo, R. Purrello, and L. M. Scolaro, *J. Phys. Chem. B*, 2000, **104**, 9416–9420.

(36) M. Castriciano, A. Romeo, V. Villari, N. Micali, and L. M. Scolaro, *J. Phys. Chem. B*, 2003, **107**, 8765–8771.

(37) S. M. Vlaming, R. Au-gulls, M. C. Stuart, J. Knoester, and P. H. M. Loosdrecht, *J. Phys. Chem. B*, 2009, **113**, 2273–2283.

(38) B. Friesen, B. Wiggins, J. L. McHale, U. Mazur, and K. W. Hipps, *J. Am. Chem. Soc.*, 2010, **132**, 8554–8556.

(39) R. Purrello, L. M. Scolaro, E. Bellacchio, S. Gurrieri, and A. Romeo, *Inorg. Chem.*, 1998, **37**, 3647–3648.

(40) R. Purrello, A. Raudino, L. M. Scolaro, A. Loisi, R. Bellacchio, and R. Laceri, *J Phys Chem B*, 2000, **104**, 10900–10908.

(41) A. Mammana, M. De Napoli, L. Rosario, and R. Purrello, *Bioorg. Med. Chem.*, 2005, **13**, 5159–5163.

(42) R. Lauceri, A. D'Urso, A. Mammana, and R. Purrello, *Chirality*, 2008, **20**, 411–419.

(43) G. de Miguel, M. Martín-Romero, J. Pedrosa, E. Muñoz, M. Pérez-Morales, T. Richardson, and L. Camacho, *Phys. Chem. Chem. Phys.*, 2008, **10**, 1569–1576.

(44) L. Zhang, Q. Lu, and M. Liu, *J. Phys. Chem. B*, 2003, **107**, 2565–2569.

(45) R. Lettieri, D. Monti, K. Zelenka, T. Trnka, P. Drasărc, and M. Venanzi, *NewJ. Chem.*, 2012, **36**, 1246–1254.

(46) `http://cti.itc.virginia.edu/~cmg/Demo/wheel/wheelApp.html`.

(47) P. M. R. Paulo, J. N. C. Lopes, and S. M. B. Costa, *J. Phys. Chem. B*, 2008, **112**, 14779–14792.

(48) H. Ode, S. Matsuyama, M. Hata, T. Hoshino, J. Kakizawa, and W. Sugiura, *J. Med. Chem.*, 2007, **50**, 1768–1777.

(49) T. Cheatham, T. Darden, H. Gohlke, R. Luo, K. Merz, A. Onufriev, C. Simmerling, B. Wang, R. Woods, and D. Case, *J. Comp. Chem.*, 2000, **21**, 1049–1074.

(50) M. J. Frisch et al., *Gaussian 03, Revision C.02*, Gaussian, Inc., Wallingford, CT, 2004.

(51) W. D. Cornell, P. Cieplak, C. I. Bayly, and P. A. Kollman, *J. Am. Chem. Soc.*, 1993, **115**, 9620–9631.

(52) Y. Duan, C. Wu, S. Chowdhury, M. C Lee, G. Xiong, W. Zhang, R. Yang, P. Cieplak, R. Luo, T. Lee, J. Caldwell, J. Wang, and P. Kollman, *J. Comp. Chem.*, 2003, **24**, 1999–2012.

(53) M. W. Mahoney and W. Jorgensen, *J. Chem. Phys.*, 2000, **112**, 8910–8922.

(54) W. Jorgensen and J. D. Madura, *J. Am. Chem. Soc.*, 1983, **105**, 1407–1413.

(55) P. Florová, P. Sklenovský, P. Banáš, and M. Otyepka, *J. Chem. Theory Comput.*, 2010, **6**, 3569–3579.

(56) J.-P. Ryckaert, G. Ciccotti, and H. Berendsen, *J. Comput. Phys.*, 1977, **23**, 327–341.

(57) U. Essmann, L. Perera, M. L. Berkowitz, and T. Darden, *J. Chem. Phys.*, 1995, **103**, 8577–9593.

(58) G. Tiberio, L. Muccioli, R. Berardi, and C. Zannoni, *Chem. Phys. Chem.*, 2009, **10**, 125–136.

(59) H. J. C. Berendsen, J. P. M. Postma, W. F. van Gunsteren, A. Di Nola, and J. R. Haak, *The Journal of Chemical Physics*, 1984, **81**, 3684–3690.

(60) D. Paschek, H. Nymeyer, and A. E. Garcìa, *J. Struct. Biol.*, 2007, **157**, 524–533.

(61) J. Wang, P. Cieplak, and P. A. Kollman, *J. Comput. Chem.*, 2000, **21**, 1049–1074.

(62) A. Onufriev, D. Bashford, and D. A. Case, *Proteins*, 2004, **55**, 383–394.

(63) M. S. Shell, R. Ritterson, and K. A. Dill, *J. Phys. Chem. B*, 2008, **112**, 6878–6886.

(64) S. K. Kandasamy and R. G. Larson, *Chem. Phys. Lipids*, 2004, **132**, 113–132.

(65) S. J. Marrink, H. J. Risselada, S. Yefimov, D. P. Tieleman, and A. H. de Vries, *J. Phys. Chem. B*, 2007, **111**, 7812–7824.

(66) L. Monticelli, S. K. Kandasamy, X. Periole, R. G. Larson, D. P. Tieleman, and S. J. Marrink, *J. Chem. Theory and Comput.*, 2008, **4**, 819–834.

(67) J. Wong-Ekkabut, S. Baoukina, W. Triampo, I. M. Tang, and L. Monticelli, *Nat. Nanotechnol*, 2008, **3**, 363–368.

(68) C. A. López, A. J. Rzepiela, A. H. de Vries, L. Dijkhuizen, P. Hünenberg, and S. J. Marrink, *J. Chem. Theory and Comput.*, 2008, **4**, 819–834.

(69) G. Rossi, L. Monticeli, S. R. Puisto, I. Vattulainen, and T. Ala-Nissila, *Soft Matter*, 2011, **7**, 698–708.

(70) X. Periole and S.-J. Marrink, in *Biomolecular Simulations: Methods and Protocols*, ed. L. Monticelli and E. Salonen, Springer Protocols, 2012.

(71) S. Marrink, A. H. de Vries, and A. E. Mark, *J. Phys. Chem. B*, 2004, **108**, 750–760.

(72) W. F. van Gunsteren and H. J. C. Berendsen, *J. Comput. Aid. Mol. Des.*, 1987, **1**, 171–176.

(73) T. Straatsma and H. J. C. Berendsen, *J. Chem. Phys.*, 1988, **89**, 5876–5886.

(74) A. E. Mark, in *Encyclopedia of Computational Chemistry*, ed. P. Schleyer, John Wiley & Sons, 1998.

(75) A. Villa and A. E. Mark, *J. Comput. Chem.*, 2002, **23**, 548–553.

(76) W. F. van Gunsteren and H. J. C. Berendsen, *Mol. Sim.*, 1988, **1**, 173–185.

(77) G. Bussi, D. Donadio, and M. Parrinello, *J. Chem. Phys.*, 2007, **126**, 014101.

(78) M. Parrinello and A. Rahman, *J. Appl. Phys.*, 1981, **52**, 7182.

(79) S. P. Songca and B. Mbatha, *J. Pharm. Pharmacol.*, 2000, **52**, 1361–1367.

(80) A. B. Ormond and H. S. Freeman, *Dyes and Pigments*, 2013, **96**, 440–448.

Part V

Summary

Chapter 10

Summary

This thesis deals with the propagation of chirality from the molecular to the supramolecular and the macroscopic level in self-assembling systems. In particular, three topics are addressed:

I. the organization of helical particles in anisotropic and chiral phases;

II. the linear aggregation and formation of cholesteric phases by double-stranded nucleic acid oligomers;

III. self-assembly of porphyrin-peptide conjugates in water. These problems have been addressed using different theoretical and computational methods.

The research has been carried out in collaboration with experimentalists (II and III) , and with other theoreticians (I).

Part II presents a theoretical and computational investigation of the the anisotropic and chiral phases formed by helical particles. This study is motivated by the ubiquity of the helical shape: from natural polynucleotides and polypeptides to synthetic polymers, there is a variety of systems featuring the helix as the basic structural unit. We have focussed on simple model helices made of fused hard spheres. We have performed a detailed investigation of the phase diagram and we have analysed the relationship between helix structure and phase behaviour. This has been done using Onsager theory, which can be viewed as a form of the classical Density Functional Theory implemented at the level of the second virial approximation. In parallel, Monte Carlo simulations of the same helical particles were performed by research groups in Venice and in Madrid. The combined investigation was meant to compensate for the limits of each single approach.

Chapter 2 focuses on the uniform nematic phase and on the isotropic-to-nematic (IN) transition. The main goal of this study was to rationalize the changes in the phase behaviour on going from straigh rod-like to quite tortuous helical particles. Theory allowed us to identify for each helical system the approximate boundaries of the nematic phase; this served as a guide for subsequent, more demanding MC simulations. Theory and simulations agree in predicting a shift of the IN transition to higher density with increasing radius and decreasing pitch of the helix. We have found that the aspect ratio, which is usually taken as the key quantity for the IN transition, is not a suitable descriptor for helices, since there are specific effects of helical parameters. This study has also a methodological objective: we wanted to evaluate the accuracy of Onsager theory in the case of non-convex particles. We have found that for high helicity Onsager theory departs from numerical simulations, even when a modified form of the Parsons-Lee rescaling is included to account for the non-convexity of particles. This points to the need of a more effective theory for hard non-convex particles, a field that remains largely unexplored.

Chapter 3 presents a study of the cholesteric phase formed by hard helices as a function of the structural parameters of the particles. Our systematic investigation confirms the expectation, based on geometry considerations, that the cholesteric organization has a non-monotonic dependence upon the helix parameters. In particular, the handeness of the particles does not necessarily correspond to that of the phase: so, right-handed helical particles can form either a right- or a left-handed cholesteric phase, depending on their specific structure. For strongly curled helices we predict very tight cholesteric pitches, of the order of one hundred times the characteristic length of particles, which have never been evidenced in real systems.

In Chapter 4 we report the full phase diagram of hard helices, which reveals a zoo of phases with peculiarities that depend on the helical parameters. The most important result is the discovery of a novel chiral nematic phase, which we have called screw-like nematic(N_s), originating from the specific helical shape of the particles. It appears at very high density and, similarly to the cholesteric, is still a nematic phase in that helices are homogeneously distributed and mobile with their long axis preferentially oriented along the same direction, the main director However, differently from the cholesteric, the N_s phase is characterized by a long range correlation of the C_2 ($\hat{\mathbf{w}}$) symmetry axes of helices. These are preferentially oriented along an axis that spirals around the main director with a periodicity equal to the pitch of the helical particles. We have fully characterized the N_s phase, evidenced by MC simulations, by suitable order parameters and correlation functions and, using Onsager theory we have given a theoretical understanding of the entropy driven nematic-to-screw-like nematic phase transition. Experimental evidences of a phase with the features of the screw-like nematic have been presented for helical flagella [E. Barry et al., *Phys. Rev. Lett.*,2006, **96**, 018305]; in this case the phase modulation, in the μm range, could be observed by polarized optical microscopy. Our study suggests that the N_s organization must be a general feature for helical particles at high density, and we hope that it can stimulate further investigation in systems, like DNA and helical polymers, where experimental detection can be challenging.

In Part III we have studied the linear aggregation and formation of liquid crystal phases by double-stranded nucleic acid oligomers. It is well known that, above a certain concentration, solutions of double stranded B-DNA, with a number of base pairs higher than about one hundred, exhibit a left-handed cholesteric phase. Recently, it has been discovered that even short oligomers of nucleic acids form a cholesteric phase. However in this case both left- and right-handed organization was observed, depending on the sequence [G. Zanchetta et al., *P.*

Natl. Acad. Sci. USA, 2010, **107**, 17497-17502], and this result remained unexplained.

Chapter 5 deals with the relationship between the sequence of oligonucleotides and the properties of their cholesteric phase, ignoring the effect of aggregation. Since the systems are polyelectrolytes, the theory described in Chapter 3 has beenextended to take in account electrostatics, at the level of the linearized Poisson-Boltzmann equation. In particular we have focused on a set of DNA dodecamers with self-complementary sequences. The structural differences deriving from the sequence were taken into account by a coarse grained (CG) representation of the systems, based on crystallographic data. Calculations were performed for linear aggregates of oligomers, with fixed aggregation length. We have found that in these systems, irrespective of sequence, steric interactions lead to a right-handed cholesteric phase, whereas electrostatic repulsions promote a left-handed organization. Based on this study we can propose an explanation for the experimental changes in phase chirality as a function of the NA sequence. Such changes would reflect a switch from a regime of lower DNA concentration, where electrostatic interactions play a role, to a very high concentration condition, where best packing controls the mutual orientation of DNA aggregates. The sequence would determine the phase handedness by controlling the density range in which the cholesteric phase exists.

Then, in Chapter 6, we develop a theoretical model for the cholesteric phase formed by DNA oligomers with hard core interactions, which integrates the theory for cholesteric order with that for linear aggregation in the nematic phase. This is the first theory which allows to predict the cholesteric properties of self-assembling systems and their dependence on temperature and concentration as a result of the interplay of aggregation and orientational order. this allows a quanitative comparison with experimental data. The theory has been applied to two DNA dodecamers with self-complementary sequences which form duplexes with different geometry and experimentally have been found to form cholesteric phases with opposite handedness. The same CG representation described in Chapter 5 has been used. We have been able to analyze the dependence of various phase properties on the aggregation length and we have found interesting effects, which include re-entrance. We have seen that aggregation amplifies the differences between oligomers with different sequence. For one of the systems under investigation the theoretical results are in reasonable agreement with the experimental behavior: the cholesteric handedness (right) is correctly predicted and the pitch is about ten times longer than the measured value, a discrepancy ascribable to the fact that the model neglects the flexibility of aggregates. On the contrary, for the other system both the predicted pitch and cholesteric handedness are wrong. Our interpretation is that a mechanism based only on steric repulsions is not sufficient in the latter case. These results seem to support our suggestion, based on the simpler approach outlined in Chapter 5, that the relevant interactions that control the formation of the cholesteric phase in DNA oligomers may change with sequence.

Part IV deals with self-assembly of porphyrin-peptide conjugates. In particular, we have studied the behaviour of conjugates between 5-(4′-carboxyphenyl)-10,15,20-triphenylporphyrin

(TPP) and the peptide [Leu^{21}] magainin (GIGKFLHSAKKFGKAFVGEILNS). This system was synthesized in the group of Professor Marina Gobbo (Università di Padova) and subsequent characterization by UV-Vis absorption spectroscopy and circular dichroism experiments gave indication of chiral aggregation. We have used Molecular Dynamics simulations to explore the interactions within conjugates and between them in water and to investigate the stability and structure, in particular the chirality, of their aggregates.

Chapter 7 introduces some concepts of circular dichroism and exciton coupling theory and gives a brief review of the state of the art of self-assembly of porphyrin based systems. Chapter 8 presents all atom Molecular Dynamics simulations of single TPP-[Leu^{21}] magainin and of aggregates of different lengths of this conjugate, both in implicit and explicit water. We have found that the peptide chain folds on porphyrin, interacting with it through its hydrophobic amino acids and exposing to solvent the polar ones. In the presence of two or more conjugates, there are also face-to-face interactions between porphyrins. Both kinds of interactions contribute to the stabilization of aggregates. However, the time scale of atomistic simulations was found to be insufficient to fully characterize the behaviour of aggregates; their final structure was found to depend on the starting configuration and no clear preferential arrangement could be inferred.

In Chapter 9, we present Molecular Dynamics simulations based on the coarse-grained MARTINI force field. First, the force field parameters for TPP covalently linked to glycine were derived. Then, simulations of aggregates of TPP-[Leu^{21}] magainin and TPP covalently linked to a shorter peptide were performed. We have shown that the coarse-grained model retains the atomistic chemical structure, with the advantage that longer trajectories can be obtained (some μs). Therefore, it has allowed us to overcome the problems of sampling and timescale found in atomistic simulations. The chirality of aggregates has been quantified by suitable descriptors. For the conjugates with shorter peptide, we have found that rod-like aggregates are stable along the trajectory, although single porphyrins can easily rotate around the axis perpendicular to their molecular plane. In the aggregates porphyrins stack on top of each other, with a slight relative shift of their centers of mass and a net, yet not strong preference for a right-handed configuration. The chiral peptide chains are responsible for this breaking of chiral symmetry. In the case of TPP-[Leu^{21}] magainin the longer tails affect the structure of aggregates, which are less regular and mobile. The simulations evidence strong interactions between hydrophobic amino acids of different chains and of these aminoacids with porphyrins. A special role is played by phenylalanine (F): F-F and F-TPP interactions compete in guiding the structure of aggregates. Although both right- and left-handed relative configurations of pairs of porphyrins are found, the former prevail. This is in agreement with the exciton couplet observed in circular dichroism experiments. The right-handed configuration allows the peptide chains to have a proper orientation to optimize the interactions of the hydrophopic aminoacids with each other and with porphyrins, while excluding water.

Part VI

Appendix

Appendix A

Wigner functions and spherical irreducible tensors [1]

A.1 Euler angles and rotation matrix

The relative orientation of two Cartesian reference systems xyz and XYZ is defined univocally by three angles. They can be given in several ways, Euler angles being one of them and they define the transformation that brings the system on the other

$$\{x,y,z\} \overset{(\alpha,\beta,\gamma)}{\longrightarrow} \{X,Y,Z\} \tag{A.1}$$

decomposed in the following three successive rotations:

$$\{x,y,z\} \overset{\alpha(z)}{\longrightarrow} \{x',y',z'\} \overset{\beta(y')}{\longrightarrow} \{x'',y'',z''\} \overset{\gamma(z'')}{\longrightarrow} \{X,Y,Z\} \tag{A.2}$$

1. Rotation of an angle α around the z-axis ;
2. Rotation of an angle β around the y'-axis ;
3. Rotation of an angle γ around the z''-axis.

The α and γ range are $[0,2\pi]$, instead the range of β is $[0,\pi]$. The corrisponding rotation matrices have the following forms:

$$R_x(\gamma) = \begin{pmatrix} \cos\gamma & \sin\gamma & 0 \\ -\sin\gamma & \cos\gamma & 0 \\ 0 & 0 & 1 \end{pmatrix}$$

$$R_y(\beta) = \begin{pmatrix} \cos\beta & 0 & -\sin\beta \\ 0 & 1 & 0 \\ \sin\beta & 0 & \cos\beta \end{pmatrix}$$

$$R_z(\alpha) = \begin{pmatrix} \cos\alpha & \sin\alpha & 0 \\ -\sin\alpha & \cos\alpha & 0 \\ 0 & 0 & 1 \end{pmatrix} \tag{A.3}$$

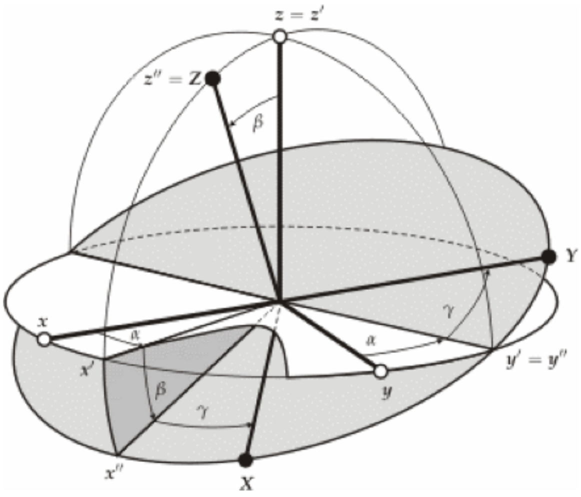

Figure A.1: Scheme of relative orientation of two Cartesian reference systems (xyz and XYZ).

A.2 Wigner rotation matrix

1. Definition:

$$\begin{aligned} D^L_{MK}(\alpha,\beta,\gamma) &= e^{-\imath M\alpha} d^L_{MK}(\beta) e^{-\imath K\gamma} \\ d^L_{MK}(\beta) &= [(L+M)!(L-M)!(L+K!)(L-K)!]^{1/2} \\ &\times \sum_i (-1)^i \frac{\left(\cos\frac{\beta}{2}\right)^{2L-2i-M+K}\left(-\sin\frac{\beta}{2}\right)^{2i+M-K}}{(L-M-i)!(L-K-i)!(i+M-K)!} \end{aligned} \tag{A.4}$$

2. Symmetry properties:

$$\begin{aligned} d^L_{MK}(\beta) &= (-1)^{M-K} d^L_{KM}(\beta) = (-1)^{M-K} d^L_{-M-K}(\beta) = d^L(KM)(-\beta) \\ D^{L*}_{MK}(\alpha,\beta,\gamma) &= (-1)^{M-K} D^{L*}_{-M-K}(\beta) = D^{L*}_{MK}(-\alpha,\beta,-\gamma) \end{aligned} \tag{A.5}$$

3. Orthogonality

$$\int d\mathbf{\Omega} D^{L_1}_{M_1K_1}(\mathbf{\Omega}) D^{L_2}_{M_2K_2}(\mathbf{\Omega}) = \frac{8\pi^2}{2L+1}\delta_{L_1,L_2}\delta_{M_1,M_2}\delta_{K_1,K_2} \tag{A.6}$$

4. Couple representation of the product of two Wigner matrix

$$\begin{aligned} D^{L_1}_{M_1K_1}(\mathbf{\Omega}) D^{L_2}_{M_2K_2}(\mathbf{\Omega}) &= \sum_{L=|L_1-L_2|}^{L_1+L_2} C(L_1,L_2,L;M_1,M_2,M) C(L_1,L_2,L;K_1,K_2,K) D^L_{MK}(\mathbf{\Omega}) \\ &= \sum_{L=|L_1-L_2|}^{L_1+L_2} (2L+1) \begin{pmatrix} L_1 & L_2 & L \\ M_1 & M_2 & M \end{pmatrix} \begin{pmatrix} L_1 & L_2 & L \\ K_1 & K_2 & K \end{pmatrix} D^{L*}_{MK}(\mathbf{\Omega}) \end{aligned} \tag{A.7}$$

where $C(L_1,L_2,L;M_1,M_2,M)$ and $C(L_1,L_2,L;K_1,K_2,K)$ are the Clebsh-Gordan coefficients, $\langle L_1M_1,L_2M_2|L-M\rangle$ and $\langle L_1K_1,L_2K_2|L-K\rangle$, and those ones that appear in the second identity are the $3j$ coefficients:

$$\begin{pmatrix} L_1 & L_2 & L \\ M_1 & M_2 & M \end{pmatrix} = (-1)^{L_1-L_2-M}\sqrt{2L+1}\,\langle L_1M_1, L_2M_2|L-M\rangle$$
$$\begin{pmatrix} L_1 & L_2 & L \\ K_1 & K_2 & K \end{pmatrix} = (-1)^{L_1-L_2-K}\sqrt{2L+1}\,\langle L_1K_1, L_2K_2|L-K\rangle \tag{A.8}$$

5. Integral of the product of three Wigner matrix

$$\int d\mathbf{\Omega}\, D^{L}_{MK}(\mathbf{\Omega})D^{L_1}_{M_1K_1}(\mathbf{\Omega})D^{L_2}_{M_2K_2}(\mathbf{\Omega}) = 8\pi^2 \begin{pmatrix} L_1 & L_2 & L \\ M_1 & M_2 & M \end{pmatrix}\begin{pmatrix} L_1 & L_2 & L \\ K_1 & K_2 & K \end{pmatrix} \tag{A.9}$$

A.3 Spherical irreducible tensors

The transformation of a cartesian tensor $T_{\chi\chi'}$ for rotation can be easy expressed if the tensor is rewritten on the irreducible spherical components T_{LM} which transform on basis of the Wigner matrix: $T^L_K = \sum_M D^L_{MK}(\Omega)T^L_M$.

The conversion of a tensor $a_\alpha(\alpha = x, y, z)$ of cartesian components to spherical components $a_\mu(\mu = 1, 0, -1)$ can be express through a transformation matrix U:

$$a_\mu = \sum_\alpha U_{\mu\alpha}a_\alpha \tag{A.10}$$

in explicit form

$$\begin{pmatrix} a_{-1} \\ a_0 \\ a_1 \end{pmatrix} = \begin{pmatrix} U_{-1x} & U_{-1y} & U_{-1z} \\ U_{0x} & U_{0y} & U_{0z} \\ U_{1x} & U_{1y} & U_{1z} \end{pmatrix}\begin{pmatrix} a_x \\ a_y \\ a_z \end{pmatrix} \tag{A.11}$$

where

$$U = \begin{pmatrix} \frac{1}{\sqrt{2}} & \frac{-i}{\sqrt{2}} & 0 \\ 0 & 0 & 1 \\ -\frac{1}{\sqrt{2}} & -\frac{i}{\sqrt{2}} & 0 \end{pmatrix} \tag{A.12}$$

In explicit form, the irreducible spherical components are

$$a_{-1} = T_{-1} = \left(\frac{1}{2}\right)^{1/2}(X - \imath Y) \tag{A.13a}$$

$$a_0 = T_1 = Z \tag{A.13b}$$

$$a_1 = T_1 = -\left(\frac{1}{2}\right)^{1/2}(X + \imath Y) \tag{A.13c}$$

The irreducible spherical components of a tensor of second rank have the following form:

$$T_{LM} = \sum_{\sigma\sigma'} C(11L; \sigma\sigma' m)T_{\sigma\sigma'} \tag{A.14}$$

where

$$T_{\sigma\sigma'} = \sum_{\chi\chi'} U_{\sigma\chi} U_{\sigma'\chi'} T_{\chi\chi'} \tag{A.15}$$

In explicit form

$$T_{0,0} = -\frac{\{T^{XX} + T^{YY} + T^{ZZ}\}}{\sqrt{3}} \tag{A.16a}$$

$$T_{1,-1} = \frac{\{(T^{ZX} - T^{XZ}) - i(T^{ZY} - T^{YZ})\}}{2} \tag{A.16b}$$

$$T_{1,0} = -\frac{\{i(T^{XY} - T^{YX})\}}{\sqrt{2}} \tag{A.16c}$$

$$T_{1,1} = \frac{\{(T^{ZX} - T^{XZ}) + i(T^{ZY} - T^{YZ})\}}{2} \tag{A.16d}$$

$$T_{2,-2} = \frac{\{T^{XX} - T^{YY} - \imath(T^{XY} + T^{YX})\}}{2} \tag{A.16e}$$

$$T_{2,-1} = \frac{\{T^{XZ} + T^{ZX} - \imath(T_{YZ} + T^{ZY})\}}{2} \tag{A.16f}$$

$$T_{2,0} = \frac{\{T^{ZZ} - (T^{XX} + T^{YY})\}}{\sqrt{6}} \tag{A.16g}$$

$$T_{2,1} = -\frac{\{T^{XZ} + T^{ZX} + \imath(T^{YZ} + T^{ZY})\}}{2} \tag{A.16h}$$

$$T_{2,2} = \frac{\{T^{XX} - T^{YY} + \imath(T^{XY} + T^{YX})\}}{2} \tag{A.16i}$$

Appendix B

Molecular dynamics [2, 3]

Molecular dynamics simulation consists of the numerical solution of the Newton equations of motion for a molecular system

$$\mathbf{f}_i = m\ddot{\mathbf{r}}_i \tag{B.1}$$

or equivalently the solution of the classical Hamiltonian equation:

$$\begin{aligned} H\left(\mathbf{p}_i, \mathbf{r}_i\right) &= \sum_{i=1}^{N} \frac{\mathbf{p}_i}{2m_i} + V(\mathbf{r}_i) \\ \dot{\mathbf{p}}_i &= -\frac{\partial H}{\partial \mathbf{r}_i} = \mathbf{f}_i \\ \dot{\mathbf{r}}_i &= \frac{\partial H}{\partial \mathbf{p}_i} = \frac{\mathbf{p}_i}{m} \end{aligned} \tag{B.2}$$

where $\mathbf{p}_i$, m_i and $\mathbf{r}_i$ are the linear momentum, the mass and the position of atom i respectevely, $V(\mathbf{r}_i)$ is the potential energy. We need able to calculate the forces $\mathbf{f}_i$ acting on the atoms, which are usually derived from a potential energy $V(\mathbf{r}^N)$, with $\mathbf{r}^N = (\mathbf{r}_1, \mathbf{r}_2, .., \mathbf{r}_N)$ represented the complete set of $3N$ atomic coordinates.

Potential energy can be expressed as

$$V(\mathbf{r}) = V_{nonbonded} + V_{bonded} \tag{B.3}$$

where $V_{nonbonded}$ represents nonbonded interactions between atoms and V_{bonded} represents the bonding potentials. Figure B.1 shows an example of the potential terms. The potential energy $V_{nonbonded}$ is traditionally split into 1-body, 2-body, 3-body . . . terms:

$$V_{nonbonded}(\mathbf{r}^N) = \sum_i v((\mathbf{r}_i)) + \sum_i \sum_{j>i} v(\mathbf{r}_i, \mathbf{r}_j) + ... \tag{B.4}$$

where the term $v((\mathbf{r}))$ represents an externally applied potential field or the effects of the container walls, $v(\mathbf{r}_i, \mathbf{r}_j)$ $[v(\mathbf{r}_{ij})]$ represents the pair potential interactions. It is usual to consider only the pair potential and neglect the higher order interactions. Commonly the pair potentials are the Lennard-Jones potential

$$v^{\mathrm{LJ}}(r) = 4\epsilon\left[\left(\frac{\sigma}{r}\right)^{12} - \left(\frac{\sigma}{r}\right)^{6}\right] \tag{B.5}$$

and , if electrostatic charges are present, the appropriate Coulomb potentials:

$$v^{\text{Coulomb}}(r) = \frac{q_1 q_2}{4\pi\epsilon_0 r} \tag{B.6}$$

where σ is the diameter and ϵ, the well depth, q_1 and q_2 are the charges and ϵ_0 is the permittivity in vacuum.

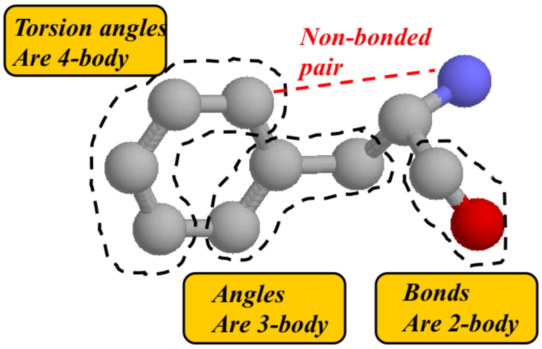

Figure B.1: Typical examples of potential terms used in common force-field.

For molecules we must also consider the intramolecular bonding interactions derived from simple physical forces

$$V_{bonded} = V_{intramolecular} = V_{bond} + V_{angle} + V_{torsional} \tag{B.7}$$

where

$$\begin{aligned} V_{bond} &= \frac{1}{2}\sum_{\text{bonds}} k^r_{ij}(r_{ij} - r_{eq})^2 \\ V_{angle} &= \frac{1}{2}\sum_{\substack{\text{bend}\\\text{angle}}} k^\theta_{ijk}(\theta_{ijk} - \theta_{eq})^2 \\ V_{torsion} &= \frac{1}{2}\sum_{\substack{\text{torsional}\\\text{angle}}} \sum_m k^{\phi,m}_{ijlk}(1 + \cos(m\phi_{ijkl} - \gamma_m)) \end{aligned} \tag{B.8}$$

whit $r_{ij} = |\mathbf{r}_i - \mathbf{r}_j|$ the separation between adjacent pairs of atoms, r_{eq} the equilibrium distance, θ_{ijk} the angle between successive bonds vectors such as $\mathbf{r}_i - \mathbf{r}_j$ and $\mathbf{r}_j - \mathbf{r}_k$, ϕ_{ijkl} the dihedral angles defined by the atoms i, j, k and l, k^r_{ij}, k^θ_{ijk} and $k^{\phi,m}_{ijlk}$ the strength parameters of the bonds, bend angle and torsional angle potentials.

Knowing the potential energy function $V(\mathbf{r}^N)$, the next step is to calculate the atomic forces, and then it is possible to determine the acceleration of each atom in the system. Integration of the equations of motion yields a trajectory that describes the positions, velocities and accelerations of the particles as they vary with time. From this trajectory, the average values of properties can be determined. This method is deterministic: The state of the system at any future time can be predicted from its current state. For any step in the integration, the force acting on each atom is assumed to be constant during the time interval and the forces on the atoms are computed and combined with the current positions and velocities to generate new positions and velocities a short time ahead.

Appendix C

List of scientific publications

The work of this PhD thesis originated the following scientific publications:

Papers

- E. Frezza, F. Tombolato, A. Ferrarini *Soft Matter* **7**, 9291 (2011)
- E. Frezza, A. Ferrarini, H.B. Kolli, A. Giacometti, G. Cinacchi, *J. Chem. Phys.* **138**, 164906 (2013)

Submitted/In Preparation

- H. B. Kolli, E. Frezza, G. Cinacchi, A. Ferrarini, A. Giacometti, T. Hudson, From rods to helices: new evidence of a screw-like nematic phase *J. Chem. Phys.* submitted
- H. B. Kolli, E. Frezza, A. Ferrarini, A. Giacometti, G. Cinacchi, T. Hudson, C. de Michele, F. Sciortino, *Soft Matter*, in preparation
- E. Frezza, A. Ferrarini, H.B. Kolli, A. Giacometti, G. Cinacchi, in preparation
- E. Frezza, A. Ferrarini, C. De Michele, *Macromolecules*, in preparation
- E. Frezza, L. Monticelli, A. Ferrarini, M. Gobbo, , in preparation

Bibliography

(1) A. D. Varshalovich, N. A. Moskalev, and V. Kersonskii, *Quantum Theory of Angular Momentum*, World Scientific, New York, 1995.

(2) M. P. Allen and D. J. Tildesley, *Computer simulation of Liquids*, Clarendon Press, Oxford, 1987.

(3) D. Frenkel and B. Smit, *Understanding Molecular Simulation: From Algorithms to Applications*, Academica, San Diego, 2002.

Acknowledgements

Finally these three years have passed and it is time to thank all the people without whom this thesis would not have been possible.

For the first part, I am grateful to Prof. Achille Giacometti, Hima Bindu Kolli (Università Ca' Foscari di Venezia) and Dr. Giorgio Cinacchi (Universidad Autónoma de Madrid) for Monte Carlo simulations of hard helical particles.

For the second part, I gratefully acknowledge Prof. Tommaso Bellini and Dr. Giuliano Zanchetta (Università degli Studi di Milano) for stimulating discussion and for sharing with us their results. I thank Dr. Lourdes Campos (Universitat Politècnica de Catalunya, Barcelona) for information on crystals of oligonucleotides. My acknowledgment goes also to Dr Cristiano De Michele ("Sapienza" - Università di Roma) for the theory of linear aggregation of B-DNA oligomers.

For the third part, I am grateful to Prof. Marina Gobbo (Università degli Studi di Padova) who shared with us the fascinating problem of self-assembly of porphyrin-peptide conujagates and synthesised and characherized them. My acknowledgment goes also to Dr. Luca Monticelli (INSERM and Istitut de Biologie et Chemie des Protéines, Lyon) who hosted me in Paris and helped me in the development of the MARTINI force field for porphyrin.

After these institutional acknowledgments, I would like to thanks my parents, Patrizia and Gian Paolo, and the rest of my family for their continued support throughout my life and my university career.

My thanks to my friends and colleagues for the great time I had in the last three years. In particular, I would like to thank my classmate Agnese for her support and encouragement. Many thanks to Giorgia, Serena, Silvia and Anna, my fencer friends. Many thanks to Giulia and Cristina for their support, the atmosphere and their friendship in our group. My thanks to Daniel for his cookies, and to Silvia, Marzio, Mirco for the lunch time. Many thanks to Fishdog divers: Every moment with them is full of fun and laughs.

Last but not least, thanks to Mattia for his encouragement, patience, friendship and love: Many thanks for believing in me even when I did not, our life together is an amazing adventure every day.